The Nature of Flat Galaxies

Inauguraldissertation

zur Erlangung der Würde eines Doktors der Philosophie
vorgelegt der
Philosophisch-Naturwissenschaftlichen Fakultät
der Universität Basel

von

Stefan Johann Kautsch

aus Salzburg (Österreich)

Basel, 2006

Genehmigt von der Philosophisch-Naturwissenschaftlichen Fakultät

auf Antrag von
Prof. Dr. Eva K. Grebel und Prof. Dr. John S. Gallagher

Basel, den 24. Oktober 2006

Prof. Dr. Hans-Jakob Wirz
Dekan

0.1 Abstract

Disk galaxies range from bulge-dominated early-type galaxies to late types with little or no bulge. Cosmological models do not predict the formation of disk-dominated, essentially bulgeless galaxies, yet these objects exist. A particularly striking and poorly understood example of bulgeless galaxies are flat or superthin galaxies with large axis ratios. We therefore embarked on a study aimed at a better understanding of these enigmatic objects, starting by compiling a statistically meaningful sample with well-defined properties. The disk axis ratios can be most easily measured when galaxies are seen edge-on. We used data from the Sloan Digital Sky Survey (SDSS) in order to identify edge-on galaxies with disks in a uniform, reproducible, automated fashion. In the five-color photometric database of the SDSS Data Release 1 (2099 deg^2) we identified 3169 edge-on disk galaxies, which we subdivided into disk galaxies with bulge, intermediate types, and simple disk galaxies without any obvious bulge component. We subdivided these types further into subclasses: Sa(f), Sb(f), Sc(f), Scd(f), Sd(f), Irr(f), where the (f) indicates that these galaxies are seen edge-on. We find that approximately 15% of the edge-on disk galaxies in our catalog are flat galaxies, demonstrating that these galaxies are fairly common, especially among intermediate-mass star-forming galaxies. Bulgeless disks account for roughly one third of our galaxies when also puffy disks and edge-on irregulars are included.

Interactions between galaxies can transform their morphology, and thus lead to a morphology-density relationship even in regions where galaxies are sparsely distributed. We study environments of pure disk galaxies–the simple disk systems–in comparison to systems with bulges as a way to explore how environment relates to galaxy morphology. We study neighbors around the target disk galaxies and seek statistical relationships between local galaxy densities and galaxy structures. The observed trends are interpreted in the context of models for galaxy formation and evolution. Galaxies consisting of simple stellar disks exist in environments ranging from galaxy groups to the isolated field. This distribution overlaps with that of systems with prominent bulges, although galaxies with large bulges are systematically rare at low densities. The edge-on simple disk systems are similar in size but about one magnitude less luminous than galaxies containing bulges. Thus the morphology-density trend among edge-on systems is both one of luminosity, and thus likely stellar mass, and structure. The simple disk galaxies also are bluer, implying star formation extends over a longer time. These characteristics are discussed in terms of the roles of initial angular momentum and interactions in defining the structures of disk galaxies. The presence of simple disks in isolation and also moderate size groups suggests that groups bridge between field regions where galaxy properties are determined by very local conditions and clusters where the global environment dominates.

The last part of this thesis contains a deep K_s-band imaging survey of a sample of edge-on galaxies selected from our catalog. K_s-band permits us to obtain stellar mass distributions of the nuclear and disk components on a uniform basis and fairly unimpeded by dust. We measure morphologies and structural parameters of these components in different galaxy types with special emphasis on thick disks as evolutionary tracers. The thin and thick disk properties are compared with predictions from merger models and pure infall scenarios to constrain galaxy evolution models. The combination of optical and K_s-band colors allows us to constrain the distribution of dust and the vertical color gradients in these galaxies.

0.2 Zusammenfassung

Die Morphologie von Scheibengalaxien erstreckt sich über die frühen Scheibentypen mit grosser zentraler Aufwölbung bis hin zu jenen späten Typen, die keinen solchen Bulge besitzen. Numerische kosmologische Modelle können die Entstehung solcher bauchlosen Galaxien jedoch nicht erklären, obwohl sie zahlreich im Universum vorkommen. Besonders rätselhafte Objekte sind die flachen und superdünnen Galaxien mit grossen Achsenverhältnissen, was auf besonders "kalte" Scheiben schliessen lässt. Um die Häufigkeit der verschiedenen Typen von Scheibengalaxien zu bestimmen führen wir eine Untersuchung der Sloan Himmelsdurchmusterung durch. Dies erlaubt es uns, die Scheibengalaxien in einheitlicher und automatisierter Weise zu katalogisieren. Um jene Galaxien mit Bulge von den bulgelosen zu trennen, benützen wir die Scheibengalaxien, die man in Kantenansicht sieht. Damit haben wir eine grosse Anzahl von Scheibengalaxien gefunden und können sie mit Hilfe eines Programmes in mehrere Gruppen unterteilen: Sa(f), Sb(f), Sc(f), Scd(f), Sd(f), Irr(f), wobei das (f) ihre Kantenansicht ausdrückt. Ungefähr ein Drittel der Objekte in diesem Katalog sind Scheibengalaxien ohne Bulge. Dies demonstriert das häufige Vorkommen dieser Spezies, speziell unter den sternenbildenden Galaxien mittlerer Masse.

Wechselwirkungen zwischen Galaxien können deren Morphologie verändern. Deshalb kann die Beschaffenheit der Umgebung von Galaxien ihre Erscheinungsform beeinflussen. Wir untersuchen Unterschiede in den Umgebungen zwischen Scheibengalaxien mit und ohne Bulge-Komponente und suchen nach Einflüssen der Umgebungsdichte auf die Strukturen unserer Programmgalaxien. Wir finden, dass nahezu alle untersuchten Scheibengalaxien in Umgebungen liegen, die jenen von Galaxiengruppen entsprechen. Trotzdem können wir beobachten, dass es einen leichten systematischen Trend zur geringerer Umgebungsdichte bei den bulgelosen Galaxien – den einfachen Scheibengalaxien – gibt. Aus diesen Ergebnissen sehen wir, dass die Umgebung zwar formgebende Eigenschaften hat, diese jedoch aufgrund der relativ geringen Dichten auch in den Anfangsbedingungen der Protogalaxien, vor Allem im ursprünglichen Drehimpuls, zu suchen sind. Somit kann man die Gruppenumgebung als Übergangsbereich bezeichnen, wo interne und äussere formbestimmende Vorgänge herrschen.

Der letzte Teil dieser Arbeit beinhaltet die Nahinfrarot-Beobachtungen einiger Scheibengalaxien in Kantenansicht. Das infrarote Licht ermöglicht es, die stellare Massenverteilung ohne die abdunkelnde Wirkung von Staub in den Galaxien nachzuvollziehen. Mit Hilfe der Kombination von dem optischen und nahinfraroten Erscheinungsbild der Galaxien können wir die Staubverteilung und vertikale Farbgradienten der Objekte untersuchen. Ausserdem messen wir die Morphologien und Strukturparameter in den ausgewählten Galaxien um ihren Werdegang nachempfinden zu können. Speziell die Frage nach der Häufigkeit und Beschaffenheit der dicken und dünnen Scheibenkomponenten steht dabei im Vordergrund, da diese die globale Entwicklung von Scheibengalaxien offenbaren können.

Contents

0.1 Abstract . . . 3
0.2 Zusammenfassung . . . 4
Contents . . . i
List of Figures . . . xvi
List of Tables . . . xviii
0.3 Danksagung an: . . . xix

1 Introduction **1**
1.1 Late-Type Disk Galaxies in General . . . 3
1.2 Properties of Disk Galaxies . . . 3
1.3 Models of Evolution . . . 8

2 A Catalog of Edge-on Disk Galaxies **11**
2.1 Introduction . . . 11
2.2 Training set and selection criteria . . . 12
2.2.1 The data base . . . 12
2.2.2 Definition of a training set . . . 13
2.2.3 Definition of the query . . . 13
2.3 Target selection . . . 14
2.3.1 Isophote fitting . . . 14
2.3.2 Measuring the luminosity-weighted mean ellipticity and concentration index . . . 15
2.3.3 Choosing the limiting values of CI and ε . . . 15
2.4 The classification of edge-on galaxies . . . 19
2.5 The Catalog . . . 20
2.6 Completeness considerations from sample comparisons . . . 25
2.6.1 A comparison of our automatically selected galaxy sample with our visually classified sample . . . 25
2.6.2 A comparison of the Revised Flat Galaxies Catalog with our catalog . . . 25
2.7 The influence of dust and distance . . . 27
2.8 Discussion . . . 31
2.9 Conclusions and Summary . . . 31

3 Morphology of Edge-on Disk Galaxies **35**
3.1 Introduction . . . 35
3.2 Morphological Discriminators . . . 35
3.2.1 Colors . . . 35
3.2.2 Profile Likelihoods . . . 39
3.2.3 Texture . . . 41
3.2.4 Axial Ratio . . . 41
3.2.5 Isophotal Ellipticity . . . 42
3.2.6 Adaptive Ellipticity . . . 43
3.3 DR5 Extension of the Catalog of Edge-on Disks . . . 44

3.4 Properties of the DR5 edge-on disk galaxies: Results . . . 47
3.5 Discussion and Summary . . . 49
3.6 Detection Rate and Stability . . . 52
3.7 Mass, Extinction and Colors . . . 53

4 The Environment of Edge-on Disk Galaxies 57
4.1 Introduction . . . 57
4.2 Data Analysis . . . 58
4.2.1 Target Selection . . . 58
4.2.2 Search Volumes and Malmquist Bias . . . 59
4.2.3 Selection Biases . . . 63
4.3 Results . . . 65
4.3.1 Morphologies of the Neighbor Galaxies . . . 73
4.3.2 General Distribution of Disk Galaxies . . . 73
4.4 Discussion . . . 77
4.4.1 Environmental Settings . . . 77
4.4.2 Bulges . . . 79
4.4.3 Morphology-Density . . . 80
4.4.4 Nature . . . 80
4.4.5 Nurture . . . 81
4.5 Summary . . . 81
4.6 Additional Points . . . 82
4.6.1 Galaxy Transformation in Galaxy Clusters . . . 82
4.6.2 Secular Evolution and Pseudobulges . . . 83

5 Structure of Simple Disk Galaxies 87
5.1 Introduction . . . 87
5.1.1 Thick Disk . . . 91
5.1.2 Thick Disks in Late-Type Disk Galaxies . . . 92
5.1.3 Predictions by the Models . . . 93
5.1.4 Motivation . . . 94
5.2 Target Selection . . . 94
5.3 Observation and Data Reduction . . . 98
5.3.1 Observing in the Near Infrared . . . 98
5.3.2 Data Reduction . . . 102
5.3.3 Photometric Calibration and Third Iteration . . . 107
5.3.4 Reduction and Calibration of the SDSS Images . . . 110
5.4 Morphological Image Analysis . . . 111
5.4.1 Flatness of the Galaxies . . . 111
5.4.2 Bulge Size of the Galaxies . . . 112
5.4.3 Results . . . 112
5.4.4 Discussion . . . 114
5.4.5 CAS Morphology . . . 118
5.4.6 Results . . . 118
5.4.7 Discussion . . . 122
5.5 Detailed Structure Analysis . . . 124
5.5.1 Sample Selection . . . 124
5.5.2 Isophote Fitting . . . 124
5.5.3 Creation of Color Maps . . . 125
5.5.4 Galaxy Model Fitting . . . 126
5.5.5 Results . . . 129
5.5.6 Discussion and Summary . . . 144

A morf_invest **151**

B AMOR for CI **159**

C AMOR for CAS **161**

D Observed Galaxies in the Near Infrared **163**

List of Figures

1.1 A schematic overview of the manifold morphologies of galaxies. The sphere-dominated early-type galaxies (E, S0) are drawn on the left side. The disk-dominated morphologies (Sc, Irr) are shown on the right side. The spiral galaxies are shown with (top) or without (bottom) a central bar. The galaxies are presented at different viewing angles as indicated in the outer-right column. This diagram: drawn and by courtesy of B. Binggeli. 2

1.2 UGC 10043. This image shows an edge-on galaxy with a prominent, spheroidal bulge. The outer edges of the disk are warped. This is a five band image of $200'' \times 200''$ from the SDSS DR5 Image List Tool. North to the top, east to the left. 4

1.3 UGC 5173. This galaxy is a typical edge-on spiral galaxy with bulge and an organized dust lane–the dark line in the disk. This is a five band image of $200'' \times 200''$ from the SDSS DR5 Image List Tool. North to the top, east to the left. 4

1.4 UGC 9422. This object represents an intermediate type between disk galaxies with and without bulge. This galaxy shows a slight central light concentration. The bright star in the upper right corner shows four refraction spikes which can imitate an edge-on disk galaxy in automated classification codes. This is a five band image of $200'' \times 200''$ from the SDSS DR5 Image List Tool. North to the top, east to the left. 5

1.5 UGC 9856. The figure shows a simple disk galaxy without a central bulge component. This is a five band image of $200'' \times 200''$ from the SDSS DR5 Image List Tool. North to the top, east to the left. 5

1.6 UGC 7321. This is a simple disk galaxy with an extreme ratio between major and minor axis and represent a typical superthin galaxy. This is a five band image of $200'' \times 200''$ from the SDSS DR5 Image List Tool. North to the top, east to the left. 6

1.7 UGC 4704. The figure shows a very late simple disk galaxy with a transition morphology between ordered simple disks and the bulgeless disks of puffy irregulars. The deep blue color indicates large amount of hot and young stars and the lack of dust between the stars. The bright and knotty blue regions are places of recent star formation. At the left bottom part of the image, a face-on disk galaxy is shown. This is a five band image of $200'' \times 200''$ from the SDSS DR5 Image List Tool. North to the top, east to the left. 6

1.8 UGC 7064. A galaxy with two apparent bulges. This could be a projection effect of a spheroidal galaxy in the fore/background, lying exactly in the line of sight to the edge-on disk and simulating the left bulge. The third disk object from the left is a projected foreground star. This is a five band image of $200'' \times 200''$ from the SDSS DR5 Image List Tool. North to the top, east to the left. 7

1.9 UGC 6973. The image shows an edge-on galaxy with bulge, overlapped with a face-on disk and a bright star in the left corner. These two galaxies from this system are probably in the stage of ongoing interpenetration. This is a five band image of $200'' \times 200''$ from the SDSS DR5 Image List Tool. North to the top, east to the left. . 7

2.1 Number distribution of the visually selected galaxies versus their concentration index (CI). 16

2.2 Number distribution of the visually selected galaxies versus their weighted mean ellipticity of the isophotes (ε). 17

2.3 The left image is a typical member of the class of galaxies with bulge Sb(f): SDSS J020405.91-080730.3. A typical example of the Scd(f) intermediate class is in the middle: SDSS J102903.90+611525.8. Simple disk galaxies Sd(f) have an appearance like SDSS J135309.65+045739 at the right. All images are cutouts from the DR3 Image List Tool. These images have a scale of 90 square arcsec. 17

2.4 The main separation diagram. The symbols are cited in the key and represents the various morphological types. The borders of the general classes are marked with long-short dotted lines. The additional short dotted lines corresponds to the subgroup boarders within the general classes. 18

2.5 Logarithmic number distribution of the angular diameters of the catalog galaxies. . . . 21

2.6 Separation diagram with the emphasized size samples. Galaxies with angular diameters larger than 60 arcsec are indicated with filled points, smaller galaxies with fine dots. The upper inset shows the number distribution of the concentration index, the bottom inset that of the weighted mean ellipticity. Objects with a diameter $a \leq 60$ arcsec are denoted by the dashed line. The others are indicated by a filled black line. 22

2.7 Separation diagram with the recovered RFGC galaxies. Galaxies of the different morphological types are indicated by small symbols as given in the legend, recovered galaxies from the RFGC with large filled points. The upper inset shows the number distribution for the recovered RFGC galaxies of the concentration index, the bottom inset that of the weighted mean ellipticity. 26

2.8 Comparison of the depth of this catalog versus the recovered RFGC objects. The objects of the RFGC are large filled points, the catalog galaxies are small dots. 28

2.9 Comparison of the depth of this catalog versus the recovered RFGC objects. The objects of the RFGC are large filled points, the catalog galaxies are small dots. 29

2.10 Distribution of the ε versus the total surface brightness. The different color-coded dots represent the various morphological galaxy types and are explained in the key. 32

2.11 Distribution of the CI versus the total surface brightness. The different color-coded dots represent the various morphological galaxy types and are explained in the key. . . 33

3.1 Morphological separation diagram with the apparent g magnitude against the color $u-g$ as suggested by Strateva et al. (2001) for the Catalog galaxies. The different color-coded classes of the Catalog are given in the legend. The vertical line represent the limiting value that divides early from late morphologies as found by Strateva et al. (2001). . . 36

3.2 Same as Fig. 3.1. Only the galaxies with bulge are plotted. 36

3.3 The morphological discriminator CI in dependency of the color $u - g$. The different colored dots represent the various morphological galaxy types from the Catalog and are explained in the key. The vertical line represent the limiting value that divides early from late morphologies as found by Strateva et al. (2001). 37

3.4 The morphological discriminator ε in dependency of the color $u - g$. The different colored dots represent the various morphological galaxy types from the Catalog and are explained in the key. The vertical line represent the limiting value that divides early from late morphologies as found by Strateva et al. (2001). 38

3.5 Comparison of our CI with the profile likelihood from SDSS. The profile likelihood is expected to separate galaxies that are bulge dominated with de Vaucelours profiles from the exponential disk dominated galaxies at a value of 1.03 (Bernardi et al. 2003) as shown by the horizontal line. The different color-coded dots represent the various morphological galaxy types from the Catalog and are explained in the key. 39

3.6 Comparison of our ε with the profile likelihood from SDSS. The profile likelihood is expected to separate galaxies that are bulge dominated with de Vauceulours profiles from the exponential disk dominated galaxies at a value of 1.03 (Bernardi et al. 2003) as shown by the horizontal line. The different color-coded dots represent the various morphological galaxy types from the Catalog and are explained in the key. 40
3.7 Distribution of the axial ratios and morphological type. The axial ratio is measured with our code from the Catalog. The different color-coded dots represent the various morphological galaxy types from the Catalog and are explained in the key. The curve represent the distribution of idealized simple ellipses. The different morphological classes are related to the simple isophotal axial ratios and simple disks represent the flattest systems. 41
3.8 Same as Fig. 3.7 but with the axial ratio derived directly from SDSS parameters. . . . 42
3.9 Comparison of the ε derived in the Catalog with the isophotal ellipticity *ell* from SDSS. The different color-coded dots represent the various morphological galaxy types from the Catalog and are explained in the key. 43
3.10 Correlation between CI and *ell* shows that it is not an optimal separation diagram. The line at CI=2.7 divides galaxies with bulge from the bulgeless ones. The dots with different colors stand for the various classes from the Catalog and are explained in the legend. 44
3.11 Correlation between the two luminosity weighted elliptical quantities, ε and ϵ respectively. The different color-coded dots represent the various morphological galaxy types from the Catalog and are explained in the key. 45
3.12 The separation diagram with ϵ on the abscissa and the CI on the ordinate. The color dots are cited in the key and represent the classes from the Catalog. The line at CI=2.7 separates galaxies with bulge from the bulgeless. 45
3.13 Number distribution of the automately selected galaxies from the Catalog (different color lines as cited in the key) versus their adaptive ellipticity ϵ. 46
3.14 Distribution of the DR5 sample galaxies and its surface brightness. The left diagram shows the correlation with the CI and the right diagram that with the ϵ. The DR5 edge-on sample galaxies are divided into several morphological classes with the limits given in Table 3.1 and color coded as explained in the key. The simple disk galaxies have the lowest surface brightnesses. 48
3.15 Correlation of the effective Petrosian radius [$''$] in the i and g band of the DR5 edge-on galaxies. 49
3.16 Correlation of the radius containing 90% of Petrosian flux [$''$] in the i and g band of the DR5 edge-on galaxies. 49
3.17 Distribution of the axial ratios of the DR5 sample. The DR5 edge-on sample galaxies are divided into several morphological classes with the limits given in Table 3.1 and color coded as explained in the key. The simple disk galaxies have the flattest shape. . 50
3.18 The superthin galaxy UGC 9242. The image is a $6'.5 \times 6'.5$ cutout of the DR5 Image List Tool. North is to the top, east to the left. 51
3.19 Distribution of the morphological types of the Catalog (color dots as cited in the key) versus the absolute blue u magnitude which is strongly dust dependent. The curve follows the general distribution of the classes and has its maximum value at the Sa(f) - Sb(f) classes. 54
3.20 Distribution of the morphological types of the Catalog (color dots as cited in the key) versus the absolute red z magnitude. The z filter is the less dust diluted filter in the SDSS system. The curve traces on average the decrease of the total stellar mass from early to the latest classes. 54
3.21 Color-magnitude diagram of $g-r$ vs. r. 55
3.22 Color-color diagram of $g-r$ vs. $u-g$ 55
3.23 Color-color diagram of $r-i$ vs. $g-r$ 55
3.24 Color-color diagram of $i-z$ vs. $r-i$ 55

4.1 Redshift distribution of the target galaxies Sa(f) (top left), Sb(f) (middle left) and Sd(f) (bottom left). The neighbors of Sa(f) are plotted top right, Sb(f) neighbors (middle right) and Sd(f) neighbors (bottom right). The ordinate indicates the absolute r magnitude (M_r). 60

4.2 Distribution of M_r of the Sa(f) (top left), Sb(f) (middle left) and Sd(f) (bottom left) target galaxies. The corresponding neighbors are plotted on the right side. The bin size is half a magnitude. The dashed line of Sb(f) targets indicate the artificial target sample. The appropriate dashed line on the right represent the neighbor distribution of the artificial target sample. 61

4.3 This pie diagram shows the fraction of higher luminosity neighbors around target galaxies in the large cylinder. The bright gray slice represents the targets without detection of higher luminosity neighbors. The medium gray slice is for those with one detected luminous neighbor and the dark gray slice indicates the percentages of two or more luminous neighbors for a target galaxy. The distance (d) to the nearest higher luminosity neighbor of the targets is indicated below the values of the percentages. 64

4.4 Same as Fig. 4.3 but for the small cylinder. 64

4.5 This histogram illustrates the fractional distribution of the target galaxies with numbers of neighbors within the large cylinder. The horizontally-hatched histogram bars represent the galaxy class with large bulges, Sa(f), the solid bars are the intermediate-size bulge galaxies, Sb(f), and the thick lined bars correspond to the Sd(f) simple disk galaxies. All targets with more than 10 neighbors are located at the position of "11" on the plot's abscissa. 66

4.6 Same as Fig. 4.5 but for the small cylinder. 66

4.7 Projected space distribution around the target galaxies (bar in the center) in kiloparsecs of neighbors stacked and rotated in the large cylinder. Neighbors of an Sa(f) target are indicated as stars, neighbors of Sb(f) as squares and those of Sd(f) as crosses. Eq.1, Eq.2 locate for the equatorial quadrants, Pol.1,Pol.2 the polar quadrants around the targets. The mean distance between Sa(f) targets and neighbors is 587.1 kpc, for Sb(f) it is 595.4 kpc and for Sd(f) 704.7 kpc. 68

4.8 Same as Fig. 4.7 but for the small cylinder. The mean distance between Sa(f) targets and neighbors is 137.9 kpc, for Sb(f) it is 143.9 kpc and for Sd(f) 198.8 kpc 69

4.9 Projected space distribution like Fig. 4.8 around each target type including density contours. Left: Sa(f) neighbors; middle: Sb(f) neighbors; right: Sd(f) neighbors. . . . 70

4.10 Cumulative distribution of the projected distance in kiloparsecs of Sa(f) neighbors (dashed line), Sb(f) neighbors (dotted line) and Sd(f) neighbors (chain dotted line) as a fraction of the total number of the neighbors. The uniform distribution function $f(x) = \frac{x^2}{1000^2}$ is the solid line. 71

4.11 Same as Fig. 4.10 but for the small cylinder. The uniform distribution function is $f(x) = \frac{x^2}{300^2}$. 72

4.12 Distribution of the absolute z magnitude (left) and the isophotal major axis [kpc] (right) of the targets for Sa(f) (top); Sb(f) (middle); Sd(f) (bottom) 74

4.13 Number of counted neighbors in the large cylinder versus isophotal major axis [kpc] (left) and absolute z magnitude (right) of the targets: Sa(f) (top); Sb(f) (middle); Sd(f) (bottom). 75

4.14 Morphological distribution of Sa(f) neighbors (stars), Sb(f) neighbors (squares) and Sd(f) neighbors (crosses). The abscissa indicates the color u-r and the ordinate the concentration index in the r band as morphological indicators. The region for the early-type galaxies is top right and for the late types bottom left. The dashed lines indicate the morphological borders. The arrows are located at the mean values for each target class. The bold arrow indicates the mean of the colors of Sd(f) neighbors that differs significantly from the Sa(f) and Sb(f) neighbor colors. Although the arrows for the CI show offsets, they differ in a statistically significant only between Sb(f) and Sd(f). The median u-r value is for Sa(f): 2.03, Sb(f): 2.05, Sd(f): 1.69, the median concentration index value is for Sa(f): 2.58, Sb(f): 2.63, Sd(f): 2.35. 76
4.15 This cone diagram shows the cosmological large-scale distribution of galaxies in the SDSS equatorial stripes $130 < RA < 241$ and $-9 < DEC < 8$ (upper half circle) and $63 > RA > 346$, $-8 < DEC < 10$ (lower half circle). The circles indicate the distances of the same redshift. Sa(f) targets are indicated as red dots, Sb(f) as green and Sd(f) as blue dots. The fine dots are the galaxies from a comparison sample. 78

5.1 This figure is a schematic edge-on view of the main components of the Milky Way. The sun in the thin disk is indicated by a circle and the directions to the North (NGP) and South (SGP) Galactic Pole are indicated by arrows. The components are marked in this figure. By courtesy of R. Buser. 89
5.2 This figure shows an edge-on view of the MW's disk and halo components of the plane of the MW near the solar neighborhood. The space density distributions of the disk components and the halo are shown schematically (top) and analytically (bottom). The different exponential decrease of the density (ordinate ρ) with increasing vertical distance above and below from the midplane of the MW (abscissa z) of the different disks is drawn. The vertical dashed lines show the scale heights of the thin disk ($h_z = 300pc$) and the TD ($h_{zTD} = 1000pc$). By courtesy of R. Buser. 89
5.3 This figure shows the age-metallicity relation of the various components in the Milky Way. The different components are explained in the legend. This correlation of decreasing age of the stars with increasing metallicity from halo to the thin disk stars indicates an overall related evolution. Otherwise, the scatter of the halo field stars and particularly the bulge stars is very large and therefore are hints for unrelated origins. The sun is a thin disk field star with metallicity [Fe/H]= 0. By courtesy of R. Buser. . 90
5.4 The contours of the of 3D in the K_s (left) and r(right) band. The scale is 122"×57". . 95
5.5 The NTT dome on the right side and a view towards other telescopes at La Silla. . . . 96
5.6 This figure shows the median of the fluxes of the dark frames at different DIT. The flux is nearly linearly decreasing at the exposures with DIT below 10sec. 102
5.7 An example of a frame full of donut-like ghost features after dark and flat field correction. The target galaxy lays in the bottom quadrant on the left side of the frame. 104
5.8 The final image of the combined 38 frames after the first iteration. The target galaxy SDSS J005315.44-084416.4 is located in the center of the image. 106
5.9 The final mask image from the SExtractor of the target galaxy SDSS J005315.44-084416.4 in the center and its surroundings which are also masked. 107
5.10 The final image of the target galaxy SDSS J005315.44-084416.4 after the second iteration. 108
5.11 Photometric regression diagram for the standard stars in the K_s band. The ordinate shows the magnitudes of the zeropoint and the abscissa the airmass. The straight line is the fitted regression line. 110
5.12 Photometric regression diagram for the standard stars in the J band. The ordinate shows the magnitudes of the zeropoint and the abscissa the airmass. The straight line is the fitted regression line. 110
5.13 The differences between the flatness in the optical r and NIR K_s filter. The green line shows the relationship $\varepsilon_r = \varepsilon_{K_s}$ 113

5.14 The differences between the flatness in the optical i and NIR K_s filter. The green line shows the relationship $\varepsilon_i = \varepsilon_{K_s}$ 113
5.15 The separation diagrams in the optical and the NIR bands. 114
5.16 The differences between the concentration index in the optical r and NIR K_s filter. The green line shows the relationship $CI_r = CI_{K_s}$ 115
5.17 The differences between the concentration index in the optical i and NIR K_s filter. The green line shows the relationship $CI_i = CI_{K_s}$ 115
5.18 The contours of the central region of 1C in the K_s (left) and r (right) band. CI_{K_s} - CI_r = 0.328. The scale is $30'' \times 18''$. 115
5.19 The contours of the central region of 1D in the K_s (left) and r (right) band. CI_{K_s} - CI_r = 0.714. The scale is $30'' \times 18''$. 116
5.20 The contours of the central region of 1A in the K_s (left) and r (right) band. CI_{K_s} - CI_r = 0.303. The scale is $14'' \times 10''$. 116
5.21 The contours of the of 3D in the K_s (left) and r (right) band. CI_{K_s} - CI_r = 0.146. The scale is $61'' \times 44''$. 117
5.22 The contours of the central region of 3D in the K_s (left) and r (right) band. CI_{K_s} - CI_r = 0.146. The scale is $14'' \times 10''$. 117
5.23 The correlation between asymmetry and clumpiness of the target galaxies in the optical and the NIR bands. The optical values show a relation between A and S. A and S are derived using the absolute value method. 120
5.24 Same as Fig. 5.23 but A and S are derived using the square method 120
5.25 Concentration index versus asymmetry of the galaxies in the optical and the NIR bands. The correlation between these two morphological discriminators is very small. The values of the CI and the A are smaller in the K_s band than in the optical bands. CI and A are derived using the absolute value of these objects. 121
5.26 Same as Fig. 5.25 but using the square method for deriving the parameters. 121
5.27 No correlation is shown in this figure between the clumpiness and the central light concentration, i.e., bulgesize of the targets. S is derived using the absolute value method. 122
5.28 Same as Fig. 5.27 but using the square method for deriving S. 122
5.29 Correlation between the concentration index and the total surface brightness in the optical and the NIR bands. No correlation between these two parameters is found. . . 123
5.30 Correlation between the asymmetry index and the total surface brightness in the optical and the NIR bands. No correlation between these two parameters is found. 123
5.31 Correlation between the clumpiness index (absolute values method) and the total surface brightness in the optical and the NIR bands. Galaxies with lower surface brightnesses have a more clumpy distribution. 123
5.32 Correlation between the clumpiness index (square values method) and the total surface brightness in the optical and the NIR bands. Galaxies with lower surface brightnesses have a more clumpy distribution. 123
5.33 This figure shows the radial surface brightness profiles of the central ten pixels of the galaxy's radius. The profiles of the different colors indicate the different target galaxies as shown in the legend. The central light excess is very small indicating that the galaxies are nearly bulgeless. 129
5.34 This figure shows the axial ratio (ordinate) in correlation with the central five pixels of the vertical averaged height (abscissa). The different color coded lines corresponds to the different target galaxies as indicated in the legend. This figure shows that the innermost pixels have small axial ratios and then their value is suddenly rising to high values. This indicates round isophotes at the nuclear region but the disk is already dominant at small vertical distances. 129

5.35 Left: Vertical K_s surface brightness distribution of the azimuthally averaged elliptical isophote levels of the galaxy 3A. The height z perpendicular to the galaxy midplane is given in pixel values. The green line illustrates the exponential old thin disk model. The blue line shows the exponential thick disk model. Right: Radial K_s surface brightness distribution of the azimuthally averaged elliptical isophote levels of 3A. The green and the blue curve presents the inner and outer part of the galaxy model by Matthews et al. (1999b). The vertical lines in both surface brightness diagrams show the 2 (black), 1 (turquoise) and 0.5 (yellow) σ levels above the background. 132

5.36 Left: Vertical K_s surface brightness distribution of the azimuthally averaged elliptical isophote levels of the galaxy 1A. The height z perpendicular to the galaxy midplane is given in pixel values. The green line illustrates the exponential old thin disk model. The blue line shows the exponential thick disk model.
Right: Radial K_s surface brightness distribution of the azimuthally averaged elliptical isophote levels of 1A. The green and the blue curve presents the inner and outer part of the galaxy model by Matthews et al. (1999b). The vertical lines in both surface brightness diagrams show the 2 (black), 1 (turquoise) and 0.5 (yellow) σ level above the background. 132

5.37 Left: Vertical K_s surface brightness distribution of the azimuthally averaged elliptical isophote levels of the galaxy 3B. The height z perpendicular to the galaxy midplane is given in pixel values. The green line illustrates the exponential old thin disk model. The blue line shows the exponential thick disk model.
Right: Radial K_s surface brightness distribution of the azimuthally averaged elliptical isophote levels of 3B. The green and the blue curve presents the inner and outer part of the galaxy model by Matthews et al. (1999b). The vertical lines in both surface brightness diagrams show the 2 (black), 1 (turquoise) and 0.5 (yellow) σ level above the background. 133

5.38 Left: Vertical K_s surface brightness distribution of the azimuthally averaged elliptical isophote levels of the galaxy 2B. The height z perpendicular to the galaxy midplane is given in pixel values. The green line illustrates the exponential old thin disk model. The blue line shows the exponential thick disk model.
Right: Radial K_s surface brightness distribution of the azimuthally averaged elliptical isophote levels of 2B. The green and the blue curve presents the inner and outer part of the galaxy model by Matthews et al. (1999b). The vertical lines in both surface brightness diagrams show the 2 (black), 1 (turquoise) and 0.5 (yellow) σ level above the background. 133

5.39 Left: Vertical K_s surface brightness distribution of the azimuthally averaged elliptical isophote levels of the galaxy 1C. The height z perpendicular to the galaxy midplane is given in pixel values. The green line illustrates the exponential old thin disk model. The blue line shows the exponential thick disk model.
Right: Radial K_s surface brightness distribution of the azimuthally averaged elliptical isophote levels of 1C. The green and the blue curve presents the inner and outer part of the galaxy model by Matthews et al. (1999b). The vertical lines in both surface brightness diagrams show the 2 (black), 1 (turquoise) and 0.5 (yellow) σ level above the background. 134

5.40 Left: Vertical K_s surface brightness distribution of the azimuthally averaged elliptical isophote levels of the galaxy 1D. The height z perpendicular to the galaxy midplane is given in pixel values. The green line illustrates the exponential old thin disk model.
Right: Radial K_s surface brightness distribution of the azimuthally averaged elliptical isophote levels of 1D. The green and the blue curve presents the inner and outer part of the galaxy model by Matthews et al. (1999b). The vertical lines in both surface brightness diagrams show the 2 (black), 1 (turquoise) and 0.5 (yellow) σ level above the background. 134

5.41 Left: Vertical K_s surface brightness distribution of the azimuthally averaged elliptical isophote levels of the galaxy 3D. The height z perpendicular to the galaxy midplane is given in pixel values. The green line illustrates the exponential old thin disk model. The blue line shows the exponential thick disk model.
Right: Radial K_s surface brightness distribution of the azimuthally averaged elliptical isophote levels of 3D. The green and the blue curve presents the inner and outer part of the galaxy model by Matthews et al. (1999b). The vertical lines in both surface brightness diagrams show the 2 (black), 1 (turquoise) and 0.5 (yellow) σ level above the background. 135

5.42 Left: Vertical K_s surface brightness distribution of the azimuthally averaged elliptical isophote levels of the galaxy 3Ealtern. The height z perpendicular to the galaxy midplane is given in pixel values. The green line illustrates the exponential old thin disk model.
Right: Radial K_s surface brightness distribution of the azimuthally averaged elliptical isophote levels of 3Ealtern. The green and the blue curve presents the inner and outer part of the galaxy model by Matthews et al. (1999b). The vertical lines in both surface brightness diagrams show the 2 (black), 1 (turquoise) and 0.5 (yellow) σ level above the background. 135

5.43 Left: Vertical K_s surface brightness distribution of the azimuthally averaged elliptical isophote levels of the galaxy 3E. The height z perpendicular to the galaxy midplane is given in pixel values. The green line illustrates the exponential old thin disk model.
Right: Radial K_s surface brightness distribution of the azimuthally averaged elliptical isophote levels of 3E. The green and the blue curve presents the inner and outer part of the galaxy model by Matthews et al. (1999b). The vertical lines in both surface brightness diagrams show the 2 (black), 1 (turquoise) and 0.5 (yellow) σ level above the background. 136

5.44 Left: Vertical K_s surface brightness distribution of the azimuthally averaged elliptical isophote levels of the galaxy 2Ealtern. The height z perpendicular to the galaxy midplane is given in pixel values. The green line illustrates the exponential old thin disk model. The blue line shows the exponential thick disk model.
Right: Radial K_s surface brightness distribution of the azimuthally averaged elliptical isophote levels of 2Ealtern. The green and the blue curve presents the inner and outer part of the galaxy model by Matthews et al. (1999b). The vertical lines in both surface brightness diagrams show the 2 (black), 1 (turquoise) and 0.5 (yellow) σ level above the background. 136

5.45 scale height versus central surface brightness of the thin disk. No correlation is shown. 137

5.46 scale height versus central surface brightness of the thick disk. No correlation is shown. 137

5.47 scale height of the thin disk versus scale height of the thick disk in pixel values. Galaxies with large scale heights of the thin disk have also large scale heights of the thick disk. The green line shows the correlation $h_z = h_{zTD}$. 137

5.48 scale height of the thin disk versus scale height of the thick disk in kiloparsecs. Galaxies with large scale heights of the thin disk have also large scale heights of the thick disk. The green line shows the correlation $h_z = h_{zTD}$. 137

5.49 entral surface brightness of the thin disk versus the central surface brightness of the thick disk. The data seem to be linearly correlated. The green line shows the correlation $\mu_0 = \mu_{0TD}$. 138

5.50 The ratio of central surface brightness to the scale height of the thin disk versus the ratio of the central surface brightness to the scale height of the thick disk. This figure shows a linear correlation of the thin and thick disk components. The scale heights are given in kiloparsecs. 138

5.51 The ratio of the scale height to the central surface brightness of the thin disk versus the ratio of the scale height to the central surface brightness of the thick disk. This figure shows a linear correlation of the thin and thick disk components. The scale heights are given in pixel values. 138

5.52 The ratio of the scale height to the central surface brightness of the thin disk versus the ratio of the scale height to the central surface brightness of the thick disk. This figure shows a linear correlation of the thin and thick disk components. The scale heights are given in kiloparsecs. 138

5.53 Top left: Vertical K_s surface brightness distribution of the azimuthally averaged elliptical isophote levels of 3A. The green and blue line illustrates the exponential old thin disk and thick disk model, respectively.
Top right: Axial ratio of the azimuthally averaged elliptical isophote levels in relation to the surface brightness of the levels. The vertical black line shows the 2 σ level above the background.
Bottom left: The change of the axial ratios (ordinate) with increasing distance z from the galaxy midplane (abscissa) is shown in this diagram. 140

5.54 Top left: Vertical K_s surface brightness distribution of the azimuthally averaged elliptical isophote levels of 1A. The green and blue line illustrates the exponential old thin disk and thick disk model, respectively.
Top right: Axial ratio of the azimuthally averaged elliptical isophote levels in relation to the surface brightness of the levels. The vertical black line shows the 2 σ level above the background.
Bottom left: The change of the axial ratios (ordinate) with increasing distance z from the galaxy midplane (abscissa) is shown in this diagram. 140

5.55 Top left: Vertical K_s surface brightness distribution of the azimuthally averaged elliptical isophote levels of 3B. The green and blue line illustrates the exponential old thin disk and thick disk model, respectively.
Top right: Axial ratio of the azimuthally averaged elliptical isophote levels in relation to the surface brightness of the levels. The vertical black line shows the 2 σ level above the background.
Bottom left: The change of the axial ratios (ordinate) with increasing distance z from the galaxy midplane (abscissa) is shown in this diagram. 141

5.56 Top left: Vertical K_s surface brightness distribution of the azimuthally averaged elliptical isophote levels of 2B. The green and blue line illustrates the exponential old thin disk and thick disk model, respectively.
Top right: Axial ratio of the azimuthally averaged elliptical isophote levels in relation to the surface brightness of the levels. The vertical black line shows the 2 σ level above the background.
Bottom left: The change of the axial ratios (ordinate) with increasing distance z from the galaxy midplane (abscissa) is shown in this diagram. 141

5.57 Top left: Vertical K_s surface brightness distribution of the azimuthally averaged elliptical isophote levels of 1C. The green and blue line illustrates the exponential old thin disk and thick disk model, respectively.
Top right: Axial ratio of the azimuthally averaged elliptical isophote levels in relation to the surface brightness of the levels. The vertical black line shows the 2 σ level above the background.
Bottom left: The change of the axial ratios (ordinate) with increasing distance z from the galaxy midplane (abscissa) is shown in this diagram. 142

5.58 Top left: Vertical K_s surface brightness distribution of the azimuthally averaged elliptical isophote levels of 1D. The green and blue line illustrates the possible exponential thin disk models, respectively.
Top right: Axial ratio of the azimuthally averaged elliptical isophote levels in relation to the surface brightness of the levels. The vertical black line shows the 2 σ level above the background.
Bottom left: The change of the axial ratios (ordinate) with increasing distance z from the galaxy midplane (abscissa) is shown in this diagram. 142

5.59 Top left: Vertical K_s surface brightness distribution of the azimuthally averaged elliptical isophote levels of 3D. The green and blue line illustrates the exponential old thin disk and thick disk model, respectively.
Top right: Axial ratio of the azimuthally averaged elliptical isophote levels in relation to the surface brightness of the levels. The vertical black line shows the 2 σ level above the background.
Bottom left: The change of the axial ratios (ordinate) with increasing distance z from the galaxy midplane (abscissa) is shown in this diagram. 143

5.60 Top left: Vertical K_s surface brightness distribution of the azimuthally averaged elliptical isophote levels of 3Ealtern. The green line illustrates the exponential old thin disk model.
Top right: Axial ratio of the azimuthally averaged elliptical isophote levels in relation to the surface brightness of the levels. The vertical black line shows the 2 σ level above the background.
Bottom left: The change of the axial ratios (ordinate) with increasing distance z from the galaxy midplane (abscissa) is shown in this diagram. 143

5.61 Top left: Vertical K_s surface brightness distribution of the azimuthally averaged elliptical isophote levels of 3E. The green illustrates the exponential old thin disk disk model.
Top right: Axial ratio of the azimuthally averaged elliptical isophote levels in relation to the surface brightness of the levels. The vertical black line shows the 2 σ level above the background.
Bottom left: The change of the axial ratios (ordinate) with increasing distance z from the galaxy midplane (abscissa) is shown in this diagram. 144

5.62 Top left: Vertical K_s surface brightness distribution of the azimuthally averaged elliptical isophote levels of 2Ealtern. The green and blue line illustrates the exponential old thin disk and thick disk model, respectively.
Top right: Axial ratio of the azimuthally averaged elliptical isophote levels in relation to the surface brightness of the levels. The vertical black line shows the 2 σ level above the background.
Bottom left: The change of the axial ratios (ordinate) with increasing distance z from the galaxy midplane (abscissa) is shown in this diagram. 144

5.63 Left: $K_s - r$ color map of 3A. We use the inverse illustration: Bright pixels indicate regions of dominating K_s NIR light. In dark regions, the optical r band light dominates. The scale is $76.''1 \times 26.''5$.
Right: Vertical surface brightness distribution of the azimuthally averaged elliptical isophote levels in K_s (red) and r (green) band of 3A, respectively. 145

5.64 Left: $K_s - r$ color map of 1A. We use the inverse illustration: Bright pixels indicate regions of dominating K_s NIR light. In dark regions, the optical r band light dominates. The scale is $57.''9 \times 23.''4$.
Right: Vertical surface brightness distribution of the azimuthally averaged elliptical isophote levels in K_s (red) and r (green) band of 1A, respectively. 145

5.65 Left: $K_s - r$ color map of 3B. We use the inverse illustration: Bright pixels indicate regions of dominating K_s NIR light. In dark regions, the optical r band light dominates. The scale is $97.''5 \times 34.''1$.
Right: Vertical surface brightness distribution of the azimuthally averaged elliptical isophote levels in K_s (red) and r (green) band of 3B, respectively. 146
5.66 Left: $K_s - r$ color map of 2B. We use the inverse illustration: Bright pixels indicate regions of dominating K_s NIR light. In dark regions, the optical r band light dominates. The scale is $75.''7 \times 22.''2$.
Right: Vertical surface brightness distribution of the azimuthally averaged elliptical isophote levels in K_s (red) and r (green) band of 2B, respectively. 146
5.67 Left: $K_s - r$ color map of 1C. We use the inverse illustration: Bright pixels indicate regions of dominating K_s NIR light. In dark regions, the optical r band light dominates. The scale is $124'' \times 38.''5$.
Right: Vertical surface brightness distribution of the azimuthally averaged elliptical isophote levels in K_s (red) and r (green) band of 1C, respectively. 147
5.68 Left: $K_s - r$ color map of 1D. We use the inverse illustration: Bright pixels indicate regions of dominating K_s NIR light. In dark regions, the optical r band light dominates. The scale is $100.''6 \times 32.''5$.
Right: Vertical surface brightness distribution of the azimuthally averaged elliptical isophote levels in K_s (red) and r (green) band of 1D, respectively. 147
5.69 Left: $K_s - r$ color map of 3D. The galaxy lies vertical in this image. We use the inverse illustration: Bright pixels indicate regions of dominating K_s NIR light. In dark regions, the optical r band light dominates. The scale is $177.''1 \times 60.''6$.
Right: Vertical surface brightness distribution of the azimuthally averaged elliptical isophote levels in K_s (red) and r (green) band of 3D, respectively. 148
5.70 Left: $K_s - r$ color map of 3Ealtern. The galaxy lies vertical in this image. We use the inverse illustration: Bright pixels indicate regions of dominating K_s NIR light. In dark regions, the optical r band light dominates. The scale is $137.''1 \times 88.''4$.
Right: Vertical surface brightness distribution of the azimuthally averaged elliptical isophote levels in K_s (red) and r (green) band of 3Ealtern, respectively. 148
5.71 Left: $K_s - r$ color map of 3E. We use the inverse illustration: Bright pixels indicate regions of dominating K_s NIR light. In dark regions, the optical r band light dominates. The scale is $79.''3 \times 35.''7$.
Right: Vertical surface brightness distribution of the azimuthally averaged elliptical isophote levels in K_s (red) and r (green) band of 3E, respectively. 149
5.72 Left: $K_s - r$ color map of 2Ealtern. We use the inverse illustration: Bright pixels indicate regions of dominating K_s NIR light. In dark regions, the optical r band light dominates. The scale is $100.''6 \times 31.''1$.
Right: Vertical surface brightness distribution of the azimuthally averaged elliptical isophote levels in K_s (red) and r (green) band of 2Ealtern, respectively. 150

D.1 1A. The scale is 3.55×2.06 arcmin. 163
D.2 1B. The scale is 3.55×2.06 arcmin. 163
D.3 1C. The scale is 3.55×2.06 arcmin. 164
D.4 1D. The scale is 3.55×2.06 arcmin. 164
D.5 1E. The scale is 3.55×2.06 arcmin. 164
D.6 2B. The scale is 3.55×2.06 arcmin. 165
D.7 2C. The scale is 3.55×2.06 arcmin. 165
D.8 2D. The scale is 3.55×2.06 arcmin. 165
D.9 2E. The scale is 3.55×2.06 arcmin. 166
D.10 2Ealtern. The scale is 3.55×2.06 arcmin. 166
D.11 3A. The scale is 3.55×2.06 arcmin. 166
D.12 3B. The scale is 3.55×2.06 arcmin. 167

D.13 3C. The scale is 3.55×2.06 arcmin. 167
D.14 3D. The scale is 3.55×2.06 arcmin. 167
D.15 3E. The scale is 3.55×2.06 arcmin. 168
D.16 3Ealtern. The scale is 3.55×2.06 arcmin. 168

List of Tables

2.1 Limiting Values. These are the values of the limits of the morphological classes. The values are valid for the SDSS g and r bands. The value for the i band is the same as in the other filters for ε. For CI it is slightly higher because i is more sensitive for the dominant redder bulge stars. In this case one should add a value of 0.1 to the numbers of the CI in this table. In general, note that the galaxies near boundaries have the least certain classification. 20
2.2 Catalog: Structural Parameters. The complete version of this table is available from the CDS. Here we are presenting the first 15 entries (out of 3169) as an example. . . . 23
2.3 Photometric Parameters and Redshifts. The complete version of this table is available from the CDS. Here we are presenting the first 15 entries (out of 3169) as an example. 24
2.4 Galaxy classes and their fractions. The absolute numbers of galaxies in the various morphological subclasses and their percentages with respect to the catalog entries as a whole are listed in this table. 25

3.1 Limiting Values for the adaptive ellipticity ϵ and concentration index CI. These are the values of the limits of the morphological classes. The values are valid for the SDSS r band. In general, note that the galaxies near boundaries have the least certain classification. 46
3.2 Galaxy classes and their fractions. The absolute numbers of galaxies in the main morphological classes and their percentages with respect to the catalog entries as a whole are listed in this table. For comparison the numbers and percentages of the Catalog are given in the fourth and fifth column. 47

4.1 Target galaxies and their neighbors. The complete version of this Table is available from the CDS. Here we are presenting the first 5 entries (out of 206) as an example. . 62
4.2 Neighbor numbers in the quadrant zones of the large search cylinder. 67

5.1 Selected Galaxies 97
5.2 A SOFI SOFI_img_obs_AutoJitterArray Template 99
5.3 Properties of the Observations 101
5.4 Selected Standard Stars in K_s 109
5.5 Selected Standard Stars in J 109
5.6 Photometric Solution 109
5.7 Morphological Parameters of the Galaxies 112
5.8 Results of the CAS 118
5.8 continued. 119
5.9 The Magnitudes and Petrosian Radii of the Targets in Comparison with 2MFGC . . . 125
5.10 The derived Structural Parameters of the Galaxies. The mean value of the thin disk scale height is $\langle h_z \rangle = 426 \pm 147$pc. For the thick disk it is $\langle h_z TD \rangle = 543 \pm 205$pc. The mean of the ratios of the scale heights is $\langle \frac{h_z TD}{h_z} \rangle = 1.4 \pm 1.8$. 139

B.1 AMOR Control File for Computing the Concentration Index 160

C.1 AMOR Control File for the Computation of CAS Morphological Parameters 162

0.3 Danksagung an:

Betreuer Prof. Dr. Eva K. Grebel & Prof. Dr. John “Jay” S. Gallagher, III; all jene vom Astronomischen Institut der Universität Basel – speziell Fabio D. Barazza, Andreas Koch und Thorsten Lisker – und dem Max-Planck-Institut für Astronomie in Heidelberg und allen Anderen, die mich unterstützt haben; meine Familie und natürlich alle meine Freunde...

Chapter 1

Introduction

Galaxies appear in many different morphologies. These manifestations can be reduced into two basic geometries: a sphere–generally an ellipsoid–and a layer of a sphere, the disk. All other morphologies represent a continuum from triaxial ellipsoids of the ellipticals (E), the early-type galaxies, to the latest types consisting of distorted disks, the irregulars (Irr).

In Fig. 1.1 it is shown that the sequence of the morphology is a flattening and decrease of the spheroidal component with a continuous increase of the disk component from the ellipticals via the lenticulars (S0) to the spirals (S) and irregular galaxies. The optical morphology of a galaxy is determined by the positions of the galaxy's stars. And these positions are ultimately determined by the stellar paths, i.e., the orbits of the stars in a galaxy.

This morphological scheme is also a sequence of the averaged physical properties of the objects. For instance, the majority of the stars in the early-type galaxies are old and of red color and exhibit random and eccentric orbits, i.e., their velocity dispersion is large and the systems are dynamically hot. On the other hand, the blue, young and intermediate age stars in disks rotate in ordered, nearly circular orbits around the galaxy's center. The amount of interstellar material (ISM), dust and gas, is growing from early to late-type galaxies, indicating an increasing reservoir to form stars and planets.

Most of the total mass of the disk galaxies is gathered in an invisible, eventually sphere-like envelope made out of the enigmatic dark matter, thus, the total mass to light ratio is very large in the latest disks. In contrast to that, this dark, nearly spheroidal triaxial dark halo of the disk galaxies, is filled with baryonic matter (stars, planets, ISM) in elliptical galaxies and consequently the total mass to light ratio is small. Beside many other physical properties such as star-formation activity and history; metallicity; luminosity; mass and surface brightness distributions in the different morphological types, these extragalactical systems are also located in different environments. Mass-rich ellipticals are often clustered together with similar types. In contrast to that, disk-dominated galaxies are found in galaxy groups and isolated in the field.

At the lower end of the stellar mass and luminosity spectrum, the sphere-dominated and disk-dominated systems have their small counterparts, the dwarf galaxies. The intermediate morphological objects, i.e., spirals with bulge are not found, however, in a dwarf configuration.

The appearance of the galaxies also depends on the viewing angle between a galaxy and the observer, i.e., its inclination i. In the face-on view ($i = 0^\circ$) the basic shape of disk galaxies is a circle with possible lopsidedness in the latest types (Sc, Irr). As shown in the first line of Fig. 1.1 the disk is the hosting component of the spiral arms in the galaxy types Sa, Sb, and Sc. In many disk galaxies, the part between the galaxy center and the ends of the spiral arms is occupied with a bar and is classified with the letter "B" in the type's name (fifth line in Fig. 1.1).

At an inclination of $i = 90^\circ$, a galaxy is seen from its edge. This edge-on view is shown in the third line of Fig. 1.1. It is clearly seen that the central spheroidal component of the early-type disk galaxies (S0, Sa) has totally disappeared in the latest types (Sc, Irr). The edge-on view has the advantage that the vertical structure of the objects can be studied. In addition, the different object types can be distinguished easily based on the apparent disk thickness and bulge size.

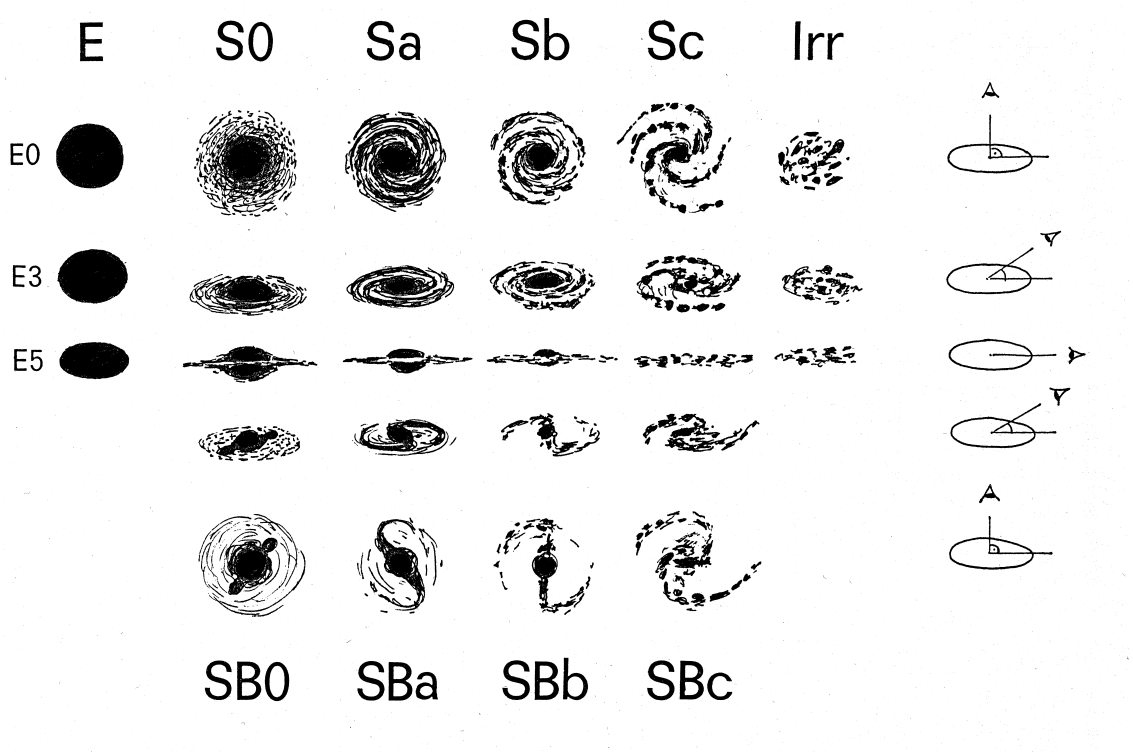

Figure 1.1: A schematic overview of the manifold morphologies of galaxies. The sphere-dominated early-type galaxies (E, S0) are drawn on the left side. The disk-dominated morphologies (Sc, Irr) are shown on the right side. The spiral galaxies are shown with (top) or without (bottom) a central bar. The galaxies are presented at different viewing angles as indicated in the outer-right column. This diagram: drawn and by courtesy of B. Binggeli.

A special type of thin and elongated galaxies without bulges was found in various galaxy surveys. Ogorodnikov (1957, 1958) and Vorontsov-Vel'yaminov (1967, 1974) were one of the first scientists who paid attention to these needle-shaped galaxies. It was thought that these systems are very elongated, prolate ellipsoids made out of gravitational collapsing elliptical gas clouds (Fujimoto 1968). The needles would represent slowly rotating systems in the form of Jacobi ellipsoids (Ogorodnikov 1957) and were once believed to be the initial form of spiral galaxies: Spiral galaxies evolve from this needles which disintegrate to a halo and forms the disk stars in the magnetic field of the needle which then settles into an oblate ellipsoid (Ogorodnikov 1958). However, the needles would be gravitationally and kinematically unstable systems and it became evident that these objects are bulgeless "simple disk" galaxies seen edge-on (Heidmann et al. 1972). In the Fig. 1.1 this flat appearance of the edge-on Sc type is drawn. A general class of very late type spirals is the class of Sd galaxies with the thinnest bulgeless disks and located between Sc and Irr. These latest disks are therefore also called flat (Karachentsev 1989) or superthin (Goad & Roberts 1979) galaxies and represent the class of the edge-on simple disk galaxies.

1.1 Late-Type Disk Galaxies in General

During the last decade an increasing number of studies of late-type, edge-on and disk-dominated galaxies has been conducted, reflecting a growing interest in understanding these galaxies in the framework of galaxy evolution and cosmological models. Models describing the chemodynamical evolution of disk galaxies within a slowly growing dark matter halo can successfully reproduce many of the observed properties of Milky-Way-type disk galaxies (Samland & Gerhard 2003; Samland 2004). Models with high merger rates as mandated in hierarchical merger scenarios face a number of problems when comparing the predicted properties of galactic subcomponents with observations (e.g., Abadi et al. 2003a). It is even more difficult to succeed in producing disk-dominated, essentially bulge-less late-type galaxies, making simple disk objects an evolutionary enigma.

In numerical cold dark matter (CDM) simulations the resulting disks are smaller, denser, and have lower angular momentum than observed. Major mergers increase the angular momentum (e.g., Gardner 2001), but also destroy stellar disks, hence it seems unlikely that simple disk galaxies suffered major mergers in the recent past. Adding feedback alleviates the angular momentum problem to some extent (e.g., Sommer-Larsen et al. 2003; Robertson et al. 2005). However, D'Onghia & Burkert (2004) point out that dark halos that did not suffer major mergers have too low an angular momentum to begin with. This prevents them from producing the observed extended disks from the collapse of their associated baryons, since the specific angular momentum of the gas cannot be *increased* by feedback processes. In contrast to that, Okamoto et al. (2005) used a hydrodynamic simulation within a ΛCDM Universe with a quiet merger history and various models of star formation and feedback. They found that the shock-induced models have realistic morphological results of disk-dominated galaxies. But these simulated galaxies exhibit unrealistic flat surface profiles, are too large and–contrary to the previous studies–have too much angular momentum. The origin of disk-dominated galaxies remains a puzzle.

1.2 Properties of Disk Galaxies

Overall, disk galaxies show a multitude of different morphologies ranging from disk galaxies with a substantial bulge and with high surface brightness to bulgeless low-surface-brightness (LSB) galaxies (e.g., Schombert et al. 1992; Matthews et al. 1999b) and various complex bulge/disk combinations in between (e.g., Matthews & de Grijs 2004). A potpourri of edge-on disk galaxies from the Sloan Digital Sky Survey Data Release 5 (SDSS DR5, see Sect. 3.3) is shown in the following figures. Fig. 1.2 shows UGC 10043, a galaxy with a prominent bulge component and a flat disk with clumpy dust distribution. This galaxy has a triaxial bulge and has been analyzed in detail by Matthews & de Grijs (2004). A "classical" early-type edge-on spiral galaxy with a bulge is UGC 5173, shown in Fig. 1.3. The typical organized dust lane in the middle of edge-on disk galaxies with bulge is clearly shown in UGC 5173.

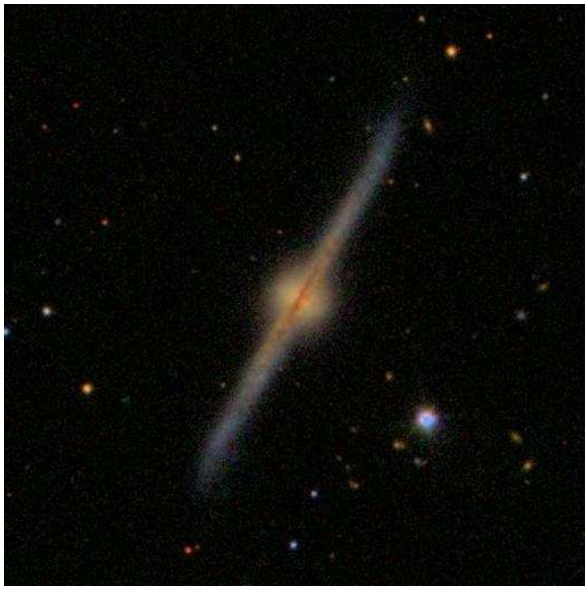

Figure 1.2: UGC 10043. This image shows an edge-on galaxy with a prominent, spheroidal bulge. The outer edges of the disk are warped. This is a five band image of $200'' \times 200''$ from the SDSS DR5 Image List Tool. North to the top, east to the left.

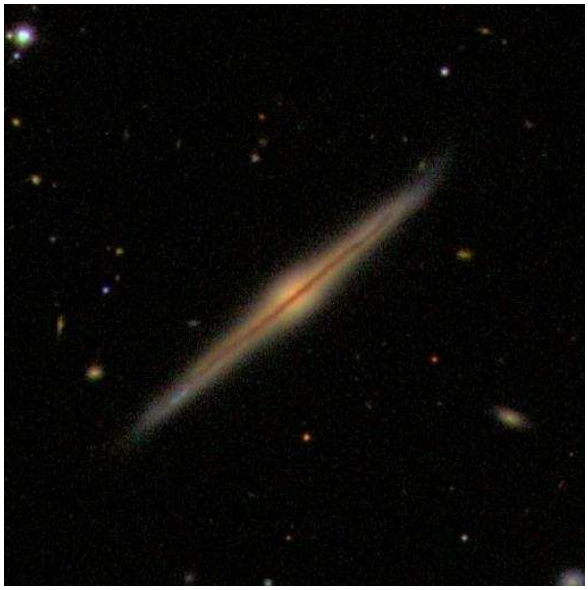

Figure 1.3: UGC 5173. This galaxy is a typical edge-on spiral galaxy with bulge and an organized dust lane–the dark line in the disk. This is a five band image of $200'' \times 200''$ from the SDSS DR5 Image List Tool. North to the top, east to the left.

UGC 9422 (Fig. 1.4) represents an intermediate type with no obvious bulge component but the galaxy does have a slight central light concentration. This galaxy is slightly inclined with respect to an exactly edge-on view.

A typical simple disk galaxy (UGC 9856) is presented in Fig. 1.5. The redder and orange colors in this galaxy type represent generally older stellar populations than in those with blue colors (Matthews et al. 1999b). In Fig. 1.6 a representative of the flattest simple disks is shown, the superthin galaxy UGC 7321. Several studies explored the unique properties of the flattest disks on the basis of this simple LSB disk (e.g., Matthews et al. 1999b; Matthews 2000). The latest morphological types are the irregulars. UGC 4704 (Fig. 1.7) is a transition object between ordered simple disks and the puffy disks of the bulgeless irregulars. These galaxies contain mostly young and hot stars, which are indicated by the blue color. The bright blue knots represent regions of recent star formation. Because of the lack of dust in the late simple disks, these LSB galaxies are nearly transparent and not reddened by dust.

Figures 1.8 and 1.9 show extravagant examples of edge-on galaxies from our analyzed sample. UGC 7064 (Fig. 1.8) is a galaxy with two apparent bulges. Since a galaxy with two bulges is dynamically highly unlikely, we may be seeing the result of a projection effect or of an ongoing interaction. In short, the second, left spheroidal component is possibly a galaxy currently merging with the disk. If this is not a projection effect, then this object would be the first galaxy discovered with two bulges. Figure 1.9 also shows galaxies during strong interaction: an interpenetration between a face-on (left) and an edge-on (right) galaxy–if it is not a projection effect. All these figures are optical five color cutouts from the SDSS DR5 Image List Tool[1] and have a size of $200'' \times 200''$. North is to the top, east to the left.

While certain properties such as the asymptotically flat rotation curves seem to be shared by most disk galaxies, simple disks differ in other key properties such as surface brightness and scale length. The optical structure of these pure disk systems consists of large axial ratios, very small disk scale heights and no spheroidal bulge component. They appear to be pure exponential disk galaxies with

[1] http://cas.sdss.org/astrodr5/en/tools/chart/list.asp

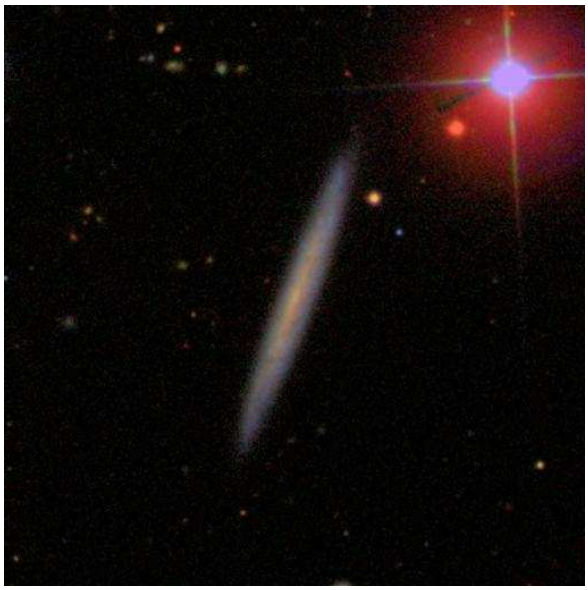

Figure 1.4: UGC 9422. This object represents an intermediate type between disk galaxies with and without bulge. This galaxy shows a slight central light concentration. The bright star in the upper right corner shows four refraction spikes which can imitate an edge-on disk galaxy in automated classification codes. This is a five band image of $200'' \times 200''$ from the SDSS DR5 Image List Tool. North to the top, east to the left.

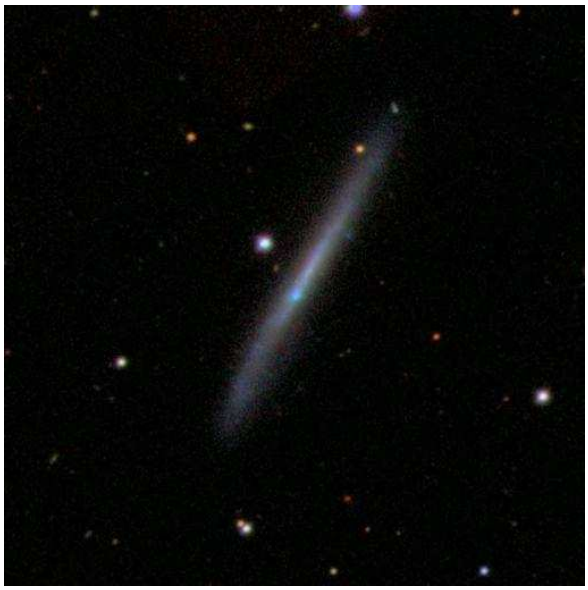

Figure 1.5: UGC 9856. The figure shows a simple disk galaxy without a central bulge component. This is a five band image of $200'' \times 200''$ from the SDSS DR5 Image List Tool. North to the top, east to the left.

Figure 1.6: UGC 7321. This is a simple disk galaxy with an extreme ratio between major and minor axis and represent a typical superthin galaxy. This is a five band image of $200'' \times 200''$ from the SDSS DR5 Image List Tool. North to the top, east to the left.

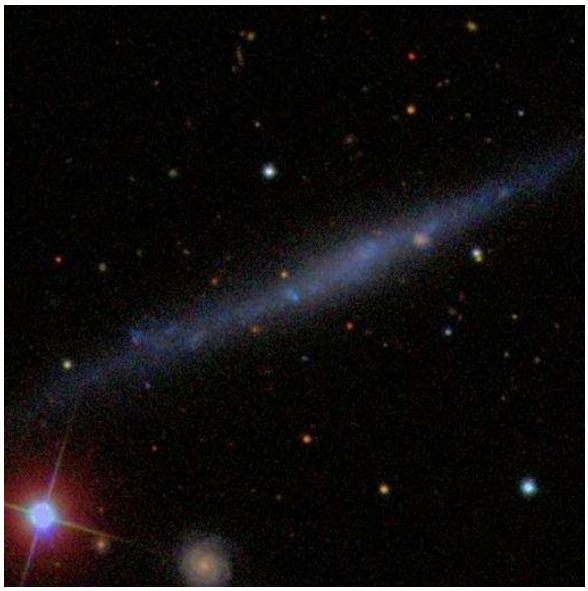

Figure 1.7: UGC 4704. The figure shows a very late simple disk galaxy with a transition morphology between ordered simple disks and the bulgeless disks of puffy irregulars. The deep blue color indicates large amount of hot and young stars and the lack of dust between the stars. The bright and knotty blue regions are places of recent star formation. At the left bottom part of the image, a face-on disk galaxy is shown. This is a five band image of $200'' \times 200''$ from the SDSS DR5 Image List Tool. North to the top, east to the left.

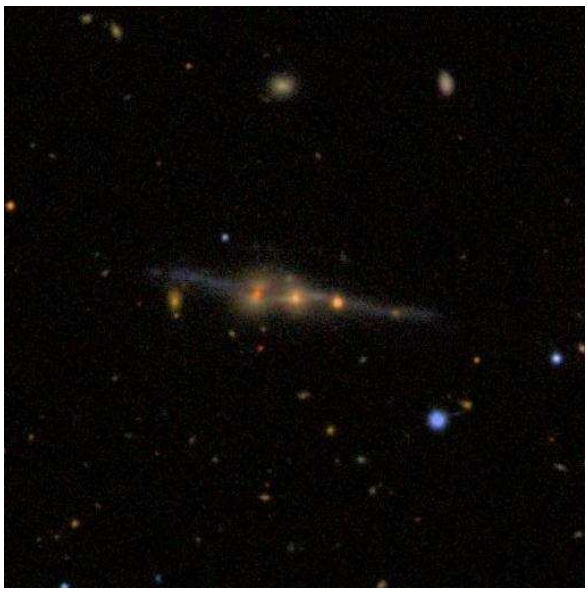

Figure 1.8: UGC 7064. A galaxy with two apparent bulges. This could be a projection effect of a spheroidal galaxy in the fore/background, lying exactly in the line of sight to the edge-on disk and simulating the left bulge. The third disk object from the left is a projected foreground star. This is a five band image of $200'' \times 200''$ from the SDSS DR5 Image List Tool. North to the top, east to the left.

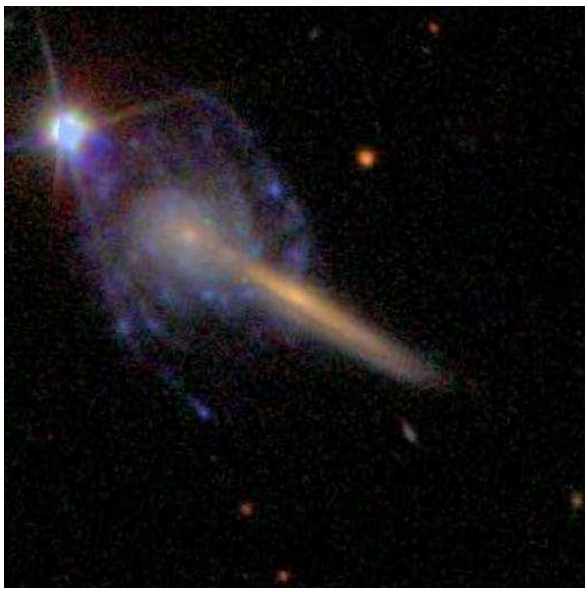

Figure 1.9: UGC 6973. The image shows an edge-on galaxy with bulge, overlapped with a face-on disk and a bright star in the left corner. These two galaxies from this system are probably in the stage of ongoing interpenetration. This is a five band image of $200'' \times 200''$ from the SDSS DR5 Image List Tool. North to the top, east to the left.

extended thin stellar disks and possibly an underlying thick disk component (Dalcanton & Bernstein 2002). Simple disk galaxies are a common galaxy type with special global properties such as low optical surface brightness, low star-formation rates and high neutral gas fractions (Goad & Roberts 1981; Bergvall & Rönnback 1995; Matthews et al. 1999a, 2001). They also contain molecular gas as shown recently with the detections of CO in some simple disk galaxies but the fractions of dust are small (Matthews & Gao 2001; Böker et al. 2003; Matthews et al. 2005; Stevens et al. 2005).

Rotation curves of flat galaxies slowly rise, often with nearly linear solid-body forms, and thus resemble the rotation curves of dwarf galaxies (Goad & Roberts 1981; Karachentsev & Xu 1991; Matthews et al. 1999a) and in terms of structural type they extend from late-type spirals to Magellanic irregulars. These flat rotation curves also indicate a massive dark halo (Karachentsev 1991). Also the emission line ratios ([NII]/Hα and [NII]/[SII]) of these galaxies are small are small (Goad & Roberts 1981). As a result they concluded that these galaxies have low ionization levels, lack prominent active nuclei, and probably had low and variable star formation rates.

Observations of simple disk galaxies offer the unique opportunity to constrain galaxy evolution in the most under-developed galaxies (in terms of star formation and dynamics) in the nearby Universe. Simple disk galaxies are well-suited probes for studying environmental effects on disk thickness and morphology; disk surface brightness and bulge formation. In HI surveys most simple disks appear to be isolated (Matthews & van Driel 2000) whereas Dalcanton & Bernstein (2002) suggest that their detection of potential thick disks indicates past interactions, (see also Reshetnikov & Combes 1997). The homogeneous all-sky distribution of these galaxies indicates that the late-type spirals are mostly located in the field (Karachentsev et al. 1993). This means that the flat galaxies are located not in or near major clusters or rich groups.

In order to understand how these systems form and evolve we need to understand the morphological systematics from bulgeless disks to disk galaxies with a dominant spheroidal bulge.

1.3 Models of Evolution

Historically, models consider disk formation as the result of the collapse of a gaseous protogalaxy (e.g., Fall & Efstathiou 1980)). Disks may then form from inside-out around a pre-existing classical bulge (Athanassoula 2005a) or via smooth accretion of material (Steinmetz & Navarro 2002). On the other hand, intense star formation will also lead to the formation of a bulge or a dense nucleus in a bulgeless disk galaxy, aided by the rapidity of the gas infall and the total amount of the accreted material (either through infall or mergers) (Noguchi 2001). Also bars, formed via instabilities of a disk, can transport material to the disk center. The subsequent star formation may build up an additional bulge component, which can then stabilize the disk (Samland & Gerhard 2003; Kormendy & Fisher 2005).

Dalcanton et al. (1997) note that "gravitational collapse in any hierarchical model with Gaussian initial conditions leads to a broad distribution of halo masses and angular momenta", which could account for the observed range of properties. If the collapse is dissipational and smooth, then the specific angular momentum is conserved and the gas forms a thin, rapidly rotating disk (Dalcanton et al. 1997). This disk can evolve then into a low surface brightness disk galaxy with high angular momentum and low mass, comparable with the Sc and Sd types. On the other hand, low angular momentum protogalaxies collapses efficiently and dissipationless, resulting in normal, high surface brightness galaxies (Sa and Sb). The Gaussian distribution of the initial conditions leads to a wide range of halo masses and angular momentum which we observe in the form of the various bulge sizes of the different disk galaxies. This is because the angular momentum determines the main characteristics of disk galaxies (Fall & Efstathiou 1980) including the disk and bulge size for fixed masses (Hernandez & Cervantes-Sodi 2006). Off course, bulges can be also the consequence of gravitational interaction with other galaxies.

Dalcanton et al. (2004) found that galaxies with disk circular velocities $V_c > 120$ km s^{-1} tend to show bulges whereas more slowly rotating galaxies tend to be bulgeless. They suggest that more rapidly rotating disks (usually the higher-mass disks) are more gravitationally unstable and thus prone to fragmentation and gravitational collapse along spiral arms. This in turn leads to smaller gas scale

heights, more pronounced dust lanes, and a reduced velocity dispersion. Smaller gas scale heights imply higher densities and increased star formation rates. Slowly rotating disks, on the other hand, are stable and have low star-formation rates, implying also lower metallicities. The threshold for disks becoming gravitationally unstable would then be at $V_c > 120$ km s^{-1}, offering a convincing and internally consistent explanation for the nature of late-type spirals. Relationships between star-formation activity and gravitational instability have a long history (Quirk 1972; Kennicutt 1989; Elmegreen 2002; Li et al. 2006) and support the interpretation by Dalcanton et al. (2004).

While these scenarios offer a convincing and internally consistent explanation for the nature of disk galaxies, the frequency and stability of disk-dominated galaxies is surprising from the cosmological point of view. Hierarchical models of galaxy evolution include violent interaction phases that should destroy disky systems (e.g. Steinmetz 2003; Taylor & Babul 2003). A better knowledge of disk-dominated galaxies may hence be key for understanding their formation, evolution, and survival.

This thesis aims primarily at an evolutionary exploration of the properties of very late-type, edge-on spirals, particularly the simple disk galaxies. This includes the relative fractions of these galaxies. The frequencies of the galaxies with and without bulge and their general morphological properties are analyzed in Chapter 2. Chapter 3 contains additional points related to the previous chapter. These includes an analysis of different morphological discriminators, "scaling" relations, thickness, extinction and the high frequency of edge-on disk galaxies and the simple disks.

The correlation between properties of disks and environment allows important clues about the formation and evolutionary paths of disk galaxies and bulge growth. Chapter 4 presents a detailed study of the environment of different disk galaxies.

The shape of galaxies can be different in changing the observed wavelength of the galaxy. The near infrared bands are tracing the galaxy's mass distribution and are therefore useful to analyze the structure of the galaxies. Chapter 5 presents the observation of a sample of disk galaxies in the near infrared. This chapter also contains a detailed investigation of the morphology and the disk structures of the galaxies.

The Appendices of this thesis contain a presentation of codes which are used in order to perform a quantitative morphological determination and classification of the here studied edge-on disk galaxy samples.

Chapter 2

A Catalog of Edge-on Disk Galaxies

2.1 Introduction

The need for a homogeneous search for mainly bulgeless edge-on galaxies was recognized by Karachentsev (1989), who wanted to use these objects in order to investigate large-scale streaming motions in the Universe. He used photographic data in order to identify and catalog these systems. The resulting catalogs are the "Flat Galaxy Catalogue" (hereafter FGC) (Karachentsev et al. 1993) and its extension, the "Revised Flat Galaxy Catalogue" (hereafter RFGC) by Karachentsev et al. (1999). This RFGC is an all-sky survey and contains the largest published compilation of visually selected bulgeless edge-on galaxies: 4236 objects in total. He used the ratio of the major and minor axis as the selection criteria in order to collect these edge-on galaxies. A collection of edge-on disk galaxies in the near infrared is provided in "The 2MASS-selected Flat Galaxy Catalog" (Mitronova et al. 2004). Since the appearance of these highly inclined disks is essentially needle-like and does not exhibit a distinct bulge component Karachentsev (1989) called them "flat galaxies". Flat galaxies are thin edge-on spiral galaxies which seem to be (nearly) bulgeless and of late morphological Hubble type (Sc/Sd and later). A few years earlier, Goad & Roberts (1979) and Goad & Roberts (1981) already called attention to edge-on galaxies with extreme axial ratios. They called these systems "superthin galaxies". Superthin and flat galaxies belong to the same group, which we will summarize here under the term "simple disk galaxies".

In order to contribute to a better characterization of these objects, we carried out the work presented here, which aims at compiling an uniform sample of disk-dominated galaxies from modern CCD data at optical wavelengths. The Sloan Digital Sky Survey (SDSS) with its homogeneous, deep, large-area coverage provides an ideal data base for the identification of such galaxies. The SDSS (York et al. 2000) is carrying out multi-color imaging of one quarter of the sky, followed by medium-resolution spectroscopy primarily of galaxies and other objects of interest down to certain magnitude limits. These data are pipeline-reduced and the resulting images, astrometry, photometry, structural parameters, and calibrated spectra are released to the public after a proprietary period (Stoughton et al. 2002; Abazajian et al. 2003, 2004, 2005).

The SDSS with its resolution, dynamic range, and photometric accuracy allows one to study statistical properties and biases of disk galaxies such as their structure, intrinsic properties, overall frequency, and global scaling relations. The formation and evolution scenarios can be probed by studying the detailed structure and morphology (e.g., bulges, bars, halos, knots, and lanes) and comparing these with predictions from models (e.g., Samland & Gerhard 2003; Samland 2004; Immeli et al. 2004). Also the frequency of warps of the edge-on galaxies and possible relations with the environment can be studied easily using the SDSS. Warps should be relatively frequent since Reshetnikov (1995) showed that about 40% of the FGC galaxies have pronounced warps. Radial and vertical color gradients in these systems can shed light on the assembly of structure and on the evolutionary state using the available multi-color photometry.

In addition, the SDSS spectra enable the estimation of the properties of the stellar populations, of

the star formation rates, central activity, and metallicities. The redshifts from the catalog allow one to estimate the luminosities and sizes of the galaxies and the distribution of these properties. Also the environment of the cataloged galaxies can be investigated to probe the distribution of the surrounding satellites, the Holmberg effect, external influences on morphological evolution, and the local density and properties (frequency, position, and alignment) in a cluster environment.

We confined our search of the SDSS data base to edge-on disk galaxies, which facilitates the definition of an effective selection criterion. The choice of edge-on galaxies in particular is the only way to reliably select pure disk galaxies based on their optical morphologies. Altogether, we collected 3169 edge-on galaxies from the SDSS Data Release 1 (SDSS DR1). These systems can be subdivided into subclasses according their appearance.

This paper is organized as follows: In §2.2 we describe the training set of galaxies and the resulting selection criteria. In §3 the actual target selection is explained. The classification of the detected objects is presented in §4, followed by a description of the catalog (§2.5). Comparisons to evaluate the completeness of our selection are presented in §6. The influence of dust extinction on the galaxy selection is discussed in §7. Different types of galaxies and their subclasses are discussed in §2.8. The last Section §2.9 contains the summary and conclusions.

2.2 Training set and selection criteria

2.2.1 The data base

Our intent is to find edge-on galaxies with dominant stellar disks. We are using Karachentsev et al.'s catalogs as a starting point in order to carry out a systematic and reproducible selection of these kinds of galaxies. The object selection in the FGC and RFGC was based on the visual identification of galaxies with an axial ratio of a/b ≥ 7 and a major axis diameter a $\gtrsim 40''$ in the blue band on copies of the POSS-I and ESO/SERC photographic plates. The availability of the SDSS database permits us to carry out a survey using deep, homogeneous, five-color CCD data that are superior to the less deep, inhomogeneous photographic plates. An added advantage of the SDSS is that it will ultimately allow us to carry out such a search in an automated, objective, repeatable fashion. This certainly does not render the earlier studies superfluous since the SDSS is not an all-sky survey and since the earlier identifications provide a valuable training set for the definition of the selection criteria to be applied to the digital data. Furthermore, the SDSS permits us to identify not only simple-disk candidates, but also edge-on galaxies in general and to investigate the properties of all of these different morphological types.

We have analyzed SDSS data from DR1 (Abazajian et al. 2003), which was the largest publicly available data set when this work was started. DR1 provides 2099 deg^2 of imaging data observed in the five SDSS filters *ugriz*. The *r*-band depth of these data is approximately 22.6 mag. Meanwhile the data releases 2 (DR2) (Abazajian et al. 2004), 3 (DR3) (Abazajian et al. 2005), and 4 (DR4) (Adelman-McCarthy et al. 2005) are available, which cover successively larger areas on the sky. As detailed in Abazajian et al. (2004), changes were made to the data processing software between DR1 and DR2, but no such changes occurred for DR3 as compared to DR2 (Abazajian et al. 2005). We compared the SDSS photometry parameters in DR1 and DR2 for our galaxies and found no significant changes. However, in all of the releases some galaxies are affected by so-called "shredding" (e.g., Abazajian et al. 2003, 2004; Kniazev et al. 2004a), i.e., these galaxies are detected as two or more independent objects. This is found in particular for extended objects with substructure and diameters $\geq 1'$. A comparison of the different data releases showed that shredded target galaxies are similarly miss-classified in all of these releases. Some of the galaxies that were correctly identified in DR1 turned out to be shredded in the later releases. Hence we decided to continue to work with DR1 for the pilot study presented here.

2.2.2 Definition of a training set

In order to quantify a training set for the selection of disk-dominated edge-on galaxies we searched for all RFGC galaxies with a right ascension between 00 00 00 and 02 12 00 in the DR1 database, using the RFGC coordinates. In this coordinate range we expect to recover 47 RFGC galaxies in the DR1. It turned out that two of these objects have significantly different coordinates from the galaxies detected in the SDSS, while a third galaxy has a very different angular diameter in the RFGC as compared to the SDSS. For the remainder, the difference between the RFGC coordinates and the SDSS coordinates is typically smaller than ± 0.001 degrees ($3.6''$). For this "training set" that we re-identified in the SDSS, we found that the structural parameters have slightly smaller values in the DR1 as compared to the RFGC. We tested various combinations of SDSS structural and photometric parameters that would allow us to recover the galaxies in the training set (and additionally other edge-on disk galaxies in the SDSS). Ultimately, these galaxies should be recovered by performing an automated search of the SDSS photometric catalog database.

2.2.3 Definition of the query

As the result of this empirical approach, we finally adopted the parameters listed below for subsequent queries of the DR1 "Best Galaxy Table" (Abazajian et al. 2003). The DR1 "Best Galaxy Table" is the table in the SDSS database containing all parameters for galaxies that are of the highest quality at the time of the data release.

- Axial ratio in the g band: $a/b > 3$, where a and b are the major and minor axis, respectively.
- Angular diameter (isophotal major axis of the galaxy in the "blue" g filter) $a > 30''$.
- Colors in the range of $-0.5 < g - r < 2$ mag and $-0.5 < r - i < 2$ mag.
- Magnitude limit in the g filter < 20 mag.

These requirements are summarized in the Structured Query Language (SQL) as written below:

```
SELECT *
FROM Galaxy as G
WHERE G.petroMag_g < 20
and (G.isoA_g/G.isoB_g) > 3
and G.isoA_g > 15 # 15'' isophotal radius
and (G.g - G.r) between -0.5 and 2
and (G.r - G.i) between -0.5 and 2
```

With these conditions we are able to essentially reproduce all of the RFGC criteria and to recover the training set. In addition to the RFGC galaxies, our query parameters yield a much larger number of flat edge-on galaxies and other disk-dominated objects. This increase in numbers is in part due to the higher resolution and depth of the DR1 as compared to the photographic plates, but also due to our intention to collect all edge-on disk galaxies (including those with bulges). The latter is facilitated particularly by our relaxed choice of minimum axis ratios.

The images of the thus found objects were then downloaded from the DR1 "Data Archive Server" (DAS) using the SDSS rsync server. We downloaded the so-called "corrected imaging frames" (fpC) in the five SDSS bands. For a detailed description of the fpC frames we refer to the on-line description in the SDSS webpages[1].

[1] http://www.sdss.org/dr1/dm/flatFiles/fpC.html

2.3 Target selection

After a visual inspection we removed contaminants from our object list. The contaminants are mostly spikes (from very bright stars) and artifacts such as satellite or meteorite tracks which resemble an edge-on galaxy. Also strongly spike-blended edge-on galaxies were rejected. Additionally, obvious non-edge-on systems and unknown objects were removed. The obvious non-edge-on systems are objects where a bright bar in a faint disk simulates an edge-on disk. Apart from these contaminants, our selection criteria produce a fairly uniform sample of extended disk-dominated galaxies including objects with small bulges and bulgeless simple disks. All in all, 3169 objects were assembled in our catalog. Some early-type edge-on spiral galaxies are also included in the catalog, but internal dust lanes introduce a bias in excluding a fraction of these galaxies. This will be discussed in greater detail in Section 2.7. Additionally, our sample is limited by our selection criteria and by the SDSS photometry itself. The following biases affect our selection: (1) Edge-on galaxies with very faint disks around bulges and bright centers. (2) "Shredded galaxies". (3) Galaxies with unusual colors caused by an AGN and/or dust. The edge-on galaxies remaining in our sample after visual inspection and removal of contaminants fall into three general morphological groups:

- Pure bulgeless disks/simple disks
- Galaxies with a disk and an apparent bulge
- Objects with disks and central light concentration but no obvious bulge-like structure. These may be considered an intermediate class between the simple disks and galaxies with bulges. This group also comprises edge-on disky irregulars.

Out of these galaxies, an effort was made to select by eye objects spanning the full range in properties including different disk thicknesses, different bulge sizes, and presence or absence of dust lanes. The result is a subsample of 129 galaxies that is our morphological "reference set". Via visual inspection we subdivided this reference set into 42 simple disks, 37 galaxies with a bulge, and 50 intermediate types with central light excess. We then used this subsample to further automate the separation process and to develop a code to recover these general classes of edge-on galaxies in the SDSS DR1.

We found that the luminosity-weighted mean value of the ellipticity (hereafter ε) of the elliptical isophotes is a very robust separator between simple disks and the other edge-on types. In combination with the concentration index (hereafter CI) we can also exclude galaxies with an apparent bulge. The CI clearly separates galaxies with bulge from those without an apparent spheroidal component. This will be detailed in the following sections.

2.3.1 Isophote fitting

The following analysis is performed with the MIDAS analysis package developed by the European Southern Observatory. We applied it to the frames in all five SDSS filters, but only used the results for the three most sensitive bands *gri*. Unless explicitly specified otherwise, magnitudes quoted below refer to each of the separate bands. Firstly, we subtract the sky and the "softbias" from all frames. The softbias is an additional offset of 1000 counts per pixel in order to avoid negative pixels in the images. The sky and softbias were subtracted as mean values from the images. The values of the sky and softbias are stored in the header of each fpC frame. Then we use the MIDAS surface photometry package "surfphot" to fit ellipses to the isophotes of our galaxies. The innermost ellipse is fitted adopting the center coordinates given by the DR1 photometric database. The intensity of the innermost isophote is derived from the luminosity of the brightest pixel in a box (8×8 pixel) that corresponds to the galaxy center. In steps of 0.2 mag the program fits ellipses until an isophote is reached that corresponds to a surface brightness of $\mu = 25$ mag arcsec^{-2}. This implies that on average 20 – 30 isophote levels are plotted for every galaxy depending on the size and brightness. This isophote algorithm is based on the formulae of Bender & Moellenhof (1987).

2.3.2 Measuring the luminosity-weighted mean ellipticity and concentration index

We use the resulting values of the isophote levels and the major (a) and minor (b) axes in order to derive the luminosity weighted mean ellipticity of the elliptical isophotes (ε). ε is defined as

$$\varepsilon = \frac{\sum_{i=1}^{n} \epsilon_i \cdot I_i}{\sum_{i=1}^{n} I_i} \tag{2.1}$$

and

$$\epsilon_i = 1 - \frac{b_i}{a_i} \tag{2.2}$$

is the ellipticity of the ith isophote, whereas

$$I_i = z_i \cdot ((a \cdot b)_i - (a \cdot b)_{i-1}) \cdot \pi \tag{2.3}$$

is the intensity between two isophote levels. The isophote level is indicated by z_i.

For the CI of these objects we used the ratio of the following SDSS parameters

$$CI = petrorad\_90 \cdot petrorad\_50^{-1} \tag{2.4}$$

This is the ratio of the Petrosian radii (petrorad) that contain 90% and 50% of the Petrosian flux in the same band, respectively (see Stoughton et al. 2002). The Petrosian radius is the radius of a circular aperture at which the "Petrosian ratio" is set to a fixed value of 0.2. This "Petrosian ratio" is the ratio of the surface brightness in an annulus at a certain radius to the mean surface brightness within a circle with this radius. As discussed in Strauss et al. (2002) the use of circular apertures instead of elliptical apertures is fairly insensitive to inclination. Similarly, the Petrosian magnitudes are derived from the Petrosian flux using a circular aperture centered on every object. The advantage of this method is that this allows an unbiased measurement of a constant fraction of the total galaxy light using the technique based on that of Petrosian (1976). For a detailed description of the Petrosian parameters used in the SDSS we refer to Blanton et al. (2001) and Yasuda et al. (2001).

The CI is known as a morphological separator between early- and late-type galaxies (see, e.g., Strateva et al. 2001; Shimasaku et al. 2001; Nakamura et al. 2003; Shen et al. 2003; Kniazev et al. 2004a). With the CI and with ε as separators we recover our visually selected subgroups of the training set very well automatically. Therefore we applied this procedure to all edge-on galaxies in our catalog. The values of ε and CI are derived with a program implemented with FORTRAN 77 which is presented in the Appendix A.

2.3.3 Choosing the limiting values of CI and ε

In order to determine which choices of CI distinguish best between the general types of edge-on galaxies we use a histogram with the distribution of the CIs of the visually "classified" galaxies in our training subsample (Figure 2.1). Clearly, the majority of the simple disk galaxies has a CI < 2.7, hence we adopt a CI of 2.7 as the boundary condition to differentiate between simple disks and intermediate-type galaxies from those of with an obvious bulge component. A slightly lower value was often used in previous morphological studies of galaxies from the SDSS in order to separate between S0/Sa-type spirals and later spiral types (Strateva et al. 2001; Shimasaku et al. 2001; Nakamura et al. 2003; Shen et al. 2003). Contrary to our study these authors did not limit their samples to edge-on galaxies. Disky irregular galaxies exhibit very low CIs: the limit is CI < 2.15 (see also discussion in Kniazev et al. 2004a). Unfortunately it is not possible to separate the intermediate type from simple disks using only the CI. As one can see in the histogram the two remaining classes are merged at low values of the CI despite their different morphological appearance.

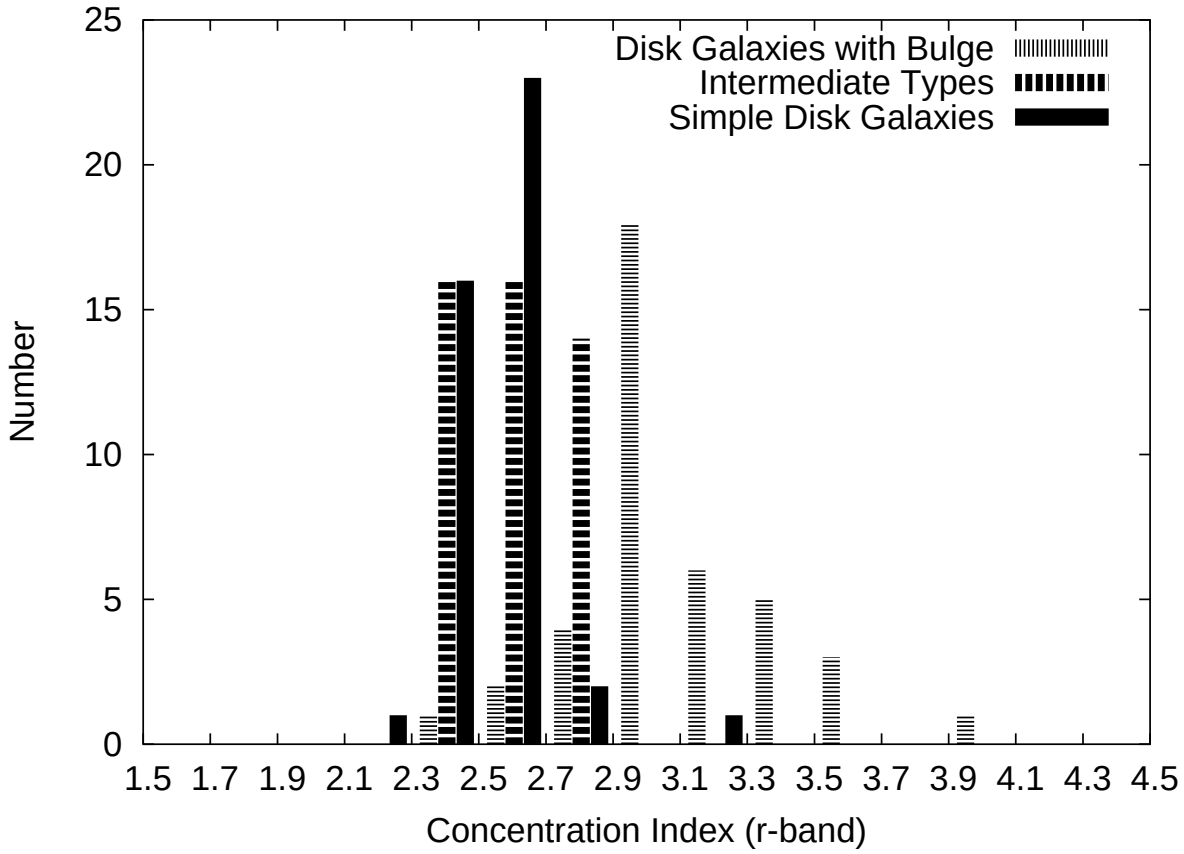

Figure 2.1: Number distribution of the visually selected galaxies versus their concentration index (CI).

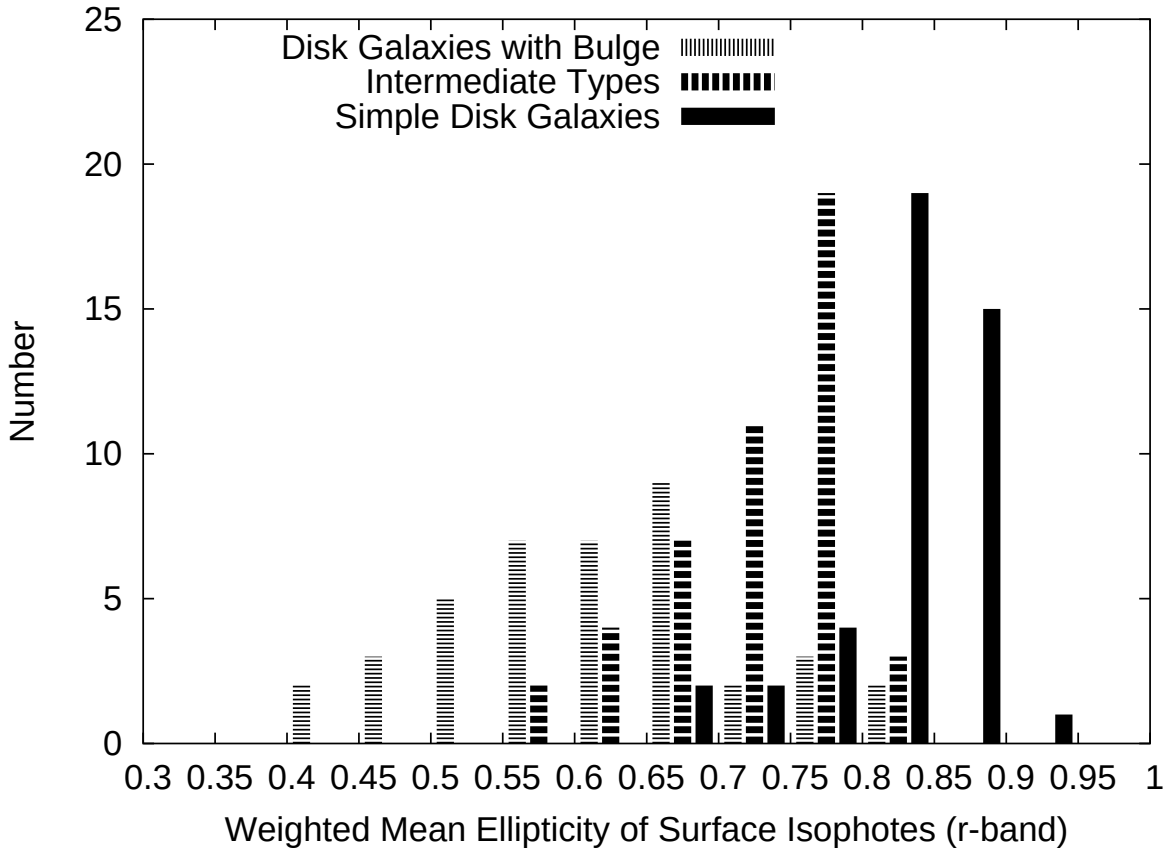

Figure 2.2: Number distribution of the visually selected galaxies versus their weighted mean ellipticity of the isophotes (ε).

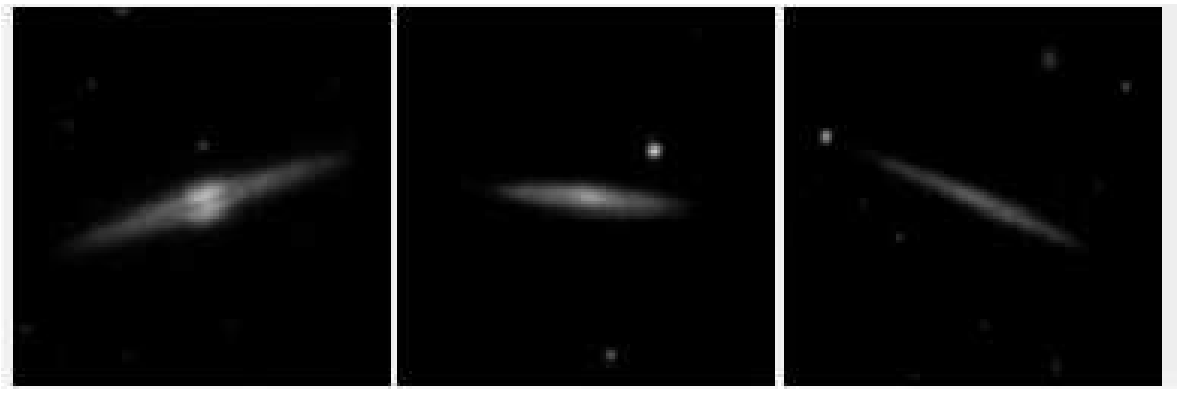

Figure 2.3: The left image is a typical member of the class of galaxies with bulge Sb(f): SDSS J020405.91-080730.3. A typical example of the Scd(f) intermediate class is in the middle: SDSS J102903.90+611525.8. Simple disk galaxies Sd(f) have an appearance like SDSS J135309.65+045739 at the right. All images are cutouts from the DR3 Image List Tool. These images have a scale of 90 square arcsec.

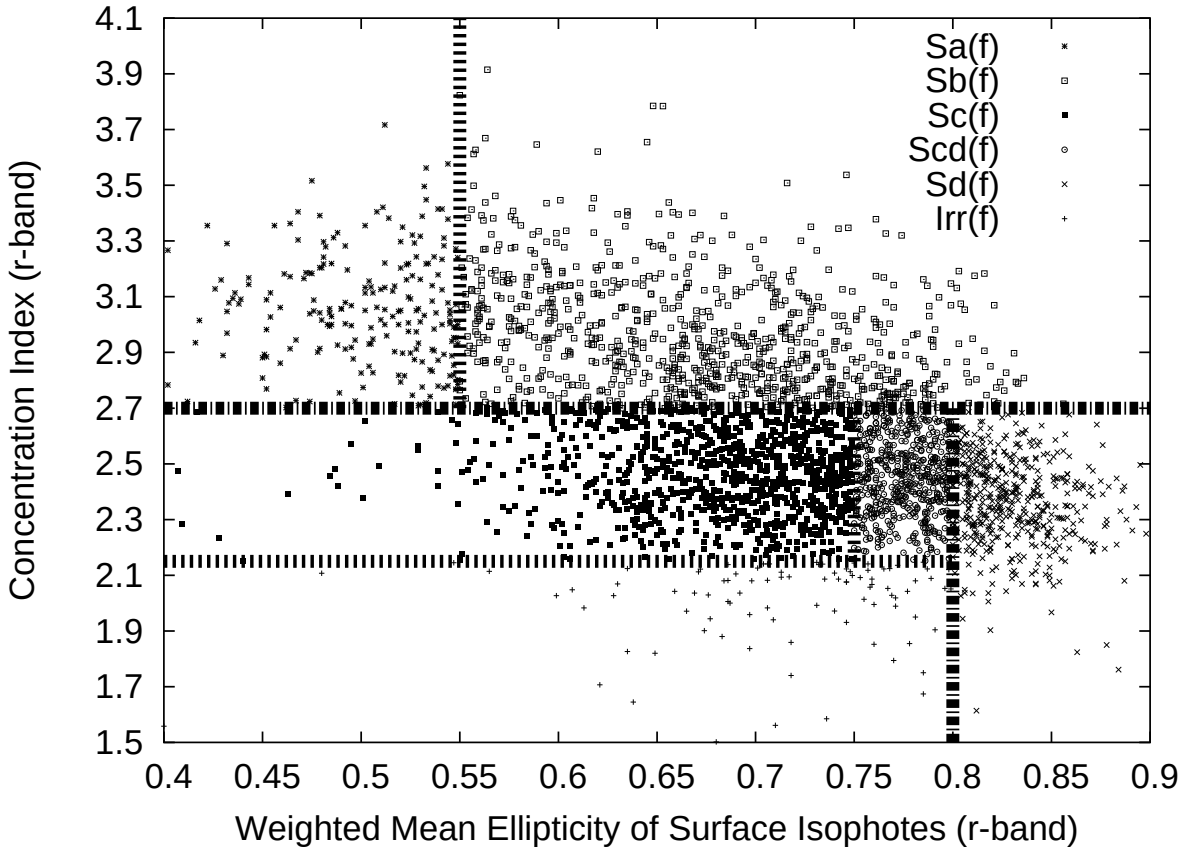

Figure 2.4: The main separation diagram. The symbols are cited in the key and represents the various morphological types. The borders of the general classes are marked with long-short dotted lines. The additional short dotted lines corresponds to the subgroup boarders within the general classes.

For that reason we use the weighted mean ellipticity of the isophotes ε as the second discriminator. Other possible morphological separators from the literature such as colors, asymmetry index, and profile likelihoods (Strateva et al. 2001), as well as decomposition (Kelly & McKay 2004) and Gini index (Abraham et al. 2003; Lotz et al. 2004) turned out not to be useful for the sensitive characterization of edge-on galaxies (Kautsch & Grebel 2003) probably because of the influence of dust and of the galaxy inclination on these separators.

We again use a histogram of the number distribution (Fig.2.2) of the ε values of the training subsample. In this case we intend to separate the intermediate types from the simple disks. We defined the region of $0.75 \leq \varepsilon < 0.8$ as the transition zone between the classes and a value of $\varepsilon = 0.8$ as the sharp border. This limiting value allows us to select the best simple disk candidates and the transition types. Additionally, with $\varepsilon < 0.55$ we can divide the class of galaxies with a bulge into early and later types.

2.4 The classification of edge-on galaxies

In order to flag these systems we follow the terminology introduced by de Vaucouleurs (1959). In his scheme, spiral galaxies are marked with an additional letter referring to the shape of the spiral arms, e.g., "r" means ring shaped and "s" s-shaped spiral structure when seen face on. We will instead use an "f" to indicate that a galaxy is flat, i.e., contains an edge-on component with or without a bulge. Furthermore, we introduce the following subclasses: galaxies with bulges (Sa(f), Sb(f)); simple disks (Sd(f)), Sc(f) and an intermediate group between Sc(f) and Sd(f) called Scd(f), and disky edge-on irregulars (Irr(f)). Representative examples of the general class members are shown in Fig.2.3. The three galaxies shown are for the Sb(f) class (SDSS J020405.91-080730.3), for the Scd(f) class (SDSS J102903.90+611525.8), and for the Sd(f) class (SDSS J135309.65+045739.3). These galaxy images are three-color (*g, r, i*) composites provided by the SDSS DR3 Image List Tool and have a scale of $90''$ in X and Y direction. The separation diagram, Figure 2.4, exhibits CI and ε in order to separate these classes. The abscissa represents the luminosity-weighted mean ellipticity of the isophotes ε. The ordinate shows the concentration index CI as taken from the SDSS. The values are given in the SDSS r band[2]. The automatically recovered simple disk galaxies are hereafter marked with Sd(f), the intermediate types with Scd(f) and Sc(f), the galaxies with bulges with Sa(f) and Sb(f), and irregulars with Irr(f). The lines mark the borders between the general classes and the subtypes in our new classification within the general classes. The selection parameters for the *g, r, i* bands are listed in Table 2.1.

In the histogram in Fig. 2.5 we plotted the number distribution of the apparent diameters of our galaxies. The majority of our objects is smaller than $60''$ ($\sim 88\%$ of all catalog objects). Only $\sim 2\%$ of all galaxies in our catalog have a diameter larger than $100''$ (Fig. 2.5). In order to check the influence of the size of the objects on our separation we plotted galaxy samples with different angular size (less than and greater than $60''$) in Fig. 2.6. This permits us to test whether higher resolution affects the separation process, in particular whether bright centers and extended disks bias the classification. The upper inset shows the number distribution of the CIs. Both size samples follow the same distribution. In the bottom inset the number distribution of ε is presented. Galaxies with diameters $a > 60''$ tend to have slightly higher values of ε, since these galaxies tend to be closer to us, facilitating the detection of more highly eccentric isophotes in the outer regions of these extended objects.

Using visual inspection we found that all Sd(f) types with an angular diameter $a > 60''$ show the appearance of a simple disk. Consequently they are assigned to the correct class by the automated algorithm. We therefore conclude that the defined limiting values of our catalog are still robust enough

[2]For the selection from the photometric database we used the g band in order to make the parameters comparable to those used for selecting the FGC. In the following diagrams, however, we refer to the r band. This filter is mostly used in the other studies involving the CI (Shimasaku et al. (2001); Nakamura et al. (2003); Shen et al. (2003)) because its quantum efficiency is the highest of all SDSS bands (Stoughton et al. 2002). In addition it includes the red light of the bulge which is important to separate galaxies with bulges from bulgeless galaxies.

Table 2.1: Limiting Values. These are the values of the limits of the morphological classes. The values are valid for the SDSS g and r bands. The value for the i band is the same as in the other filters for ε. For CI it is slightly higher because i is more sensitive for the dominant redder bulge stars. In this case one should add a value of 0.1 to the numbers of the CI in this table. In general, note that the galaxies near boundaries have the least certain classification.

Class	ε		CI	
	lower limit	upper limit	lower limit	upper limit
Sa(f)	$--$	< 0.55	≥ 2.70	$--$
Sb(f)	≥ 0.55	$--$	≥ 2.70	$--$
Sc(f)	$--$	< 0.75	≥ 2.15	< 2.70
Scd(f)	≥ 0.75	< 0.80	≥ 2.15	< 2.70
Sd(f)	≥ 0.80	$--$	$--$	< 2.70
Irr(f)	$--$	< 0.80	$--$	< 2.15

so that size and resolution do not affect the classification. The influence of resolution on the separation is discussed in section 2.7.

2.5 The Catalog

The main catalog is listed in Tables 4.1 and 2.3. The structural parameters of the catalog entries are shown in Table 4.1. Table 2.3 contains the photometric parameters and the redshifts. All entries are ordered by increasing right ascension. The full tables are available from the CDS. These tables contain all edge-on galaxies with disks that fulfill our automatic selection criteria, ranging from early-type spirals to late-type spirals and irregulars. In total, our catalog contains 3169 objects.

Table 4.1 is organized as follows: Column (1) presents the galaxy name in the SDSS nomenclature, which is consistent with the IAU nomenclature requirements. The following two columns (2) and (3) contain the coordinates of the galaxies, i.e., right ascension and declination for the epoch J2000. Column (4) indicates the general class (simple disks: Sd(f); intermediate types: Sc(f), Scd(f) and Irr(f); galaxies with bulge: Sa(f) and Sb(f)). The columns (5), (6), (7) show our derived value of ε in the *g*, *r*, and *i* bands. Columns (8), (9), and (10) contain the CI in these same bands. The angular diameter in *g*, *r*, and *i* in arcsec is presented in columns (11), (12), and (13). The axial ratios in the *g*, *r*, *i* bands are derived from the ratio of $isoA/isoB$ of the SDSS parameters and are listed in columns (14), (15), and (16). $isoA$ is the isophotal major axis and $isoB$ the isophotal minor axis of an isophote with a surface brightness of $\mu = 25$ mag arcsec^{-2} (in the respective band) as given by the DR1 pipeline.

Table 2.3 starts with the SDSS designation of the galaxy (column (1)) followed by our proposed class in column (2). Petrosian magnitudes and their uncertainties are provided in the *g, r, and i* bands in columns (3) to (8). The total surface brightness in *g, r, i* is given in columns (9), (10), and (11). We derived it using the parameters $petroMag + rho$, which are given in the SDSS DR1 database. In this database, rho is five times the logarithm of the Petrosian radius in the *i* band. The Petrosian magnitudes and their uncertainties as well as the total surface brightnesses were adopted from the SDSS DR1 archive. The Petrosian magnitudes and the total surface brightnesses are corrected for Galactic foreground extinction with the extinction values of Schlegel et al. (1998) as given in the SDSS database. If a value of the spectroscopic redshift *z* and its uncertainty are available from the SDSS database, this measurement is listed in columns (12) and (13); otherwise these values are denoted as zero.

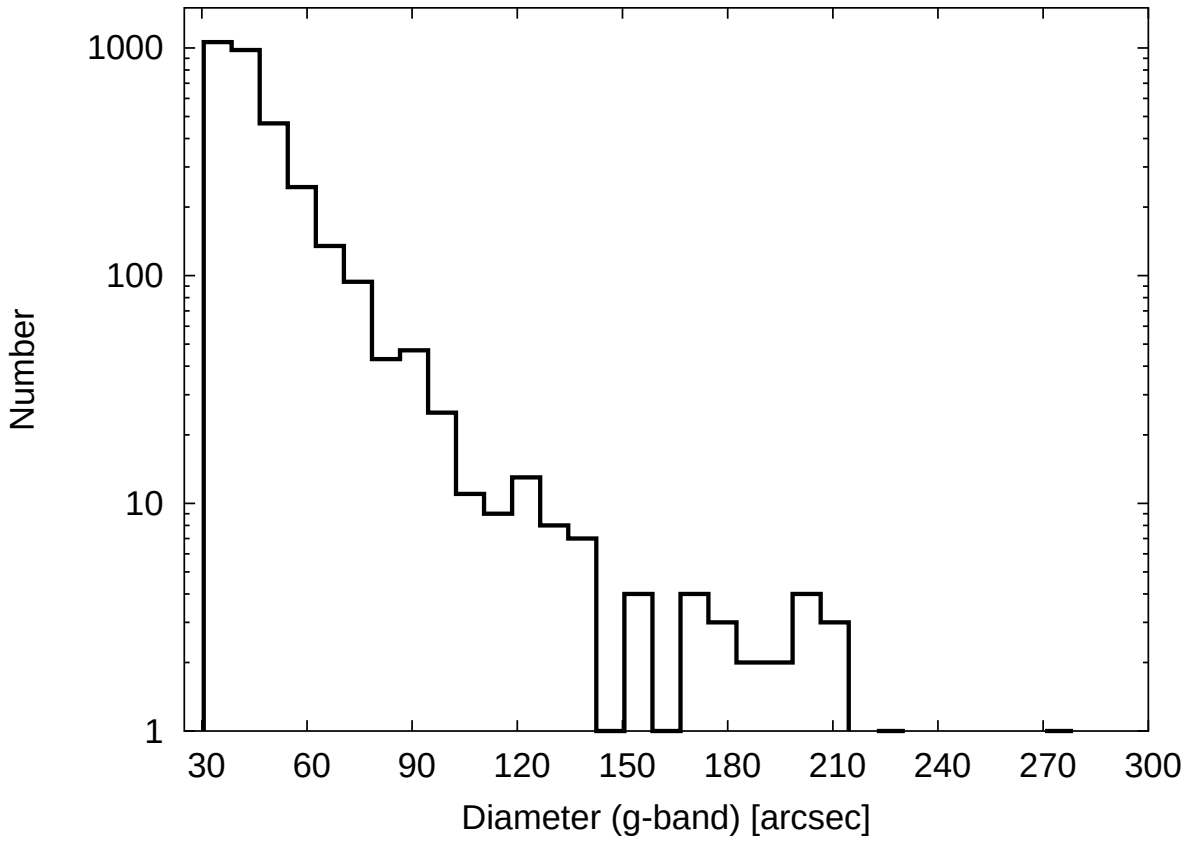

Figure 2.5: Logarithmic number distribution of the angular diameters of the catalog galaxies.

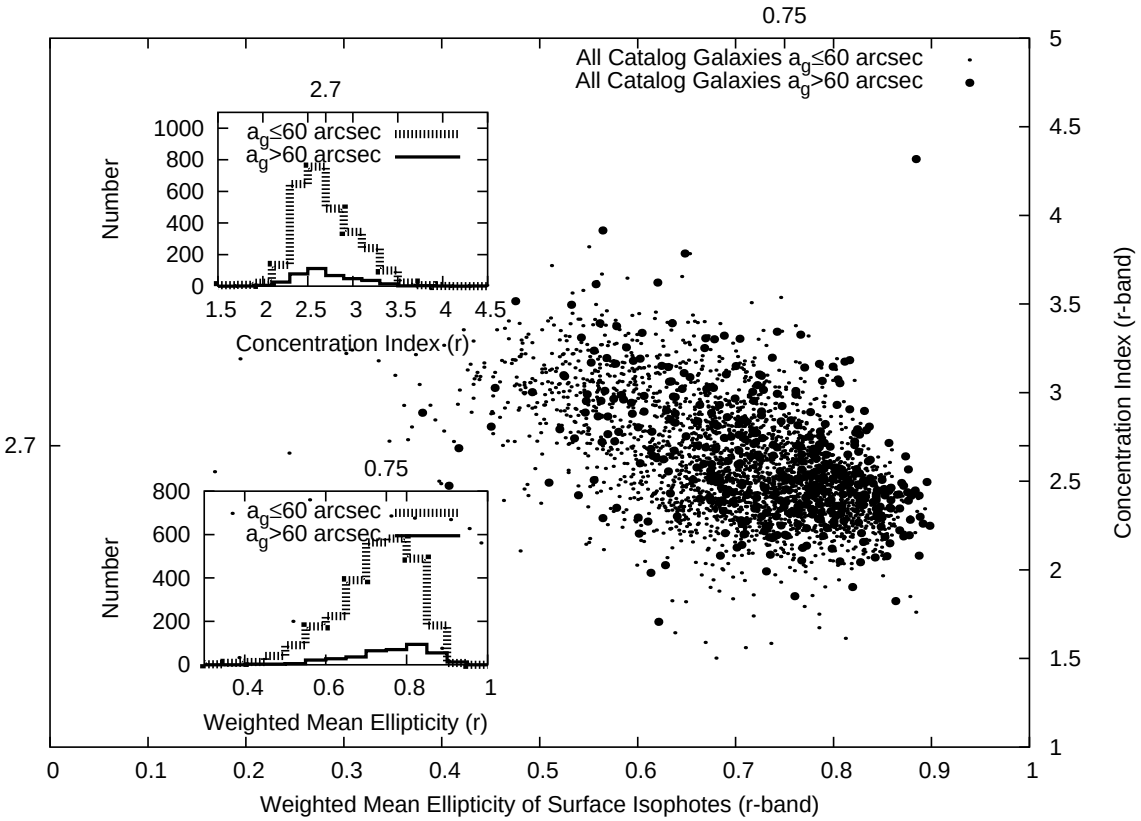

Figure 2.6: Separation diagram with the emphasized size samples. Galaxies with angular diameters larger than 60 arcsec are indicated with filled points, smaller galaxies with fine dots. The upper inset shows the number distribution of the concentration index, the bottom inset that of the weighted mean ellipticity. Objects with a diameter $a \leq 60$ arcsec are denoted by the dashed line. The others are indicated by a filled black line.

Table 2.2: Catalog: Structural Parameters. The complete version of this table is available from the CDS. Here we are presenting the first 15 entries (out of 3169) as an example.

Name	RA (J2000)	DEC (J2000)	Class	ε(g)	ε(r)	ε(i)	CI(g)	CI(r)	CI(i)	a(g)	a(r)	a(i)	a/b(g)	a/b(r)	a/b(i)
SDSS J000003.33-104315.8	00 00 03.335	-10 43 15.899	Sb(f)	0.746	0.740	0.735	2.801	3.032	3.162	37.730	41.511	42.443	5.863	5.294	4.469
SDSS J000151.29-092430.3	00 01 51.294	-09 24 30.368	Scd(f)	0.815	0.785	0.779	2.091	2.286	2.337	32.166	31.807	32.652	5.373	4.396	4.453
SDSS J000222.39-102543.6	00 02 22.395	-10 25 43.635	Sd(f)	0.854	0.838	0.827	2.046	2.286	2.289	32.657	24.546	25.162	9.395	4.871	4.213
SDSS J000301.47-001901.8	00 03 01.470	-00 19 01.862	Sb(f)	0.625	0.635	0.629	3.031	3.406	3.556	32.782	33.914	35.620	5.102	3.859	3.361
SDSS J000347.01-000350.3	00 03 47.017	-00 03 50.305	Sc(f)	0.749	0.713	0.691	2.497	2.381	2.750	35.999	34.902	37.593	5.507	4.446	4.339
SDSS J000530.43-095701.2	00 05 30.432	-09 57 01.224	Sd(f)	0.870	0.828	0.811	2.132	2.246	2.307	37.430	34.892	37.712	5.941	4.732	4.915
SDSS J000542.53-111048.8	00 05 42.531	-11 10 48.860	Sb(f)	0.770	0.767	0.761	2.868	2.754	2.922	41.873	36.395	43.693	5.972	4.536	5.789
SDSS J000619.88-092744.8	00 06 19.884	-09 27 44.894	Sc(f)	0.703	0.694	0.688	2.478	2.547	2.549	33.052	35.984	39.172	3.804	3.665	3.728
SDSS J000628.86-004702.9	00 06 28.865	-00 47 02.918	Sa(f)	0.505	0.527	0.519	2.845	2.874	2.972	45.955	55.102	58.408	4.187	4.241	3.734
SDSS J000641.10-105825.9	00 06 41.101	-10 58 25.946	Sc(f)	0.696	0.705	0.651	2.539	2.652	2.669	39.452	44.229	47.994	3.658	3.574	3.212
SDSS J000741.22-004145.3	00 07 41.222	-00 41 45.350	Sc(f)	0.675	0.667	0.650	2.481	2.699	2.715	31.690	35.123	32.730	3.758	3.249	2.406
SDSS J000919.54+003557.2	00 09 19.547	+00 35 57.258	Sb(f)	0.718	0.683	0.677	2.973	3.204	3.302	51.629	53.034	53.238	6.022	4.868	4.462
SDSS J000924.17+003216.2	00 09 24.172	+00 32 16.245	Scd(f)	0.810	0.795	0.814	2.227	2.506	2.136	30.648	32.993	32.352	6.731	6.445	5.573
SDSS J000941.16-003152.4	00 09 41.166	-00 31 52.414	Sa(f)	0.498	0.502	0.513	3.026	3.051	3.129	40.068	42.329	43.317	4.367	3.656	3.231
SDSS J000949.38-004103.1	00 09 49.382	-00 41 03.194	Scd(f)	0.791	0.782	0.767	2.529	2.586	2.599	33.298	31.220	31.124	6.737	5.007	4.007

Table 2.3: Photometric Parameters and Redshifts. The complete version of this table is available from the CDS. Here we are presenting the first 15 entries (out of 3169) as an example.

Name	Class	mag(g)	mag err(g)	mag(r)	mag err(r)	mag(i)	mag err(i)	μ(g)	μ(r)	μ(i)	z	z err
SDSS J000003.33-104315.8	Sb(f)	17.32	0.09	16.57	0.04	16.01	0.06	22.30	21.56	21.00	0.0829	0.1038E-03
SDSS J000151.29-092430.3	Scd(f)	17.71	0.03	17.13	0.02	16.89	0.04	22.45	21.86	21.63	0.0760	0.5085E-04
SDSS J000222.39-102543.6	Sd(f)	18.51	0.06	17.93	0.05	17.59	0.05	22.89	22.30	21.96	0.0000	0.0000E+00
SDSS J000301.47-001901.8	Sb(f)	17.51	0.13	16.60	0.10	16.13	0.10	21.60	20.69	20.23	0.0843	0.9440E-04
SDSS J000347.01-000350.3	Sc(f)	17.49	0.02	17.02	0.02	16.68	0.02	22.41	21.95	21.60	0.0625	0.6732E-04
SDSS J000530.43-095701.2	Sd(f)	17.67	0.04	17.20	0.03	16.86	0.04	22.74	22.27	21.93	0.0550	0.7188E-04
SDSS J000542.53-111048.8	Sb(f)	17.40	0.04	17.10	0.05	16.91	0.04	22.31	22.01	21.82	0.0400	0.4851E-04
SDSS J000619.88-092744.8	Sc(f)	16.93	0.01	16.29	0.02	15.95	0.01	21.85	21.21	20.88	0.0555	0.1026E-03
SDSS J000628.86-004702.9	Sa(f)	16.08	0.03	15.16	0.03	14.71	0.03	19.66	18.75	18.29	0.0443	0.9348E-04
SDSS J000641.10-105825.9	Sc(f)	16.64	0.84	16.25	0.99	15.90	0.87	22.89	22.50	22.15	0.0227	0.5682E-04
SDSS J000741.22-004145.3	Sc(f)	16.92	0.02	16.18	0.02	15.81	0.02	21.42	20.67	20.30	0.0735	0.1082E-03
SDSS J000919.54+003557.2	Sb(f)	16.52	0.10	15.72	0.08	15.30	0.06	21.11	20.30	19.88	0.0600	0.9067E-04
SDSS J000924.17+003216.2	Scd(f)	18.36	0.04	17.62	0.02	17.44	0.05	22.76	22.01	21.83	0.0798	0.6654E-04
SDSS J000941.16-003152.4	Sa(f)	16.42	0.04	15.69	0.04	15.31	0.04	20.85	20.12	19.73	0.0000	0.0000E+00
SDSS J000949.38-004103.1	Scd(f)	17.94	0.04	17.39	0.03	17.04	0.04	22.70	22.15	21.80	0.0390	0.5695E-04

Table 2.4: Galaxy classes and their fractions. The absolute numbers of galaxies in the various morphological subclasses and their percentages with respect to the catalog entries as a whole are listed in this table.

General Class	Number	Percentages
Sa(f)	222	7.01
Sb(f)	843	26.60
Sc(f)	1005	31.71
Scd(f)	503	15.87
Sd(f)	501	15.81
Irr(f)	95	3.00
Total	3169	100.00

2.6 Completeness considerations from sample comparisons

2.6.1 A comparison of our automatically selected galaxy sample with our visually classified sample

In order to estimate the completeness of our general morphological groups, we compare the results from our code with those from the visual inspection using the reference set that we compiled to automate the separation process. Here we compare the three general classes, which are galaxies with bulge, intermediate types, and simple disk objects. According to the previously defined limiting values for the three general types, class Sd(f) contains 501 simple disks. The comparison with our visual galaxy classification shows an agreement of 97%. Using our automated procedure, we identified 1065 objects from the bulge class (Sa(f) and Sb(f)). 88% of these were also identified as clear bulge galaxies in our visually selected reference set. The intermediate class contains the largest fraction of galaxies (1603 objects). This class is not homogeneous and contains Sc(f), Scd(f) and Irr(f) types. The comparison with the reference set indicates a completeness of 69%, i.e., 31% belong to other classes using visual inspection. 88% of these 31% seem to belong to the simple disk class when classified by eye. This suggests that the automated classified intermediate class contains a large number of Sd(f) types.

The division between the classes is necessarily somewhat arbitrary, and galaxies close to a boundary may in many cases also be considered members of the adjacent class. For instance, uncertainties can be introduced by variations in galaxy properties which are a form of "cosmic noise". We required our visual subdivision to be consistent with the earlier studies (Karachentsev et al. 1993, 1999).

The number of Sd(f) objects is relatively low. However, we intentionally chose fairly conservative separation criteria in order to minimize possible contamination of our thus selected simple disk sample. If we use a more generous lower limiting value of $\varepsilon \geq 0.75$ and include the Scd(f) objects as simple disks, the simple disk object class contains 1004 galaxies (extended simple disk sample of seemingly bulgeless types, Scd(f) and Sd(f)). This corresponds to 32% of the total catalog and enlarges the simple disk class by a factor of two. With this selection, however, the contamination by other types is larger than with the more rigorously defined limits for simple disks. Table 2.4 contains the absolute numbers and percentages of the various classes in comparison to the entries in the catalog as a whole.

2.6.2 A comparison of the Revised Flat Galaxies Catalog with our catalog

We searched for the RFGC galaxies in the SDSS DR1 using the coordinates given in the RFGC and recovered 328 objects. Then we checked how many of these galaxies are recovered in our catalog using our selection criteria. We found 273 objects in common. The remaining 55 RFGC galaxies were studied to find out why they were not recovered. In most cases objects are not recovered because they are not detected as SDSS targets ("Photoobjects"). This is the case if a galaxy is located near the borders of the SDSS footprint area, which has the consequence that this object is not included in the "Best Galaxy Table" and subsequently not detected in the SDSS "Galaxy" catalog. In the cases

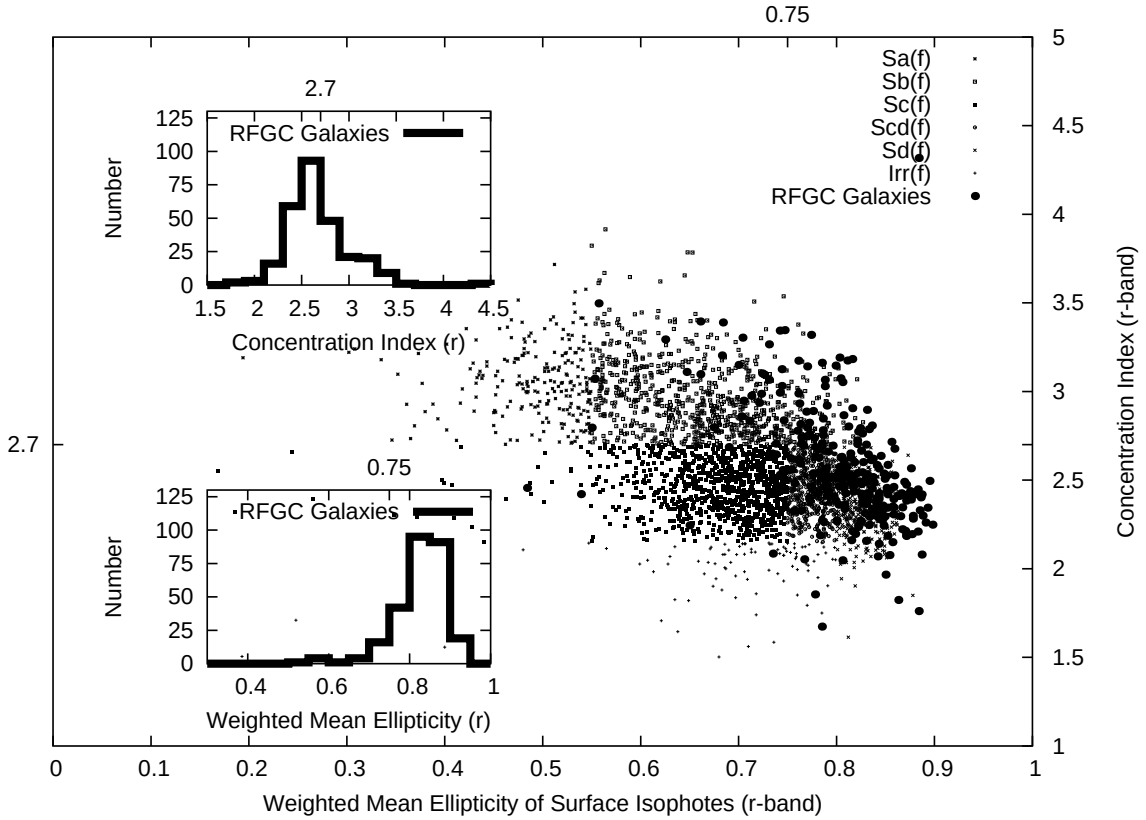

Figure 2.7: Separation diagram with the recovered RFGC galaxies. Galaxies of the different morphological types are indicated by small symbols as given in the legend, recovered galaxies from the RFGC with large filled points. The upper inset shows the number distribution for the recovered RFGC galaxies of the concentration index, the bottom inset that of the weighted mean ellipticity.

of relatively extended objects these systems are "shredded" by the SDSS detection software and thus not included in our catalog. Furthermore, there are a few cases where the SDSS shows a galaxy with an inclination deviating from an edge-on orientation at a given set of RFGC coordinates. A small subset of RFGC galaxies are not really edge-on galaxies. If RFGC galaxies are very close to nearby bright foreground stars, they are also rejected by the SDSS software. We conclude that we recovered all RFGC galaxies that conform to our selection criteria except for those missed by the SDSS software and for those that are not edge-on. Hence the RFGC is more complete than our catalog for nearby (and hence seemingly large) edge-on systems. The RFGC is also more complete in terms of spatial coverage since it does not suffer from the detection problems near the bright stars or edges of stripes.

We plot the location of the recovered RFGC galaxies in our separation diagram in Fig. 2.7. It is clearly seen that most of the RFGC objects belong to the Scd(f) and Sd(f) class (184 of 273). Additionally, a smaller number of RFGC systems is found in the Sb(f), Sc(f) and Irr(f) classes. This is illustrated in the two inserted histograms in Figure 2.7: RFGC objects clearly exceed our chosen limits for simple disk galaxies in the case of both discriminators, the CI (upper inset) and the ε (bottom inset). That means that Karachentsev et al. (1993) and Karachentsev et al. (1999) did not only select simple disk systems, but also included some mixed-morphology galaxies, whose classification we can now correct thanks to the CCD data.[3]

[3]Note, however, that our catalog contains *all* edge-on disk galaxies that we identified with our selection criteria, including mixed-morphology and bulge-dominated galaxies. The galaxy type can be found in Table 4.1 and Table 2.3 as explained earlier.

With our separation routine we have thus improved the identification of simple disks in contrast to the flat galaxies catalogs. There are several reasons for this improvement: One is that the CCD images of the SDSS have a greater uniformity than the earlier employed blue POSS-I and ESO/SERC photo plates. In addition, the SDSS imaging data are deeper—they are 50% complete for point sources at g = 23.2 mag (Abazajian et al. 2003). The limiting magnitude of the blue POSS-I plates is 20 mag(R) (see Minkowski & Abell 1963, page 481), and of the ESO/SERC J plates is 22.5 mag(B) (Reid et al. 1991). Because of the higher sensitivity, depth, and resolution of the SDSS, we can identify more substructure within our galaxies, which leads to a more accurate classification. This improved classification benefits from our choice of the SDSS r-band, which has the highest photon efficiency in the SDSS.

Our selection parameters include galaxies with smaller diameters and extend to fainter magnitudes. A comparison of the magnitudes and diameters of the recovered RFGC objects and the remaining galaxies from our catalog is shown in Fig. 2.8. As is to be expected, the figure shows that our catalog contains objects with smaller diameter as well as fainter objects. Furthermore, our catalog contains galaxies not detected in the RFGC but with diameters and luminosities in the range of the RFGC galaxies. Note that we also have a larger number of more luminous galaxies at a given diameter. This is the consequence of permitting smaller axial ratios than the RFGC, which favors a larger number of disk galaxies with a bulge. Moreover, we show in Fig. 2.9 that in order to recover the RFGC galaxies from the SDSS database, we need to use selection criteria with smaller axis ratios. The SDSS axis ratios tend to be smaller than those of the RFGC. When comparing the number of seemingly bulgeless types (our Scd(f) and Sd(f) class with $\varepsilon \geq 0.75$ and CI < 2.7), our catalog contains 1004 objects including 184 RFGC galaxies (out of 273 RFGC galaxies within the DR1 area). While we are missing galaxies near the edges of stripes etc., we still have ~ 3.7 times more simple disk galaxies than were found in the RFGC within the same area. As Fig. 2.8 illustrates, this is only in part because of the inclusion of smaller axis ratio. We attribute it also to the higher sensitivity and homogeneity of the SDSS.

It is difficult to determine absolute completeness numbers for our survey. For instance, in order to recover the initial RFGC training set, we had to decrease the angular diameters as compared to the parameters chosen in the RFGC. Furthermore, some incompleteness effects will affect all galaxies alike (e.g., the non-detection due to the location close to the border of the footprint area), whereas for instance dust will affect certain galaxy types in particular (see next section).

2.7 The influence of dust and distance

We have subdivided our edge-on galaxies in objects with bulge and in simple disk systems without a bulge component. In this section we discuss the expected influence of dust on our separation procedure and a resolution bias caused by distance.

The distribution of dust in spiral galaxies has been the subject of a lively debate over decades. Recent studies try to model the influence of dust on the surface photometry. Kuchinsky et al. (1998) compared the optical/near infrared (NIR) color gradients of edge-on galaxies with the reddening from radiative transfer models. These models use Monte-Carlo techniques in order to describe the radiative transfer of photons (including scattering, absorption, and re-emission) in different dust environments (Gordon et al. 2001). Other models were applied to edge-on galaxy examples (see, e.g., Xilouris et al. 1997, 1998; Pohlen et al. 2000; Popescu et al. 2000; Misiriotis & Bianchi 2002). The best models include a homogeneous and clumpy distribution of dust (Kuchinsky et al. 1998). Tuffs et al. (2004) computed the attenuation of stellar light at different inclinations, wavelengths, and opacities from the different geometrical components of a spiral galaxy. They found that the extinction strongly depends on the inclination. In the case of edge-on systems most of the attenuation by dust occurs in the thin disk component, which often includes a typical dust lane.

But the amount of dust in different edge-on spiral types is not constant. This was recently shown by Stevens et al. (2005) with new SCUBA observations. Their measurements show that the flat galaxy NGC 5907 (FGC 1875) contains a very high amount of neutral hydrogen but only small amount of

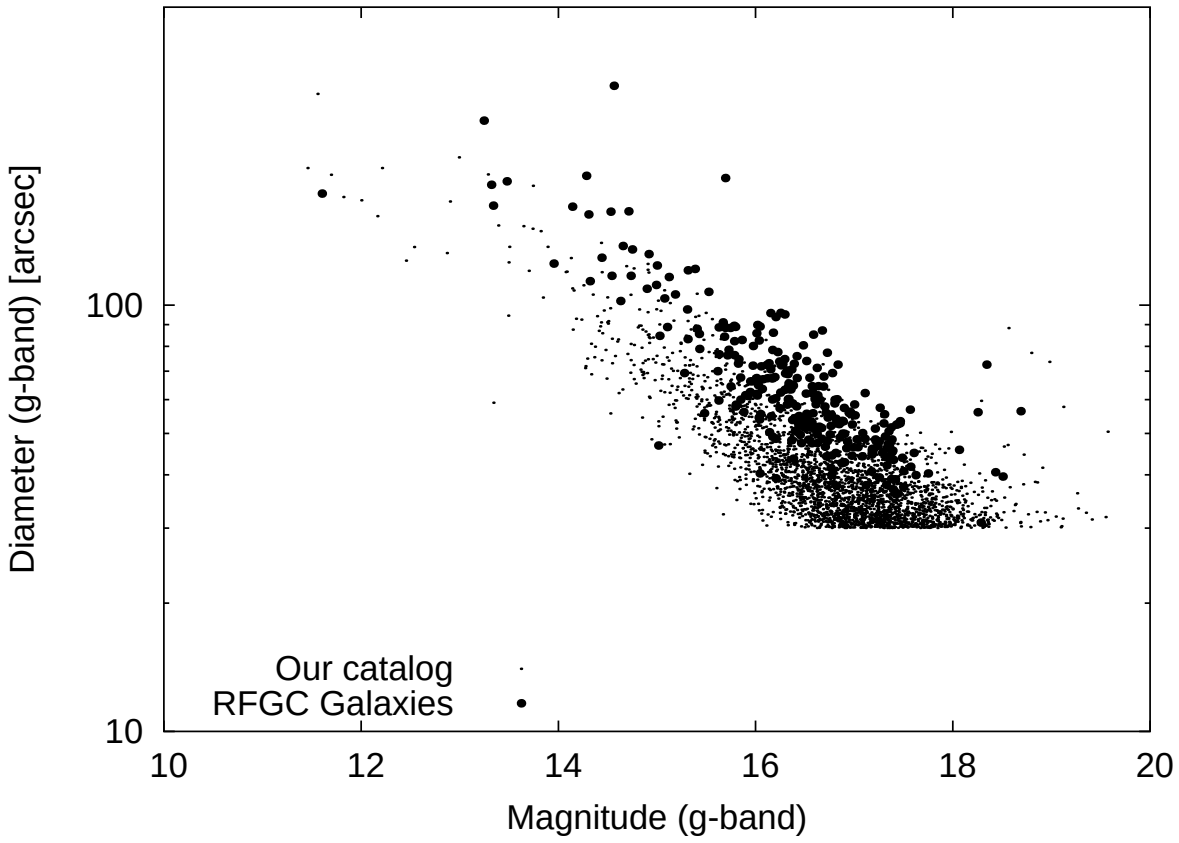

Figure 2.8: Comparison of the depth of this catalog versus the recovered RFGC objects. The objects of the RFGC are large filled points, the catalog galaxies are small dots.

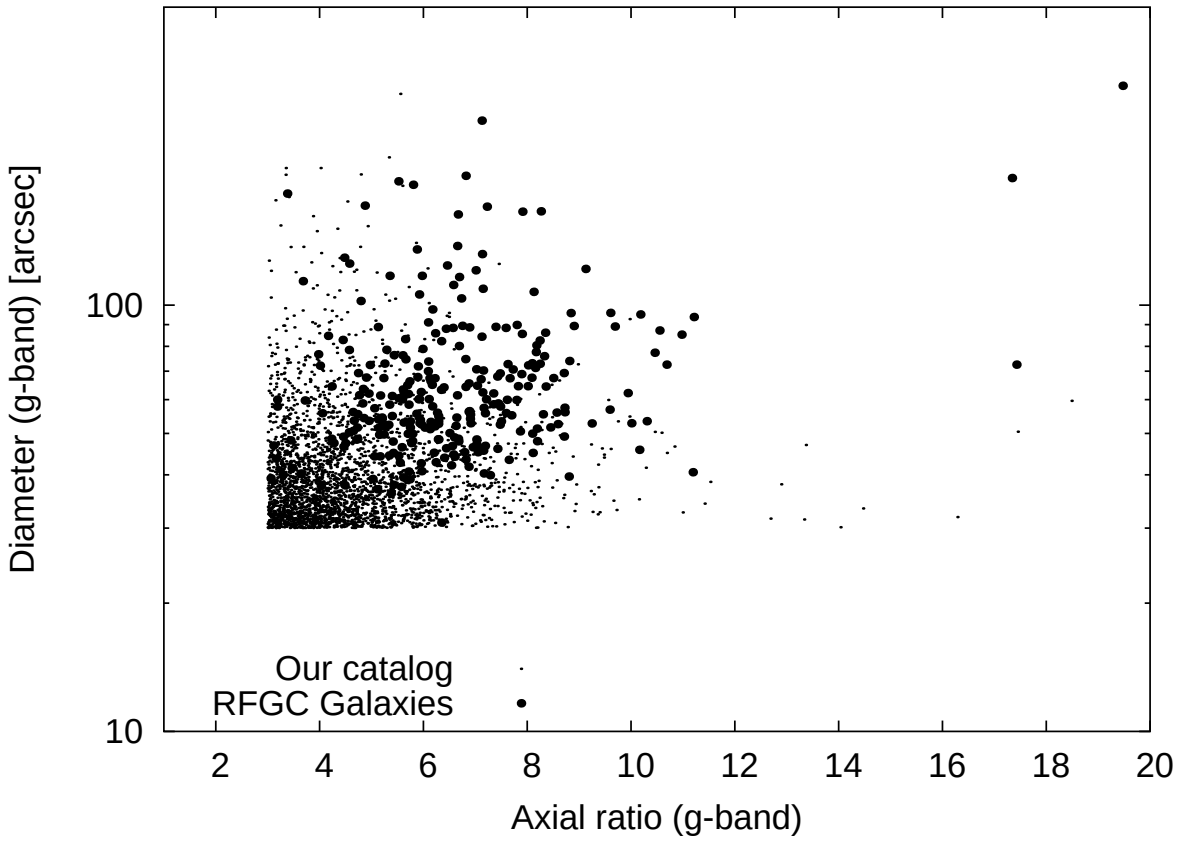

Figure 2.9: Comparison of the depth of this catalog versus the recovered RFGC objects. The objects of the RFGC are large filled points, the catalog galaxies are small dots.

total dust. A high ratio of the mass of the neutral hydrogen to the mass of cold dust implies a very low star formation efficiency. In addition, Matthews et al. (1999b) and Matthews & van Driel (2000) show the "lack of a quintessential dust lane" in the prototypical superthin galaxy UGC 7321. In another paper, Matthews & Wood (2001) conclude that the dusty interstellar medium (ISM) in this type of objects has a clumpy and patchy distribution. They derived the observed properties of dust with the aid of a multiphase ISM model and found that "≈50% of the dusty material in UGC 7321 is contained in a clumpy medium". The other half has a diffuse distribution. UGC 7321 is an LSB galaxy with a large axial ratio and no bulge component, a typical simple disk.

What are the differences in the properties of edge-on galaxies with an organized dust lane and those that exhibit a clumpy and diffuse dust distribution? Dalcanton et al. (2004) found a clear boundary between edge-ons with and without a dust lane. They conclude that the dust distribution is connected with the rotation velocity, i.e., galaxy mass. Organized dust lanes appear in high surface brightness objects with a relative rapid rotation velocity. In galaxies with rotation velocities below $V_c = 120$ km s^{-1} the dust has not settled into a thin dust lane. The dust distribution of these simple disk galaxies with typically a low surface brightness is clumpy and diffuse out to large scale heights.

What is the effect of a clumpy or an organized dust distribution on our separation values? In galaxies with a small angular size the dust lanes are unresolved, especially in those with larger distances. For these galaxies it is not a simple exercise to verify the existence of an intrinsic dust lane. In some of our larger and brighter galaxies a dust lane is visible, in others not. The dust is concentrated in the thin disk component and consequently the light attenuation caused by the thin disk is the highest (Tuffs et al. 2004). The stellar disk disappears in the extreme cases where a large amount of dust extends beyond the whole disk. Therefore the consequences of the dust attenuation of the disk are expected to be stronger in more massive galaxies like NGC 891. In these objects the probability of a dominant bulge is high. They are more metal-rich and are expected to contain more dust (mass-metallicity relation, e.g., Dalcanton et al. 2004). In general, the dust dims the thin disk with respect to the bulge brightness. This circumstance introduces three additional biases for our catalog:

1. Early-type disk galaxies: Our catalog has an incompleteness for galaxies with big bulges and attenuated underlying thin disks. In these cases the disk cannot easily be detected as a bright structure because its morphology is like a dark line in a bright bulge component. Therefore this catalog is likely to be incomplete for dusty early-type spirals, especially for the types S0(f) and Sa(f), where we may be missing the disks. This may lead to an overestimate of the number of simple disks as compared to pronounced bulge-disk systems.

2. Massive late-type spirals/massive simple disks: A bias is shown in the extreme cases where the thin disk of a high-mass simple disk galaxy is almost completely obscured by dust. In this case the galaxies may have too small an axial ratio a/b to be selected for our catalog. In the less extreme cases of high-mass simple disk galaxies the dust dims the thin disk. The influence of dust in a simple disk is that the value of ε decreases because a dusty disk appears to be thicker. For that reason, the affected galaxies may exhibit an offset toward the intermediate class in the separation diagram (Fig. 2.4). The CI of such galaxies is not distorted because these objects have no distinct bulge.

3. Objects at large distances are affected by a resolution bias. The consequences are that an unresolved dustlane dims the light of the stellar disk compared to a dust-free disk. This does not affect ε; the disk looks simply smaller. This may lead to a slight increase of the CI for disks with a bulge. However, the separation of the general classes does not seem to be displaced by the presence or absence of unresolved dust lanes. The important effect is that a strongly dimmed disk looks smaller and may fail to pass the selection criterion. The catalog will be more incomplete for small angular size disk galaxies with unresolved dust lanes. To reduce this effect we impose a minimum diameter in our search.

A future paper is planned in order to explore the effects of dust using simulated galaxies with varying amounts of dust and inclinations.

2.8 Discussion

We identified edge-on disk galaxies in the SDSS DR1, which we subdivide in the following classes:

Disk galaxies with a bulge; Sa(f), Sb(f) (CI $\geq$ 2.7): The fraction of these objects in the catalog is 34%. This class contains spiral galaxies with a bulge that are not affected by the selection effect described in section 2.7.

Intermediate class; Sc(f), Scd(f), Irr(f) (CI $<$ 2.7 & $\varepsilon < 0.8$): These late-type galaxies show a central light concentration and often a bouffant disk but no obvious bulge. With a fraction of 50% these types represent the majority in this catalog. These galaxies may have an inclination slightly smaller than edge-on or may show pronounced warps. At CI $<$ 2.15 & $\varepsilon < 0.8$ the class of disky edge-on (dwarf) irregulars appears. They show an asymmetric "puffy" disk with small clumpy (not central) light concentrations comparable to those found by Parodi et al. (2002) or blue compact dwarfs (e.g., Sandage & Binggeli 1984); see also Kniazev et al. (2004a).

Simple disk galaxies; Sd(f) (CI $<$ 2.7 & $\varepsilon \geq 0.8$): These galaxies appear to be pure bulgeless disks. Using the conservative separation values, this class contains 16% of the catalog objects.

In order to check the usefulness of our separation we visually inspected galaxies in the extreme regions in our separation diagram and found the following subgroups:

Dusty disk-dominated galaxies (CI $\gtrsim$ 2.6 & $\varepsilon \gtrsim 0.75$): These types have flat extended disks and slight central light concentration. The majority of this type appears as extended disks with dust lanes, small bulges and very blue outer disks.

Complex bulge/disk systems (CI $\gtrsim$ 3 & $\varepsilon < 0.7$): These types are mostly complex bulge-disk systems. The bulge of these systems becomes clearly visible. In some of these types a stellar disk extends out to large scale heights and forms a bright but diffuse envelope around the galaxy.

In addition to the visual inspection of all galaxies in the extreme regions in the ε–CI space we also checked galaxies located in the central regions of the selection boxes for every general type by eye. In agreement with our expectations we found simple disk systems at high ε and low CI ($0.8 < \varepsilon < 0.85$ & 2.3 $<$CI$<$ 2.4). Their appearance is blue and needle-like. Intermediate values of CI and ε reveal the region where intermediate types are concentrated ($0.7 < \varepsilon < 0.75$ & 2.5 $<$CI$<$ 2.6). This group is dominated by lenticular-shaped puffy disks and smooth central light concentration but no dominant bulge component. The center is slightly redder than the bluer outer parts in these systems. It seems that they often have extended faint LSB disks around the bright parts. We checked the central region of disk galaxies with dominant bulges ($0.65 < \varepsilon < 0.7$ & 3 $<$CI$<$ 3.1). These early-type spirals are visibly less blue than the other general types in this catalog, and galaxies with bulge are the less well-populated group. The highest concentration of galaxies can be found in the transition zone between the intermediate types and the simple disks. This indicates the lack of clear-cut boundaries between different types; instead we are seeing a continuum.

Figures 2.10 and 2.11 show a comparison of the general classes with surface brightness. As shown in these figures, the presence or absence of bulges has an influence on the overall surface brightness of a galaxy as one would expect. Simple disks and the irregulars have the lowest intrinsic surface brightnesses (i.e., the lowest stellar number densities) of all edge-on galaxies in this catalog. For this plot we use the surface brightness given in column 10 of the Table 2.3. This surface brightness is derived as explained in Section 2.3. No dust correction is applied.

2.9 Conclusions and Summary

We present for the first time a homogeneous and large dataset of uniformly selected edge-on disk galaxies. These common galaxy types are very important in order to understand the formation and

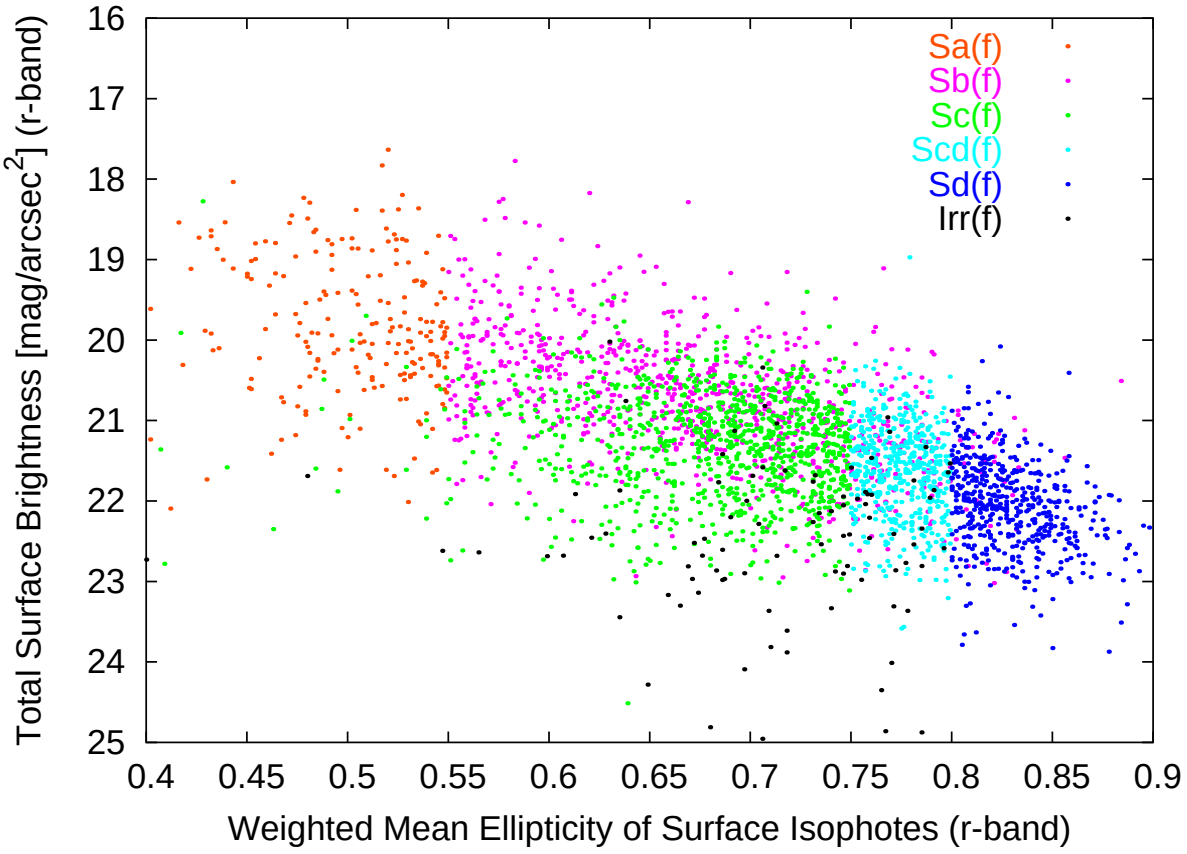

Figure 2.10: Distribution of the ε versus the total surface brightness. The different color-coded dots represent the various morphological galaxy types and are explained in the key.

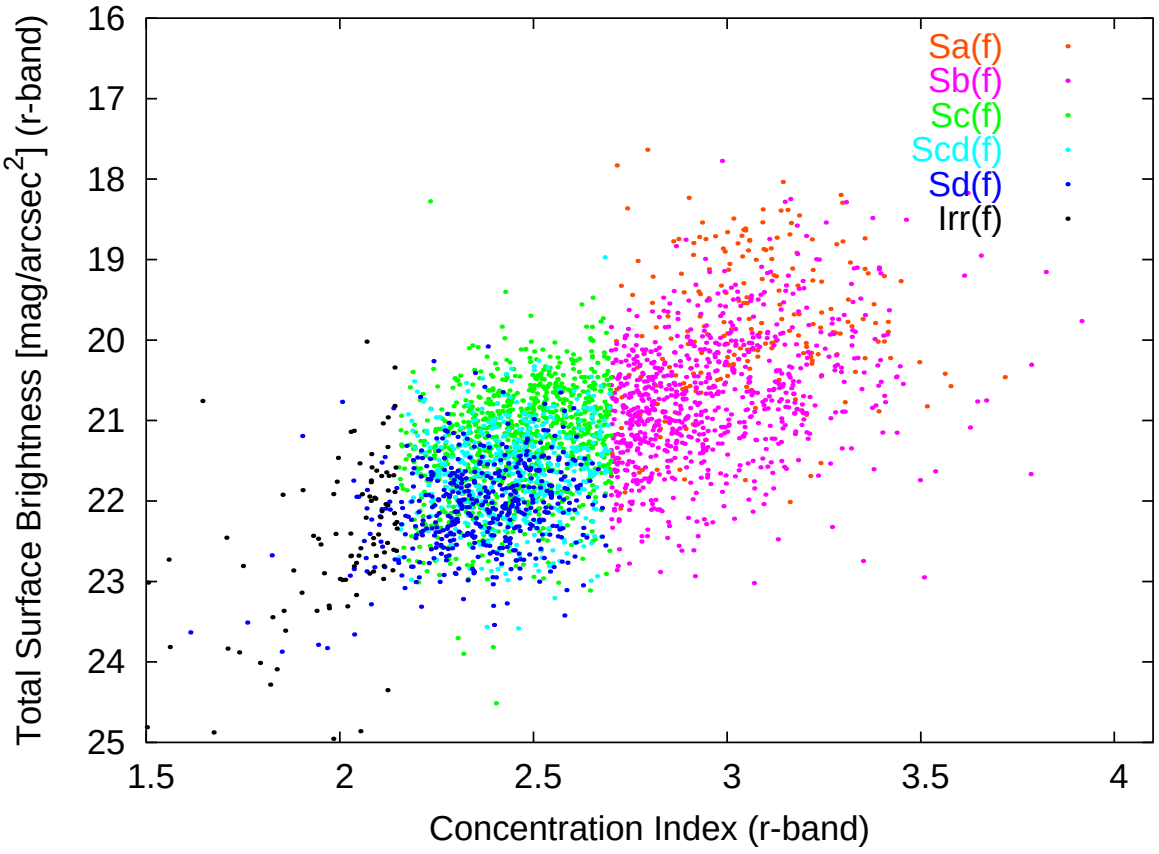

Figure 2.11: Distribution of the CI versus the total surface brightness. The different color-coded dots represent the various morphological galaxy types and are explained in the key.

evolution of disk galaxies. The galaxies are selected from the SDSS DR1 on the basis of photometric structural parameters indicative of extended stellar disks with large major to minor axis ratios.

With the aid of this method we gathered 3169 edge-on galaxies in an area of 2099 deg^2 and selected through an automated separation algorithm. Using visual inspection of the galaxies we realized that this catalog contains three general classes of crude morphological types: disk galaxies with bulge, thin bulgeless objects and intermediate types.

The separation is based on the central light concentration and the flatness of the galaxy images. The light concentration is expressed via the concentration index CI. With this CI we are able to distinguish between disk galaxies with a bulge component Sa(f) and Sb(f) and those with bulgeless appearance – the Sc(f), Scd(f), Sd(f) and Irr(f) classes. As a second discriminator we use the luminosity-weighted average of the ellipticity ε, derived from elliptical isophotes of every object. The ε allows one to distinguish several structural groups with flat disks: the early-type spirals, types Sa(f) from Sb(f); the apparently bulgeless systems from intermediate types Sc(f), Scd(f) and Irr(f) with central light concentrations; and the thin, smooth galaxies, the simple disk class Sd(f).

The simple disk class includes objects previously defined as flat and superthin galaxies and it exhibits the lowest surface brightness compared to the other classes. The axial ratios of simple disk galaxies are the largest. The intermediate class of edge-ons is composed of different types of galaxies including (dwarf) irregular systems. There is no well-defined boundary between these general classes, but instead a continuum of properties exists.

The fraction of galaxies with bulge (Sa(f), Sb(f)) is 34%, those without bulge 16% (Sd(f)) and the fraction of the intermediate class is 50%. However, we found that the intermediate object class contains also a large fraction (about 440 objects, these are nearly 30% of the intermediates) of seemingly bulgeless types. Therefore we conclude that every general class (i.e., galaxies with bulge, intermediate objects and simple disks) represents about one third of the galaxies listed in the catalog. The true numbers of our classes are somewhat lower. Dust attenuation introduces a bias such that this catalog is expected to be incomplete for early-type spirals with pronounced dust lanes. Additional incompleteness is introduced because of features of the SDSS database such as galaxy shredding, etc.

In the case of late-type spirals, dust is expected in high-mass systems and increases the apparent thickness of the disk. This results in a minor offset in the separation but has no effect on the completeness for simple disks. Unresolved dust lanes dim the disk light and lead to higher incompleteness for distant disk galaxies. A comparison with the RFGC shows that our catalog suffers from incompleteness for, e.g., galaxies close to bright stars or near the edge of the SDSS footprint area, but that it nonetheless contains almost four times as many galaxies within a given area than the RFGC. This is mainly because we included also galaxies with smaller angular diameters, but it is also a result of the homogeneity, resolution, and depth of the SDSS.

This catalog provides a large, homogeneously selected galaxy sample for which sensitive five-color photometry (and in many cases also spectroscopy) is available. SDSS spectroscopy, while covering only a portion of the galaxies because of its circular aperture of $3''$, will be useful for a wide variety of studies, for instance for deriving metallicities and for constraining the properties of the underlying stellar populations (e.g., Kniazev et al. 2004b; Bernardi et al. 2005).

While these data will be analyzed in later papers, even the raw catalog data have interesting implications. Our results re-enforce the conclusions of Karachentsev and collaborators (Karachentsev et al. 1993, 1999) that simple disk galaxies are relatively common, especially among intermediate-mass star-forming galaxies (Matthews & Gallagher 1997). Galaxy formation models must be able to produce such high angular momentum systems with reasonable frequencies. We also find that the simple disks are not a separate morphological class, but rather are at the end of a continuum that extends smoothly from bulge+disk systems. However, the simple disks tend to be lower surface brightness galaxies, indicating that the probability for bulge formation depends on host galaxy mass. This in turn can be linked to models where bulges form from internal disk instabilities through the dependence of the Toomre Q-parameter on disk surface density (e.g., Immeli et al. 2004). Similarly the properties of our sample will be useful in constraining the role of galaxy mergers in building disk-halo galaxies (e.g., Springel & Hernquist 2005; Kormendy & Kennicutt 2004). We will explore these and related issues in future papers.

Chapter 3

Morphology of Edge-on Disk Galaxies

3.1 Introduction

The separation of the edge-on galaxies from our catalog (see Chapter 2 and Kautsch et al. 2006a,b, hereafter: the Catalog) into the various morphological classes is based upon two morphological discriminators. The first parameter is the concentration index CI. This is the central light concentration which separates the galaxies with bulge from the bulgeless disks and also edge-on irregulars. For the more sensitive separation into thin simple disks from intermediate bulgeless objects as well as early and intermediate type disks with bulge we used the luminosity weighted ellipticity ε of the systems. This discriminator does not only measure the flatness of the object, it includes also the bulge size and is robust against small scale distortion like HII regions, dust knots and warps. The disadvantage of ε is that it has to be measured directly on the frames because it is no SDSS parameter in contrast to the CI. Measuring ε is therefore very time consuming when using large datasamples such as the SDSS DR5. Here we present a comparison of SDSS parameters which are morphological discriminators.

3.2 Morphological Discriminators

3.2.1 Colors

Strateva et al. (2001) favor to use the bimodality of early and late type galaxies in the color-magnitude space as a morphological discriminator. Galaxies with colors redder than $u - r = 2.2$ are considered as early types (E, S0, Sa) and blue galaxies ($u - r \leq 2.2$) are late types (Sb, Sc, Sd, Irr).

Figure 3.1 presents the color-magnitude diagram from Strateva et al. (2001) for the Catalog galaxies as indicated by the different colored dots. The vertical line represents the limiting color value of 2.2. This figure is obviously not very useful for edge-on galaxies. Only a small tendency is seen for bulgy galaxies that occupy redder regions. Plotting only galaxies with bulge in Fig. 3.2, this trend becomes weaker because it is visible that early types are distributed across the entire color range. It is not difficult to imagine that the correlations with the CI (Fig. 3.3) and the ε (Fig. 3.4) are too small in order to use the color as an alternative morphological discriminator for edge ons. This is already shown in our preliminary studies (Kautsch & Grebel 2003a,b). The reason for that is the high inclination of the Catalog galaxies. This edge-on view introduces a complicated interplay between reddening influence from various dust amount and red stellar populations affected from the age-metallicity degeneracy in the bulge and the disk. Especially the reddening by dust is strong in disks when seen edge-on (see Sect. 2.7). That means that it is not possible to distinguish the morphologies between two galaxies with different amounts of dust using color as sole discriminator.

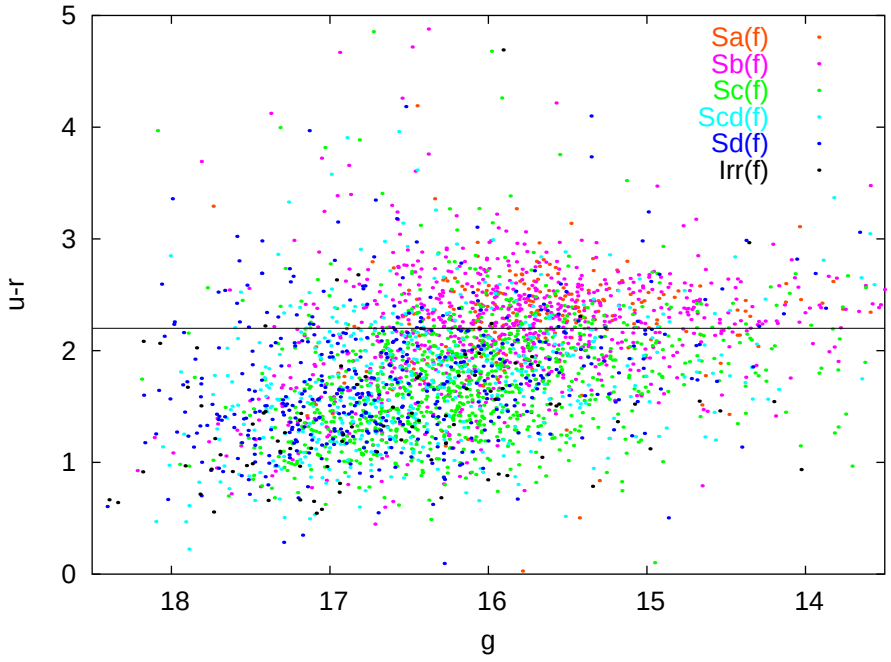

Figure 3.1: Morphological separation diagram with the apparent g magnitude against the color $u - g$ as suggested by Strateva et al. (2001) for the Catalog galaxies. The different color-coded classes of the Catalog are given in the legend. The vertical line represent the limiting value that divides early from late morphologies as found by Strateva et al. (2001).

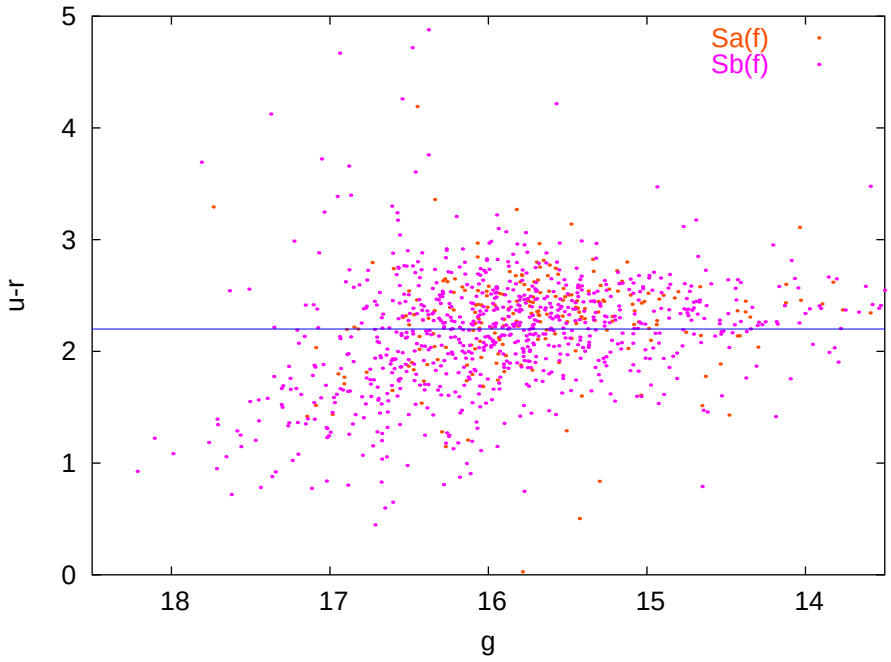

Figure 3.2: Same as Fig. 3.1. Only the galaxies with bulge are plotted.

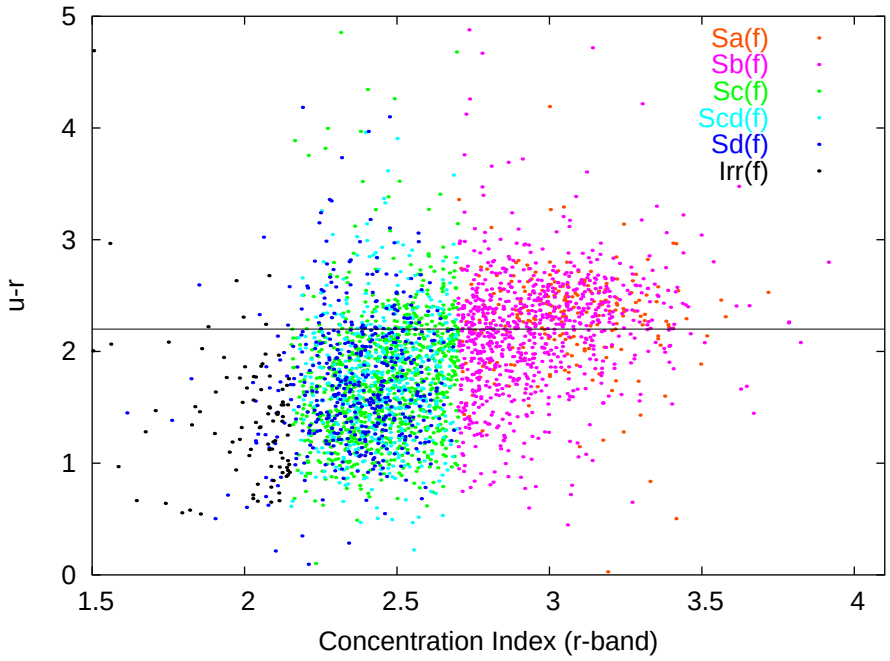

Figure 3.3: The morphological discriminator CI in dependency of the color $u - g$. The different colored dots represent the various morphological galaxy types from the Catalog and are explained in the key. The vertical line represent the limiting value that divides early from late morphologies as found by Strateva et al. (2001).

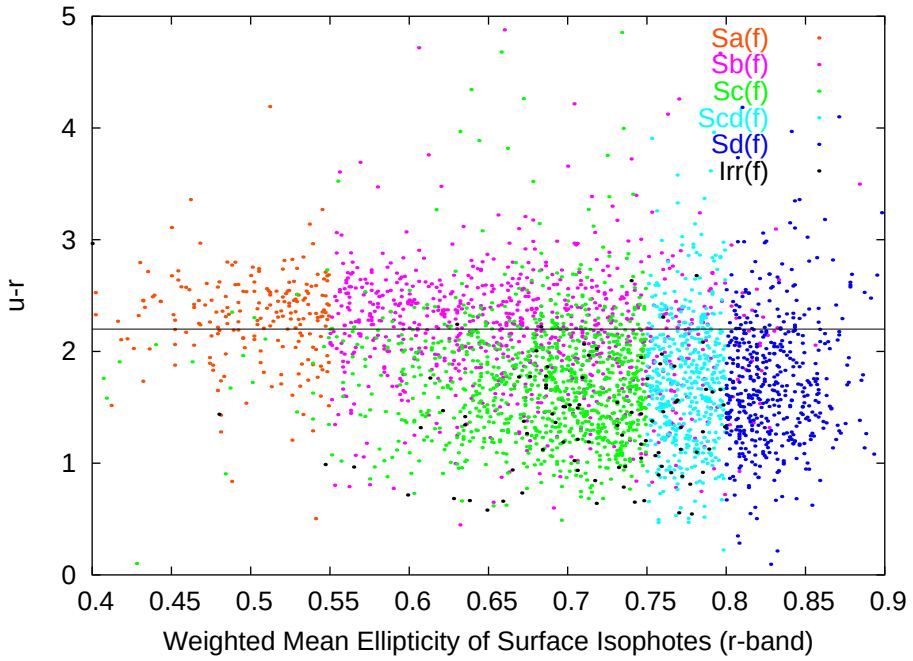

Figure 3.4: The morphological discriminator ε in dependency of the color $u - g$. The different colored dots represent the various morphological galaxy types from the Catalog and are explained in the key. The vertical line represent the limiting value that divides early from late morphologies as found by Strateva et al. (2001).

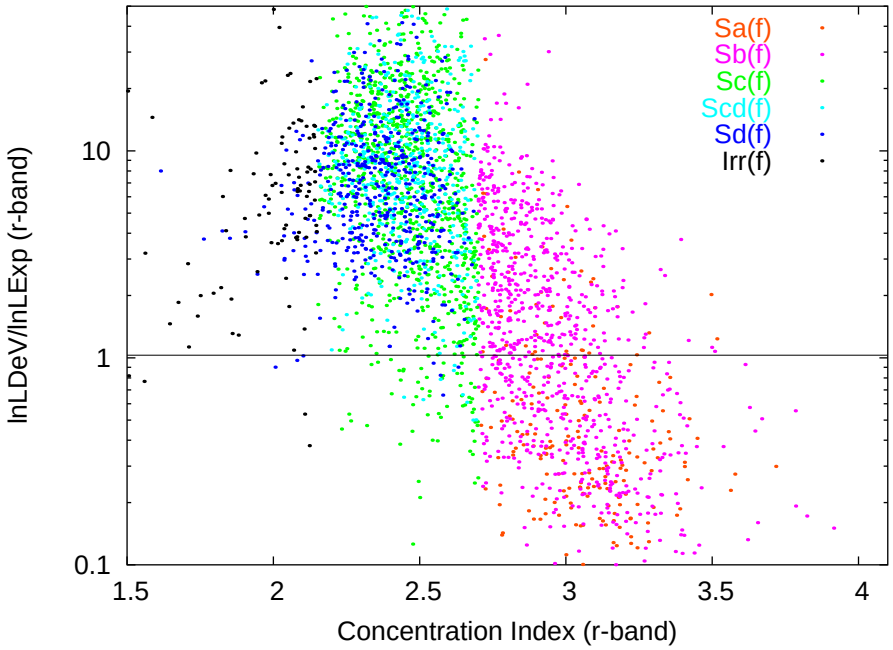

Figure 3.5: Comparison of our CI with the profile likelihood from SDSS. The profile likelihood is expected to separate galaxies that are bulge dominated with de Vaceulours profiles from the exponential disk dominated galaxies at a value of 1.03 (Bernardi et al. 2003) as shown by the horizontal line. The different color-coded dots represent the various morphological galaxy types from the Catalog and are explained in the key.

3.2.2 Profile Likelihoods

Another parameter is used to determine morphology which is based on the likelihoods of the best-fit exponential or de Vaucouleurs' profiles. It has been found that the likelihood ratio of exponential and de Vaucouleurs fits (`lnLDeV/lnLExp`) is a morphological discriminator between early (E, S0, Sa) and late types (Sb, Sc, Irr) with a limiting value of `lnLDeV_r/lnLExp_r` = 1.03 (Bernardi et al. 2003). The SDSS parameter `fracDeV` is the fraction of the total flux contributed by the de Vaucouleurs model and is therefore based on the same measurements as `lnLDeV_r/lnLExp_r`. We do not use `fracDeV` and present the results using the likelihood ratio, although other authors (e.g. Vincent & Ryden 2005) prefer to use `fracDeV` because it delineates a continuum of surface brightness profile types, from pure de Vaucouleurs profiles with `fracDeV`=1 to the pure exponential profiles (`fracDeV`=0).

Figure 3.5 and 3.6 show the correlation of the likelihood ratio with the CI and the ε, respectively. As expected, galaxies with bulge have a larger probability of a de Vaucouleurs component. Due to large scatter and insensitivity for the Catalog subgroups, also this morphological discriminator can be ruled out as being useful for the separation between the different edge-on disks. This is also due to an interplay between various aspects:

- In order to measure the surface brightness profile automatically an object has to be extended enough but not too large for including small-scale structures like warps, tidal tails etc. Also, galaxies do not necessarily follow pure exponential or de Vaucouleurs profiles.
- The edge-on view introduces dust attenuation, which can depress the stellar exponential profile of a disk giving dusty disks a wrong profile likelihood.
- Not all disks of galaxies have pure exponential profiles (e.g. Pohlen & Trujillo 2006) and not

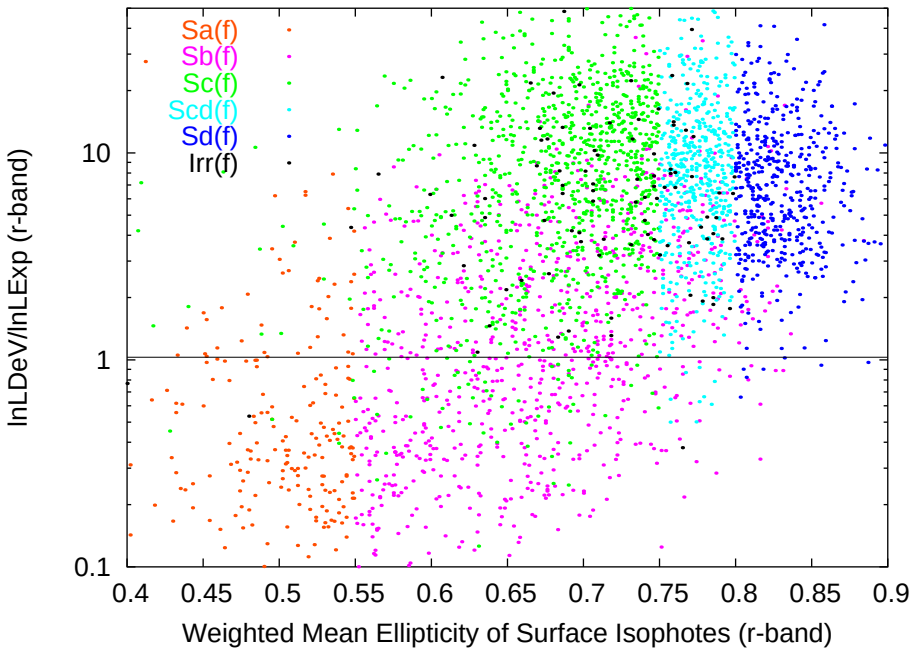

Figure 3.6: Comparison of our ε with the profile likelihood from SDSS. The profile likelihood is expected to separate galaxies that are bulge dominated with de Vaucouleurs profiles from the exponential disk dominated galaxies at a value of 1.03 (Bernardi et al. 2003) as shown by the horizontal line. The different color-coded dots represent the various morphological galaxy types from the Catalog and are explained in the key.

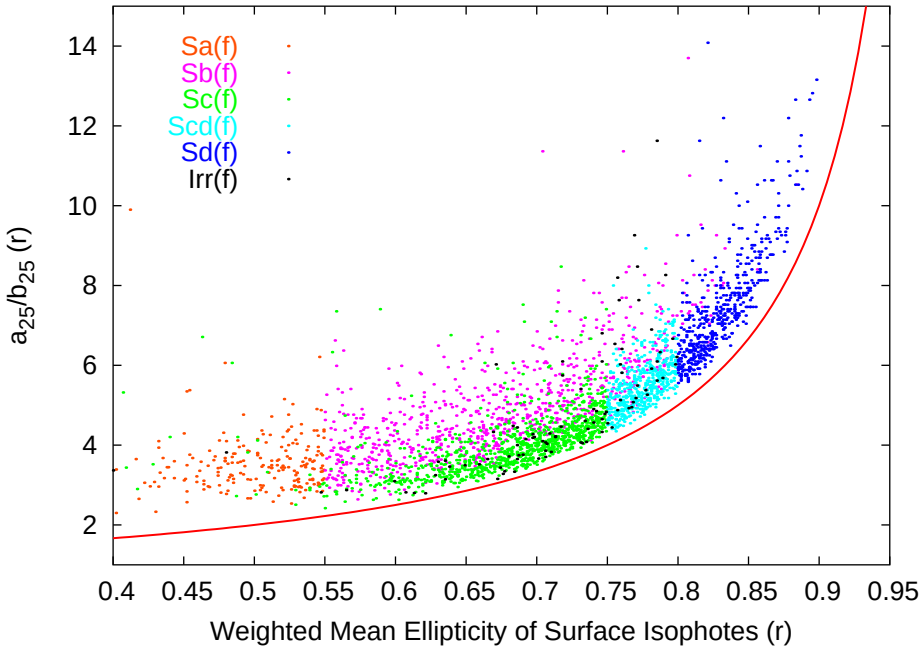

Figure 3.7: Distribution of the axial ratios and morphological type. The axial ratio is measured with our code from the Catalog. The different color-coded dots represent the various morphological galaxy types from the Catalog and are explained in the key. The curve represent the distribution of idealized simple ellipses. The different morphological classes are related to the simple isophotal axial ratios and simple disks represent the flattest systems.

all bulges can be fitted with a de Vaucouleurs profile. Galaxies that undergo secular evolution (Sect. 4.6.2) can build up "pseudobulges" with typical disk properties. This includes also exponential bulge profiles. This effect may explain the large fraction of galaxies with bulge in the exponential likelihood region.

- It is expected that the contribution of de Vaucouleurs bulges are overestimated because the inner parts are more strongly weighted than the outer parts of the galaxies in the SDSS analyzing pipelines (Strateva et al. 2001).

3.2.3 Texture

The `texture` parameter from the SDSS database measures the bilateral asymmetry of an object and could be generally used to separate the more symmetric early-type galaxies from the late types. It was found that this parameter is poorly correlated with morphology in its SDSS implementation (Strateva et al. 2001).

The asymmetry also has a different meaning for edge-ons. This will be extensively discussed in Sect. 5.4.6. In this Section we analyze the behavior of the so called CAS morphology on a subsample of Catalog galaxies in different bands including the dust-free near infrared. The CAS system includes the CI, the asymmetry and the clumpiness appearance of a galaxy.

3.2.4 Axial Ratio

The Catalog galaxies are expected to correlate with axial ratio, i.e., the ratio between length and height of a galaxy. Figure 3.7 shows ε versus the axial ratio measured from the elliptical fitted isophote at a

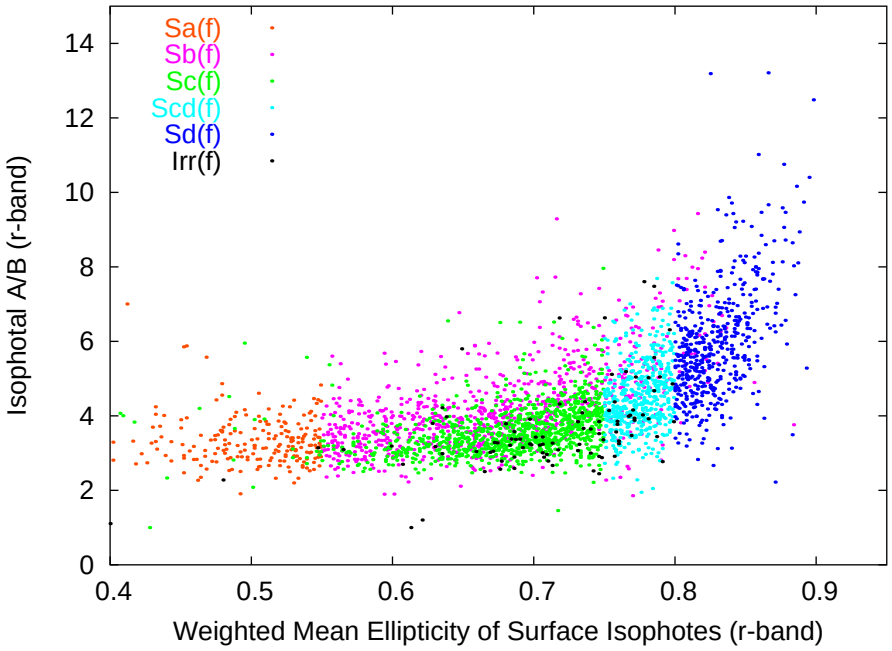

Figure 3.8: Same as Fig. 3.7 but with the axial ratio derived directly from SDSS parameters.

surface brightness of 25 mag/arcsec^2 on every galaxy with our routine described in Sect. 2.3.1. The curve represents a simple elliptical model $f(x) = \frac{1}{(1-x)}$. This figure shows that simple disks have the flattest disks and the highest axial ratios. The Sd(f), Scd(f) and Sc(f) class follows the simple elliptical function line. But earlier types (Sb(f) and Sa(f)) are less correlated because of the possible configurations of different disk+bulge sizes and luminosities. E.g., the same axial ratio but different bulge brightnesses lead to different values of the flatness ε. Irr(f) types are bulgeless but have small axial ratios indicating a puffed up disk.

Also the SDSS provides the isophotal major (`isoA`) and minor (`isoB`) axis of an object that is measured from the isophote that corresponds to a surface brightness of 25 mag/arcsec^2 in the given band. Due to different algorithms in our and in the SDSS routine, Fig. 3.8 has slightly more scatter than the figure shown before. However, simple disks have the largest axial ratios.

In both Figs., 3.7 and 3.8, the maximal possible flatness is about $\varepsilon = 0.9$ and at values below 0.4 the objects are expected to be ellipticals. The minimum value of the axial ratio is limited due to our selection criterion (see Sect. 2.2.3) and only a fraction of simple disks reach high $\frac{\texttt{isoA}}{\texttt{isoB}}$ values to be called a superthin galaxy ($\frac{A}{B} > 9$ as suggested by Goad & Roberts (1981)). In the Catalog, 23 out of 501 Sd(f) galaxies are superthins with isophotal axis ratio above nine. Sd(f) galaxies with ratios larger than 26 are not measured in the Catalog.

3.2.5 Isophotal Ellipticity

It is possible to measure the ellipticity with the isophotal axis ratio using the following Equation: $ell = 1 - \frac{\texttt{isoB}}{\texttt{isoA}}$, hereafter called " isophotal ellipticity." In contrast to that, our measured parameter ε is the luminosity-weighted mean of the elliptical fitted isophotes on each object, therefore ε is expected to be only roughly correlated with *ell*. The relation between these two ellipticities of the objects is shown in Fig. 3.9.

For the objects without bulges and no other central light concentration both ellipticities are linearly correlated. The correlation for the other objects is clearly less strong because of the luminosity

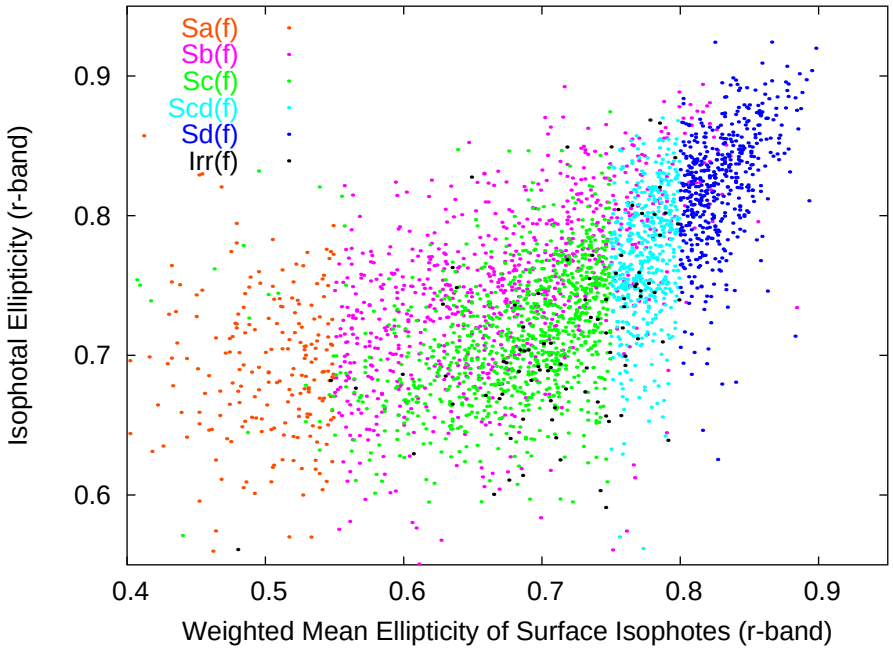

Figure 3.9: Comparison of the ε derived in the Catalog with the isophotal ellipticity *ell* from SDSS. The different color-coded dots represent the various morphological galaxy types from the Catalog and are explained in the key.

weighting of ε. This introduces lower values (rounder shape) for ε. Despite of that disadvantage, *ell* can be used as only a crude discriminator of the galaxy's shape.

In contrast to the original separation diagram of Fig. 2.4, the isophotal ellipticity in the separation diagram Fig. 3.10 can not separate Sa(f) from Sb(f) types because the higher luminosity of the Sa(f) bulges is not included in the unweighted *ell*. In addition, the Scd(f) class is merged with the Sc(f) and Sd(f) and can not separated as an individual class.

3.2.6 Adaptive Ellipticity

The SDSS database provides also adaptive moments of the galaxy's light. These are the second moments of the object intensity, measured using a particular scheme designed to have near-optimal signal-to-noise ratio. The moments are measured using a radial weight function interactively adapted to the shape (ellipticity) and size of the object. This elliptical weight function has a signal/noise advantage over axially symmetric weight functions. In principle there is an optimal (in terms of signal-to-noise) radial shape for the weight function, which is related to the light profile of the object itself. In practice a Gaussian with size matched to that of the object is used, and is nearly optimal. Details can be found in Bernstein & Jarvis (2002) and Vincent & Ryden (2005).

The SDSS provides the sum of the second moments in CCD row and column direction for each object $\tau = \texttt{mRrCc} = M_{xx} + M_{yy}$ and the ellipticity (polarization) components

$$e_+ = \texttt{mE1} = (M_{xx} - M_{yy})/\tau \quad (3.1)$$

$$e_\times = \texttt{mE2} = 2M_{xy}/\tau \quad (3.2)$$

The adaptive second moments can be converted into an axial ratio with the relation

$$\frac{b}{a} = \sqrt{\frac{1-e}{1+e}} \quad (3.3)$$

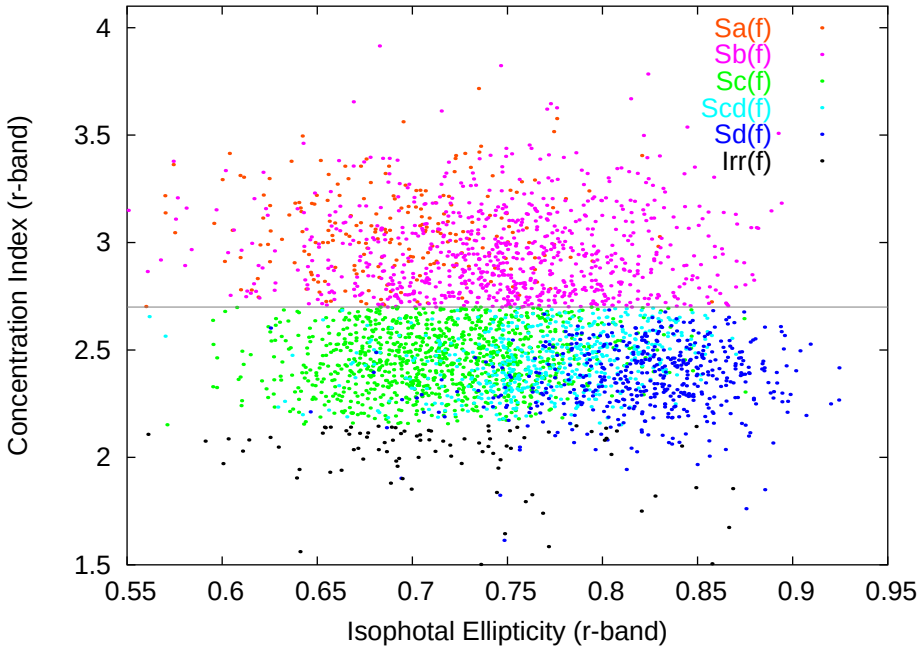

Figure 3.10: Correlation between CI and *ell* shows that it is not an optimal separation diagram. The line at CI=2.7 divides galaxies with bulge from the bulgeless ones. The dots with different colors stand for the various classes from the Catalog and are explained in the legend.

with $e = \sqrt{e_+^2 + e_\times^2}$ and the "adaptive ellipticity" is then $\epsilon = 1 - \frac{b}{a}$.

Fig. 3.11 shows the correlation between ϵ and ε, i.e., the adaptive ellipticity and our measured weighted ellipticity. Although both ellipticities are measured in a different way, the correlation between Sc(f), Scd(f) and Sd(f) is linear with small scatter. The earlier types, however, are more weighted with ϵ and have therefore smaller values in contrast to our ε and the unweighted *ell*.

We can now repeat the separation diagram and replace ε with ϵ, see Fig. 3.12. As expected, the bulgeless galaxies can be recovered. In order to determine which choices of ϵ distinguish best between the classes we use a histogram with the distribution of the ϵ of the galaxies classified in the Catalog (Fig. 3.13). It turns out that the intermediate simple disk types (Scd(f)) and simple disks (Sd(f)) are separated at a value of $\epsilon = 0.82$ and Scd(f) from Sc(f) at $\epsilon = 0.78$. In contrast to our old definition, Sa(f) and Sb(f) galaxies are best divided at $\epsilon = 0.4$. Together with the CI definitions values from Table 2.1 it is possible to recover the classes of the Catalog of edge-on disk galaxies in an easy way using only the adaptive ellipticity. The disadvantage is that scatter is larger than in our original separation diagram of Fig. 2.4. The new limiting values for these types in SDSS r band are summarized in Table 3.1.

3.3 DR5 Extension of the Catalog of Edge-on Disks

The new separation is applied to all edge-on galaxies from the SDSS DR5. The parameters of these objects are extracted using the same query as defined in the Catalog (please consult the erratum by Kautsch et al. 2006b). Because of the much larger sky coverage of the DR5 (8000 deg^2 versus 2099 deg^2 in DR1) it is not practical to inspect the objects in order to find wrong objects like stellar spikes or shredded galaxies. Therefore we include four additional conditions to this query. With these add ons saturated galaxies, galaxies near survey borders, faint galaxies and shredded galaxies should be

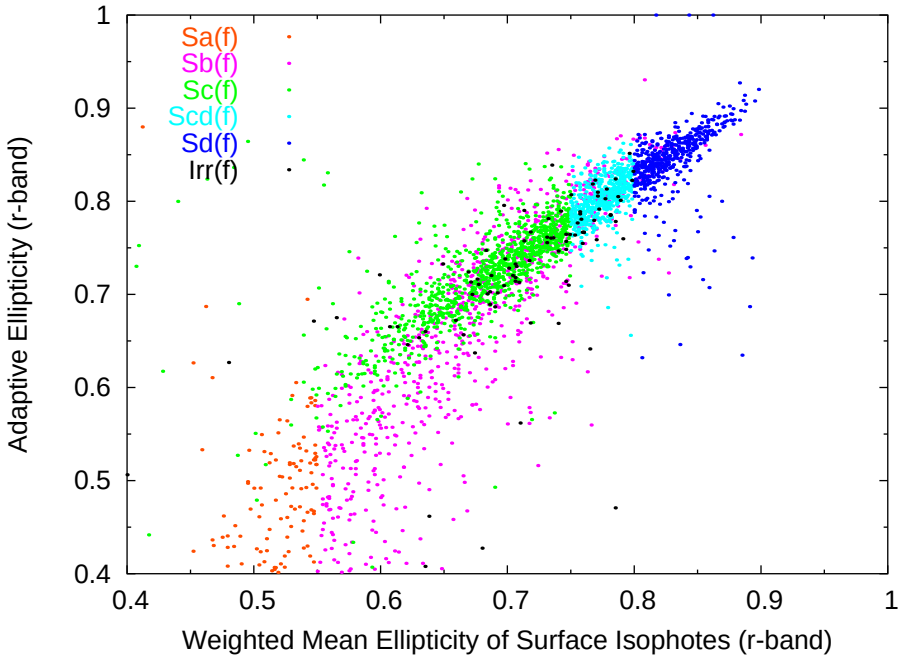

Figure 3.11: Correlation between the two luminosity weighted elliptical quantities, ε and ϵ respectively. The different color-coded dots represent the various morphological galaxy types from the Catalog and are explained in the key.

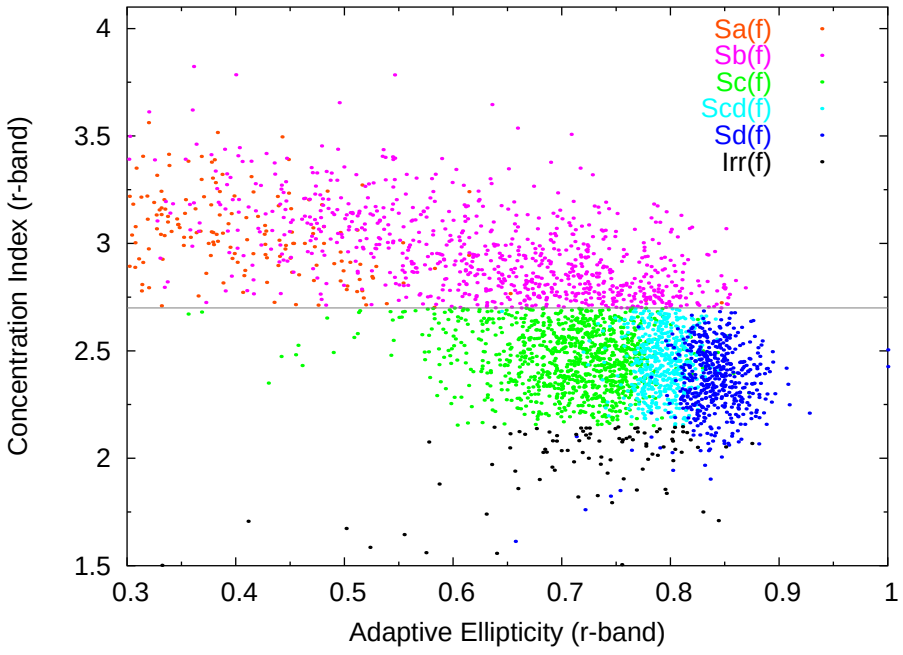

Figure 3.12: The separation diagram with ϵ on the abscissa and the CI on the ordinate. The color dots are cited in the key and represent the classes from the Catalog. The line at CI=2.7 separates galaxies with bulge from the bulgeless.

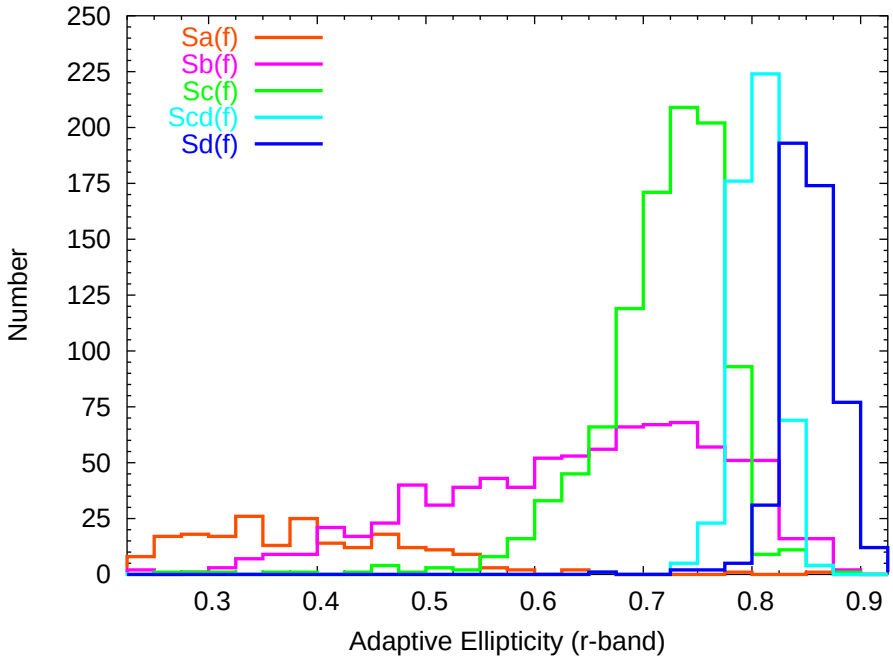

Figure 3.13: Number distribution of the automately selected galaxies from the Catalog (different color lines as cited in the key) versus their adaptive ellipticity ϵ.

Table 3.1: Limiting Values for the adaptive ellipticity ϵ and concentration index CI. These are the values of the limits of the morphological classes. The values are valid for the SDSS r band. In general, note that the galaxies near boundaries have the least certain classification.

Class	ϵ		CI	
	lower limit	upper limit	lower limit	upper limit
Sa(f)	$--$	< 0.4	≥ 2.70	$--$
Sb(f)	≥ 0.4	$--$	≥ 2.70	$--$
Sc(f)	$--$	< 0.78	≥ 2.15	< 2.70
Scd(f)	≥ 0.78	< 0.82	≥ 2.15	< 2.70
Sd(f)	≥ 0.82	$--$	$--$	< 2.70
Irr(f)	$--$	< 0.82	$--$	< 2.15

Table 3.2: Galaxy classes and their fractions. The absolute numbers of galaxies in the main morphological classes and their percentages with respect to the catalog entries as a whole are listed in this table. For comparison the numbers and percentages of the Catalog are given in the fourth and fifth column.

General Class	Number	Percentages	Number	Percentages
Sa(f)	1018	10	222	7
Sb(f)	3046	30	843	26
Sc(f)	3369	34	1005	32
Scd(f)	890	9	503	16
Sd(f)	950	10	501	16
Irr(f)	758	7	95	3
Total	10031	100.00	3169	100.00

avoided.

The query is performed on CASJobs[1]. These batch query services allow interactive access to the SDSS databases. We are using the following query written in the Structured Query Language (SQL) on the DR5 context:

```
SELECT *
into mydb.edge_on_dr5_simple from Galaxy as G
WHERE G.petroMag_g < 20
and (G.isoA_g/G.isoB_g) > 3
and G.isoA_g > 37.8 # 37.8 pixels are 15'' of isophotal radius
and (G.g - G.r) between -0.3 and 3
and (G.r - G.i) between -0.3 and 3
and (G.flags & (dbo.fPhotoFlags('SATURATED'))) = 0
and (G.flags & (dbo.fPhotoFlags('EDGE'))) = 0
and (G.flags & (dbo.fPhotoFlags('ELLIPFAINT'))) = 0
and (G.flags & (dbo.fPhotoFlags('BLENDED'))) = 0
```

With this query we found 10070 objects. 39 of all objects have no adaptive parameters, hence our study sample contains 10031 systems. With eyeball inspection of randomly selected subsamples we derived a rate of $10.25\% \pm 2.5\%$ of falsely selected objects. The largest fraction of these contaminating systems are shredded and not edge-on galaxies with spiral arms, bars or similar elongated regions classified as an individual object. A smaller group of false objects contains stellar refraction spikes, empty regions, very faint galaxies/stars and elongated chains of galaxies/stars.

The morphological classes consist of similar relative numbers as we found in the Catalog. Table 3.2 contains the absolute numbers and percentages of the different classes in comparison to the entries in the DR5 sample as a whole.

3.4 Properties of the DR5 edge-on disk galaxies: Results

Figure 3.14 shows the correlation between galaxy class defined by the ε (indicated as color coded dots) and surface brightness. The surface brightness correlates with bulge size (left diagram) and flatness (right diagram). The flattest systems are about four magnitudes fainter indicating a much lower stellar number density in these systems. The puffy irregulars are located at the lowest surface brightness end. Therefore, the simple disk galaxies can be mostly described as low-surface brightness galaxies like the irregulars. The large scatter is caused by the falsely included objects.

[1] http://casjobs.sdss.org/CasJobs/

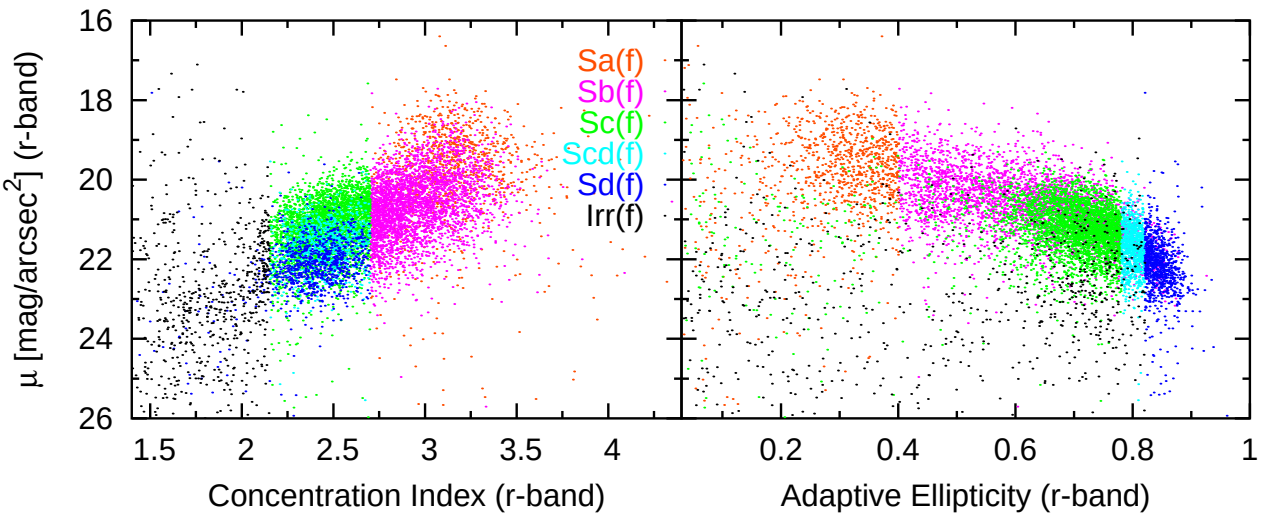

Figure 3.14: Distribution of the DR5 sample galaxies and its surface brightness. The left diagram shows the correlation with the CI and the right diagram that with the ϵ. The DR5 edge-on sample galaxies are divided into several morphological classes with the limits given in Table 3.1 and color coded as explained in the key. The simple disk galaxies have the lowest surface brightnesses.

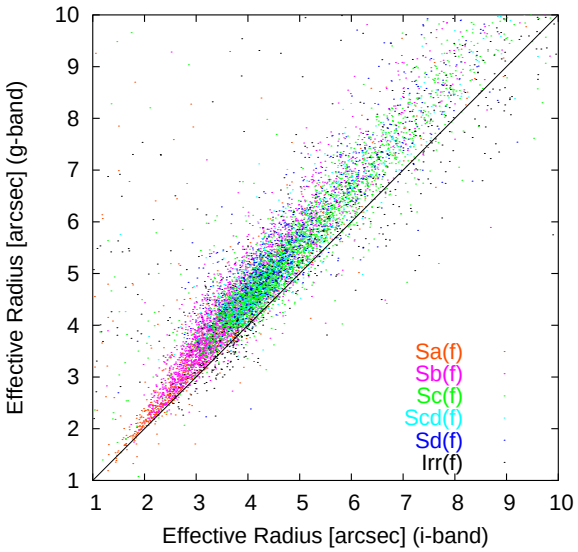

Figure 3.15: Correlation of the effective Petrosian radius [″] in the i and g band of the DR5 edge-on galaxies.

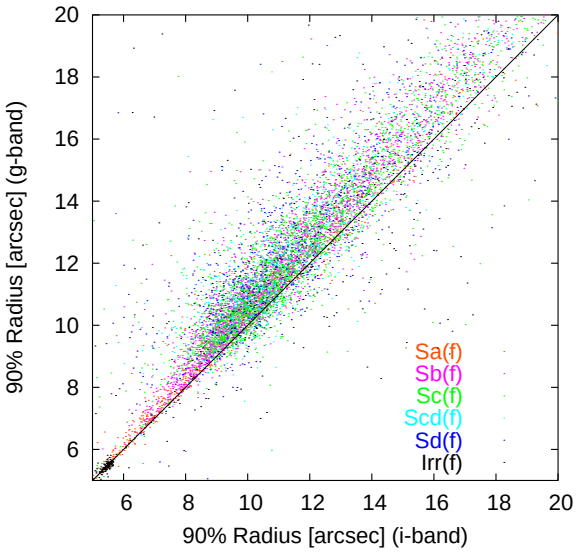

Figure 3.16: Correlation of the radius containing 90% of Petrosian flux [″] in the i and g band of the DR5 edge-on galaxies.

Figure 3.15 shows the correlation between the radius containing 50% of Petrosian flux in the g and i band. Both radii are similar in the Sa(f) class. The radii are larger in the blue band at later types compared to a fixed red radius. The Sb(f) types span the largest value range between similar and dominant bluer effective radii and the later types are embedded in this space. This is probably an effect of the dust which shortens the radius in the dust rich galaxies in the dust sensitive blue band. The effect is smaller for the later types. A similar trend is also shown between the radius that contains 90% of Petrosian flux in the g and i band, see Fig. 3.16. In this figure, Irr(f), Sa(f) and several Sb(f) have similar 90% radii in both colors. In contrast to the previous figure, the fraction of the types later than Sb(f) with a larger extension in the blue light is large.

Figure 3.17 shows the distribution of the isophotal axial ratios in correlation with the adaptive ellipticities. The large scatter in this figure is due to the wrong classified objects, see above for an approximation of this contamination. The lowest axial ratios are given due to our SQL query. As expected, the early-type spirals (Sa(f) and early Sb(f)) have low axial ratios because of the presence of a bulge in these galaxies. Otherwise, Irr(f) also have small axial ratios, although they do not show a bulge (as indicated with the high values of ϵ). This means that their morphology is dominated by a puffed simple disk.

High values can only be reached by organized simple disk galaxies. The Sd(f) class contains 57 superthin galaxies with axial ratios ≥ 9. But the maximum values measured on simple disks in the DR5 are not larger than 14. As an example, Fig. 3.18 shows the image of UGC 9242. This is a superthin galaxy with an isophotal axial ratio of 11, selected from our Sd(f) sample. It represents one of the thinnest galaxies in our sample. The superthin galaxies are probably underrepresented in the SDSS sample because of shredding effects in the SDSS algorithms.

3.5 Discussion and Summary

We have analyzed different morphological discriminators from the SDSS and their correlation with edge-on disk galaxy types from the Catalog. We found that $u - r$ colors and profile likelihoods are generally correlated with our galaxy classes but have large scatter probably due to the strong and complicated influence of dust reddening and attenuation on edge-on disks.

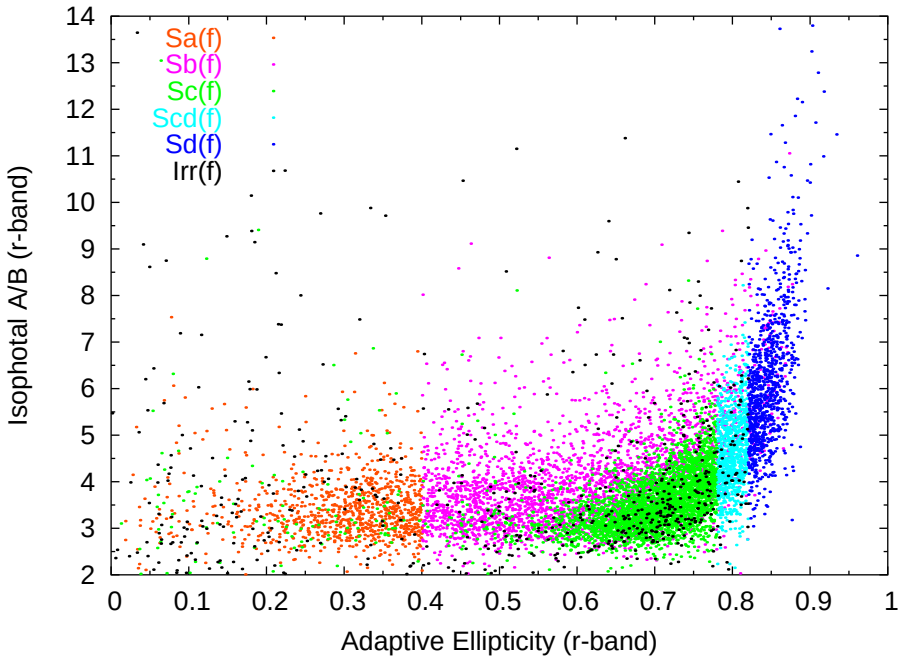

Figure 3.17: Distribution of the axial ratios of the DR5 sample. The DR5 edge-on sample galaxies are divided into several morphological classes with the limits given in Table 3.1 and color coded as explained in the key. The simple disk galaxies have the flattest shape.

We derived the isophotal ellipticity from the isophotal minor and major axis as given in the SDSS. These parameters correlate only with large scatter with the morphological classes from the Catalog. This is because of the different disk+bulge components which are not considered if using simple and unweighted isophotal ellipticities. From the adaptive moments in the SDSS we computed the adaptive ellipticities. These quantities show a good correlation with our measured isophotal ellipticity because both parameters include the weighting of the galaxy's light.

We repeated the process to select edge-on objects and created an extension of the Catalog with all edge-on disk galaxies from the SDSS DR5. The adaptive ellipticity is used to separate the galaxies found in the SDSS DR5 into the galaxy classes from the Catalog; these are Sa(f), Sb(f), Sc(f), Scd(f), Sd(f) and Irr(f). These types have similar relative fractions as they do have in the Catalog with SDSS DR1 data. Only the numbers of bulgeless galaxies are a few percent smaller which is due to a larger contamination of wrong objects at earlier types. A fraction (10.25%) of false objects has to be accepted if the full sample can not be inspected by eye. Around $\gtrsim$ 25% of the galaxies appear to be bulgeless. This large number shows that simple disk systems are very frequent but enigmatic types of disk galaxies.

The galaxy classes in our DR5 extension of the Catalog depend on surface brightness. That means that the density of the disk stars decreases with the later simple disk galaxies and has values of low surface brightness galaxies for the thinnest disks and irregulars. Bulgeless galaxies tend to show larger effective and 90% radii in the blue. This effect indicates a radial color gradient in these galaxies. An effect of dust is not expected in these types because it would make the galaxies smaller in the dust sensitive blue band and the contrary is observed for the bulgeless galaxies. Different reasons are possible for such color gradients such as a dust, metallicity or age gradient. Simple disk galaxies tend to show this type of color changes which are probably explained by an stellar population gradient (e.g. Matthews et al. 1999b). The observed radial gradients are indicative of star formation progressing with time from inside out.

Figure 3.18: The superthin galaxy UGC 9242. The image is a $6'.5 \times 6'.5$ cutout of the DR5 Image List Tool. North is to the top, east to the left.

The isophotal axial ratios of the DR5 sample and the Catalog depend on the morphological galaxy classes. For the Sa(f) and Sb(f) the axial ratio is a discriminator of the bulge to disk ratio. Sa(f) and early Sb(f) have therefore similar bulge to disk ratios but the luminosity weighted ellipticity, i.e., the flatness of the galaxy shape, is larger in the Sb(f) class.

Then, the axial ratios are growing from the nearly bulge-free intermediate class Sc(f) to the bulgeless Scd(f) and Sd(f) types. The increase of the axial ratio with the weighted ellipticity is nearly linear and shows that axial ratio and disk flatness are the same discriminators for a bulgeless galaxy's shape. The relation between axial ratios and morphological type is consistent with Guthrie (1992) and Karachentsev et al. (1997). In addition, this indicates that the disk thickness decreases from early to late bulgeless galaxies. This can be explained with the larger disk scale heights of early type disks and the more probable detection of thicker thick disks in the earlier types (van der Kruit & Searle 1981a,b; Yoachim & Dalcanton 2006).

The flattest organized simple-disk galaxies have the largest axial ratios. A small fraction of the simple disks have extreme axial ratios and represent the group of superthin galaxies. The axial ratios of the superthin galaxies correspond on average to the axial ratio of the thin disk of the Milky Way, which is $10 < \frac{a}{b} < 12$ (Buser 2000). We found a limit of axial ratios at a value of $\frac{isoA}{isoB} \approx 14$ with no galaxy above this border. In principle this is in agreement with the study by Guthrie (1992) who found maximal values for edge-on galaxies of $\frac{A}{B} \leq 16$ (this maximum value is found for UGC 9242 in her sample). The value differences are due to Guthrie's data which were micrometer measured on the blue POSS plate copies.

We conclude that disk galaxies reach a natural limit of their disk thickness. The thinnest galaxies avoid values of isophotal axial ratio above ≈ 15 and weighted ellipticity values above 0.9. Thinner and less dense galaxies may not exist because these disks would be unstable and suddenly after their formation be shredded or destroyed after weak gravitational interaction with other galaxies, this is probably observed in the Irr(f), see next Paragraph. It would be interesting to compare the circular velocities (and shape of the rotation curve) with the axial ratios (and also the disk flatness) of the simple disk galaxies in our Catalog with, e.g., the compilation by Dalcanton et al. (2004). The dynamic stability of a disk could then be established as we expect that the superthin objects have very cold disks. Unfortunately, previous studies found an absence of a correlation between the axial ratio and rotation velocity of the HI line half width (Matthews & van Driel 2000; Zasov et al. 2002). But a correlation between the disk thickness and the mass of the dark halo around these galaxies is found (Zasov et al. 2002). Recent considerations show that only a massive dark halo or bulge can stabilize the thinnest stellar disks (Sotnikova & Rodionov 2006) against disintegration.

However, the latest morphological types, the bulgeless irregular galaxies Irr(f) have thicker disks compared to the Scd(f) and Sd(f). The axial ratios of Irr(f) are comparable to that of the Sc(f) and earlier type. This suggests a major-axis symmetric puffed disk. This is probably because the irregular disks show this sign of disintegration if rotation is to small for these rotation supported systems. A detailed comparison of the dynamics of different simple disks (Scd(f), Sd(f), Irr(f)) would shed light onto the possible disk stability/thickness relation and would be a link between pure morphological properties (the shape) and pure physical stages (the dynamics) of a galaxy. This would give a new context of the morphology-physics relation could lead to a new holistic classification of galaxies.

3.6 Detection Rate and Stability

In the sections before we found roughly 1/3 of edge-on galaxies in the SDSS DR1 to be bulgeless. This is a large number, especially if we remember the fact that the formation and evolution of simple disks is not understood so far. The problem is that—in general—a hierarchical Universe is built up by merging of small mass units into larger ones. Merging of equal mass units results in an increase of chaotic motions of its particles, i.e., star and gas, and a spheroidal morphology of the resulting system. But we do see, however, 1/3 of the disk systems without signatures of a spheroidal bulge component, a result of such merging processes (Steinmetz 2003; Athanassoula 2005b). The simple disk galaxies have generally small stellar masses compared to the galaxies with bulge, therefore it is much more difficult

for the bulgeless to survive a merging event. And these events were quite common in an ancient epoch of violent merging in the Universe (Steinmetz & Navarro 2002; Steinmetz 2003; Abadi et al. 2003a)

Hence, it is difficult to explain the high frequency of simple disk galaxies in a Universe where structures were grown by hierarchical clustering as generally accepted today. We can speculate about the detection rates of the bulgeless objects. They are possibly common because:

- Several regions in the Universe did not undergo hierarchical evolution, because clustering could be a stochastic process. In these quiet zones, simple disks formed by gravitational collapse and evolved. However, hierarchical merging should act at every place, where gravitation dominates the cosmic expansion.
- The bulges grow due to secular evolution (see Section 4.6.2).
- Simple disk galaxies formed in recent times in isolation, especially in cosmic voids out of dark and isolated gas clouds. In this case the stars of these galaxies should be of young age, which is not observed (Matthews et al. 1999b).

In addition, simple disks are robust due to properties related to the mass in a spheroidal component in the hierarchical context. Disk galaxies could be stabilized by a dark halo which is thought to be an important component in these objects. Karachentsev (1991) and Zasov et al. (2002) showed that the mass of a dark halo increases as the disk thickness (and surface brightness) decreases. Sotnikova & Rodionov (2006) analyzed this relationship between the mass of a spherical component and the thickness of stellar disks and found that the presence of, e.g., a dark halo or bulge, must have a stabilizing effect in that sense that the dark halo mass must be more than one stellar disk mass. And consequently, the thinnest, simple disks are expected to exhibit large halo masses to be stable against radial disintegration and vertical heating. It was also shown by early numerical N-body simulations (Ostriker & Peebles 1973) that a dynamically hot halo could stabilize flattened galaxies. Gallagher & Hudson (1976) already started a search for a low-luminosity hot halo that could stabilize the cold disks. No such halo was found, only recent observations with very deep exposures (Zibetti & Ferguson 2004) and stacked images (Zibetti et al. 2004; Caldwell & Bergvall 2006) found low luminous baryonic coronae around edge-on disk galaxies.

3.7 Mass, Extinction and Colors

Edge-on galaxies are sensitive to the reddening and dust attenuation. This influence is shown in several results in earlier sections and qualitatively discussed in Sect. 2.7. In the Figs. 3.19 and 3.20 we plot ε versus the absolute magnitude in the SDSS u and z band. The u band, centered on 3551 Å (Stoughton et al. 2002), is expected to be the most sensitive passband on dust because it is the bluest band in the SDSS. In Fig. 3.19 all galaxies have similar magnitudes on average, only simple disks are slightly fainter. The curve in this figure follows the general trend of the different disk classes. It is slightly raising from types Sa(f), Sb(f) and has its saddle point finally at the transition between Sa(f) and Sb(f). Then it slightly decreases to the Scd(f) and Sd(f).

In contrast to that, the magnitudes are continuously decreasing from the early to the latest types as illustrated by the nearly straight curve when using the reddest filter from SDSS. This is the z band with an effective wavelength centered on 8932 Å (Stoughton et al. 2002). At these red wavelengths the magnitudes are much less affected by dust compared to bluer passbands. The decrease of the z magnitudes can be interpreted as a decline of the stellar mass with later galaxy type and bulge size if we use z as an approximate mass indicator.

Therefore, the differences between u and z reflect the different reddening due to different amounts of dust in the morphological classes. Figure 3.19 shows that the fractional amount of dust follows the curve and is–on average–low for simple disks as discussed in Sect. 2.7 and highest in the Sb(f) class. Also the different sensitivity to different stellar populations of the two bands could also explain this trend. Young stellar populations dominates the blue light and are less visible in the earliest types. Therefore the curve decreases at the left side in Fig. 3.19.

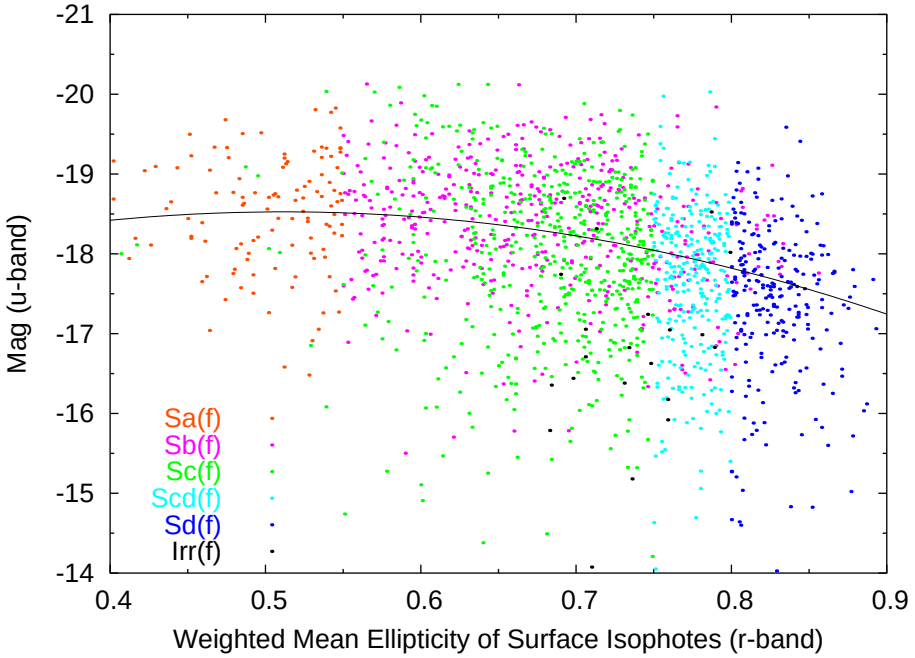

Figure 3.19: Distribution of the morphological types of the Catalog (color dots as cited in the key) versus the absolute blue u magnitude which is strongly dust dependent. The curve follows the general distribution of the classes and has its maximum value at the Sa(f) - Sb(f) classes.

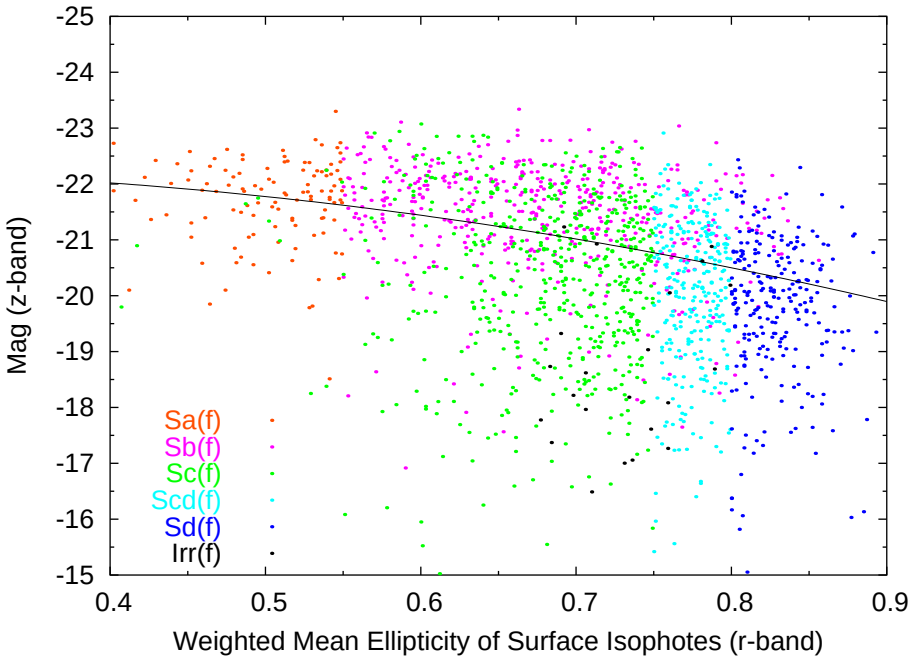

Figure 3.20: Distribution of the morphological types of the Catalog (color dots as cited in the key) versus the absolute red z magnitude. The z filter is the less dust diluted filter in the SDSS system. The curve traces on average the decrease of the total stellar mass from early to the latest classes.

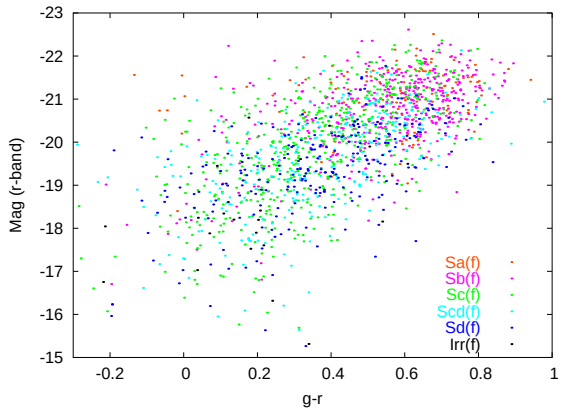

Figure 3.21: Color-magnitude diagram of $g-r$ vs. r.

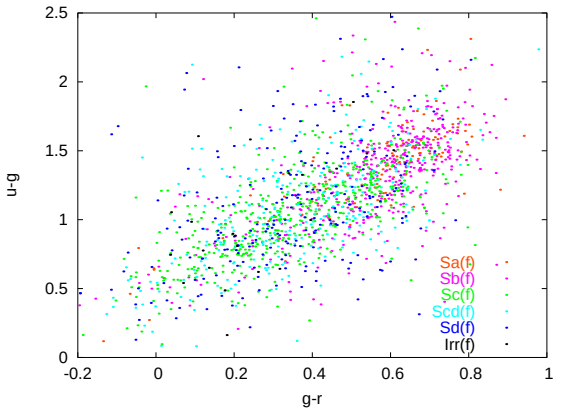

Figure 3.22: Color-color diagram of $g-r$ vs. $u-g$

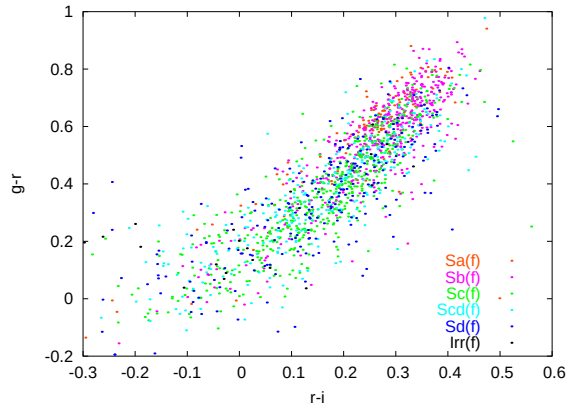

Figure 3.23: Color-color diagram of $r-i$ vs. $g-r$

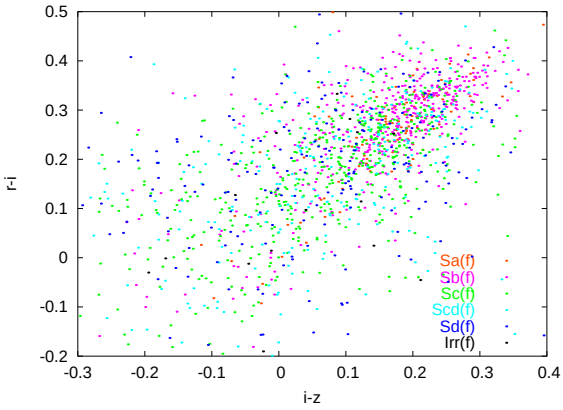

Figure 3.24: Color-color diagram of $i-z$ vs. $r-i$

Figure 3.21 shows the $g-r$ vs. r color-magnitude diagram of the Catalog galaxies. The early disks have the highest luminosities at all colors. A correlation is shown between luminosity and color of the types. The scatter is large and only the early types (Sa(f), Sb(f)) can be slightly distinguished from the later types. At luminosities brighter than Mag(r)=-17.5 the slope is rising from bluer to redder colors. With fainter magnitudes the galaxies show a trend in the other direction. Because no dust correction is applied to the galaxies, an interpretation of the dominating stellar populations is difficult.

Figures 3.22, 3.23, 3.24 show the color-color diagrams of the Catalog galaxies. In Figs. 3.22 and 3.24 the scatter is large. The best correlation is shown in Fig. 3.23. This is probably an effect of the different sensitivity of the SDSS filters. g, r, i are the most robust and sensitive filters whereas the u, z filters are of lower sensitivity and therefore contain the largest uncertainties. In general the figures show that the early types are generally redder than the later disks but without sharp borders of the classes.

Due to the complicated interplay between dust and stellar populations an interpretation is difficult. The statistical trend reveals that on average the light from the earlier types is dominated from red stars and that of the later types from bluer stars. It is not difficult to imagine that the red light dominates in galaxies with bulge and the largest amount of dust. This means that these galaxies are red due to red stars in the bulge and a reddening due to the dust and red stars in the disk. However, also some galaxies with bulge show blue colors which can be either due to the absence of dust or real bluer stars (e.g., dominating star bursts).

Chapter 4

The Environment of Edge-on Disk Galaxies

4.1 Introduction

The widely accepted paradigm of galaxy evolution is based on the models of hierarchical clustering through mergers of cold dark matter halos (e.g., Kauffmann & White 1993; Lacey & Cole 1993; Pearce et al. 2001; Steinmetz & Navarro 2002; Steinmetz 2003)). This model represents a continuous interplay of violent periods of major mergers and relaxed phases of smooth accretion of material and minor mergers during which star formation progresses at a modest rate set by internal factors. In these scenarios, the environment of galaxies naturally plays an important role in the evolution of the properties of galaxies, e.g. through interactions with companions.

One of the best known and observed relationships between environment and galaxy evolution is the morphology-density relation (MDR). This relation, discovered decades ago, describes the decreasing fraction of late-type galaxies and increasing numbers of early-type galaxies with increasing local galaxy density (e.g., Oemler 1974; Melnick & Sargent 1977; Dressler 1980; Postman & Geller 1984). Large databases like the Sloan Digital Sky Survey (SDSS, York et al. 2000; Stoughton et al. 2002) provide excellent datasets that allow studies of the MDR to be advanced in statistically significant ways. Recent studies of the MDR in galaxy clusters confirm that the fraction of luminous galaxies with late-type morphologies decreases with increasing local galaxy density and vice versa for early types and that central cluster regions of galaxy clusters are almost free of late-type disk galaxies (e.g., Goto et al. 2003; Kuehn & Ryden 2005; Thomas & Katgert 2005).

Early-type disk galaxies and lenticulars are most frequent in clusters of galaxies. In contrast, isolated regions are generally occupied by a larger fractional population of late-type disks (Karachentsev et al. 2004; Varela et al. 2004; Sulentic et al. 2005). Flat, seemingly bulgeless edge-on disks often seem to be relatively isolated (Karachentsev & Karachentseva 1974; Karachentsev et al. 1993, 1999; Karachentsev 1999). Such low density regions, however, are not completely free of early-type galaxies, i.e., also E and S0/Sa galaxies are found among very isolated regions but their fractions are small (Stocke et al. 2004; Sulentic et al. 2005). The MDR is a statistical effect.

Trends in the MDR are least clear when galaxy densities are low. Different authors find a variety of possible MDR relationships; e.g. the existence (Tran et al. 2001) or non-existence (Whitmore 1995) of the MDR for massive galaxies in group environments. Studies comparing galaxy populations in voids, the least dense regions of the present day universe, to those in typical galaxy group environments, however, find significant statistical differences. The void galaxy populations tend to have relatively higher recent stellar birthrates, later structural types, and lower luminosities (Grogin & Geller 1999, 2000; Nakamura et al. 2003; Rojas et al. 2004, 2005). These results can be understood if galaxies with high stellar masses, which tend to be early type systems, are rare in the low density voids (Hoyle et al. 2005).

In this paper we investigate the preferred environments of disk-dominated galaxies that resemble the galaxy populations found in voids. Galaxies whose stars are concentrated in a disk are likely to be transformed to earlier morphological types in dense environments by a variety of processes, e.g., ram pressure stripping (Gunn & Gott 1972; Roediger & Hensler 2004) gas evaporation (Fujita 2004) and tidal interactions/harassment (Pfleiderer & Siedentopf 1961; Moore et al. 1998, 1999; Mastropietro et al. 2005). Also violent mergers, which can occur across a range of galaxy environments, are expected to cause dramatic changes in the morphology of galaxy disks, and stellar disks may be completely disrupted (Toomre 1977; Gardner 2001; Steinmetz 2003; Taylor & Babul 2003; Benson et al. 2004). These and related theoretical studies show that a disk galaxy subject to significant external perturbations is unlikely to remain a simple disk system with ongoing star formation. At minimum the disk will become thicker and dynamically warmer; it also is possible for a central stellar bulge to grow and star formation rates to decline if gas is lost or exhausted by rapid star formation (as in merger-induced starbursts). Hence, star forming galaxies consisting only of a simple stellar disk should be very sensitive to environmental effects, including those associated with the density of neighboring galaxies.

The main question that we intend to explore is whether or not the structures of disk galaxies retain signatures of processes that set their morphologies. For example, is bulge prominence or disk flatness, dependent on environment (nurture)? If no environmental connections can be found, then internal processes, probably set in motion during or soon after formation (nature) becomes the most likely evolutionary agent. Most of the environmental studies outside of galaxy clusters are based on measurements of the projected distances to neighboring galaxies. When disk galaxies are the subjects, then the target spirals are classified using a variety of approaches (e.g., Karachentseva 1973; Karachentsev & Karachentseva 1974; Karachentsev et al. 1993, 1999; Karachentsev 1999; Stocke et al. 2004; Varela et al. 2004; Allam et al. 2005).

Here we present an investigation based on a well-defined and uniformly selected sample of edge-on disk galaxies (Kautsch et al. 2006a). The target selection and definition of the search volume is presented in Sect. 4.2.1 and Sect. 4.2.2, respectively. The results are shown in Sect. 4.3 and are then and discussed in Sect. 4.4. Sect. 4.5 summarizes the results of this study.

4.2 Data Analysis

4.2.1 Target Selection

The galaxies in this study are chosen from the edge-on disk galaxy catalog by Kautsch et al. (2006a,b). This catalog contains 3169 disk-dominated "flat" galaxies taken from the SDSS Data Release One (DR1) (Abazajian et al. 2003). In our catalog the galaxies are selected on the basis of their projected axial ratios and then are subdivided into several morphological classes. This ensures the inclusion only of galaxies with prominent stellar disks. The main structural classes are defined as galaxies with a bulge, denoted as Sa(f) and Sb(f), simple disk galaxies with no obvious bulge component Sd(f), and intermediate types Sc(f), Scd(f), Irr(f), between these two extremes. We find about 1/3 of the edge on disk galaxies in the nearby Universe to be seemingly bulgeless. The morphological separation is based on the central light concentration (CI) as a measurement of the bulge size and the luminosity weighted mean of the elliptical isophotes (ε) as a discriminator for the flatness of each object (for the detailed description of these parameter see Kautsch et al. (2006a)).

For the present environmental study we include only the early-type disk galaxies with obvious bulges, our Sa(f) and Sb(f) types (CI $\geq$ 2.7), and the late-type simple disk Sd(f) galaxies (CI $<$ 2.7 & $\varepsilon \geq$ 0.8). These represent the structural extremes of edge-on disk galaxies, so that we distinguish between two opposite structural classes. The difference of the two disk types with bulges is defined in the value of the galaxy flatness: Galaxies with $\varepsilon < 0.55$ have large bulges that produces rounder overall shapes and are defined as Sa(f). Galaxies with bulges and with flatter shape, $\varepsilon \geq 0.55$, are classified as Sb(f).

Out of these objects we selected those with high quality SDSS redshifts ("zStatus") and no redshift

warnings ("zWarning") as given in the flags from the SDSS database of spectra (SpecObj). We limited ourselves to galaxies within a redshift range of $0.03 < z < 0.05$. This covers the peaks of the redshift distribution of the catalog galaxies and avoids nearby galaxies with large peculiar velocities. Additionally, nearby galaxies have large angular sizes, often leading to the problem that they are detected as more than one unique object in the SDSS archive. This multiple detection of single objects in the SDSS is called "shredding" (Abazajian et al. 2003, 2005; Kniazev et al. 2004a). Objects with redshifts higher than 0.05 are not used in order to suppress selection effects arising from decreasing spatial resolution and declining sensitivity with increasing distance (see discussion in Sect. 7 by Kautsch et al. (2006a)).

We use the SDSS Query Analyzer (sdssQA)[1] on the Data Release 4 archive (Adelman-McCarthy et al. 2005) to detect the neighbors within two search cylinders defined in space and redshift centered on each of our edge-on target galaxies. In this paper we use the term "neighbors" to denote galaxies that have the potential to be in spatial proximity to our selected edge-on target galaxies. All targets which are located near SDSS DR4 footprint area borders are not included in this study, a situation that occurs mostly for objects near the southern limit of the SDSS equatorial stripe. This criterion allows us to avoid having incomplete search cylinders in some cases.

4.2.2 Search Volumes and Malmquist Bias

In order to investigate the environment of our target galaxies we count the galaxies in a search cylinder centered on every target object. The "large cylinder" search volume has a projected radius of 1 Mpc and a line-of-sight depth set by the radial velocity difference of up to $\pm$300 km s^{-1} with respect to the target galaxy. We use a Hubble constant of H_0=71 km s^{-1} Mpc^{-1} to compute all distances. This choice of parameters allows us to locate companion galaxies that could reasonably have interacted with our target systems during a cosmic time span as it corresponds to the approximate size of a typical galaxy group (e.g. Ramella et al. 2002; Karachentsev 2005).

Figure 4.1 shows the distribution of the absolute magnitudes of the three target samples (left) and their selected neighbors (right) in the search cylinder. Because we are using a magnitude-limited sample of galaxies we consider effects of the Malmquist bias. Due to this bias the observer sees an increase on averaged luminosities with larger redshift (e.g., Teerikorpi 1997). This bias can introduce two effects: preferential detection of more luminous objects ("top Malmquist") and the tendency to miss faint galaxies ("bottom Malmquist") with increasing redshift. Fortunately, the top Malmquist bias is small for our sample (see Fig. 4.1) and therefore can be safely ignored. In order to handle the bottom Malmquist, we divided our sample into two subgroups. For the subsample that contains the targets in the small redshift range from 0.03 to 0.035, we do not apply any luminosity restriction. For the other subsample containing targets from $0.03 < z < 0.05$ we consider only galaxies brighter than $M_r = -18.85$ as normal lower cutoff luminosity limit. This cutoff value corresponds to the SDSS limit for spectroscopic targeting of $r = 17.77$ at $z = 0.05$, the maximum redshift for the subgroup.

The second search volume is designed to detect nearby companions down to the spectroscopic magnitude limit of the SDSS (Petrosian magnitude in the r band < 17.77). This allows us to detect most possible companions almost as faint as Large-Magellanic-Cloud-like satellites. However, the reader should be aware that a detection bias occurs due to the placement of the SDSS spectroscopy fibers; see Sect. 4.2.3. We call this the "small cylinder" with a projected radius of 300 kpc, and a velocity space around the target of $\pm$300 km s^{-1}. We surveyed galaxy populations within small cylinders only for edge-on target galaxies within the redshift range $0.03 < z \leq 0.035$ and therefore do not apply a sharp lower luminosity cutoff to our sample.

[1] http://cas.sdss.org/astro/en/help/download/sdssQA/

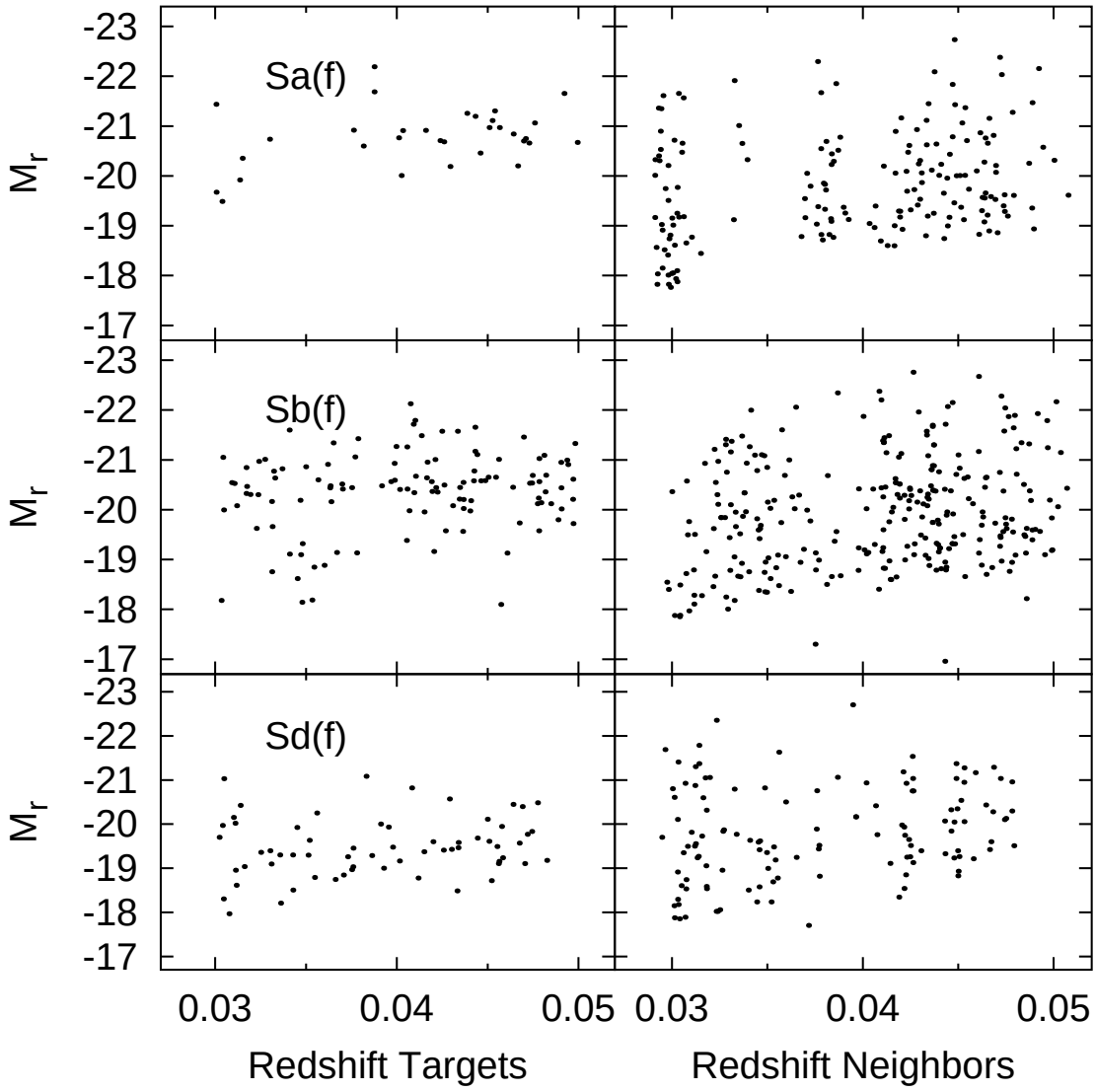

Figure 4.1: Redshift distribution of the target galaxies Sa(f) (top left), Sb(f) (middle left) and Sd(f) (bottom left). The neighbors of Sa(f) are plotted top right, Sb(f) neighbors (middle right) and Sd(f) neighbors (bottom right). The ordinate indicates the absolute r magnitude (M_r).

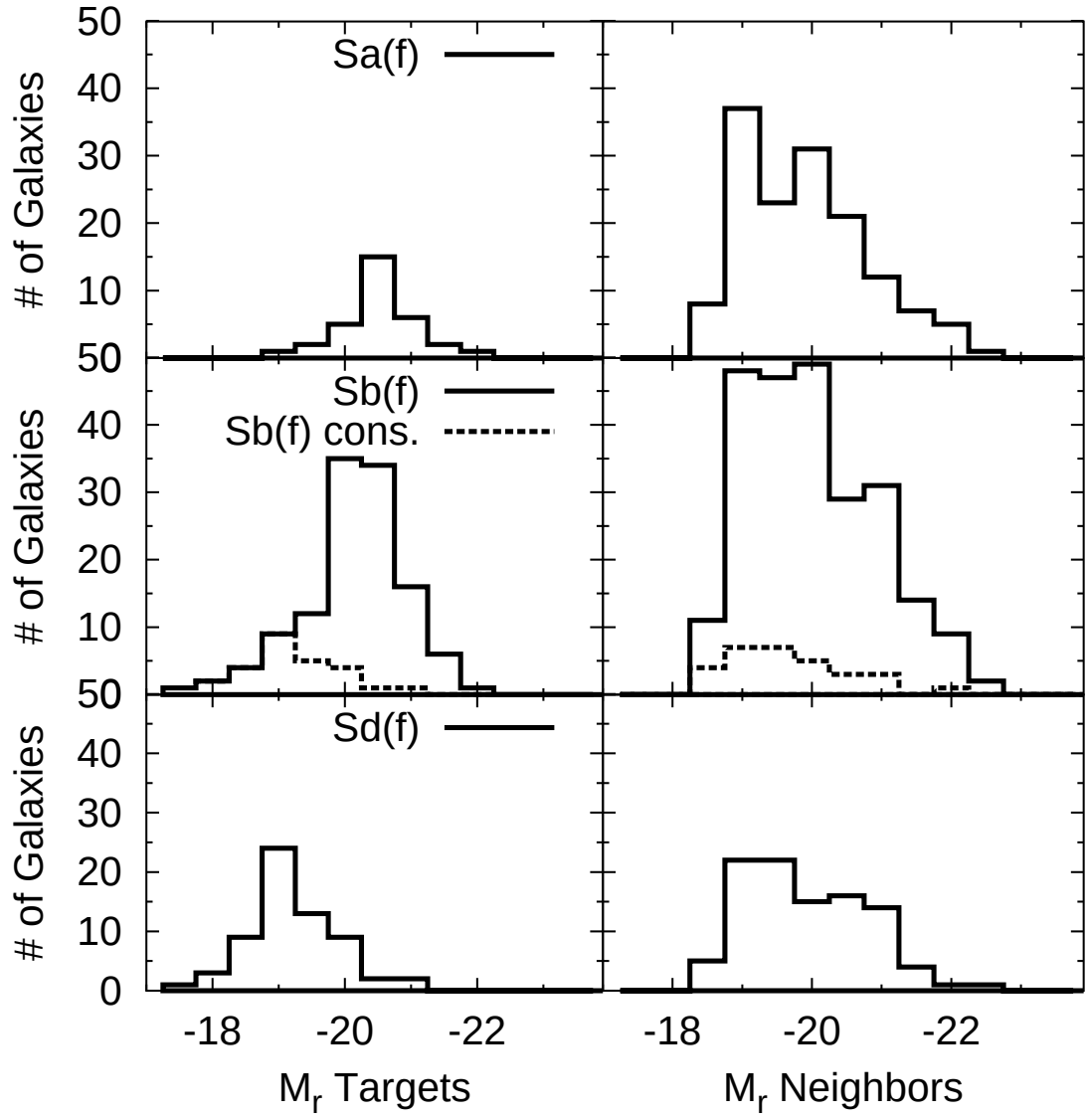

Figure 4.2: Distribution of M_r of the Sa(f) (top left), Sb(f) (middle left) and Sd(f) (bottom left) target galaxies. The corresponding neighbors are plotted on the right side. The bin size is half a magnitude. The dashed line of Sb(f) targets indicate the artificial target sample. The appropriate dashed line on the right represent the neighbor distribution of the artificial target sample.

Table 4.1: Target galaxies and their neighbors. The complete version of this Table is available from the CDS. Here we are presenting the first 5 entries (out of 206) as an example.

Name	RA (J2000)	Dec (J2000)	Class	z	r	$\#^{\mathrm{L}}$	$\#^{\mathrm{S}}$	$\mathrm{Dist}^{\mathrm{L}}$	$\mathrm{Dist}^{\mathrm{S}}$
SDSS J000628.86-004702.9	00 06 28.863	-00 47 02.914	Sa(f)	0.0443067	15.2487936	1	9999	1000	9999
SDSS J001343.81-002735.7	00 13 43.811	-00 27 35.748	Sa(f)	0.0314869	15.3474751	0	1	1000	300
SDSS J002011.52+000024.6	00 20 11.528	+00 00 24.644	Sb(f)	0.0440691	16.2550220	1	9999	1000	9999
SDSS J002710.54-101920.4	00 27 10.545	-10 19 20.407	Sb(f)	0.0480933	15.5667963	4	9999	561.74	9999
SDSS J002924.12+001856.7	00 29 24.123	+00 18 56.796	Sb(f)	0.0454310	15.8309298	2	9999	1000	9999

4.2.3 Selection Biases

Any survey of galaxy populations will have to deal with a variety of biases:

• *Interlopers:* Within the search volume, galaxies may be found that are not potential interaction partners. These projected neighbors may not be physically connected; e.g. in a region with a simple Hubble flow $\delta v = 300$ km s^{-1} corresponds to a spatial separation of about 4.5 Mpc. Unfortunately, due to peculiar motions in galaxy groups, we cannot safely use a smaller velocity interval. The redshift accuracy of ≈ 30 km s^{-1} of the SDSS means that the effects of redshift errors should be minor. This bias leads to a possible overestimate of the number of neighbors (see Prada et al. 2003).

• *Blended objects:* Galaxies that are covered or blended by foreground stars or projected galaxies are not detected.

Therefore, all comparison samples are likely somewhat incomplete and infrequently affected by interlopers and blending objects. But overall the level of incompleteness should affect all the potential neighbors of the three disk-galaxy samples alike. The relative ratio of the sample properties is therefore little affected by the interlopers and blended objects.

• Underestimation of neighbor numbers also can occur because the spectroscopic fibers cannot be positioned closer than 55 ″. Hence very *close neighbors* will be missed. At $z = 0.035$, the maximum redshift for the small volume, this fiber positioning limit corresponds to a projected distance of ≈ 40 kpc.

• *Relative galaxy masses:* This bias plays the most important role for this study because it directly affects the results: Perturbations of galaxies by their neighbors will depend on their relative masses. Thus, for example, a close interaction with a low-mass neighbor may be less damaging than a more distant collision with a much more massive system. We do not know the galaxies' masses and so we use their optical luminosity as an approximate mass indicator.

If all of the systems had similar luminosities, independent of their structural class, then we could just count the number of companions and this would be a fair comparison of the relative densities of the environments. Even in this case we would need to assume that galaxies with the same luminosity have roughly the same dark matter halo mass; an assumption that may not strictly hold. We show in Fig. 4.1 the absolute magnitude[2] distributions of the targets and their neighbors with redshift. Apart from the Malmquist bias (see Sect. 4.2.2) we find that the Sa(f) galaxies in our sample are typically one magnitude more luminous than the Sd(f) systems (see also Sandage & Tammann 1981).

This luminosity offset is shown in the Fig. 4.2, which displays the distribution of M_r for the different target galaxies (left) and that of their neighbors when they lie above the cutoff luminosity limit within the large cylinder (right). Thus we have a bias against including lower fractional luminosity neighbors that becomes more serious as the luminosity of the target galaxy gets fainter. Since most of the Sd(f) targets themselves are intrinsically faint, we will miss most of their lower luminosity neighbors, which will below our magnitude cutoff. On the other hand, for the Sa(f) and Sb(f) targets, with their brighter intrinsic luminosities, the range in brightness of fainter detectable companions will necessarily be larger.

We used two statistical tests to study whether we can nevertheless compare the environments of the three galaxy target types. For the first test we count only the objects in the large cylinder that are associated with targets that are fainter than $M_r = -20.0$ and do not use a sharp lower luminosity cutoff. With this condition we compare only similar objects. Using Student‘s t-test and the Kolmogorov-Smirnov test for M_r of the neighbors we found that the null hypothesis cannot be rejected. The null hypothesis is that the samples are taken from the same population. This means consequently that we did not find significant statistical differences between the three samples, i.e., these samples represents similar means and distributions.

[2]Throughout this paper we use the Petrosian magnitude in the r or z band as given in the SDSS DR4 database. We corrected this magnitude for Galactic foreground extinction with the values by (Schlegel et al. 1998) and also provided by the SDSS. The absolute magnitudes (M_r, M_z) are derived with the aid of the distance modulus using the apparent magnitude and the redshift z (also from SDSS) assuming a linear Hubble flow with no peculiar velocity corrections. We did not apply a correction for internal extinction within the galaxies.

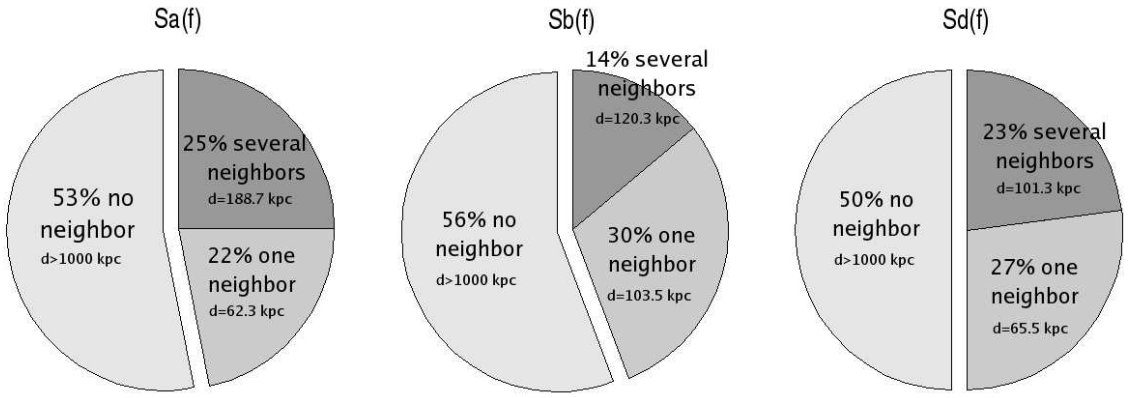

Figure 4.3: This pie diagram shows the fraction of higher luminosity neighbors around target galaxies in the large cylinder. The bright gray slice represents the targets without detection of higher luminosity neighbors. The medium gray slice is for those with one detected luminous neighbor and the dark gray slice indicates the percentages of two or more luminous neighbors for a target galaxy. The distance (d) to the nearest higher luminosity neighbor of the targets is indicated below the values of the percentages.

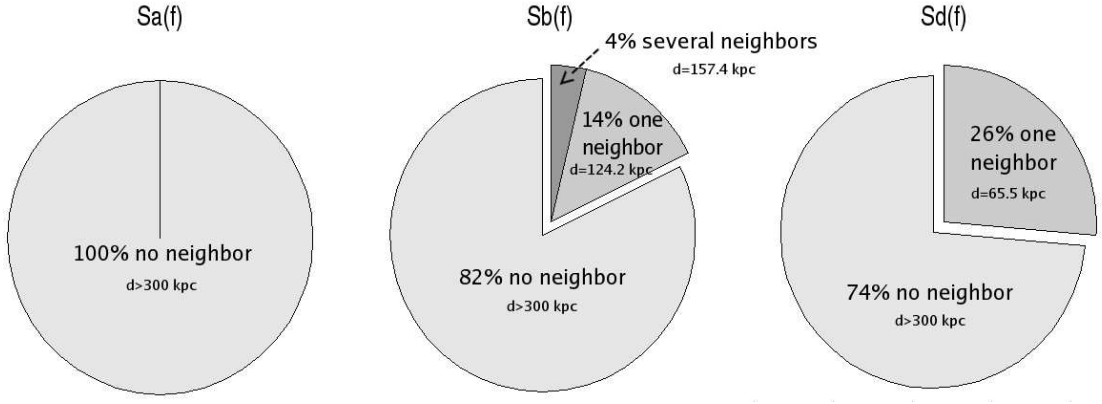

Figure 4.4: Same as Fig. 4.3 but for the small cylinder.

As a second test we constructed an artificial subset of Sb(f) galaxies drawn from the main sample with the same median M_r, similar redshift distribution, and the same high luminosity slope as that of the Sd(f) galaxy population distribution (for the Sa(f) objects this is not possible because of the low number of faint targets). This is illustrated in Fig. 4.2 with the dashed line on the left part of the figure. Then we selected the neighbors of this subsample and derived their mean values. The distribution of the neighbors of the Sb(f) subsample is indicated by a dashed line on the right side of the histogram. Comparing now this distribution with that of the Sd(f) neighbors we see that the two selections exhibit the same shape. Again, we use the Student‘s t-test and the Kolmogorov-Smirnov test and find no difference between these two samples.

Consequently, we conclude that when the neighbor luminosity distributions for the Sb(f) and Sd(f) target classes are selected in similar ways, their luminosity distributions are comparable. Because of the limitations in our sample, this result applies mainly to neighboring galaxies with $M_r < -18.5$.

4.3 Results

The properties of target galaxies and their numbers of neighbors are shown the Table 4.1. The complete version of this Table is available from the CDS[3]. Our paper contains only the first five rows as an example. This table is organized as follows: Column (1) presents the galaxy name in the SDSS nomenclature. The following two Cols. (2) and (3) contain the coordinates of the galaxies, i.e., right ascension and declination for the epoch J2000. The morphological class of the target galaxy is specified in Col. (4). Column (5) indicates redshift z of the target and (6) the apparent magnitude in the r band. In Col. (7) the number of all detected neighbors for the large cylinder is given. The total number of neighbors from the small cylinder is written to Col. (8). Column (9) gives the distance (in kpc) to the nearest brighter neighbor in the large cylinder and the same quantity is presented in Col. (10) for the small cylinder. The term nearest brighter neighbor refers to the galaxy with the closest projected separation from each target that is more luminous than the target itself. A value of 1000 kpc (300 kpc) indicates that the nearest brighter neighbor lies outside of the large (small) search cylinder. The number 9999 is used in this Table to indicate quantities that we could not measure.

In order to evaluate possible influences of neighbors on the target galaxies we first consider only the objects that are apparently more luminous than the targets. This is shown in Fig. 4.3 and 4.4 for the large and small cylinders, respectively. When counting the neighbors within the large cylinder, we found that about half of all targets, independent of their structural class, have no brighter neighbor. The fraction of the targets with one more luminous neighbor, and more than one neighbor is also not significantly different between the target types, and corresponds to roughly 1/4 of each neighbor class. In these figures we also give the projected distance to the nearest neighbor, which is surprisingly low for simple disk galaxies. This exercise shows that the fraction of dominant neighbors is comparable for all edge-on disks in our sample. In the case of the small cylinder the frequency of higher luminosity neighbors for the Sb(f) and the simple disk Sd(f) samples are also very similar. For the Sa(f), however, we do not detect any brighter neighbors, which is an effect due to the very small number of the Sa(f) targets and their high apparent luminosities.

Next we include *all* neighbors selected by our process, whether or not they are more luminous than the targets. The results in Fig. 4.5 for the large cylinders show that the Sd(f) sample has a higher fraction of targets without detectable neighbors compared to the earlier types. Even so Sd(f) targets usually are located in environments with several neighbors. We also found that 5 out of the total 55 Sd(f) galaxy targets have more than four neighbors. These results agree with the findings from our earlier preliminary studies; see Kautsch & Grebel (2004); Kautsch et al. (2005). For the small cylinder in Fig. 4.6, the Sa(f) galaxies have more companions than are found for the other types; these galaxies are in locally dense environments.

Now we investigate the trend *within* the large search cylinders around the targets for all detected neighbors, independent of their luminosities. Figure 4.7 shows the projected spatial distribution (in kpc) of all neighbors within the large cylinders (out to 1 Mpc) stacked on top of each other. Figure 4.8 shows the same for the small cylinders (radius of 300 pc). In these figures the major axes of the target galaxies' disks are rotated to the position angle of zero. The same coordinate transformation is applied to the neighbors of each target system. For this we used the two-dimensional rotation matrix $\mathbf{R}_{\phi}^{\text{`}}$ where the objects are rotated relative to fixed axes. The matrix can be written as

$$\mathbf{R}_{\phi}^{\text{`}} = \begin{pmatrix} \cos\phi & -\sin\phi \\ \sin\phi & \cos\phi \end{pmatrix} \tag{4.1}$$

i.e.,

$$\begin{pmatrix} x \\ y \end{pmatrix} = \mathbf{R}_{\phi}^{\text{`}} \cdot \begin{pmatrix} x_0 \\ y_0 \end{pmatrix} \tag{4.2}$$

The position angle of the target galaxy is ϕ. x and y are the distances in kpc between the target with the right ascension α_0 and declination δ_0 and the neighbor galaxy with α and δ (c.f., Karachentsev et

[3]Centre de Données astronomiques de Strasbourg (CDS), via anonymous ftp to cdsarc.u-strasbg.fr (130.79.128.5) or via http://cdsweb.u-strasbg.fr/cgi-bin/qcat?J/A+A/

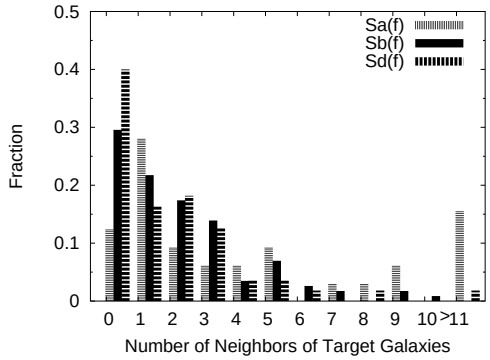

Figure 4.5: This histogram illustrates the fractional distribution of the target galaxies with numbers of neighbors within the large cylinder. The horizontally-hatched histogram bars represent the galaxy class with large bulges, Sa(f), the solid bars are the intermediate-size bulge galaxies, Sb(f), and the thick lined bars correspond to the Sd(f) simple disk galaxies. All targets with more than 10 neighbors are located at the position of "11" on the plot's abscissa.

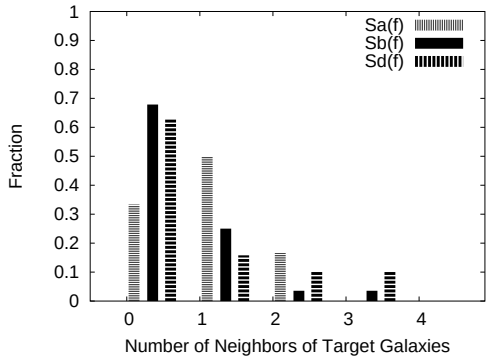

Figure 4.6: Same as Fig. 4.5 but for the small cylinder.

Table 4.2: Neighbor numbers in the quadrant zones of the large search cylinder.

	Eq. 1	Eq. 2	Pol. 1	Pol. 2
Sa(f)	38	50	28	29
Sb(f)	69	52	51	50
Sd(f)	30	23	17	17
All	137	125	96	96

al. 1993). This distance is derived with the equations

$$x_0 = ((\frac{z_0 c}{H_0}) \cdot 1000) \tan((\alpha - \alpha_0) \cdot \cos(\delta)) \quad [\text{kpc}] \tag{4.3}$$

$$y_0 = ((\frac{z_0 c}{H_0}) \cdot 1000) \tan(\delta - \delta_0) \quad [\text{kpc}] \tag{4.4}$$

where z_0 is the redshift of the target and c is the speed of light. The neighbors of the three different target groups are indicated as given in the legend of the Figs. 4.7 and 4.8: The vertical bar in the center illustrates the location and major axis direction of the target galaxies. The diagonal lines separate the data points of Fig. 4.7 into four quadrants. The neighboring galaxies near the extension of the targets' major axes are located in the equatorial zones (Eq1, Eq2) and those projected along the minor axes are in the polar wedges (Pol1, Pol2).

In these two Figs. (4.7, 4.8) no outstanding difference is seen between the neighbors of the three different disky target types; only mild trends of differing concentration towards the targets and preferred hemispheres exist, and these do not have high statistical weights. The number of neighbors in the small cylinder (Fig. 4.8) is too low for a meaningful analysis. In the large cylinder, we find that the angular distribution is nearly isotropic. A marginal difference is present between the polar and equatorial wedges at a moderate σ level. For that, we counted the neighbors of each target class in each quadrant separately and found a small deficit of neighbors at the polar cones, the exact numbers are given in Table 4.2. The deficit is similar for the different target classes, for all classes it is $\frac{N(\text{Eq1+Eq2})}{N(\text{Pol1+Pol2})} = \frac{262}{192} = 1.36 \approx 1.4$ when using Table 4.2. This average factor of 1.4 is also similar to that derived from the small search volume, where we also used $\sqrt{(N)}$ counting statistics to estimate the σs. Using counting statistics we can derive the σ_{tot} of both populations:

$$\sigma_{tot} = \sqrt{\frac{1}{N(\text{Eq1} + \text{Eq2})} + \frac{1}{N(\text{Pol1} + \text{Pol2})}} \tag{4.5}$$

$$= \sqrt{(\frac{1}{262} + \frac{1}{192})} \tag{4.6}$$

$$= 0.09 \approx 0.1 \tag{4.7}$$

assuming $\sigma(N) = N^{-1/2}$. Hence, the formal equatorial to polar wedge count ratio is $\frac{N(\text{Eq1+Eq2})}{N(\text{Pol1+Pol2})} \pm \sigma_{tot} \approx 1.4 \pm 0.1$. The corresponding one sigma level can be derived using:
$1\sigma\text{level} \approx \frac{1.4}{1\sigma_{tot}} = \frac{1.4}{0.1} = 14$, therefore the difference of the two wedges seems to be significantly different. Although this appears formally robust, we work only in two-dimensional layers and do not account for projection effects, which may influence this distribution. Pending a more detailed analysis we consider the angular distribution to be marginally isotropic.

Figure 4.9 shows the stacked and rotated densities of nearby galaxies as in Fig. 4.7, but for each target class separately (left side: Sa(f) neighbors; middle: Sb(f) neighbors; right: Sd(f) neighbors). In addition, we plotted contour levels using DS9 and tuned its contour parameters to a contour level value of 25 and a contour smoothness of 32 and used a linear scale. SAOImage DS9 is an astronomical imaging and data visualization application.[4] A smooth relation between the targets and

[4]http://hea-www.harvard.edu/RD/ds9/

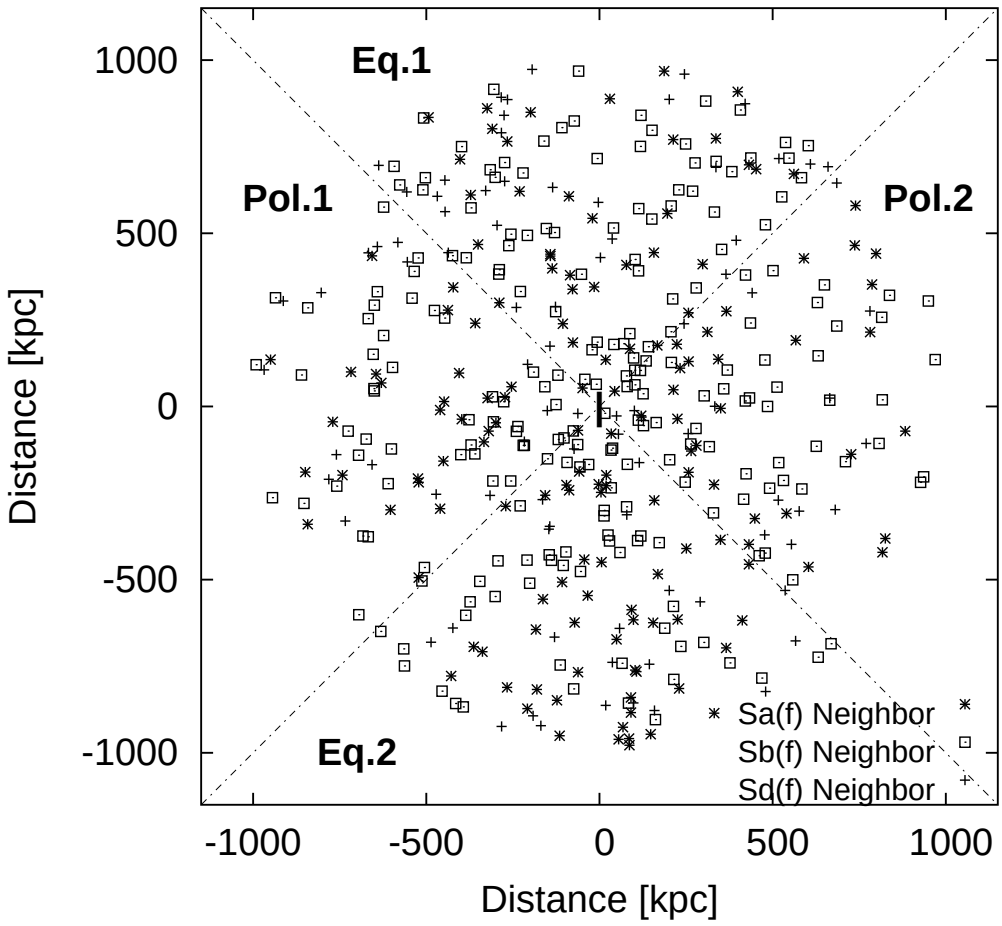

Figure 4.7: Projected space distribution around the target galaxies (bar in the center) in kiloparsecs of neighbors stacked and rotated in the large cylinder. Neighbors of an Sa(f) target are indicated as stars, neighbors of Sb(f) as squares and those of Sd(f) as crosses. Eq.1, Eq.2 locate for the equatorial quadrants, Pol.1,Pol.2 the polar quadrants around the targets. The mean distance between Sa(f) targets and neighbors is 587.1 kpc, for Sb(f) it is 595.4 kpc and for Sd(f) 704.7 kpc.

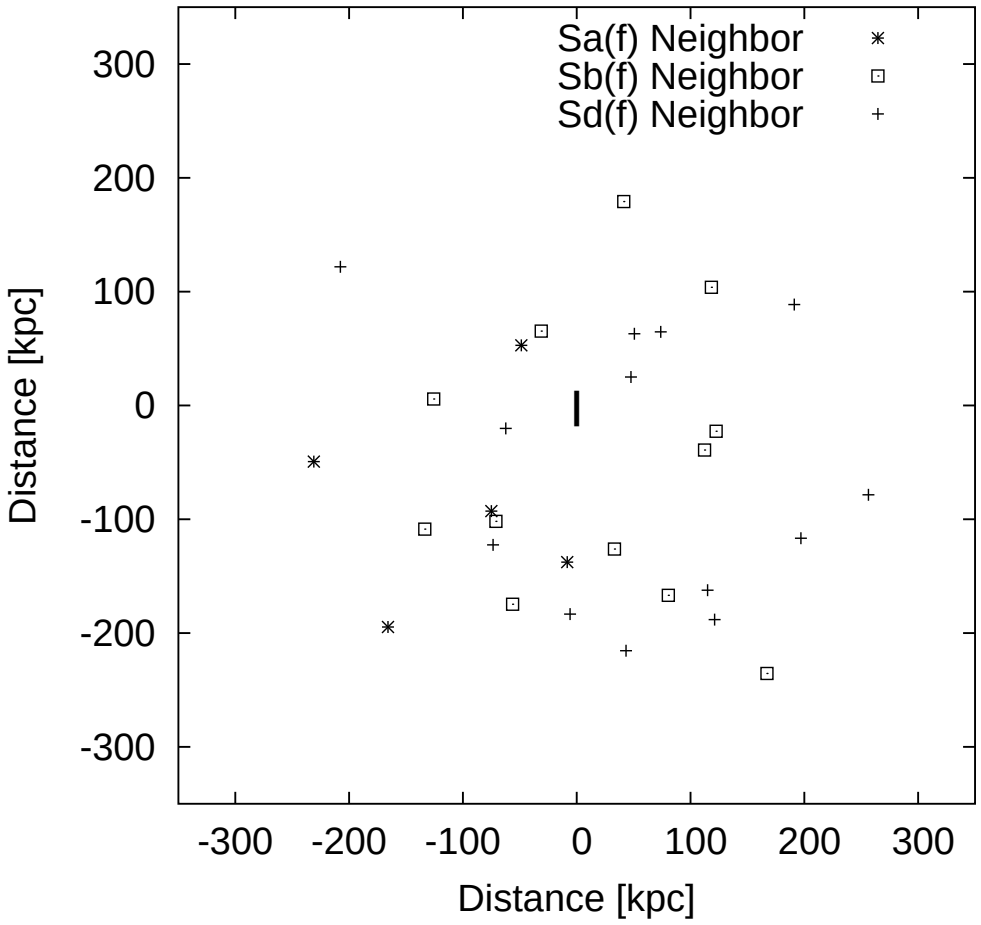

Figure 4.8: Same as Fig. 4.7 but for the small cylinder. The mean distance between Sa(f) targets and neighbors is 137.9 kpc, for Sb(f) it is 143.9 kpc and for Sd(f) 198.8 kpc

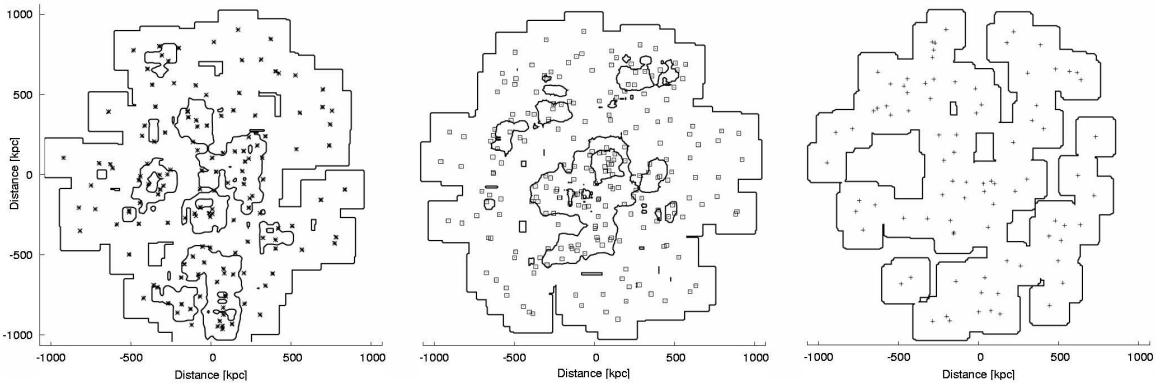

Figure 4.9: Projected space distribution like Fig. 4.8 around each target type including density contours. Left: Sa(f) neighbors; middle: Sb(f) neighbors; right: Sd(f) neighbors.

the environments is found. Sa(f) have generally the most dense and clustered environment on average. The subclustering appears to be slightly less strong for the Sb(f) but density increases towards the position of the targets. The least clustered and concentrated environments are found around Sd(f) galaxies. This distribution is mostly isotropic as shown in Fig. 4.10.

This continuous trend could be explained in terms of the average positions of the targets in galaxy groups. The Sa(f) evidently are located in the denser and central regions of richer groups that are likely to have substructure, whereas Sb(f) are in slightly less dense regions off center regions or near the centers of less dense galaxy groups. We draw these conclusions on the high mean density and low radial gradients of the Sa(f) sample, and large scale substructure seen as a partial ring in the Sb(f) plot. The concentration towards the targets in contrast to the Sa(f) where no central clustering is detected suggesting a evenly distributed dense region of the Sa(f). The simple disk Sd(f) targets are surrounded by a relatively low density and uniform distribution of neighbors. The lack of concentration towards the neighbors suggests a minimal physical connection between the targets and neighbors, as could be found in the outer parts of galaxy groups or lower density and more diffuse galaxy clouds. These trends appear to smoothly vary from Sa(f) to the Sd(f) classes.

The cumulative growth of the numbers of objects in the three complete galaxy target samples as a function of physical distance to their neighbors is shown in Fig. 4.10 for the large and Fig. 4.11 for the small cylinder. The overall trends are roughly similar for the Sa(f) and Sb(f) classes. In the large cylinder, Sd(f) neighbors show a uniform distribution at radii larger than 500 kpc which is illustrated with the solid line. At radii below 400 kpc, the distribution of the Sd(f) neighbors approaches that of the other types. Otherwise, the distribution of the Sa(f) neighbors comes suspicious close to the uniform distribution at $\approx$ 200kpc and continue to be less clustered than the neighbors of Sb(f) and Sd(f). However, these trends on small radii may be somewhat biased, the general trend qualitatively seen here seems to be that at least at radii smaller that 400 kpc the distribution of all three samples are similar.

A Kolmogorov-Smirnov test leads to results that are difficult to interpret: For the radial distributions in the large cylinder of neighbors of all systems, the null hypothesis that the distributions are drawn from the same population can be rejected with a small probability. The mean distance between Sa(f) targets and neighbors is 587.1 kpc, for Sb(f) it is 595.4 kpc and for Sd(f) 704.7 kpc in the large cylinder. These values support the similar distribution between the Sa(f) and the Sb(f) neighbors and their clustering compared the the distribution of the Sd(f) neighbors. The statistical significance of the small cylinders is not meaningful because of the small numbers of detected neighbors. However, the mean distance between Sa(f) targets and neighbors is 137.9 kpc, for Sb(f) it is 143.9 kpc and for Sd(f) 198.8 kpc in the small cylinder. This reflects the result also found for the large cylinder.

Figure 4.12 shows the distribution of the absolute magnitudes in the SDSS z band of the Sa(f) (top left), Sb(f) (middle left) and Sd(f) (bottom left). The z band is the reddest filter available from SDSS

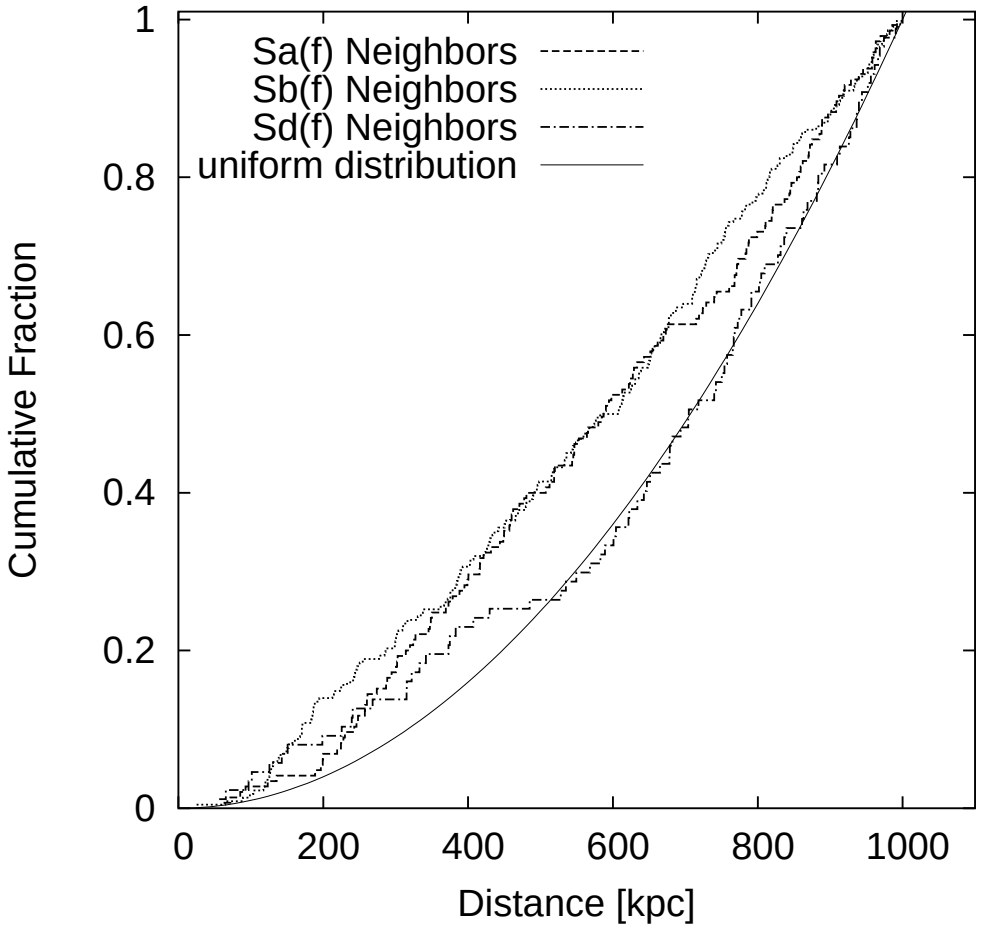

Figure 4.10: Cumulative distribution of the projected distance in kiloparsecs of Sa(f) neighbors (dashed line), Sb(f) neighbors (dotted line) and Sd(f) neighbors (chain dotted line) as a fraction of the total number of the neighbors. The uniform distribution function $f(x) = \frac{x^2}{1000^2}$ is the solid line.

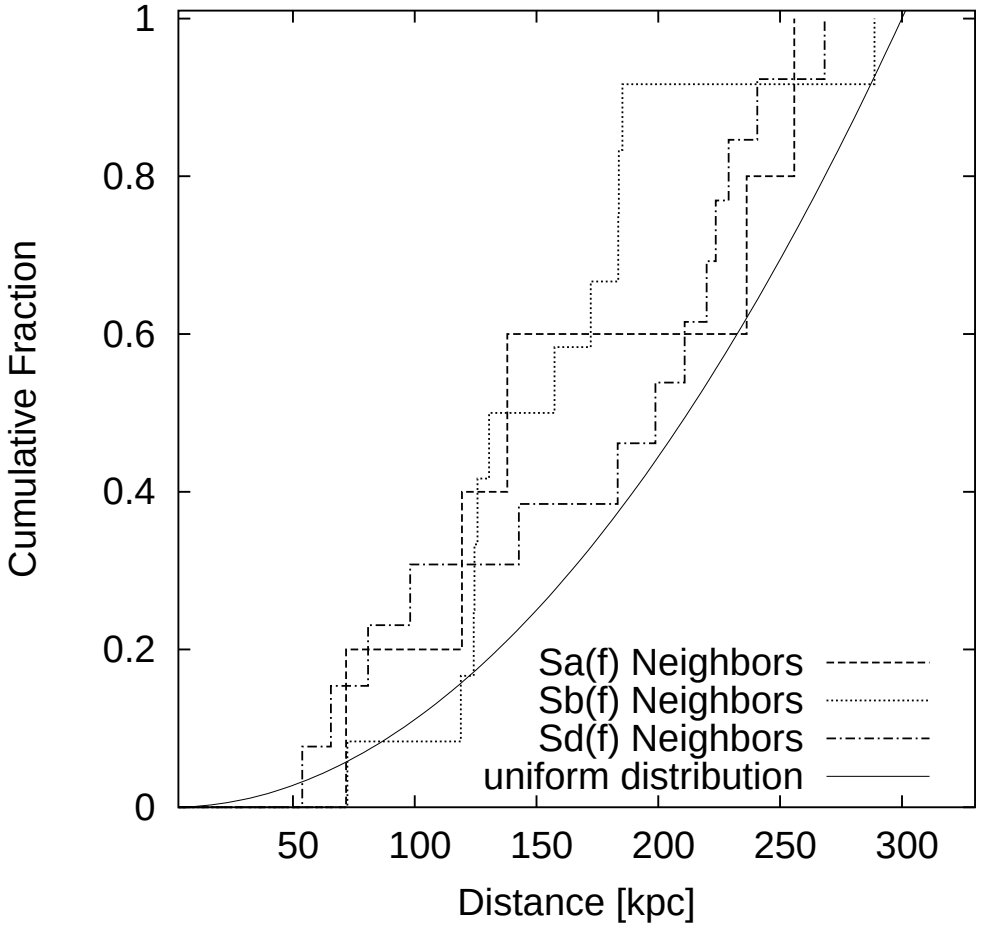

Figure 4.11: Same as Fig. 4.10 but for the small cylinder. The uniform distribution function is $f(x) = \frac{x^2}{300^2}$.

and has the lowest extinction, but at the price of reduced photometric accuracy. This figure shows that the luminosity differences between simple disks and galaxies with bulges are not obviously due to dust attenuation, as the comparison with the bluer r filter in Fig. 4.2 might suggest. The luminosity offsets probably also represent differences in stellar mass, as might be expected for galaxies with pronounced bulges versus those containing only relatively flat stellar disks. The right part of Fig. 4.12 shows that on average the dimensions of all targets are similar. The axes are derived using the SDSS isophotal major axis in z as given in the SDSS database. According to Stoughton et al. (2002) the length of this axis is given by the locations of the 25 magnitudes per square arcsecond isophote of the object in each filter. In Fig. 4.13 we plot the number of the neighbors of Sa(f) (top), Sb(f) (middle) and Sd(f) (bottom) versus the major axis (left) and M_z (right) of the target galaxy for the large cylinder. The diameters of the program targets are unaffected by the numbers of neighbors. Also the luminosities of the targets appear to be roughly independent from the number of neighbors although the diagrams show a slight trend that the luminosities are brighter the larger the numbers of neighbors.

4.3.1 Morphologies of the Neighbor Galaxies

The morphologies of neighboring galaxies can be estimated using characteristics provided by the SDSS data tables. We utilize the color u-r and the concentration index as our main morphological indicators by adopting values given in Strateva et al. (2001). Galaxies with u-r<2.22 and a concentration index lower than 2.6 are classified as late-type galaxies (Sb, Sc, Irr). Early-type galaxies within this classification are E, S0 and Sa. The concentration index is the ratio of the Petrosian radii (petrorad) that contain 90% and 50% of the Petrosian flux in the same band, respectively (see Stoughton et al. 2002). The morphologies of the neighbors of the three different target classes are given in Fig. 4.14 for the large cylinder. For the small cylinder we do not present the figure because of the low number of neighbors. Again, stars and squares represent a neighbor of an Sa(f) and Sb(f) objects, respectively. Crosses are the neighbors of Sd(f) systems.

The horizontal and vertical dashed lines represent the morphological borders of the color and the concentration indices dividing early and late type galaxies as given in Strateva et al. (2001). The arrows at the top of the plots show the mean colors for the Sa(f)- or Sb(f)- or Sd(f)-neighbor galaxies. The mean values of the concentration indices for the neighbors are indicated as arrows on the right ordinate of the plots. Figure 4.14 indicates that the neighbors of Sa(f) and Sb(f) targets do not have preferred morphologies; their morphological types cover the full range. We assessed these trends using Student‘s t-test, and we found that the null hypothesis that the mean of the neighbor colors are the same can be rejected between the neighbors of Sa(f) and Sd(f) (significance=99%) and the neighbors of Sb(f) and Sd(f) (significance=97%). For the CI we found that the null hypothesis that the mean of the neighbor CI are the same can be rejected between the neighbors of Sb(f) and Sd(f) (significance=99%). This effect is in the sense that neighbors of Sd(f) galaxies have bluer colors than those of the other systems and possibly also lower degrees of central light concentration. In the other cases we cannot reject the null hypothesis that the neighbors have the same mean colors and CI.

4.3.2 General Distribution of Disk Galaxies

In order to illustrate the large scale environments of our targets we plot a cone diagram, Fig. 4.15. This diagram presents the spatial distribution of all galaxies with distances derived from the SDSS redshifts of type Sa(f) (red dots), Sb(f) (green dots) and Sd(f) (blue dots) from the catalog of Kautsch et al. (2006a). The fine dots are comparison galaxies of any type with spectroscopic redshifts and brighter than 20 mag in the g band as given in the SDSS database. Here we used the g band instead of the more efficient r band because the g was also used to select the edge-on galaxies for our catalog from the SDSS as described in Kautsch et al. (2006a). The g band initially was chosen in order to come as close as possible to the selection parameters of older edge-on galaxy catalogs (Karachentsev et al. 1993, 1999).

Figure 4.15 shows the distribution of the galaxies in the equatorial stripes $130 < RA < 241$, $-9 < DEC < 8$ (upper half circle) and $63 > RA > 346$, $-8 < DEC < 10$ (lower half circle).

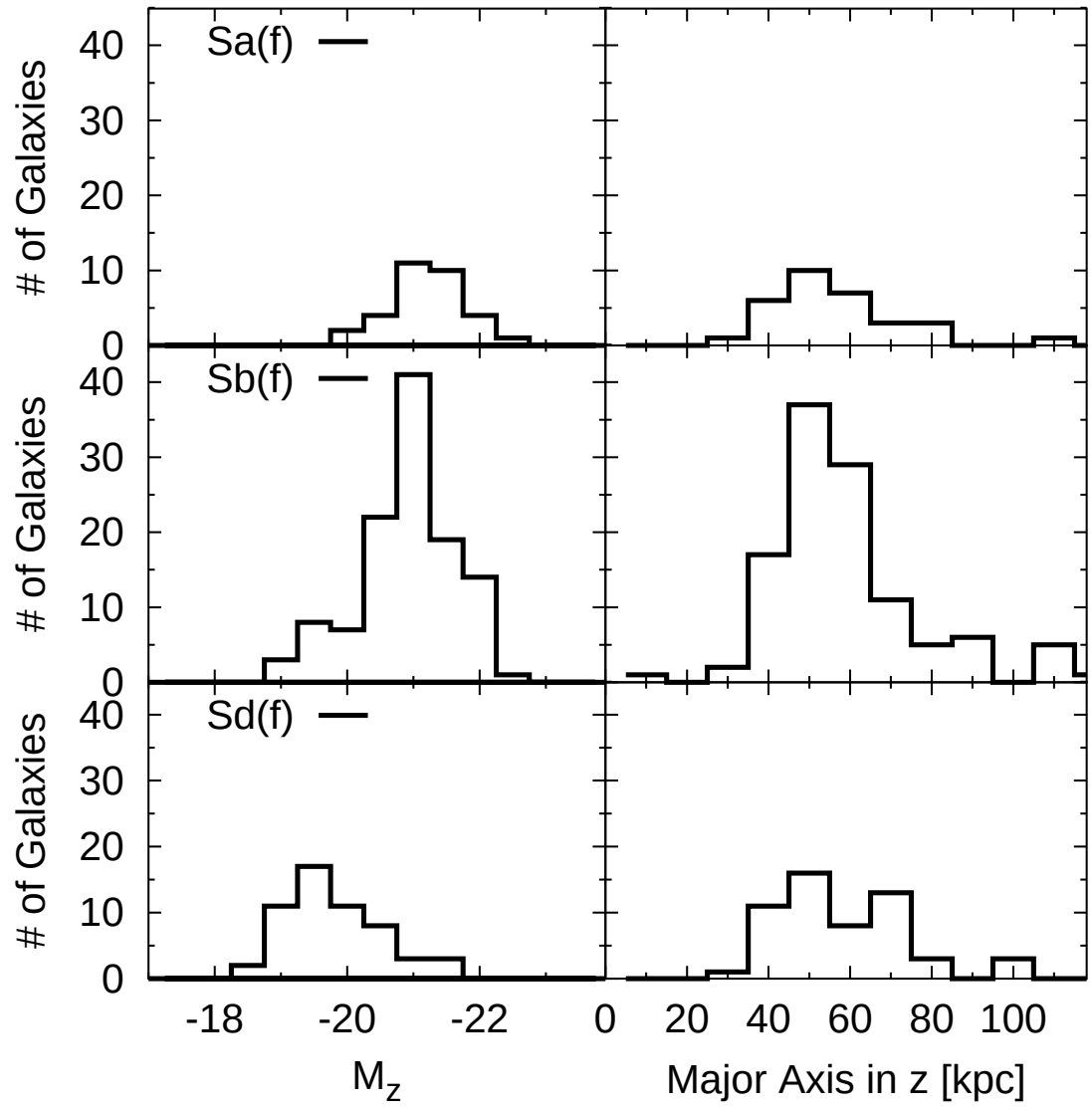

Figure 4.12: Distribution of the absolute z magnitude (left) and the isophotal major axis [kpc] (right) of the targets for Sa(f) (top); Sb(f) (middle); Sd(f) (bottom)

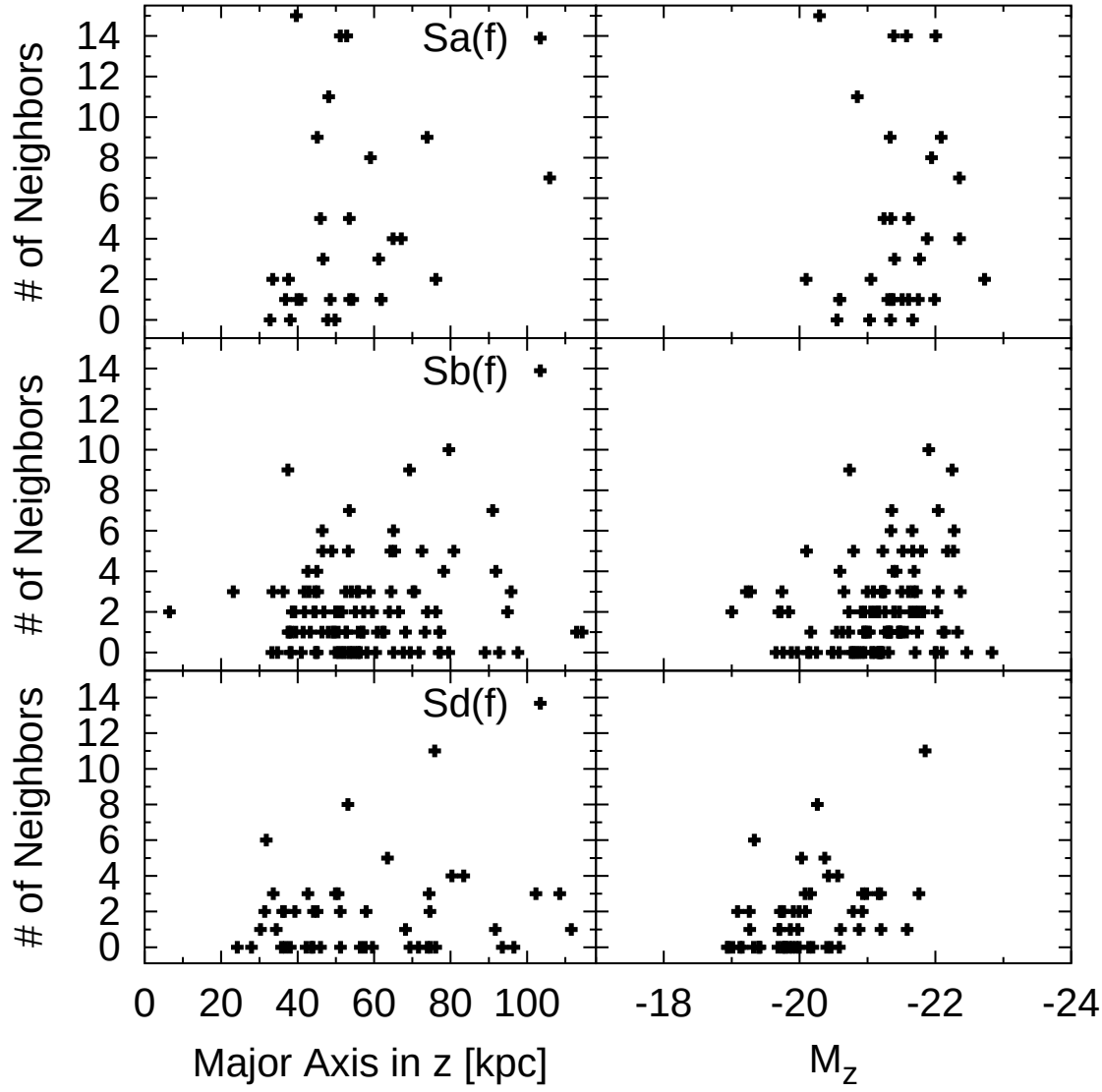

Figure 4.13: Number of counted neighbors in the large cylinder versus isophotal major axis [kpc] (left) and absolute z magnitude (right) of the targets: Sa(f) (top); Sb(f) (middle); Sd(f) (bottom).

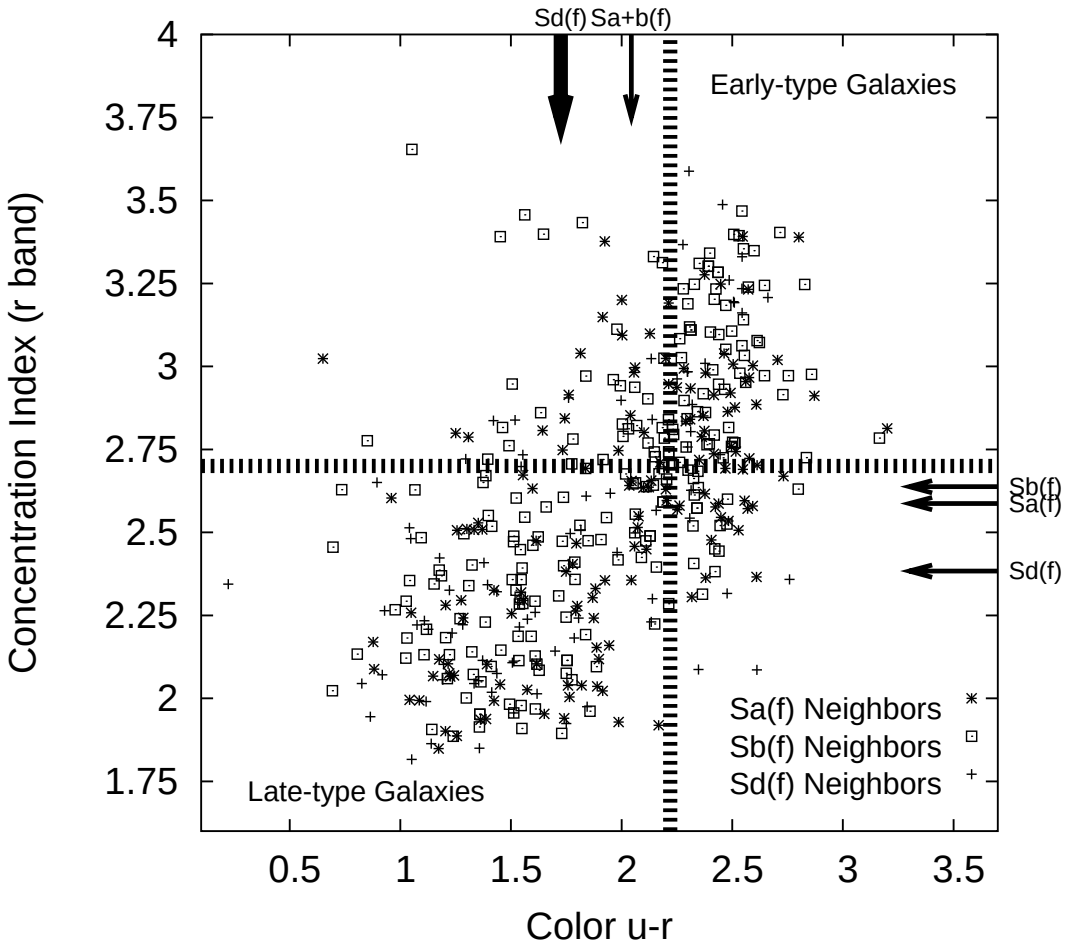

Figure 4.14: Morphological distribution of Sa(f) neighbors (stars), Sb(f) neighbors (squares) and Sd(f) neighbors (crosses). The abscissa indicates the color *u-r* and the ordinate the concentration index in the *r* band as morphological indicators. The region for the early-type galaxies is top right and for the late types bottom left. The dashed lines indicate the morphological borders. The arrows are located at the mean values for each target class. The bold arrow indicates the mean of the colors of Sd(f) neighbors that differs significantly from the Sa(f) and Sb(f) neighbor colors. Although the arrows for the CI show offsets, they differ in a statistically significant only between Sb(f) and Sd(f). The median *u-r* value is for Sa(f): 2.03, Sb(f): 2.05, Sd(f): 1.69, the median concentration index value is for Sa(f): 2.58, Sb(f): 2.63, Sd(f): 2.35.

Qualitatively, the positions of all three galaxy types tend to be along the outer borders of the filaments although some of types lie in isolated field regions. In this respect the simple disk galaxies follow the pattern to statistically prefer less dense regions in large scale structures that are seen in other samples of lower luminosity late-type galaxies (e.g., Wild et al. 2005, and references therein). The galaxy surface densities are too low for us to have significant contamination by galaxy clusters (Abell et al. 1989, Table 2A).

In addition, we compare the fraction of our catalog galaxies which are also included in the "Catalog of Very Isolated Galaxies from the Sloan Digital Sky Survey Data Release 1" by Allam et al. (2005), which represents 2980 very isolated galaxies found in the SDSS DR1. Their isolation criterion is based on Karachentseva (1973), who defined a galaxy to be isolated if the projected distance to the nearest neighbor is 20 times larger than the diameter of the neighboring galaxy and the diameter of the target galaxy is between 1/4 and 4 times the diameter of the neighboring galaxy. For a detailed description see Section 3 of Allam et al. (2005). In making this comparison we chose galaxies from our catalog that have comparable magnitudes to those in Allam et al. (2005). This comparison recovered only 6 of 175 Sa(f), 39 of 663 Sb(f) and 28 of 442 Sd(f), respectively. This is a very small overlap ranging from 3% to 6%, indicating that only a few percent of our catalog galaxies are really very isolated. However, Allam et al. (2005) galaxies are not restricted to edge-on view or any morphological criterion.

4.4 Discussion

4.4.1 Environmental Settings

The morphologies of galaxies can be linked to environment through a variety of mechanisms ranging from those associated with conditions at the time of formation to later effects of tides, gas accretion and removal, and interactions with companion systems (e.g., Nagashima et al. 2005; Avila-Reese et al. 2005). Most of the galaxies in this study are located in moderate to low galaxy density regions that are typical of galaxy groups. The simple disk systems, especially the Sd(f) class, while being in regions of moderate galaxy density in this study seem o be structurally similar to the typical L_* systems found in voids (Rojas et al. 2004). While on the one hand this could favor interpretations focusing on connections between structure and initial conditions (Okamoto & Nagashima 2003), recent numerical simulations (e.g., Mastropietro et al. 2005) demonstrate that environmentally driven transformations may also work in the outer, less dense parts of galaxy clusters. Do they then also play a role in typical galaxy groups? For example, it is difficult to undergo a post-formation merger if you are a galaxy with no nearby companions? Unfortunately it still is not clear whether a MDR is observed among typical smaller galaxy groups, and so the issue of environmental modification of major group members remains controversial (Whitmore 1995; Tran et al. 2001). We cannot resolve the nature versus nurture question at this point of the discussion.

All target disk galaxy classes in this study tend to follow galaxy filaments, which suggest that they prefer an environment comparable to that of galaxy groups (Fig. 4.15). Only a small percentage of our sample is found to be very isolated in the cone diagrams and in comparison with the Allam et al. (2005) catalog of very isolated galaxies. If we assume that simple disk galaxies are generally also low surface brightness galaxies (LSB) (Karachentsev et al. 1993, 1999; Matthews et al. 1999b) then our results are similar to that of Rosenbaum & Bomans (2004). They show that their LSB systems are located in the outer parts of filaments or in voids. They conclude that the isolation of the LSB takes place on scales of large galaxy groups and the large scale structure of the filaments as also shown in our Fig. 4.15. In contrast to the results of Rosenbaum & Bomans (2004) and ours, Bothun et al. (1993) found that LSB disk galaxies tend to avoid the group environment but their statistics are may be biased (see discussion in Rosenbaum & Bomans 2004).

We found most of the target galaxies have neighbors, but differences exist in the distribution of the neighboring systems suggesting that the Sd(f) are statistically in less dense locations than the Sb(f) and Sa(f) systems. Also Rosenbaum & Bomans (2004) found that in regions similar to that covered by our large cylinder LSB galaxies follow the distributions of high surface brightness galaxies but "...all

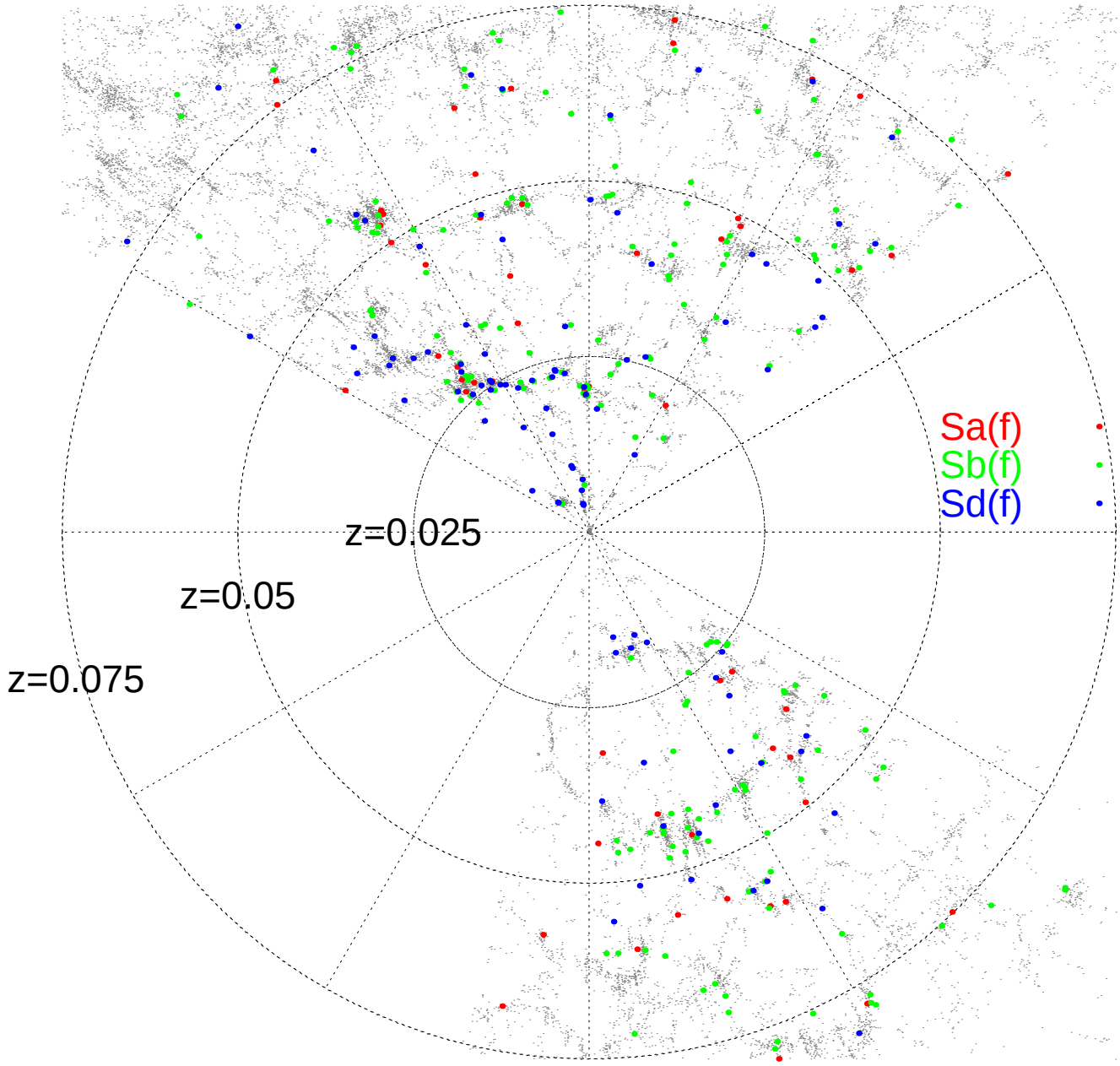

Figure 4.15: This cone diagram shows the cosmological large-scale distribution of galaxies in the SDSS equatorial stripes $130 < RA < 241$ and $-9 < DEC < 8$ (upper half circle) and $63 > RA > 346$, $-8 < DEC < 10$ (lower half circle). The circles indicate the distances of the same redshift. Sa(f) targets are indicated as red dots, Sb(f) as green and Sd(f) as blue dots. The fine dots are the galaxies from a comparison sample.

the LSB mean values lie systematically (but partially not significant) below the corresponding high surface brightness galaxies'value." We found a non-negligible scatter within the smooth statistical trend between neighboring galaxy densities and morphologies. This scatter lies between two extremes. On the one hand, some galaxies with prominent bulges are located in isolated regions. This could be due to a variety of possible effects, e.g.

1. Random effects of local clustering, where two galaxies born close to each other in an overall isolated location could have interacted or have cannibalized their neighbors. Detailed studies of the stellar structure and its dynamics would shed light on this suggestion.
2. Different starting conditions for galaxies in the field in principle could produce isolated and bulge dominated galaxies.
3. The bulges of these objects are box/peanut bulges, i.e., thick bars seen edge-on (Lütticke et al. 2000; Athanassoula 2005a; Bureau & Athanassoula 2005) or evolved via secular evolution (Kormendy & Kennicutt 2004; Athanassoula 2005b).
4. Objects can be missed because of their low luminosities or due to the limits in how close two spectroscopic fibers can be placed with respect to each other.

On the other hand, a small fraction of simple disks is located in dense environments. Their position could be due to fortuitous circumstances whereby these galaxies avoided interactions or recent infall into denser regions. In these cases it should be possible to observe ongoing changes in their internal structures due to interactions, which may eventually lead to thick disks (Dalcanton & Bernstein 2002; Yoachim & Dalcanton 2005, 2006) and warps (Matthews & de Grijs 2004).

Otherwise, the fractions of brighter neighbors, and therefore potential perturbers, that could drive morphological transformations in both environments, are the same for the three disk galaxy types (Figs. 4.3 and 4.4), suggesting that all targets with detected neighbors have similar numbers of more massive, dominant possible interaction partners. It is also shown that the simple disks have close massive potential disruptor, sometimes closer than those of galaxies with bulge. The fact that galaxies are more spread out around the Sd(f) may imply that strong interactions are less likely.

We find that the morphologies of neighbors (Fig. 4.14) of targets with bulge (Sa(f) and Sb(f)) are evenly distributed over all types and only the neighbors of simple disks (Sd(f)) are statistically tilted toward slightly bluer galaxy types and have slightly smaller central light concentrations. This is an effect of the location of the Sd(f) galaxies in the less dense outer parts of groups, where the galaxies tend to be bluer due to more active star formation than in the denser regions (Gómez 2003; Kauffmann et al. 2003). The placement of Sd(f) galaxies in the outer zones of groups is also supported by their location in environments with smooth density distribution (Fig. 4.9) and the deficit of neighbors seen at the cumulative distance distribution (Fig. 4.10).

We found a generally isotropic angular distribution of neighboring systems around the targets. A small excess of neighbors may exist along the major axis of the disks, i.e. the equatorial zones (Fig. 4.7 and 4.8). Therefore we can neither confirm nor refute the presence of a Holmberg effect or similar effects such as polar great circles or planes of companions on small scales around group disk galaxies (Kroupa et al. 2004; Koch & Grebel 2006) or large superplanes within groups (e.g., Karachentsev & Marakov 1996; Hartwick 2000; Sawa & Fujimoto 2005).

4.4.2 Bulges

In general, bulges may grow due to secular evolution (Kormendy & Kennicutt 2004; Athanassoula 2005b). We do not analyze our targets if they show typical properties of secular evolution, e.g., disky bulges etc. (Kormendy & Fisher 2005). In the secular evolution scenario, gas is transported to the galaxy center due to the loss of angular momentum and "pseudobulges" are generated from the subsequent central star formation (SF). Merging with a massive perturber would create a more massive final galaxy with a "classical" bulge (Baugh et al. 1996; Kauffmann 1996; Athanassoula 2005b). Bulges can also be formed from accreted dense satellites which sank into the disk center (Tremaine et al. 1975; Wyse et al. 1997; Benson et al. 2004).

Our results are difficult to interpret within these scenarios. Secular evolution suggests that one could not detect mass differences between a simple disk and a galaxy where the bulge was built up due to secular evolution because the galaxy is not changing its mass during this process in contrast to mass accretion during hierarchical growth. If we use the luminosities of our targets as a rough stellar mass estimator we do see clear differences between the low-luminosity (and low-mass) simple disks and brighter disks with bulge (Fig. 4.12). Therefore we may conclude that the galaxies with bulges in our sample do not have their bulge component due to dominant secular evolution. However, we also have overlap regions in the distributions of the luminosities of the three target types and cannot exclude secular evolution as bulge creator.

The major merger scenario naturally explains the luminosity/mass differences between galaxies with and without bulge. Merging with a massive partner would lead also to a larger galaxy (e.g., Cole et al. 2000). We observe for our sample systems that the diameters for all targets are similar (Fig. 4.12) and do not correlate with the number of neighbors (Fig. 4.13). If therefore the mergers can be ruled out is difficult to say because we observe differences of densities of neighbors around the three target types. However, also this model seems not to simply fit with our data. Because we are not very sensitive to smaller but still important satellites, this accretion scenario can be not discussed. We still do not escape from the nature versus nurture question at this point.

4.4.3 Morphology-Density

Does the observed structure of the target galaxies depend on intrinsic processes (nature) or extrinsic influence (nurture) and in addition, is the observed continuum comparable to the standard MDR?

Some environmental factors, such as ram-pressure stripping probably are not important in the regime of this study because of the low density of the intergroup gas, the small gravitational potential of galaxy groups and the low number of potential perturbers (Lewis et al. 2002; Okamoto & Nagashima 2003). Interactions between two galaxies are tidal and can therefore the harassment can be a factor. But the densities around the targets are low and we also do not see a down-sizing of the disk size (Fig. 4.12 and 4.13) in denser environments as expected from these scenarios[5]. On the other hand, major mergers are efficient in groups because of low velocities of the galaxies within groups and subsequent slow interactions between equal mass objects (Moore et al. 1999; Ghigna 2001). ΛCDM simulations show that strong external strong interactions within groups would cause dramatic changes in the morphology up to the demolition of the disks and the build-up of a dominant spheroidal components (e.g., Gardner 2001; Steinmetz 2003; Taylor & Babul 2003; Benson et al. 2004). Simple disks are expected to be very sensitive to these mergers because of their low masses and the lack of a bulge component which could stabilize the disk during interactions (Samland & Gerhard 2003).

However, we found that the fraction of more massive, potential disruptors is the same for targets with or without bulges. In addition, the nearest perturber is located at close distances from simple disks, often closer than for galaxies with bulge. These observations suggest that the simple disks are more robust against external influences than implied by the disk models. A standard MDR driven by external transformation processes associated with the projected density of similar luminosity galaxy neighbors cannot fully account for the observations.

4.4.4 Nature

We are seeing two effects – galaxies with simple disks are of lower luminosity, thus appear to be less massive systems and prefer to avoid crowded regions. We can put these two aspects together in modern ΛCDM models by noting that less massive galaxies may experience fewer mergers and

[5]Ram-pressure stripping and evaporation of the cold disk gas in the hot ICM lead to a stopping or "strangulation" of SF in the disks and a truncation of the outer disk due to gas removal and lack of SF material. This can drive evolution from late to early disks and fosters a decrease of the disk size and growth of a bulge-dominated galaxy at the end of this transformation (Couch & Sharples 1987). Strong tidal heating leads to mass loss and subsequently to rounder galaxies and smaller disks due to stripped and dynamically-induced loss of stars.

interactions. This qualitatively agrees with the reduced prominence of bulges and lower star formation rates of simple disks (Kormendy & Kennicutt 2004). It is especially valid for Sd(f) galaxies with lower luminosities/masses, which are the least clustered objects in this sample. The Sd(f) galaxies then might have formed in locally empty environments where subsequent perturbations by substantial neighbors rarely occur. Their disky nature is also supported by the nature scenario. I.e., approximately coherent collapse may have been more important than the hierarchical growth because galaxies forming in less dense environments may statistically have formed from protogalaxies with higher angular momentum than those in higher density regions (Lee 2006). If the collapse is dissipational and smooth, then the specific angular momentum is conserved and the gas forms a thin, rapidly rotating disk (Dalcanton et al. 1997). This disk can evolve to a low surface brightness disk galaxy with high angular momentum and low mass, comparable with the Sd(f). On the other hand, low angular momentum protogalaxies collapse efficiently, resulting in normal, high surface brightness galaxies (Sa(f)), and these are more typically formed in denser locations. The Gaussian distribution of the initial conditions leads to a wide range of halo masses and angular momentum that we observe in form of the various bulge sizes of our different sample galaxies. This is because of angular momentum is likely to be an important factor in determining the structural characteristics of disk galaxies (Fall & Efstathiou 1980) including the disk and bulge size for fixed masses (Hernandez & Cervantes-Sodi 2006).

With this intrinsic scenario our observed trends can be interpreted as resulting in part the smooth variations in the mean galaxy characteristics and scatter in individual properties that can originate in a Gaussian distribution of initial conditions during galaxy formation. This kind of effect could influence the birth locations of disk dominated galaxies, i.e., disks with high angular momentum should preferentially avoid denser locations.

4.4.5 Nurture

The denser the environment, the more possible perturbers exist. If galaxies are born in these denser regions, minor mergers and accretion of satellite companions may play an important role. Galaxies with larger bulges tend to be luminous and have higher masses than the simple disks. But all targets have all similar dimensions suggesting the accretion of satellites and fragments instead of major mergers, which would have consequently result in more extended galaxies. Minor mergers with companions, e.g. satellites resembling almost the Large Magellanic Cloud, could foster bulge growth and accelerate this development especially in galaxies with pre-existing bulges. Accretion of low mass dwarf satellites–below our detection limits–is not assumed to have critical changes on the disk+bulge structure (Governato et al 2004).

This discussion leads to a picture of the group environment as a transition zone between structure produced mainly early on by initial conditions, "nature", and situations where typical galaxies suffer significant transformations well after their birth due to interactions and thus are nurtured into their present day forms. The Sd(f) galaxies then are examples of simple galaxy formation processes, which leaves open the question as to the nature lower angular momentum galaxies that also should have formed in the least dense locations.

4.5 Summary

This work presents a study of the environments of disk galaxies through a study of the neighborhoods around edge-on galaxies with prominent stellar disks. It aims to explore and better understand the processes that could be responsible for creating and changing the overall disk and bulge structures of galaxies in the nearby Universe.

Our sample consists of a homogeneous set of edge-on disk galaxies with obvious bulges, medium-sized bulges and bulgeless simple disks selected from the edge-on disk galaxy catalog by Kautsch et al. (2006a). We investigated environments by detecting projected neighbors down to luminosities almost comparable to that of the Large-Magellanic-Cloud-like satellites within our search volumes and which are detected in the SDSS spectroscopic fibers.

Counting the number of neighbors, we found two results depending on the luminosity of the neighbors. i) The fraction of more luminous and therefore probably more massive potential perturbers around the program galaxies is the same whether or not the targets have a bulge. ii) Counting all neighbors in our search cylinders, independent from the luminosity differences between target and neighbor, we found that the program disk galaxies are mainly located in galaxy groups. We found a smooth trend for galaxies with bulges to be located in denser group regions whereas bulgeless simple disks predominate in less dense parts of the groups. Despite the non-negligible scatter of the observed smooth trend, only a marginal fraction of simple disks are located in very isolated large scale environments. We see that the Sd(f) often have a few bright neighbors–thus they are not isolated. However, the neighbors are spread out nearly uniformly over much of the large volume and show only some excess over random on smaller scales of <400 kpc. We conclude that the Sd(f) can probably survive in well separated binary pairs and are usually in locations where galaxies are not clustered and thus possibly where groups are unvirialized.

We investigate the morphologies of all detected neighbors including those of less massive companion galaxies. The morphologies of the companions span a wide range and appear to be correlated with the target disk structural type in the sense that only the mean of the Sd(f) neighbors are slightly bluer and of later morphological type. In addition, the projected space distribution of the surrounding neighbors is mostly isotropic above and below the midplane of the targets, i.e., no obvious evidence for a Holmberg effect, although we detected a marginal deficit of neighbor galaxies at extended polar regions.

Our observations generally follow the predictions from the models where the morphology of simple disk galaxies is largely determined by the initial conditions of the protogalaxies and local densities at the time of their formation. In these models, the Gaussian distribution of the protogalaxy's angular momentum determines the disky morphology, which then is not modified if the system avoids later major interactions. Additionally, the maximum of the Gaussian distribution is probably determined by the environment density because the simple disks in the models prefer to avoid crowded regions as birth place.

We conclude that the group environment is a transition zone between deterministic and environmental influences. In the group environment, the initial morphology of the disks can smoothly evolve by the accretion of material in minor mergers which increase the promote bulge growth. Rarer major mergers can produce more profound changes pushing galaxies to earlier structural types. In this picture the full range of environmentally induced transformations predominate only when galaxies are accreted into dense regions such as galaxy clusters.

4.6 Additional Points

4.6.1 Galaxy Transformation in Galaxy Clusters

In the previous sections we found that our program galaxies are located in low-density environments. However, in this section we discuss the transformation processes working in galaxy clusters. Various mechanisms such as interaction of the galaxy with the hot cluster plasma (i.e., the intra cluster medium (ICM)), merging or tidal interactions are possible engines for these reshapings. These mechanisms work dominantly in galaxy clusters. But our galaxies are mostly located in groups. However, new simulations (Mastropietro et al. 2005) show that transformations can also work in the outer, less dense parts of galaxy clusters. We therefore decided to discuss all possible mechanisms in this section although ram pressure stripping and galaxy harassment are probably not the predominant processes for morphological transformations in low-density environments, as suggested by Okamoto & Nagashima (2003).

The interaction with the ICM can cause, e.g., ram pressure stripping of the ISM (Gunn & Gott 1972; Roediger & Hensler 2004) or evaporation of the cold disk gas due to the ICM plasma (Fujita 2004). These processes lead to a stopping or "strangulation" of star formation (SF) in the disks and a truncation of the outer disk due to dying stars. This drives the spectral evolution from late to early

disks and a diminishing of the disk size and a bulge-dominated galaxy at the end of this transformation (Couch & Sharples 1987). In this framework, the MDR is a projection of the morphology-radius relation and a global effect of the ICM in the potential of galaxy clusters. However, it is difficult to hereby explain the formation of a bulge in a simple disk galaxy. In addition, the ICM is diluted at the borders of the cluster and in groups as well as low-density environments and are probably not responsible for this transformation (Lewis et al. 2002) because our objects prefer the more isolated regions.

Another mechanism is the merger scenario, which is a locally limited process. The main assumption is that small extragalactic objects merge together into larger ones and built up the galaxies in the nearby Universe (Steinmetz & Navarro 2002). The merging of disk galaxies would create spheroidal/elliptical galaxies from the destroyed disks (Toomre 1977; Steinmetz 2003; Athanassoula 2005a). Merger scenarios of bulge formation can simulate the MDR (Diaferio et al. 2001) and the deficit of intermediate disks in the older simulations (Okamoto & Nagashima 2001) can be improved by including minor merger and the following minor bursts in these simulations (Okamoto & Nagashima 2003). The merger scenario can explain the larger bulge sizes of galaxies in denser environments.

Morphological transformation can also explained within the harassment scenario. This scenario describes gravitational interaction of galaxies with other galaxies (local process) and the cluster potential (global process) with their tidal forces. The importance of tidal forces is firstly described by Pfleiderer & Siedentopf (1961) and Pfleiderer (1963). Moore et al. (1998, 1999) found that impulsive encounters are the process which turns disks in spheroidals in galaxy clusters and the process is stronger in denser regions. It was recently shown by Mastropietro et al. (2005) that it is possible to model the Hubble sequence from late-type disks to (dwarf) spheroidal systems using N-body simulations within a ΛCDM cluster with galaxy harassment and hierarchical growth. This simulation uses tidal shocks with dark matter substructures and the mean cluster potential to explain the morphological changes. In addition, these processes even work in the peripheral, less dense regions of the clusters. Strong tidal heating leads to mass loss and subsequently to rounder galaxies and smaller disks because of stripped and dynamically disintegrated stars.

In general, all of these theoretical models predict a strong influence on the morphology of disk galaxies in dense environments. In addition, these models are supported by direct observations of cluster in-falling galaxies, which show signatures of a combination of these discussed deformation scenarios (e.g., Cortés et al. 2005).

4.6.2 Secular Evolution and Pseudobulges

If a simple disk galaxy is isolated and external forces can not transform the disk, a bulge component can grow. This bulge is then called "pseudobulge" and has been formed from the disk and has subsequently similarities to that of the disk (Kormendy & Kennicutt 2004). The process that built up pseudobulges is internal, a secular evolution of the disk. In general, disk spreading leads to an outward flowing angular momentum and consequently to a lower energy state of the disk. In order to show this for disky and spheroidal systems, we generally follow the description given by Kormendy & Fisher (2005): "Galactic evolution is in transition from the early Universe dominated by hierarchical clustering to a future dominated by internal secular evolution." With this statement these authors describe the possible present and future evolution of disk galaxies. This could affect particularly the behavior of the slowly evolving, interaction-free disk galaxies from our Catalog.

If a system is supported by rotation its evolution is determined by its angular momentum transport. If the system is in equilibrium the angular momentum is constant and the total energy is minimized at a fixed angular momentum. The specific angular momentum in a ring with radius r and fixed potential $\Phi(r)$ is $L(r) = (r^3 \frac{d\Phi}{dr})^{\frac{1}{2}}$ and the same for the specific energy $E(r) = \frac{r}{2}\frac{d\Phi}{dr} + \Phi$. The deviation of the specific energy to the specific angular momentum gives the angular speed of rotation of the ring

$$\frac{dE}{dL} = \frac{d(\frac{r}{2}\frac{d\Phi}{dr} + \Phi)}{d((r^3 \frac{d\Phi}{dr})^{\frac{1}{2}})} = \Omega(r) \tag{4.8}$$

with

$$\Omega = (r^{-1}\frac{d\Phi}{dr})^{\frac{1}{2}} \tag{4.9}$$

If a mass unit at radius r_2 moves outward it gets angular momentum dL from a mass unit closer to the center ($r_1 < r_2$) and the disk spreads. This spreading lets the energy state of the disk decrease because the net change in energy, dE, is negative as a consequence that the angular speed of rotation decreases outwards due to differential rotation:

$$\begin{aligned} dE &= \Omega(r)dL && (4.10)\\ &= dE_1 + dE_2 && (4.11)\\ &= (-(\frac{dE}{dL})_1 + (\frac{dE}{dL})_2)dL && (4.12)\\ &= (-\Omega(r_1) + \Omega(r_2))dL && (4.13)\\ & && (4.14) \end{aligned}$$

The angular momentum flows outward and the disk spreads. This leads to a lower energy state, i.e., energy dissipation of the disk. Hence, disk galaxies tend to spread in two dimensions by angular momentum transport to larger radii in order to decrease their energy. Non-axissymmetric structures such as bars and oval disks support this process. The process is slow compared to the gravitational collapse and needs several billion years, therefore it is called secular evolution.

As already shown, spreading mass takes the angular momentum from inner disk radii and due to this loss of angular momentum, material shrinks towards the center. So, the disk will be rearranged. The consequences are that disk gas placed in an outer ring at ≈ 2.2 bar radii, also an additional inner ring at the ends of a bar and a dense central gas concentration occurs as shown in several simulations (for a discussion see Kormendy & Kennicutt 2004; Kormendy & Fisher 2005). The bar acts as an one-way highway for the infalling gas. The gas density can reach a high density and rapid star formation can occur in the rings and especially in the center. Various processes in the central star forming region can lead to a puff up of the disk stars and a bulgy component appears. These processes are, e.g., intrinsic velocity dispersion of the gas, disintegration of young star clusters, dynamical heating of the stars on molecular clouds (some of the processes are similar to the internal thick disk formation–see next Chapter–but on smaller scales) and many more like bar disintegration and bar thickening (for a discussion see Kormendy & Fisher 2005). The pseudobulges exhibit properties that still trace their disk origin. For edge-on galaxies, these are i) box shaped bulges; ii) nearly exponential surface brightness profiles; iii) young stars, gas and dust in the pseudobulge.

In contrast to disks, elliptical galaxies and star clusters–in general spheroidal systems–are supported by a high velocity dispersion. The specific heat is negative in these self gravitating systems with randomly moving particles. Such a system, in an equilibrium state has a radius r and consists out of N particles each with mass m and a three-dimensional velocity dispersion σ. The Virial theorem is $2W_k + W_p = 0$ with the kinetic energy $W_k = \frac{Nm\sigma^2}{2}$ and the potential energy $W_p = -\frac{G(Nm)^2}{r}$. We can write the virial theorem

$$2(\frac{Nm\sigma^2}{2}) + (-\frac{G(Nm)^2}{r}) = 0 \tag{4.15}$$

and see that an increase of σ with the numbers or mass have to increase or the radius has to decrease to keep the system in virial equilibrium.

Using the Virial theorem the total energy $E = W_k + W_p$ is negative:

$$\begin{aligned} E &= W_k + W_p && (4.16)\\ &= -W_k && (4.17)\\ &= -\frac{Nm\sigma^2}{2} && (4.18)\\ &= -N\frac{3}{2}kT && (4.19)\\ & && (4.20) \end{aligned}$$

because temperature T depends on the internal velocity $\frac{m\sigma^2}{2} = \frac{3}{2}kT$. k is the Boltzmann constant and the gravitational constant is G. The change of temperature with the change of the total energy is the specific heat C, which is negative:

$$C = \frac{dE}{dT} = \frac{d(-W_k)}{dT} \propto \frac{d(-\frac{Nm\sigma^2}{2})}{d(\sigma^2)} \tag{4.21}$$

This means that the system is supported by heat and subsequently any evolution depends on heat transport. If the system has a hotter center than the outer parts, the heat flows outwards, the center gets hotter and shrinks and the periphery cools and expands.

Chapter 5

Structure of Simple Disk Galaxies

5.1 Introduction

The Milky Way (MW)[1] is a typical disk galaxy. Therefore, the MW provides an ideal starting point to explore structural components of a disk galaxy. In broad outline, the MW consists out of two geometric and physical distinct components: a spheroid and a disk. These two main manifestations of appearance can be subdivided into two further components of the same general geometrical shape, the spheroidal halo and bulge and a thin and thick disk. The following studies are mainly dedicated to the disk components of nearly or absolutely bulgeless disk galaxies. However, in order to understand the holistic picture of disk galaxies we will shortly describe the main components of the MW from outside in and discuss their possible formation scenarios. This will be done in the next Paragraphs and we will follow in general the description by Buser (2000).

The most extended component is the halo. It is composed out of metal poor stars and globular clusters (GC), their age is comparable with the age of the Universe in the Standard model, ≈ 14 Gyrs. The density of the visible material like stars and interstellar medium (ISM), the so called baryonic matter, is very thin expressed by its low surface brightness. The stars in the halo have low rotation velocities but high velocities perpendicular to the Galactic midplane. The ratio of the ordered rotation v to the chaotic and highly eccentric movement σ of the stars and globular cluster has a small value. The velocity dispersion of the halo is therefore $\frac{V_{rot}}{\sigma} \ll 1$ which defines this components as dynamically hot.

With increasing baryonic density, the stars and some GC are compiled in a thick disk which may be nearly as old as the halo stars but the stars have intermediate metallicities (Reid & Majewski 1993; Chiba & Beers 2000). The thick disk (TD) is comparable to a central cut through the halo sphere which consists out of stars and some GC with much less random orbits but more common rotation around the center of the disk. This makes the thick disk dynamically colder than the halo but still allows the stars to travel up to one kpc away from the central plane (Chiba & Beers 2000). Therefore, its axial ratio between the major and minor axis is in the order of $\frac{a}{b} \approx 3 - 4$ (Gilmore & Reid 1983). Photometric studies of thick disk stars show that the stellar space density of the thick disk decreases exponentially in the radial direction from the Galactic center and vertically from the midplane (Buser et al. 1999).

Excursus Before we continue with the structure of the MW as a typical disk galaxy the importance of the exponential function should be discussed. This function is of great universality in astrophysics and many other sciences because many natural processes show the phenomenon of exponential growth or exponential decay. For instance, the vertical distribution of stars in many disk galaxies, i.e., the number density n decreases with distance $|z|$ above or below the midplane according to the Equation

[1] The other name of the Milky Way is "the Galaxy" with a capitalized "G", whereas extragalactical systems are called "galaxies."

$$n(z) = n_0 e^{\frac{-|z|}{h_z}} \tag{5.1}$$

h_z and n_0 are independent parameters which characterize the shape of the exponential function. In particular, h_z is the scale height of the disk, an important distance parameter that characterizes the thickness. The scale height is the distance where the number density decreases to $\frac{1}{e}$ times its number density in the midplane n_0; i.e., $\frac{n(h_z)}{n_0} = \frac{1}{e} \approx 0.37$. The scale height does not say where the disk ends because there is no border, but it indicates in a precise way the distance where the density has significantly decreased. Also the radial distribution of the MW and many other disk galaxies can be represented by exponential models (Pohlen & Trujillo 2006). However, the physical background of this global law of disk galaxies is not understood (van der Kruit & Searle 1981a). The scale height of thick disk stars in the MW, typically consisting of late-type stars of the spectral classes G and K is in the rage of 700 - 1300 pc (Jones & Lambourne 2004).

The thick disk encompasses the metal-rich thin disk. This is the component that the sun belongs to. The thin disk stars near the sun have similarly high rotation velocity (220 km s^{-1}) and move on nearly circular orbits around the Galactic center. Their average velocities perpendicular to the plane of rotation are low (20 km s^{-1}) and allow them only short periodic excursions above and below the midplane ($\pm$300 pc). Therefore, the thin disk is very flat with an axial ratio of 10 - 12. The scale height of the thin disk depends on the stellar type, i.e., main sequence stars of type G, K, M have $h_z \approx 300$ pc (the "old" thin disk), whereas the young stars (O, B) have an h_z of only 50 pc - 60 pc (Chen et al. 2001).

This observed variation reflects an age-scale height correlation in the disk. O, B stars are young while G, K, M stars span the whole range of that population (approximately 1-10 Gyrs). The older stars of the thin disk are likely found to be further away from the midplane than the more recently formed stars. This indicates an evolutionary process that operates in the disk in that sense that young stars are gradually scattered to greater heights by interactions with giant molecular clouds with masses up to $\approx 10^7 M_\odot$. These molecular gas clouds are part of the ISM and cause the disintegration. The major amount of the ISM is located in the thin disk and its scale height is larger than that of the young stars, about 150 pc. This suggests that stars can only be formed in regions of the highest densities of the ISM. The thin plane with the highest star formation rate (SFR) is the "extreme disk," a related subcomponent of the thin disk. Hence, the SFR (measured in solar masses, $M_\odot$ per year and volume) depends on the ISM density ρ in form of a power law: $SFR \propto \rho^n$, where n is a number >1.

The center of the MW as well as of many other disk galaxies is a spheroidal component again, the bulge. This component, where all other components as well have their highest spatial densities merged together, is very inhomogeneous distinguished by old age and high metallicities on average but also the largest individual ranges in each. The bulge is a dynamically warm system with large velocity dispersion. Beside the heterogeneous properties of the MW bulge, also the bulges in general are an inhomogeneous class in contrast to the other discussed components of the MW which generally appear to be similar in other observed disk galaxies. It is possible to distinguish "classical bulges" (like that from the MW) from "pseudobulges" with dynamically properties comparable to that of cold disk stars (see Sect. 4.6.2) and "peanut bulges" which are probably edge-on seen bars (Lütticke et al. 2000; Kormendy & Kennicutt 2004; Athanassoula 2005a).

An illustration of the above discussed components of the MW as a disk galaxy are shown in Fig. 5.1. This figure is a schematic edge-on view of the main components. The sun in the thin disk is indicated by a circle and the directions to the North (NGP) and South (SGP) Galactic Pole are indicated by arrows. Fig. 5.2 shows a closeup view of the MW's disk and halo components to the plane of the MW near the solar neighborhood. The space density distributions of the disk components and the halo are shown schematically (top) and analytically (bottom). The different exponential decrease of the density (ordinate ρ) with increasing vertical distance from the Galactic midplane (abscissa z) of the different disks is indicated. The vertical dashed lines show the scale heights of the thin disk

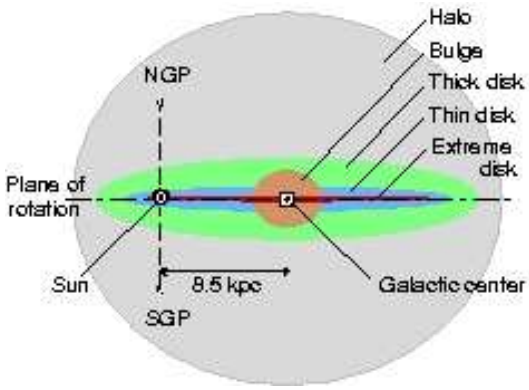

Figure 5.1: This figure is a schematic edge-on view of the main components of the Milky Way. The sun in the thin disk is indicated by a circle and the directions to the North (NGP) and South (SGP) Galactic Pole are indicated by arrows. The components are marked in this figure. By courtesy of R. Buser.

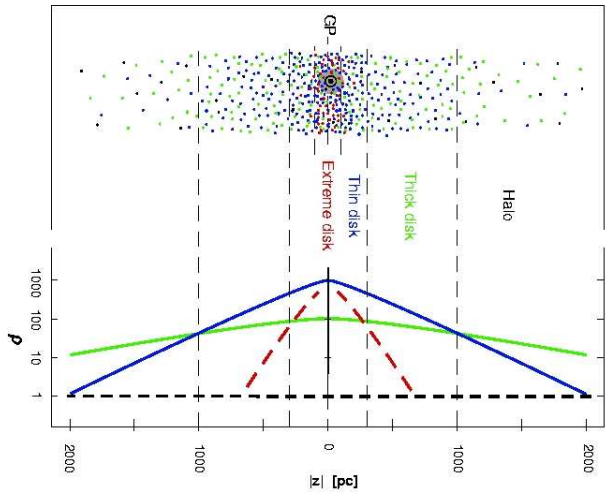

Figure 5.2: This figure shows an edge-on view of the MW's disk and halo components of the plane of the MW near the solar neighborhood. The space density distributions of the disk components and the halo are shown schematically (top) and analytically (bottom). The different exponential decrease of the density (ordinate ρ) with increasing vertical distance above and below from the midplane of the MW (abscissa z) of the different disks is drawn. The vertical dashed lines show the scale heights of the thin disk ($h_z = 300pc$) and the TD ($h_{zTD} = 1000pc$). By courtesy of R. Buser.

($h_z = 300pc$) and the TD (h_{zTD}). For 1000 thins disk stars at the solar neighborhood, only 100 TD and 1 halo star can be detected per unit volume. The Figs. 5.1, 5.2 and 5.3 were originally shown by Buser (2000) and drawn by D. Cerrito, by courtesy of R. Buser.

In the center of the MW a central star cluster surrounds a black hole (BH) (Genzel et al. 1997). The mass of this "energetic center" is enigmatically correlated with many other parameters (e.g., mass, velocity dispersion) of the bulge and the thin disk. The central BH is fueled by ISM transported via a bar from the disk to the center. This one-way Galactic gas pipeline is a disk component with similar properties as the disk (Kormendy & Kennicutt 2004).

Some astronomers believe that all the main components of the MW are correlated due to an observed large-scale metallicity gradient ranging from the halo to the disk. This is the spatial age-metallicity relation with observed mean metallicity, increasing with the increasing stellar density and flattening of the components (e.g., Henry & Worthey 1999). This correlation–among others–suggests

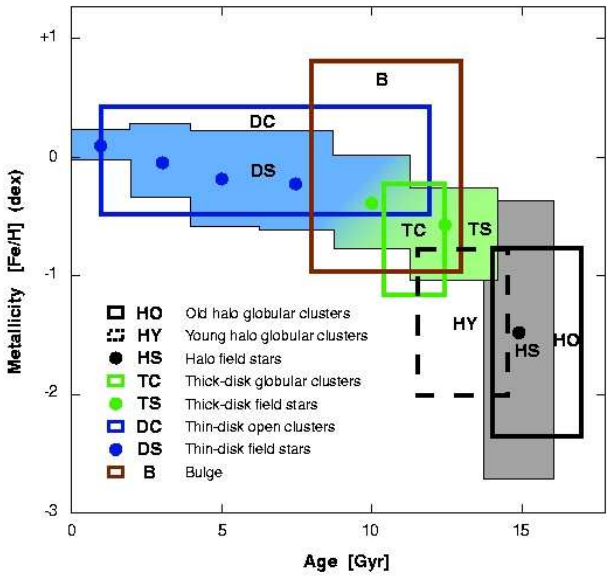

Figure 5.3: This figure shows the age-metallicity relation of the various components in the Milky Way. The different components are explained in the legend. This correlation of decreasing age of the stars with increasing metallicity from halo to the thin disk stars indicates an overall related evolution. Otherwise, the scatter of the halo field stars and particularly the bulge stars is very large and therefore are hints for unrelated origins. The sun is a thin disk field star with metallicity [Fe/H]= 0. By courtesy of R. Buser.

a global connection of the components and subsequently a common or nested formation process. The correlation between the age and the metallicity of the different disk galaxy components of the MW are shown in Fig. 5.3. The different components are explained in the legend.

The monolithic collapse scenario provides the theoretical framework where a rotating spherical cloud of metal-poor gas contracts toward its center of gravity (Eggen et al. 1962). With increasing collapse the rotation increases and with that the coupled dissipation due to the conservation of initial angular momentum leads the cloud to contracts anisotropically along the rotation axis. Energy dissipation means the loss of internal energy and/or pressure of a gas cloud due to collisions of the particles and the subsequent radiation of the lost kinetic energy. Then the potential energy dominates the particle and it falls to the gravitational center. At a certain point, the centrifugal energy and the potential energy of the rotating and contradicting cloud perpendicular to its rotation axis is in equilibrium. The cloud falls into flatter shapes until the central concentration is surrounded by a fast spinning disk of gas in rotational equilibrium. The stars and star clusters were formed in this disk and gradually enrich the remaining gas with metals from supernovae. Because stars and clusters are dissipationless they conserve their initial metallicity and velocity at the time of their birth and reflect (including their large scale structural components like spatial, chemical and kinematic properties) the major phases of the formation and evolution of the Galaxy. This scenario is then improved and some changes where made (e.g., Sandage & Fouts 1987) but the general idea of a collapsing gas cloud driven by its angular momentum in a single process remains.

With the increase of better observing technologies it was found that the MW is a very complex system interacting with its environment. In the solar neighborhood as well as high above the disks populations of stars have been found whose kinematic and chemical properties are very different from the general characteristics of the global components (Eggen 1977; Aguilar et al. 1988; Majewski 1994). This is due to the accretion of satellite galaxies and fragments into the halo of the Galaxy. Such minor merger processes are representing a continuing fate since early in MW's formation (Searle & Zinn 1978; Samland 2004). This formation and evolution scenario is called the "hierarchical clustering/growth" of galaxies.

5.1.1 Thick Disk

One of the first hints for a Galactic TD was found in the Basle Halo Program (Becker 1965), a three-color star count survey perpendicular to the MW's disk in order to reveal the stellar space density structure. A bimodality of the stellar population distribution was found: A disk of of metal-rich stars and a population of lower metallicity with a flattened ($a/b \approx 1.6$) density distribution which surrounds a thin disk (Becker 1972, 1980). This thick disk between the thin disk and the halo was also proposed as the result of a similar survey some years later by Gilmore & Reid (1983). The confirmation of the Galactic TD component was performed by fitting multi-component models with a second disk, the TD, to the measured stellar space densities of the stars in the Basle Halo Program (Fenkart 1989, and references therein).

Already before the TD in the MW was evident, extragalactic TDs were found (Burstein 1979; Tsikoudi 1979; van der Kruit & Searle 1981a,b). Burstein (1979) found an excess of light using vertical surface brightness distributions of edge-on S0 galaxies dominating that of the old (thin) disk at a height of several kpc which could not explained by the normal disk or a bulge with uniform axial ratios. This is the TD, however, Burstein claims that most spirals do not show this TD. Freeman (1978) explained the bulge and the disk to be approximately isothermal and subsequently Freeman (1980) suggested that the TD is the response of the spheroidal component of the gravitational field of the flattened disk, i.e., a deformed bulge component. After Burstein's discovery, further TD were observed with the aid of vertical surface brightness photometry also in galaxies that are seemingly bulgeless (van der Kruit & Searle 1981a). These and other observations of TD show that TD are a common component in disk galaxies and are a distinct component between the old thin disk and the halo.

Beside the question about the general meaning of the TD for the whole disk+spheroidal galaxy system, the question about the nature of the TD is important to understand the holistic picture of a

galaxy. Is the TD is an intrinsic property of a disk galaxy or is its formation explained by external influences?

The stellar density of the Galactic TD decreases exponentially radially from the Galactic center and perpendicularly to the midplane of the MW (e.g., Buser et al. 1999). The TD's scale height h_z for typically late-type stars of the spectral classes G and K is in the range of 700 - 1300 pc (Buser et al. 1999; Kerber et al. 2001; Larsen & Humphreys 2003; Jones & Lambourne 2004) or even lower (600 pc) (Chen et al. 2001) and has the vertical velocity dispersion σ_v of the TD stars of $\approx 35 \pm 3$ km s^{-1} (Freeman 1987; Chiba & Beers 2000). The mean rotation velocity $v_{rot} \approx 170$ km s^{-1} (Ojha et al. 1994). Similar to the thin disk, the properties of the TD also depend on the stellar type that is being analyzed. A study with the velocity data of a large number of metal poor stars (Beers & Sommer-Larsen 1995) show a higher mean $v_{rot} \approx 190$ km s^{-1}, $\sigma_v \approx 40$ km s^{-1} and $h_z = 1000$ pc for intermediate-metallicity TD stars.

Compared to the thin disk, the TD has lower metallicities and older ages on average and–as seen before–a larger scale height and velocity dispersion. Several studies were performed in order to analyze if the trends of these properties are continuous from the thin to the TD or clear breaks whether are seen. A continuum between thin and TD would suggest an internal origin whereas distinct properties propagate an independent build up of the components.

The vertical velocity dispersion for solar metallicity stars and below (down to Fe/H = -0.5) is smoothly rising from 15 km s^{-1} to $\leq$ 30 km s^{-1}. Then a sudden increase of $\sigma_v = 40$ km s^{-1} for low metallicity stars (Fe/H ≤ -0.6) is seen (Carney 2001). This is an example to show the difficulty to understand the TD origin. The continuum between metallicity and σ_v until a certain value can be explained be dynamical heating of the evolving thin disk (Wielen 1977) but the sudden break at lower metallicities suggests a merger origin of the TD because we observe two kinematical distinct disk components (Wyse & Gilmore 1995). Also several other studies were concentrated on the the behavior of metallicities and kinematics of the disk stars. Analyzing the ages with different discriminators, the mean ages (11 to 12 Gyr) of the thin and TD are indistinguishable (Wood et al. 1995; Carney 2001). This is in contrast to the apparent large differences between the chemical and kinematical properties of the thin and TD. In addition, the non-detection of significant gradients in kinematics and metallicities of the TD stars attenuate the intrinsic correlation between the two disk components.

Accretion of satellite galaxies at early days into the still gaseous disk shows in numerical simulations that the disk is heated and a TD is formed out of the accreted debris (Quinn et al. 1993). After such minor merging events the gas falls back to rebuild the thin disk (Freeman 1996). Another model for the TD of the MW is shown by Gilmore (1995). His model proposes that the MW is formed out of two distinct pairs of nearly indistinguishable pairs of distributions of the specific angular momentum. The metal-poor halo and metal-rich bulge is a low angular momentum pair and the thin and TD is a pair with high angular momentum. These intrinsic formation components evolved subsequently in parallel but independent ways. On the one hand, the angular momentum material formed the halo with later concentration of the enriched debris into the bulge similar to the model by Eggen et al. (1962). On the other hand, the high angular momentum material formed the thin disk which was later thickened by major mergers long time ago ($\approx$ 10 Gyr) or formed a TD with the remaining gas settling into a thin disk component later on.

5.1.2 Thick Disks in Late-Type Disk Galaxies

The first observations of TD in late-type galaxies was published by van der Kruit & Searle (1981a): The vertical surface brightness profile of NGC 5907, an edge-on bulgeless galaxy, shows an small light excess comparable to that of a TD. Dalcanton & Bernstein (2000) started a large investigation to study TD in late-type spirals. They observed 49 FGC galaxies in the optical and infrared. They further analyzed these galaxies and 2002, Dalcanton & Bernstein presented the optical ($B-R$) and optical-infrared ($R-K_s$) colormaps of their sample. Most of the colormaps show a color gradient vertical to the midplane with redder colors at larger distances. This red envelope is rounder and thicker than the thin disk ($a/b_{envelope} \approx 4, a/b_{thin} \geq 8$). Using simple stellar synthesis models by Bruzual & Charlot (2003), Dalcanton & Bernstein (2002) found that the color of the envelope is similar in each object

and corresponds to an old stellar population ($\geq$ 6 Gyr) with intermediate metallicities (Fe/H < -1). Therefore they conclude that the red envelope is a TD with comparable properties to that of the MW. The age difference between the thin and TD is larger for low-mass objects.

Dalcanton & Bernstein (2002) outlined a possible scenario of TD formation with their observations. In this scenario, a disk galaxy is formed via monolithic dissipative collapse. After a phase of only smooth accretion of material a major merger with an equal mass partner leads to the heating of the TD but does not necessarily produce a bulge as expected. The merger also leads to a high SF from gas accreted after this major merger. The following evolution of the disks is quiet and calm without any further major merger. In general, they favor the model where the age of the TD marks the end of an ancient major merging epoch. However, the TD found by Dalcanton & Bernstein (2002) may resemble the high-luminosity end of the halo stellar population found in the stacked SDSS images of thousands of edge-on galaxies and an edge-on galaxy from the Hubble-Deep Field (Zibetti & Ferguson 2004; Zibetti et al. 2004).

Yoachim & Dalcanton (2005) found large differences in the kinematics of the thin and TD components of their two observed flat galaxies. In one case they detected a counter rotation of the two disks and in the other a slower rotating TD, suggesting that only direct accretion of TD stars from infalling satellites can explain their observation in at least these two galaxies. However, this is in contrast to the before proclaimed scenario and their results should be handled with care because the observations have only a low signal-to-noise ratio.

In another paper, Yoachim & Dalcanton (2006) present optical R band surface photometry of 34 flat galaxies fitted with double-exponential profiles. They detected TD with scale heights (h_{zTD}) that are 2 to 4 times larger than the thin disk h_z (mean $h_{zTD}/h_z = 2.5$, median $h_{zTD}/h_z = 2.35$). The physical sizes of the TD are found to be 325pc $\leq h_{zTD} \leq$ 2000pc (mean: 700pc) and that of the thin disk are 100pc $\leq h_z \leq$ 1000pc (mean: 305pc) if $z_0 = 2h_z$ is assumed. Yoachim & Dalcanton (2006) also found on average 1.25 larger scale lengths for the TD compared to the thin disk. In addition, in lower mass galaxies the TD is the dominant component in both the stellar luminosity and mass. For higher mass objects the TD is a minor component and comparable to the MW TD. With these results, the authors consider a hierarchical galaxy formation scenario in which "galaxies form from a series of mergers in which subunits deposit both stars and gas." The stars built up the TD and the gas cools and settles into a thin disk. The subunits that formed the low-mass galaxies are star rich due to supernova induced gas blowout.

These recent studies speculate that formation scenarios in which thick disks forms purely by monolithic collapse or steady heating of the thin disk can be ruled out and strongly favor accretion/merger models. New chemo-dynamical (N-body/SPH) simulations of galaxy formation in a CDM Universe form thick disk stars from gas that is accreted from gas-rich building blocks in an ancient merger period and the thin disk stars form later (Brook et al. 2004, 2005). The simulated disk settles down quickly and does not evolve, conserves the thickness but grows radially since redshift $z \sim 1$ because of the absence of major mergers (Brook et al. 2006).

Another external driven process is that TD stars are formed during star formation from gas at large scale heights (Kroupa 2002). Also accretion of gas clouds and subsequent vigorous star formation can be responsible for vertical puff up of disks (Burkert et al. 1992; Samland & Gerhard 2003; Brook et al. 2006). In principle, thick disks need not form via mergers: The main internal process is vertical heating of a thin disk by dynamical scattering (e.g., Chen et al. 2001) or alternatively thick disk stars may form in massive, quickly dissolving stellar clusters (Kroupa 2002).

5.1.3 Predictions by the Models

TD formed via mergers are heated by the merger and hence "frozen" in age at the time of the merger event (Brook et al. 2006), i.e., fixed scale heights. On average, galactic disks affected by interactions or minor mergers with a mass ratio between the merging satellite and the disk of about 0.1 have ~ 1.5 times larger scale heights than seemingly unperturbed disks (Schwarzkopf & Dettmar 2000a,b). These authors observed maximum values for the galactic disk scale heights of 200pc $\leq h_z \leq$ 400pc for the unperturbed and 600pc $\leq h_z \leq$ 800pc (medium: 750pc) for the galaxies with signs of interaction.

The ratio of the scale length to scale height is ≈1.7 times larger for non-interacting galaxies, i.e., they are ≥ 50% thinner and have a ≈1.12 times redder vertical color gradient. Studies that include also equal mass mergers found 2-4 times larger scale heights for interacting galaxies (Reshetnikov & Combes 1997). However, Schwarzkopf & Dettmar (2000b) do not separate the thin and TD. Hence, their lager scale heights for interacting galaxies may resemble the existence of a TD. If merging takes place between similar mass partners, the heating could lead to much thicker disks. In the merger model, the mass of the thick disk is only determined by the initial disk mass prior to the merger event. Differences in stellar populations (i.e., colors) would be hints of external influences, whose time scales vary randomly.

The steady vertical heating of, e.g., molecular clouds in the thin disk would predict a smooth and continuous correlation between the properties (scale height, shape of the isophotes, colors) of the thin and TD in contrast to a TD caused by a sudden merging event.

If SF—whether or not induced by internal instabilities or external perturbations—is responsible for TD formation the scale height of the disk will then depend on the SF activity, which is expected to decrease with time as the Universe expands and the density around the forming galaxy decreases. Very intense SF will also lead to the formation of a bulge or a dense nucleus, aided by the rapidity of gas infall and the total amount of accreted material (either through infall or mergers) (Noguchi 2000). The low-level star formation in present-day galaxies is fed by slow accretion and results in young thin disks, but the older thick disks of these galaxies may show a considerable age spread depending on the accretion history. In this scenario, one would expect all galaxies to have thick disks unless the infall and subsequent star formation proceeded so slowly that only thin disks formed.

5.1.4 Motivation

Exploring the relations between different galactic components in different types of galaxies is a primary goal of this study. TD seem to be ubiquitous based on results of previous near-infrared surveys, but since our study will reach fainter limiting magnitudes than the preceding studies we will not only be able to get more accurate structural parameters but expect to be able to also distinguish between genuine thick disks and mere flaring of outer thin disks. In addition, we should be able for the first time to create surface brightness profiles in the infrared for simple disk galaxies and compare them with disk models. An ancillary benefit is the possibility of detecting small bulges or bars in K-band that are not seen in the optical data (e.g., due to the presence of dust; see also Dalcanton & Bernstein 2002). The combination with optical colors, which reach comparatively deep surface brightness limits, will allow us to show color gradients in the disks.

Our proposed observations will yield:

(1) Detailed morphology and structural parameters of the disks in different types of spirals.

(2) If pure thin disks are detected: A strong argument against the sole validity of merger models, since pure thin disks would form solely through slow infall.

(3) If thick disks are ubiquitous, then thick and thin disks represent fundamental components of disk formation.

5.2 Target Selection

Here we are initiating a deep K_s-band study of 15 SDSS-selected isolated edge-on galaxies comprising objects with bulges, bars, and dominantly pure disk galaxies with moderate axis ratios to large ratios. We are constraining our sample mostly to flat galaxies, but we include also comparison objects of the other classes since we want to compare their properties with the full range of edge-on spirals. For all of our targets we have homogeneous optical SDSS *ugriz* data, which reach surface brightnesses of $\sim$ 25 mag arcsec^2 in the *gri* filters (see, e.g., Kniazev et al. 2004a). We therefore selected galaxies of the main morphological classes from the Catalog. In addition, the galaxies should be bright and extended in order to observe them in an acceptable amount of time. They also should have spectral

information about their redshift in order to derive their distances. Our deep K_s imaging is designed to uncover thick disks where present and to reveal their morphologies and structural parameters.

The K-band is an ideal way to trace the stellar mass distribution in spiral galaxies. Rix & Rieke (1993) showed in a detailed photometric study that the K band at 2.2 μm is relatively unaffected by dust and young, luminous red stars. Therefore, the K band is a good indicator for the massive, older disk star population which is the dominant contributor to the stellar mass function of disk galaxies. The role of dust is shown in the Fig. 5.4 for an observed galaxy of this program, where this galaxy is shown in the optical r filter and the near infrared filter K_s. A dominant dust lane is visible in the optical r band at the right side. The K_s image on the left side is almost "dust free." Moreover, the K-band luminosity of galaxies is 5 to 10 times less sensitive for dust and stellar population effects than the optical wavelength luminosities (Bell & de Jong 2001). Therefore, the K-band is an ideal

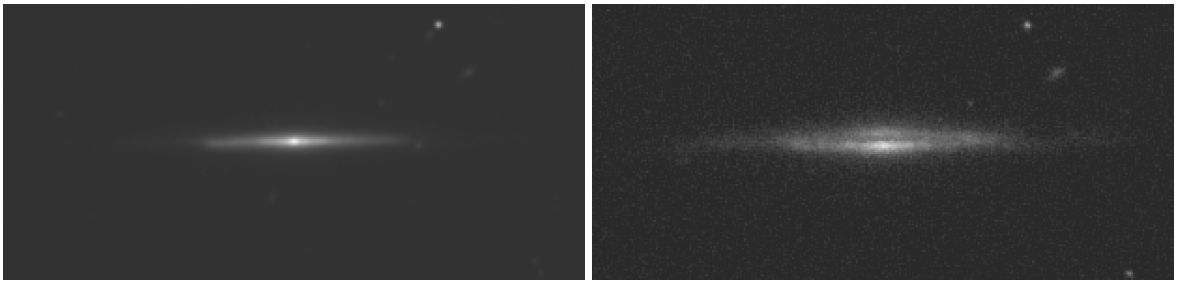

Figure 5.4: The contours of the of 3D in the K_s (left) and r(right) band. The scale is 122" $\times$57".

tracer for this purpose due to its insensitivity to dust and due to its sensitivity to the light of older populations (Westera et al. 2002). In particular, K-band imaging permits us to observe *both* the thin and thick disk as well as nuclear components fairly unimpeded by dust. Hence K-band data will allow us to measure the disk components and morphology on the same uniform basis.

The sample galaxies are selected from the Catalog. In general, the selection process was subjective and random. But selection of the targets should fit to some guidelines. The targets should be observable with the New Technology Telescope (NTT, see Fig. 5.5) at the European Southern Observatory (ESO) in La Silla, Chile. This telescope has a primary mirror diameter of 3.58m and an Alt-Az Richey-Chretien mounting. The NTT works since 1989 and pioneered the use of active optics. Its geographical coordinates are: Latitude 29° 15' south and Longitude 70° 44' west at a height of 2400 m.

The instrument Son OF Isaac (SOFI) of NTT is perfectly suited for our investigation. A medium-sized telescope with a sensitive infrared detector whose field of view exceeds the major axis of our targets by a factor of at least 5 while providing a pixel scale of 0.288 arcsec/pixel affords both sufficient resolution and a sufficiently large area for sky subtraction. We applied for observing time at ESO in Period 74 with a preferred observation date in November 2004. Therefore the targets are selected to be close to their upper culmination at this proposed place and time.

Figure 5.5: The NTT dome on the right side and a view towards other telescopes at La Silla.

Table 5.1: Selected Galaxies

SDSS Name	Prog. ID	RA	DEC	Class	a(r)	a/b(r)	z	z err	Other Names
SDSS J005315.44-084416.4	3A	00 53 15.442	-08 44 16.472	Sd(f)	49.572	6.679	0.0524471	1.00049E-4	FGC 103, RFGC 204, 2MFGC 641
SDSS J005624.60-010834.7	1A	00 56 24.610	-01 08 34.78	Sd(f)	49.795	4.306	0.0431201	7.0827E-5	PGC 3360, 2MFGC 682
SDSS J011904.42-000818.7	1B	01 19 04.430	-00 08 18.758	Sd(f)	104.654	8.107	0.0175206	6.19951E-5	FGC 149, RFGC 296, UGC 847, 2MFGC 989
SDSS J012302.78-091745.7	3B m	01 23 02.787	-09 17 45.708	Sd(f)	41.314	4.812	0.0352799	1.15575E-4	
SDSS J012731.32-102347.1	3C	01 27 31.325	-10 23 47.146	Sd(f)	46.059	6.461	0.0234098	6.8046E-5	FGC 169, RFGC 327
SDSS J013551.83-095646.5	2B	01 35 51.837	-09 56 46.538	Sd(f)	69.918	6.731	0.0195466	4.99333E-5	FGC 176, RFGC 345, 2MFGC 1214
SDSS J014102.09-092022.6	1C m	01 41 02.100	-09 20 22.631	Sd(f)	65.704	5.892	0.0181324	5.36589E-5	FGC 186, RFGC 365, 2MFGC 1271
SDSS J031136.44-003341.6	2C	03 11 36.442	-00 33 41.685	Sb(f)	37.132	4.263	0.0233224	5.93929E-5	FGC 393, RFGC 673
SDSS J031144.77+010241.4	1D	03 11 44.779	+01 02 41.417	Sd(f)	40.965	5.281	0.0254392	6.76783E-5	FGC 395, RFGC 676, UGC 2584, 2MFGC 2610
SDSS J031513.32-071614.6	3D m	03 15 13.327	-07 16 14.673	Sd(f)	81.068	4.993	0.0313751	8.97839E-5	FGC 402, RFGC 687, 2MFGC 2660
SDSS J031538.62-070443.8	2D	03 15 38.629	-07 04 43.814	Scd(f)	66.558	3.803	0.0132271	5.07879E-5	PGC 12112, 2MFGC
SDSS J033923.33-053631.2	3E-altern8 m	03 39 23.331	-05 36 31.276	Sd(f)	40.032	4.221	0.0357004	4.90648E-5	2MFGC 3032
SDSS J092353.77+014912.1	2E m	09 23 53.773	+01 49 12.191	Sd(f)	32.773	7.135	0.0564392	5.5036E-5	
SDSS J093008.57-003809.4	1E	09 30 08.575	-00 38 09.499	Sd(f)	61.171	6.481	0.0707581	1.0904E-4	2MFGC
SDSS J094801.01+020111.2	3E m	09 48 01.018	+02 01 11.262	Sd(f)	59.239	5.474	0.0356205	1.10665E-4	RFGC1635, 2MFGC 7595
SDSS J095849.83+005012.1	2E-altern8 m	09 58 49.839	+00 50 12.183	Sd(f)	66.386	6.659	0.0127472	6.27799E-5	

The selected sample is listed in Table 5.1. This table contains the object name from the Catalog in Col. (1), i.e., the name in the SDSS nomenclature, which is consistent with the IAU nomenclature requirements. The program identity code is shown in the second Col. The short name indicates the target as marked in our observing run. If another edge-on galaxy is observed in the same field then the flag "m" is given. These are galaxies that were not originally selected as targets because they are not listed in our catalog since they do not fulfill the catalog selection criteria. The following two Cols. (3) - (6) contain the coordinates of the galaxies, i.e., right ascension and declination for the epoch J2000. Column (7) indicates the general morphological class (simple disks: Sd(f); intermediate types: Scd(f) and galaxies with bulge: Sb(f)). The angular diameter in the r band in arcsec is presented in Col. (8). The axial ratios in the r band is derived from the ratio of $isoA/isoB$ of the SDSS parameters and is listed in Col. (9). The value of the spectroscopic redshift `z` and its uncertainty are available from the SDSS database, these measurements were listed in Cols. (10) and (11). Other galaxy names and notes are given in the last Col. (12), these are the names from the "Flat Galaxy Catalogue" (FGC, Karachentsev et al. 1993) and from its extension, the "Revised Flat Galaxy Catalogue" by Karachentsev et al. (RFGC, 1999) or the Uppsala General Catalogue of Galaxies (UGC, Nilson 1973) and "Principal Galaxies Catalogue" (PGC, Paturel 1989).

This sample is useful to study the structural properties of especially simple disk galaxies but it is not a statistical sample in order to establish general properties of late-type disk galaxies. The observed galaxies from this Table are presented in the Appendix D.

5.3 Observation and Data Reduction

As described above, the observations were made with the NTT equipped with SOFI. SOFI is equipped with a 1024×1024 Hawaii HgCdTe manufactured by Rockwell Scientific. This CCD chip has a pixel size of 18.5μm, with a large field view of 4'.9×4'.9 and a resolution of 0.288 arcsec/pixel. We used the filter wheel locked at the K_s ("K short") and J filter. This K_s (J) filter has a central wavelength of 2.162μm (1.247μm) and a width of 0.275μm (0.290μm). The K_s and J band are usually denoted as the near infrared ("NIR") wavelength region. The properties of the J, the K_s and a comparison with other K filters are described by Persson et al. (1998). The advantage of the K_s filter compared to the other K filter is that K_s avoids both the atmospheric absorption line at 1.9μm and the thermal background radiation beyond 2.3μm.

Observations were performed during one run with the program ID 074.B-0743(A) in visitor mode, i.e., the presence of the observer during the run at the telescope. The advantage of the visitor mode is that it is possible to perform real-time tuning of the exposure time depending on external influences such as seeing, humidity and clouds in order to ensure maximum flexibility. The observing nights were the nights 17-18, 18-19 and 19-20 November 2004. The observing conditions during these nights were as follows: A thunderstorm took place on the neighbor mountain at the evening before the first night, therefore the night had less photometric quality; the second and the third night had very good seeing conditions although the last night was a little bit windy.

5.3.1 Observing in the Near Infrared

It is a difficult and complex task to observe in the infrared (IR) wavelength region. This is because the sky background in the IR is bright and affected by strong absorption from 1μm to 2.5μm. At wavelengths below 2.3 μm the sky background is glowing due to non-thermal emission from the aurora, OH and O_2. The OH is generated in reactions between H and O_3 in the high atmosphere at an altitude of about 87 km. The hydroxide radical (OH) acts as a cleaning agent in the troposphere of the earth because it reacts with many pollutants. Therefore this radical molecule is highly reactive and short lived. The emission of the vibrational excited OH lines are strongest after sunset and low around midnight, their variations are on a scale of minutes together with diurnal variations.

At wavelengths longer than 2.3μm the background light is emitted by both the telescope and the sky. This emission is a function of temperature and therefore related to the seasons and the daytime.

Table 5.2: A SOFI SOFI_img_obs_AutoJitterArray Template

Parameter Signature	Value	Description
DET.Exp Name	2E	Exposure name
DET.DIT	15	Detector integration time (sec)
DET.NDIT	8	Number of DITS
DET.NX	1024	Number of columns
DET.NY	1024	Number of rows
DET.STARTX	1	First column of window
DET.STARTY	1	First rows of window
SEQ.NJITT	1	Number of exposures in the array
SEQ.NEXPO	38	Number of jittered exposures around each array
SEQ.JITTER.WIDTH	15	Jitter bow width (arcsec)
INS.FILT1.ID	K_s	Filterwheel 1
INS.FILT2.ID	open	Filterwheel 2
INS.IMODE	LARGE_FIELD_IMAGING	Instrument mode
SEQ.COMBINED.OFSET	F	Combined offset
SEQ.RETURN	T	Return to origin
SEQ.OFFSETALPHA.LIST	0 120 0 -120	RA offsets list (arcsec)
SEQ.OFFSETDELTA.LIST	-120 0 120 0	DEC offsets list (arcsec)

Additionally, it depends on the cleanliness of the primary mirror. These effects are less important for the observations with the K_s filter. Water vapor and carbon dioxide gas in the atmosphere cause many time varying absorption features, related especially to the humidity. These features are that strong that the atmosphere is completely opaque between the NIR filters J, H and K_s.

It is not difficult to imagine that an extragalactical object could be thousands of times fainter than the nightsky because of the air glow. For this reason, observing in the NIR is complicated and complex. In general, a source is observed and then a nearby region of the sky is subtracted from this source. The changing between the sky and target observations should be done very frequently in order to avoid variations of the sky conditions. ESO provides automated templates that are used to control SOFI and the telescope. One template for extended objects is to image the sky and target separately, this is generally called "chopping." We instead decided to observe in the "nodding" mode with "dithering". This means that on every exposure both the sky and the object are visible at the same time (nodding) on the array chip, but the target is shifted around the four arrays of the chip (dithering) to minimize effects of bad pixels and other unevenness of the chip.

Because of the flat geometry of our target objects we used the provided template "SOFI_img_obs_AutoJitterArray." This template shifts the telescope between the exposures according to a list of offsets which are relative to the previous position and are given in RA and DEC in arcsec. Then it jitters randomly around each of the defined positions. The parameters of the template are shown in Table 5.2. The parameters for the individual target objects can be consulted in the header of the exposures. In this template there are 38 exposures in total with an integration time of 15×8 sec for each exposure. Here, the Detector Integration Time (DIT) of 8 sec is the period during which the signal is integrated on the receiver diodes and NDIT of 15 is the number of detector integrations that are obtained and averaged together. These averaged frames with an integration time of DIT×NDIT represent the raw data. The exposures offset between the four quadrants of the array where they shift randomly in a square box of 15"×15" centered on the object. At the end of the template the telescope returns to the original position. The total integration time is 4560 sec (76 min) in this case (DIT×NDIT×NEXPO).

The parameters in Table 5.2 vary slightly between our different targets. The smaller objects like the example in Table 5.2 were shifted on four quadrants in the array (with offsets of 150 or 120 arcsec), these are the so called four-point observations. Extended targets were moved on two positions, these objects are SDSS J011904.42-000818.7, SDSS J014102.09-092022.6 and SDSS J031513.32-071614.6. The choice of the appropriate DIT value depends on the intensity of both the target and the background. In order to avoid saturated objects the DIT must be short but long enough to maximize the signal-to-noise

ratio (S/N). Then the NDIT value depends on the frequency of the offsetting. The DIT and NDIT for our targets is shown in Table 5.3. After editing the templates these were collected in Observation Blocks (OB) at the telescope. The OB contain all the information necessary to obtain the observation and were executed at the control center of NTT during the observing run. Table 5.3 lists the date of the observation of the first (of NEXP) exposure of the target as given in the provided "Product ID" which identifies the exposure by ESO. Also the filter and the total integration time of the targets from Table 5.1 are shown in Table 5.3.

Table 5.3: Properties of the Observations

SDSS Name	Prog. ID	Starting Date	Filter	DIT	NDIT	NEXP	Exp Time (min)
SDSS J005315.44-084416.4	3A	04-11-20/00:03:03.577	K_s	15	8	38	76
SDSS J005624.60-010834.7	1A	04-11-19/00:13:08.446	K_s	15	8	38	76
SDSS J011904.42-000818.7	1B	04-11-18/00:43:13.661	K_s	15	8	38	76
SDSS J012302.78-091745.7	3B	04-11-20/01:35:36.174	K_s	15	8	38	76
SDSS J012731.32-102347.1	3C	04-11-20/03:22:32.502	K_s	15	8	38	76
SDSS J013551.83-095646.5	2B	04-11-19/01:44:03.036	K_s	15	8	38	76
SDSS J014102.09-092022.6	1C	04-11-18/02:24:00.725	K_s	10	12	38	76
SDSS J031136.44-003341.6	2C	04-11-19/03:24:26.276	K_s	15	8	38	76
SDSS J031144.77+010241.4	1D	04-11-18/04:00:25.716	K_s	15	8	37	74
SDSS J031513.32-071614.6	3D	04-11-20/04:54:05.799	K_s	15	8	38	76
SDSS J031538.62-070443.8	2D	04-11-19/04:55:49.716	K_s	15	8	38	76
SDSS J031538.62-070443.8	2Dj	04-11-19/06:24:55.773	J	45	8	5	30
SDSS J033923.33-053631.2	3E-altern8	04-11-20/06:29:08.380	K_s	15	8	38	76
SDSS J092353.77+014912.1	2E	04-11-18/07:19:44.004	K_s	15	8	38	76
SDSS J093008.57-003809.4	1E	04-11-18/05:45:45.952	K_s	15	8	36	72
SDSS J094801.01+020111.2	3E	04-11-20/08:09:50.105	K_s	15	8	21	42
SDSS J095849.83+005012.1	2E-altern8	04-11-19/07:10:28.233	K_s	15	8	38	76
SDSS J095849.83+005012.1	2E-altern8j	04-11-19/08:38:41.299	J	45	6	4	18

5.3.2 Data Reduction

Dark

Dark frames in the IR are exposures without direct illumination of the array and the same integration DIT time as a science frame. These frames exhibit a complicated structure of combined signals which depend non-linearly on time. The components of these signals are: the shading component which depends on DIT and incident flux; the amplifier glow which is the heat from the readout amplifier. This heat depends on the number of reads during the dark current and it is linearly related with time; the dark current of randomly generated electron/hole pairs.

We collected dark frames from the ESO archive[2] which were obtained on dates as close as possible to our observing run. This is possible because darks appear to be stable over the period of observing runs. All available darks of the same DIT were combined with their median values. These new "masterdarks" were then subtracted from every individual science exposure with the same DIT.

No dark was offered for a DIT=45 sec, the typical DIT for our J band exposures. We had to create this dark artificially from the other masterdarks. For this task we measured the median flux in a certain region of the given masterdarks. The median of the fluxes for these masterdarks decrease linearly at DIT $>$ 15sec as shown in Fig. 5.6. Because of this it is possible to interpolate the masterdarks with the DIT=20sec and DIT=30sec to built up the masterdark with a DIT of 45sec.

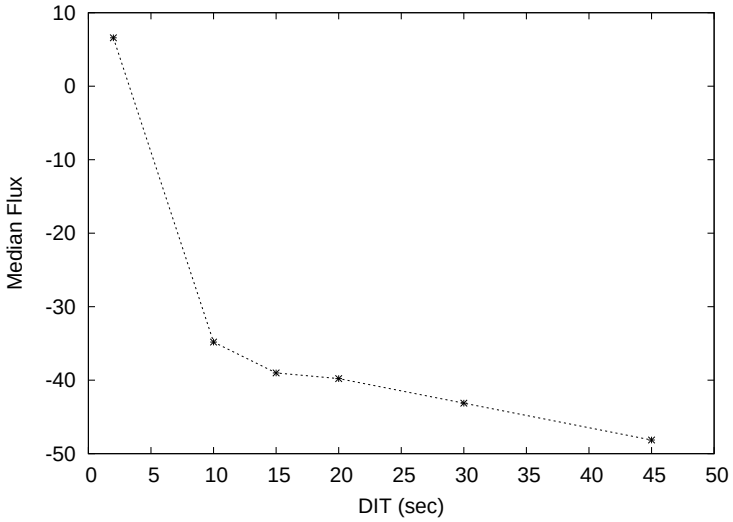

Figure 5.6: This figure shows the median of the fluxes of the dark frames at different DIT. The flux is nearly linearly decreasing at the exposures with DIT below 10sec.

According to the description in the SOFI User's Manual (Issue 1.6) the subtraction of darks brings possibly no real advantage. This is because the dark frame is only a poor approximation of the underlying bias pattern for broad band images, where the mean flux level is high. The sky subtraction would remove offsets due to fixed electronic patterns (bias) and dark current. However, we decided to follow the strategy of subtracting the darks because it is still not clear if a dark frame can be generated from science frames or whether dark frames should be created individually.

Flat Field

Flat field frames are created in order to correct the science frames for differences in the sensitivity of the pixels in the detector chip. Various methods are possible to obtain a flat field, such as observing the sky during twilight. Here we instead decided to use the dome flats because they better represent

[2]http://archive.eso.org/

the low frequency variations on the detector. They are created by imaging an illuminated and an unilluminated dome panel. The differences of the two are used to create the flat field frame. In order to correct also the effect of shading we take frames with a mask partially obscuring the frame and both the illumination on and off. Shading is a function of incident flux and therefore different for the unilluminated/illuminated exposures, the difference will contain a residual shade pattern. These partially vignetted frames remove the shading pattern which can cause in a few percent discontinuity of the zero point in the center of the array. The ESO template SOFI_ima_cal_SpecialDomeFlat for the OBs is used to obtain the correct sequence of dome flats with lamp on and off with or without obscuration. The templates were executed by the telescope engineers during the day between the first and second and the second and third night of our observing program. In general it is not necessary to obtain flat field every day because these exposure are very stable over year-long periods.

An IRAF code called `special_flat.cl`[3] was used at the telescope in order to produce the flat field image from the outputs of the special flat template. Then it is possible to estimate and remove the shade pattern because the masked part of the array is almost free of scattered light. The estimate of the shading is only valid for the masked frame but not for the unvignetted exposure. A region on the array which is common in both the vignetted and unmask frame can be used to estimate the difference.

Therefore, this procedure creates the difference of the not shaded and masked exposures with the lamp on for the high illumination and the same without lamp for the low illumination. Then the these two differences were subtracted and then the result is divided by the median/average on the frames ((Δhigh illumination - Δlow illumination)/median). The science exposures were divided by the created "special flats." The special flats obtained on November 18th were used for the observations from the first and second night and for the third night we used the special flat from November 19th.

Bad Pixel Mask

A bad pixel mask contains a map of pixels which are not usable for different reasons. For instance, these are "dead pixels" whose value lays four sigma below the mean of flats. The pixels which are four sigma above the mean of darks are the "hot pixels." "Noisy pixels" are computed from histograms of the sigma image if flats and darks are averaged. Finally the bad pixel mask contains also pixels marked as bad ("frame pixels") if they are masked by the focal plane field mask. The bad pixel mask can be retrieved from the SOFI Data Reduction web page. We used the IRAF[4] task `fixpix` to replace the bad pixels with locally interpolated values on every dark-subtracted and flat-fielded science frame.

Ghosts

The science frames show strong donut-like structures after performing dark and flat field correction. These are probably pupil ghosts which may be due to internal reflections within the objectives or the telescope. Another possibility is that these features are actually defocussed dust grains—once you are out of focus because of a layer distance from the focal plane, you image the primary mirror of the telescope. An example is shown in Fig. 5.7. In order to eliminate these structures we created a ghost mask from the combined median of all frames of one individual target object. Then all science frames of an object were divided by the ghost mask.

All frames of an object are checked to see whether they contain other disturbing features. This is the case of SDSS J093008.57-003809.4 where bright stripes were found on the right upper fringe on two frames. These two exposures were skipped and the final image is then a combination of NEXP=36

[3]This program is available from the SOFI web page in the Data Reduction section under http://www.ls.eso.org/lasilla/sciops/ntt/sofi/DataReduction.html

[4]IRAF is the Image Reduction and Analysis Facility, a general purpose software system for the reduction and analysis of astronomical data. IRAF is written and supported by the IRAF programming group at the National Optical Astronomy Observatories (NOAO) in Tucson, Arizona, USA. NOAO is operated by the Association of Universities for Research in Astronomy (AURA), Inc. under cooperative agreement with the National Science Foundation.

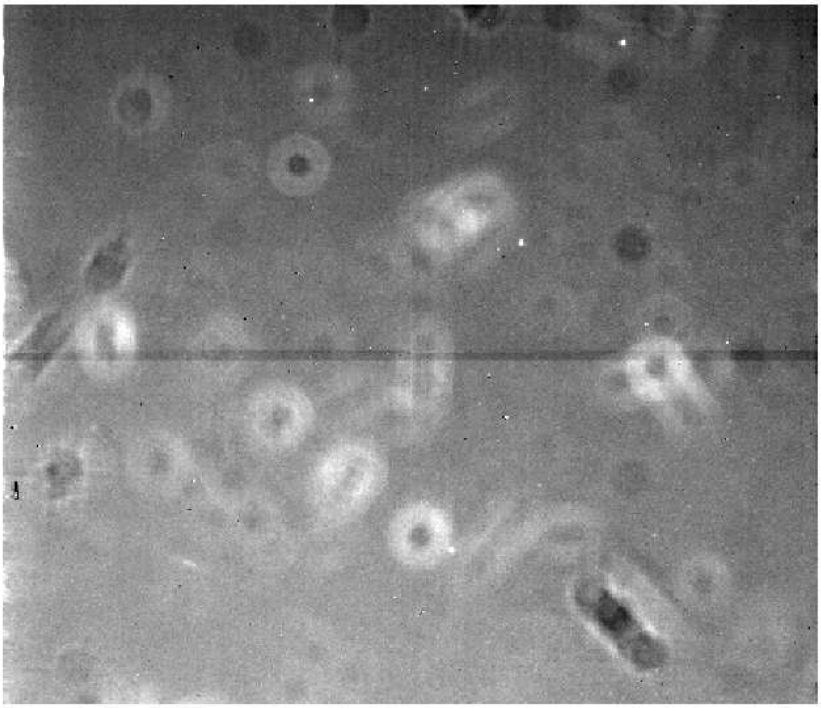

Figure 5.7: An example of a frame full of donut-like ghost features after dark and flat field correction. The target galaxy lays in the bottom quadrant on the left side of the frame.

frames. In one frame a meteor or satellite dilutes the target SDSS J031144.77+010241.4 with its spur and was therefore not used for the final combination (NEXP=37).

Sky

Because of the warm background it is necessary to subtract a sky value from every frame. We therefore took for each image of an object the three frames exposed before and after that image. The number of ±3 frames was selected because we checked the background flux variation in the sky-subtracted images later in this study. The variation is mostly less than 1% if we use ±3 and it becomes larger when using more than these six adjacent frames. This value, i.e., combining at least 5-7 images for exposure of non-crowded fields, is also advised in the new SOFI User's Manual (Issue 2.0).

Using only ±2 or less is not useful because some negative residuals from stellar objects will remain on the sky subtracted images and because of the overlapping masks which will be created later in this analysis. At the beginning and the end of an object series we did not use fewer than three adjacent images. The median of the images of all the ±3 frame sets was measured and the frames with deviations of more than 10% were rejected. This variation was only found for the object SDSS J095849.83+005012.1 in the J band. Here we skipped one frame because its deviation from the mean of the median is about 23%, that means that we are using NEXP=4 frames for the final target image of that object.

Then the ±3 frames were combined additively. The scaling parameter is set to zero which means that the additive zero level image shifts to be applied. This uses the negative of the median sky value of the ±3 frames. The resulting image represents the sky image which is then subtracted from the central image in the time series. We also checked whether the sky is better eliminated by dividing the multiplicatively scaled sky images from the central image. Here we would combine the sky frames using multiplicative image scaling. For multiplying we use the reciprocal of the sky median.

The standard stars were used to test the differences of the stellar flux of each standard star exposure

with the sky divided or subtracted. In all the checked sky corrected images the variances between the individual frames of an object are almost flat whereas the divided frames show large differences in stellar flux. The procedure of sky subtraction was repeated during a second iteration after the stars and extragalactic objects were covered by an object mask.

Image Adding

The target galaxies consist out of NEXP scientific frames. That means that in most of our cases 38 frames have to be combined for the relevant final image. Therefore the offsets between the same object in the different frames have to be measured with the IRAF `xregister` task. This task needs the position of an object in a reference frame and computes the offsets of this object in the other frames relative to the reference frame. Additionally, all frames are filled with `iminsert` into an empty image which was created with `mkimage`. This is done because the resulting frame of the combined images could contain empty regions at the borders of the individual frames. Within this blank image the individual frames are shifted according to the offsets as given in the output of `xregister` above. This shifting was executed with `imshift`. The interpolant type used to compute the output of the shifted images is a bicubic spline and the boundary value that will be given to pixels with no value is set to a constant value of -1×10^9.

The shifted frames were combined using `imcombine` with the type of the combining operation is set to "median." The lower threshold parameter of `imcombine` is tuned to -1×10^8 in order to exclude the pixels that were given very low values located at the edges of the shifted images. The combined final image is now embedded in the blank image with its maximum dimensions and the best S/N ratio at the position of a target object. This ratio decreases outwards the final image because of the smaller numbers of frames that cover the same sky region. For example, most of our objects are exposed in 38 frames obtained in the four-point observation mode, then the region around the targets is a combination of all 38 frames. The outer parts of the cross region around the target are combined from 19 (factor two less) frames and the rest parts consists only of 9-10 frames. Figure 5.35 shows an example of a combined image.

In this image the target galaxy SDSS J005315.44-084416.4 is located in the center. The dark regions with the shape of the target galaxy or stars are the result of the object subtraction from the background and the additional shifting of the frames. In order to avoid these holes in the final images of the targets, the frames have to be masked.

Image Masking

We use the program Source Extractor package (SExtractor Bertin & Arnouts 1996) to create the masks. The masks were separately created for both the target galaxy and the other objects. It is possible to manipulate a lot of parameters within SExtractor. In order to detect large number of small and faint objects the `DETECT_THRESH/ANALYSIS_THRESH` parameter is set to a low number (around 0.7). If the mask for only the target galaxy was created this value was set to a higher number like 1.5. The parameter `DEBLEND_MINCONT` separates the different sources into individual objects using a low value (we used 0.003); higher values for instance have the advantage not to detect several HII regions in a galaxy as individual sources. In order to avoid the detection of sources with the same identity number we used a high value (7.0) for the `CLEAN_PARAM`. In addition, we used a filter for good seeing. After SExtractor analyzes an input image it creates a mask image with the same size than the input image and an output table. This table contains several derived parameters for each detected source of the input frame.

The resulting image masks of the target and the other objects were then expanded using a smoothing gauss filter with the IRAF task `gauss`. The gauss factor for the masks of all sources excluding the target galaxy was set usually to 1. For the target galaxy the gauss factor was set individual in order to mask the whole object (values around 30 - 60). The parameters of the shape of the `gauss` were tuned according to the structural properties (ellipticity and position angle) from the output table of the SExtractor. This is necessary in order to expand the mask with an elliptical shape similar to that

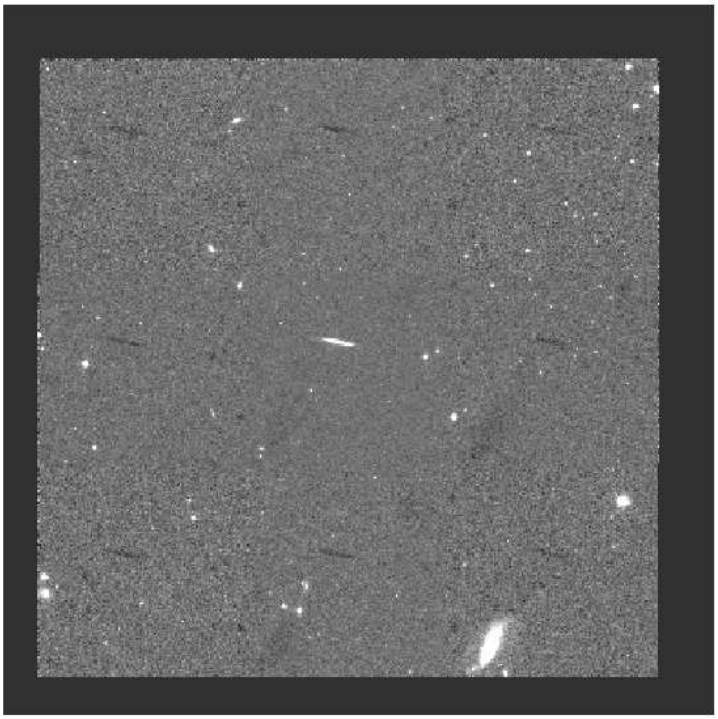

Figure 5.8: The final image of the combined 38 frames after the first iteration. The target galaxy SDSS J005315.44-084416.4 is located in the center of the image.

of the target object but with larger size in order to cover the whole light of the galaxy. After the creation of these vignetting files the masks for both the target and the other objects were combined. An example of such a final mask for the same galaxy as in Fig. 5.35 is presented in Fig. 5.9. With the aid of this final mask we created individual masks for every frame (#=NEXPO) of every target galaxy by using the offsets as described in the Sect. Image Adding.

Second Iteration

After that we repeated the reduction in a second iteration starting from the description in the section "Ghosts." This procedure has now the advantage of using the masked frames for the creation of the ghost masks and measuring the median background fluxes of the individual frames while avoiding the fluxes from the real objects. The ghost masks are combined without the contamination of the flux of the real objects and therefore represent much better the structures of these pupil ghosts. We again divided the new ghost masks from the scientific frames.

In the next step we used the masked frames for the computation of the median sky values. This sky value is also better estimated because the flux of the stars and galaxies is excluded. I.e., the masked pixels will remain out of the range of the values used in the combination of the ± 3 frames in the second iteration sky. Although the measured sky median is similar to that of the first iteration a quality check was performed. Fortunately, the differences of the sky median of every ± 3 frame serial is always small, maximum allowed values exhibit 8% difference between the highest and lowest sky. This is only measured once.

The sky images are then subtracted from the central image in the time series, the resulting images are the sky subtracted frames. These frames were shifted again into the blank image and combined using the offset list from the first iteration. The final image from the target galaxy SDSS J005315.44-084416.4 after the second iteration is shown in Fig. 5.10. As obvious in this Figure, the holes of the

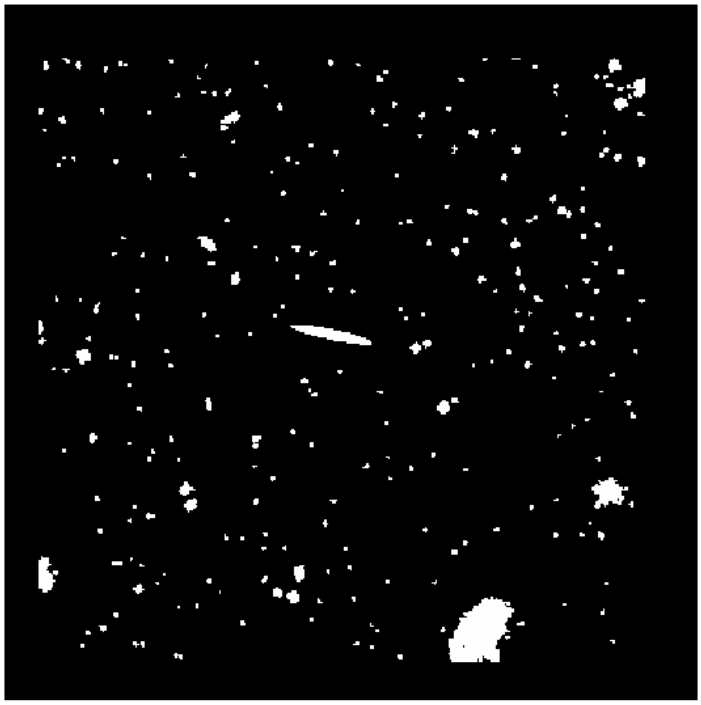

Figure 5.9: The final mask image from the SExtractor of the target galaxy SDSS J005315.44-084416.4 in the center and its surroundings which are also masked.

galaxy are filled because we used the masked sky frames.

5.3.3 Photometric Calibration and Third Iteration

The photometric calibration in the NIR depends on the variability of the column density of water vapor. This causes that the fringes of the J and K_s filter vary with the change of the water vapor. Therefore the quality of the photometry depends on the humidity and temperature in the atmosphere during the observing run. On good nights it has been possible to achieve up to 1% or better photometry. On the typical nights photometry with an accuracy of 3% - 5% could be obtained. Because the aim of this study is the analysis of the structure of these galaxies rather than high quality photometry, changes of a few percent of the humidity would not affect our investigation. A comparison (see later) shows that our run was during good photometric conditions.

Several lists of standard stars are available but all of them contain stars which were observed under different configurations, i.e., using detectors and filters that differ from those of SOFI. Our standard stars were selected from the faint standard star catalog by Persson et al. (1998). This catalog contains a list of 65 faint NIR stars between the 10th and 12th magnitude in the K band. This is much deeper than older recommended catalogs (Carter & Meadows 1995) and is optimized for megapixel arrays and large telescopes such as the Near-Infrared Camera and Multiobject Spectrometer (NICMOS) on the Hubble Space Telescope (HST). From this catalog of "NICMOS" standard stars we have chosen the stars that are as close as possible to our program objects. These standards are given in Table 5.4 and Table 5.5. The tables contain the number (Col. 1) and the magnitudes in K_s and J (Col. 5) of the standard as given by Persson et al. (1998). We observed up to five standard stars in each night as it is indicated in the starting date of the observation (Col. 2). The filter we used were the J and K_s filter and exposure times of DIT=1.2sec and DIT=2sec (see Col. 4).

Predefined OB are available at the telescope for the NICMOS standard stars. Therefore these stars by Persson et al. (1998) are the standards of choice for most of the observers at the NTT with SOFI.

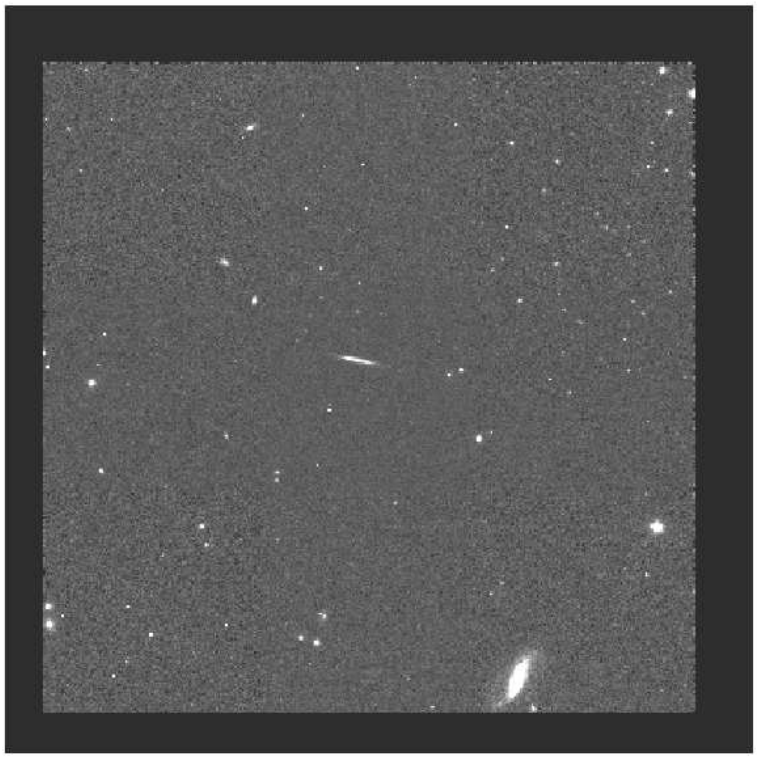

Figure 5.10: The final image of the target galaxy SDSS J005315.44-084416.4 after the second iteration.

The template for the observation of these standards we used is called "SOFI_img_cal_StandardStar." This template executes a five step observation of the selected star: A pattern of five exposures with telescope shifts in between were obtained; one in the center of the array and one in the center of each quadrant. The relative offsets are given in arcsec and typically 0, 45, -90, 0, 90 in RA and 0, 45, 0, -90, 0 in DEC. The other main configurations for the "SOFI_img_cal_StandardStar" template are DIT=1.2sec DIT=2sec, NDIT=5sec and Nexp=5sec in J and K_s.

The standards were reduced similar as the scientific targets. Darks with the same DIT were subtracted from the exposures with the stars. These darks were downloaded from the ESO archive. The special flats were divided from each standard and the bad pixels were fixed using the `fixpix` IRAF task together with the provided bad pixel mask. The sky was subtracted in the same manner as described for the target galaxies. I.e., ± 3 frames around an exposure were combined and then subtracted from that frame. Because the number of exposures of a standard is five, the maximum number of combined adjacent frames is four.

The photometry on each standard was performed using the IRAF `apphot` package. We measured the flux within a $10''$ diameter aperture as done by Persson et al. (1998). The background fit is performed using a linear algorithm in an annulus with an inner radius of $11''.52$ and a width of $4''.32$. A list of the positions of a star in the array was obtained using DS9. After running the `phot` command the measured flux in the $10''$ diameter aperture was collected in a table for each standard star frame. The corresponding airmass values (AIRM.START) of each frame were obtained from the frame header. Table 2 in the paper by Persson et al. (1998) provides the reference magnitudes for the stars. With these values from the literature it is possible to derive the magnitude of the zeropoint

$$zp = 2.5 \log(Flux/DIT) + mag(literature) \tag{5.2}$$

Figure 5.11 and Fig 5.12 show the correlation between the derived zero points and the airmasses as given in the headers for the K_s and J band, respectively. The figures show that the extinction

Table 5.4: Selected Standard Stars in K_s

Star No.	Starting Date	DIT (sec)	K_s
9103	2004-11-19/03:17:01.650	1.2	10.594
9103	2004-11-19/23:47:40.279	1.2	10.594
9104	2004-11-18/02:15:54.468	2	10.695
9104	2004-11-18/23:49:48.299	2	10.695
9105	2004-11-20/03:16:48.259	1.2	10.91
9105	2004-11-20/03:14:04.048	2	10.91
9106	2004-11-18/23:53:23.783	2	11.788
9108	2004-11-20/06:23:11.404	1.2	11.336
9109	2004-11-18/08:56:29.115	2	11.269
9111	2004-11-20/03:08:31.709	2	10.98
9134	2004-11-19/07:00:43.121	2	11.596
9187	2004-11-19/23:43:35.814	2	11.542

Table 5.5: Selected Standard Stars in J

Star No.	Staring Date	DIT (sec)	J
9103	2004-11-19/03:15:14.871	1.2	10.932
9104	2004-11-18/02:13:36.691	2	11.045
9106	2004-11-18/23:55:44.073	2	12.153
9134	2004-11-19/06:58:23.690	2	11.881

coefficient can be fitted by a linear function although it is generally not a linear function of airmass. A single zeropoint was found by simultaneously solving the three nights with the assumption of a linear correlation:

$$m = -2.5\log(Flux/DIT) + k \cdot airmass + zp \tag{5.3}$$

k is the slope (extinction coefficient) of the regression function shown in Figs. 5.11 and 5.12. The three nights did not have any sign to be non photometric (i.e., any cloud cover visible in any part of the sky). The resulting photometric solutions and associated errors are given in Table 5.6. Because of not using the averaged values for each exposure of a standard star the error of the slope (extinction coefficient) of the regression function is relatively large.

In order to estimate the quality of our photometric solution we searched for infrared observations of our sample galaxies in the literature with which to compare our resulting magnitudes. Table 5.9 shows a comparison of our derived magnitudes with those given in the 2MASS selected Flat Galaxy Catalog (2MFGC) by Mitronova et al. (2004) for the selected targets. The results are consistent. This leads to the conclusion that the conditions were good and stable in quality and therefore the nights were photometric.

Observations of simple disk galaxies were also performed by Dalcanton & Bernstein (2000). They obtained multi-wavelength imaging at the Las Campanas du Pont 2.5 m telescope (which is on the neighbor hill of the NTT site at La Silla in Chile) in the optical B and R band as well as in the NIR

Table 5.6: Photometric Solution

Filter	Nexposures	k	σ_k	mag(zp)	$\sigma_{mag(zp)}$
K_s	60	-0.052	0.010	22.425	0.013
J	20	-0.154	0.013	23.207	0.017

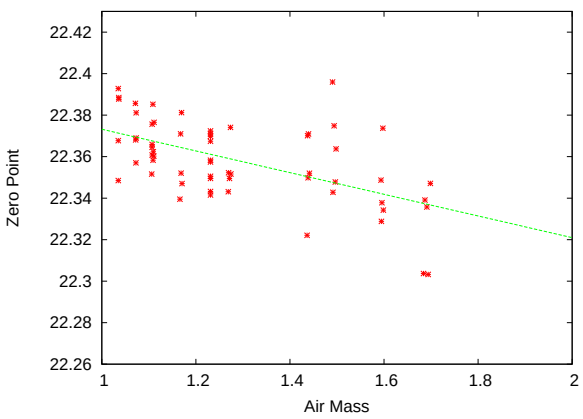

Figure 5.11: Photometric regression diagram for the standard stars in the K_s band. The ordinate shows the magnitudes of the zeropoint and the abscissa the airmass. The straight line is the fitted regression line.

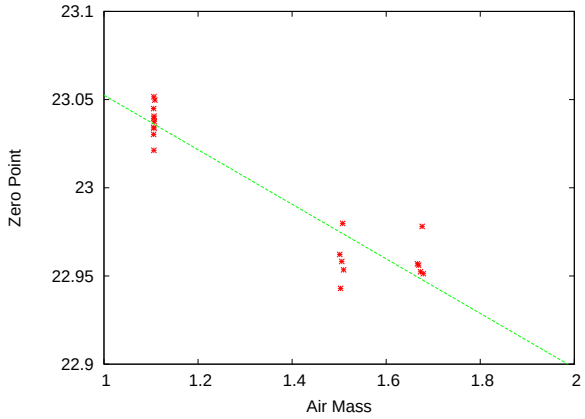

Figure 5.12: Photometric regression diagram for the standard stars in the J band. The ordinate shows the magnitudes of the zeropoint and the abscissa the airmass. The straight line is the fitted regression line.

K_s band. The galaxy sample contains 47 galaxies and was selected from the FGC. The exposure time of their K_s band observations ranges between 10 and 98 min depending on the individual objects. Dalcanton & Bernstein (2000) report that their K_s band data were obtained under photometric conditions ($\Delta m < 0.04$ mag) with seeing $0''.9$ - $1''.2$. With these conditions they report that they can reach to 22.5 mag arcsec^{-2} in K_s on $10''$ scales and a zeropoint of ≈ 21.75 mag. Compared to these observations our data exhibit a seeing in the range of $0''.4$ - $1''.2$ and a zeropoint magnitude of 22.42.

Third Iteration

We performed the last iteration step of the scientific reduction after the photometric calibration . For this purpose the airmass values of each science frame were written in a table. The headers of the frames contain the airmass value at the start and the end of an exposure. Because our targets are generally observed at low airmasses the start and end values do not vary. Therefore we used the value given in the AIRM.START header keyword. Only for the objects observed at low altitudes the start and end values differ significantly. In these cases we used the averaged airmass value.

Then every science frame is calibrated and also normalized to one sec by multiplying the frames using following expression:

$$frame_{calibrated} = (frame/t_{exp}) \cdot 10^{-0.4 \cdot (k \cdot airmasss + mag(zp)} \tag{5.4}$$

with the k and $mag(zp)$ values from Table 5.6 and airmass as well as DIT×NDIT (the exposure time of a frame) from the frame's header. The frames used for this calibration are the sky subtracted frames from the second iteration. At the end, the frames were again coadded to the resulting science image using the offset lists from the first iteration. This time we intend to conserve the flux for the final image. Therefore the interpolation type of the IRAF `imshift` command was set to "linear" as it is advised in the SOFI- Manual 2.0 on page 53.

5.3.4 Reduction and Calibration of the SDSS Images

The target galaxies from our K_s and J band observations were searched and then downloaded from the SDSS DR4 database using the Data Archive Server (DAS)[5]. The images downloaded there are the

[5]http://das.sdss.org/DR4-cgi-bin/DAS

"Corrected imaging frames" (fpC) in the SDSS bands g, r and i. These images have a field of 2048 × 1489 pixels with a pixel scale of 0.396 arcsec/pixel and an exposure time of 53.907456 sec.

All these fpC frames were masked with SExtractor using a small `DETECT_THRESH/ANALYSIS_THRESH` value in order achieve a high detection rate of all objects including the target galaxy. The created masks were then smoothed with a gauss filter with a smoothing factor of seven in order to include halos around bright stars. A visual inspection of the smoothed masks and the unmasked frames confirmed the choice of the smoothing factor.

The sky background was then measured on the masked frames and subtracted from the unmasked images. We checked the quality of the sky subtraction by comparing our sky values with those given in the fpC headers. And we found only negligible differences in both values.

In order to calibrate the fpC frames we followed the instructions as given at the SDSS web pages for deriving the calibrated magnitude[6]. The values of the zeropoint (aa), extinction coefficient (kk) and $airmass$ for the calibration function of each SDSS image are stored in the corresponding "bestTsField" tables which are also available at the DAS. With the information from these tables the sky subtracted fpC frames are calibrated and normalized using the calibration function from the SDSS webpage:

$$fpC_{calibrated} = (fpC/t_{exp}) \cdot 10^{0.4 \cdot (aa + kk \cdot airmass)} \tag{5.5}$$

The exposure time t_{exp} is always set to 53.907456 sec. The resulting calibrated images were used for the further analysis.

5.4 Morphological Image Analysis

5.4.1 Flatness of the Galaxies

The luminosity-weighted mean ellipticity ε and the concentration index CI were used in the Catalog in order to classify the galaxies from the SDSS into several morphological classes like galaxies with or without bulge and simple disks or intermediate flat galaxies. The concentration index was responsible for the separation into objects with bulge and bulgeless types. The flatness of disks was measured with the aid of the luminosity-weighted mean ellipticity. In this section we repeat this work on the observed galaxies with the K_s band data.

Isophote fitting

In order to measure ε of the galaxies we fit ellipses to the isophotes of the targets. This is performed with the MIDAS surface photometry package `SURFPHOT`. The ellipses were fitted with the task `FIT/ELL3` whose algorithm is based on the formulae of Bender & Moellenhof (1987). They developed the elliptical isophote fitting in order to detect deviations in elliptical galaxies from aligned ellipses. These deviations were used for the detection of the presence of dust, peculiar phase space distributions of the stars, disks and signs of interactions. The isophotes are fitted by ellipses by means of a least square method.

For this task we carefully measured the central pixel of a target and saved its position and luminosity. This information is then used for the program to fit the innermost ellipse. The next ellipses were fitted in steps of 0.1 mag until the background is reached. `FIT/ELL3` produces a table which contains the fitted parameters: the isophote level, the major and minor axis, the position angle of the major axis, the center of the ellipses and the noise. This is the total noise at a given major axis and represents the squared sum of the photon noise of the galaxy, the photon noise of the sky and the read-out noise.

This output table is used as input for the FORTRAN 77 code "`Mini_Morph_Invest`" which computes ε as a measurement of the flatness. The code uses the saved values of the isophote levels and the major and minor axis as parameters. This program is a shortened version of the general program `morph_invest` which was used for the Catalog. `morph_invest` is presented at the Appendix A of this

[6] http://www.sdss.org/dr4/algorithms/fluxcal.html#counts2mag

Table 5.7: Morphological Parameters of the Galaxies

SDSS Name	Prog. ID	ε_g	ε_r	ε_i	ε_{K_s}	CI_g	CI_r	CI_i	CI_{K_s}
SDSS J005315.44-084416.4	3A	0.849	0.838	0.825	0.853	2.454	2.487	2.627	2.462
SDSS J005624.60-010834.7	1A	0.864	0.858	0.857	0.879	2.317	2.349	2.425	2.652
SDSS J011904.42-000818.7	1B	0.897	0.887	0.882	0.892	2.246	2.419	2.336	2.665
SDSS J012302.78-091745.7	3Bm	0.841	0.825	0.826	0.841	2.483	2.483	2.581	2.642
SDSS J012731.32-102347.1	3C	0.868	0.865	0.856	0.861	2.097	2.297	2.278	2.250
SDSS J013551.83-095646.5	2B	0.841	0.831	0.824	0.841	2.408	2.427	2.472	2.491
SDSS J014102.09-092022.6	1Cm	0.860	0.840	0.824	0.815	2.327	2.383	2.494	2.711
SDSS J031136.44-003341.6	2C	0.601	0.553	0.536	0.555	2.898	3.073	2.747	3.216
SDSS J031144.77+010241.4	1D	0.891	0.893	0.882	0.875	2.243	2.345	2.231	3.059
SDSS J031513.32-071614.6	3Dm	0.843	0.832	0.834	0.875	2.498	2.418	2.474	2.563
SDSS J031538.62-070443.8	2D	0.765	0.760	0.753	0.774	2.430	2.415	2.429	2.630
SDSS J033923.33-053631.2	3E8m	0.810	0.802	0.797	0.808	2.280	2.323	2.470	2.587
SDSS J092353.77+014912.1	2Em	0.848	0.838	0.831	0.855	2.514	2.365	2.420	2.875
SDSS J093008.57-003809.4	1E	0.865	0.844	0.831	0.817	2.179	2.450	2.588	3.234
SDSS J094801.01+020111.2	3Em	0.811	0.818	0.814	0.832	2.529	2.601	2.539	2.396
SDSS J095849.83+005012.1	2E8m	0.855	0.845	0.835	0.847	2.226	2.331	2.295	–

work. The main formulas of the code are described in Chapter 2. The results of this investigation are shown in Col. 5 in Table 5.7. The other columns in this table show the luminosity-weighted mean ellipticity ε for the SDSS g, r, i bands as taken from the Catalog and the concentration indices CI. The computation of the CI is described in the next section.

5.4.2 Bulge Size of the Galaxies

In order to measure the bulgesize of the NIR data we selected the same approach as in the optical. The CI clearly separates galaxies with bulge from those without an apparent central spheroidal component. In the optical it was derived using the ratio of the Petrosian radii that contain 90% and 50% of the Petrosian flux in the same band using the given SDSS parameters.

Because SDSS parameters are not given for NIR bands and the 2MASS database uses different methods, we derived the CI and other morphological discriminators for our NIR targets with the aid of the AMOR software. The details of this program and the computation of the various morphological parameter are shown in the Appendix B.

5.4.3 Results

The results are gathered in Table 5.7. This table contains the Galaxy name and its program ID in the first two Cols. Cols. (3)-(5) and Cols. (7)-(9) show the ε and CI values as taken from the Catalog. The Col. (6) and Col. (10) contain the ε and CI values as derived with `Mini_Morph_Invest` and AMOR, respectively.

The comparison of ε between the optical wavelengths and the NIR is shown in Fig. 5.13 and Fig. 5.14. The differences between the r, i and K_s band data are very small (and also for the g band which is not shown there), a slight trend presents a flatter shape of most of the galaxies in the NIR. This is because the more weighted brighter and inner ellipses are flatter in the NIR because no dust disturbs the fit of the inner ellipses.

The separation diagram from the Catalog can be replotted in the optical band together with the NIR K_s band. This is shown in Fig. 5.15. This diagram shows that the differences of the CI are much stronger between the optical and the NIR wavelengths compared to the measurement of the galaxy's flatness which is shown in Fig. 5.13 and Fig. 5.14. The scatter of the CI between the optical and the NIR is also shown in Fig. 5.16 and Fig. 5.17 in more detail. The reason for this scatter is due to the

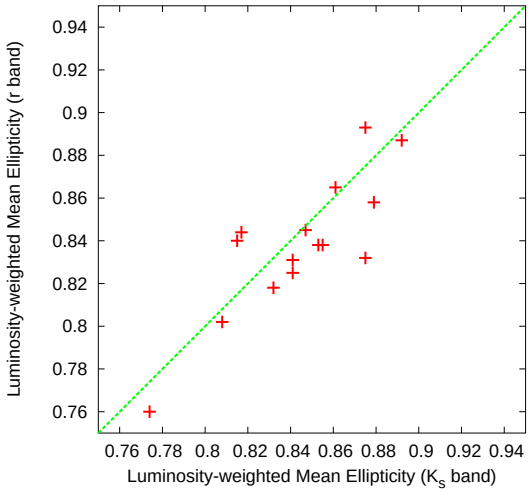

Figure 5.13: The differences between the flatness in the optical r and NIR K_s filter. The green line shows the relationship $\varepsilon_r = \varepsilon_{K_s}$

.

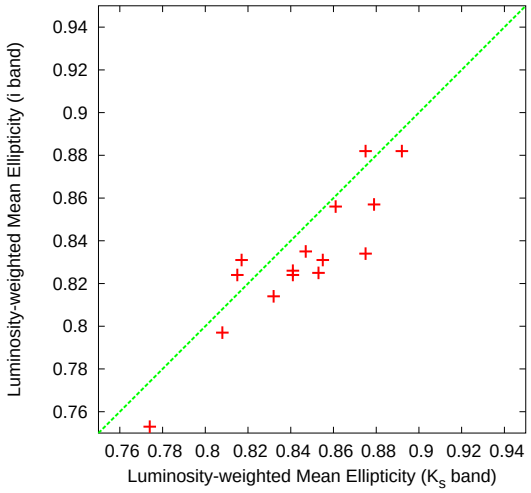

Figure 5.14: The differences between the flatness in the optical i and NIR K_s filter. The green line shows the relationship $\varepsilon_i = \varepsilon_{K_s}$

.

strong influence of dust in the optical. There, bulges and bulge-like structure can be hidden behind a screen of dust and the central light concentration is smoothed. Dust absorption features emphasize this smoothing to a knot-like light distribution in the optical disk. The K_s band is insensitive to this attenuation so that a possible bright central component can be detected. In our case some of the galaxies exhibit a much larger CI than in the optical. That means that these objects contain a brighter central component which is invisible in the SDSS bands.

The bulge region is highlighted in the Figs. 5.18, 5.19 and 5.20. These figures show the central $30'' \times 18''$ for the objects 1C and 1D and $14'' \times 10''$ for 1A in the K_s on the left and r band on the right side. Isophotes are overplotted with red lines. These contours are created with DS9 using a smoothing factor of 4 and plotting the galaxies with exactly four equidistant isophotal levels for the galaxy 1C and 1A and six for 1D. The galaxies are scaled to the same pixel scale and corrected for a common seeing. It is clearly shown that the isophotes in the K_s are made out of a much rounder shape suggesting an obscured small bulge/nucleus component in the optical galaxy frames. On the left disk side of the r band images both Fig. 5.18 and 5.19 exhibit a bend in the isophotes which traces a knot-like absorption feature and smooths the CI. This attenuation is not seen in the NIR observation of the same object.

However, it is not clear whether or not the galaxies hide a real bulge component in the optical because the light concentration can be simply the effect of the large amount of light which is integrated in the line of sight and/or a bright nucleus. Beside that, these galaxies would not be selected as bulgeless galaxies with a CI<2.7 when using the K_s filter observations contrary to the separation of the Catalog. Dealing with the numbers of Table 5.7 then 4 of 14 bulgeless galaxies would be selected as galaxies with bulge (or more precisely: as galaxies with CI≥2.7). This would lead to a overestimation of wrongly classified simple disks of ≈25% in the optical SDSS bands. Because it is not clear if it is a real bulge it is probably better to speak about dominant flocculent absorption in these galaxies.

Another trend could be revealed by Fig. 5.16 and Fig. 5.17 if using the CI difference in the different wavelengths as an indicator of dust. These diagrams show that our target galaxies have various amounts of apparent dust although their disks are very flat and extended. The typical organized dust lane is absent in these galaxies but this does not mean an overall lack of dust in these galaxies. The slope of the Tully-Fisher relation for flat galaxies increases towards longer wavelengths due to internal extinction, indicating significant amounts of dust (Karachentsev et al. 2002). It was shown by Lisenfeld & Ferrara (1998) that these types of galaxies contain dust which is less concentrated within the disk

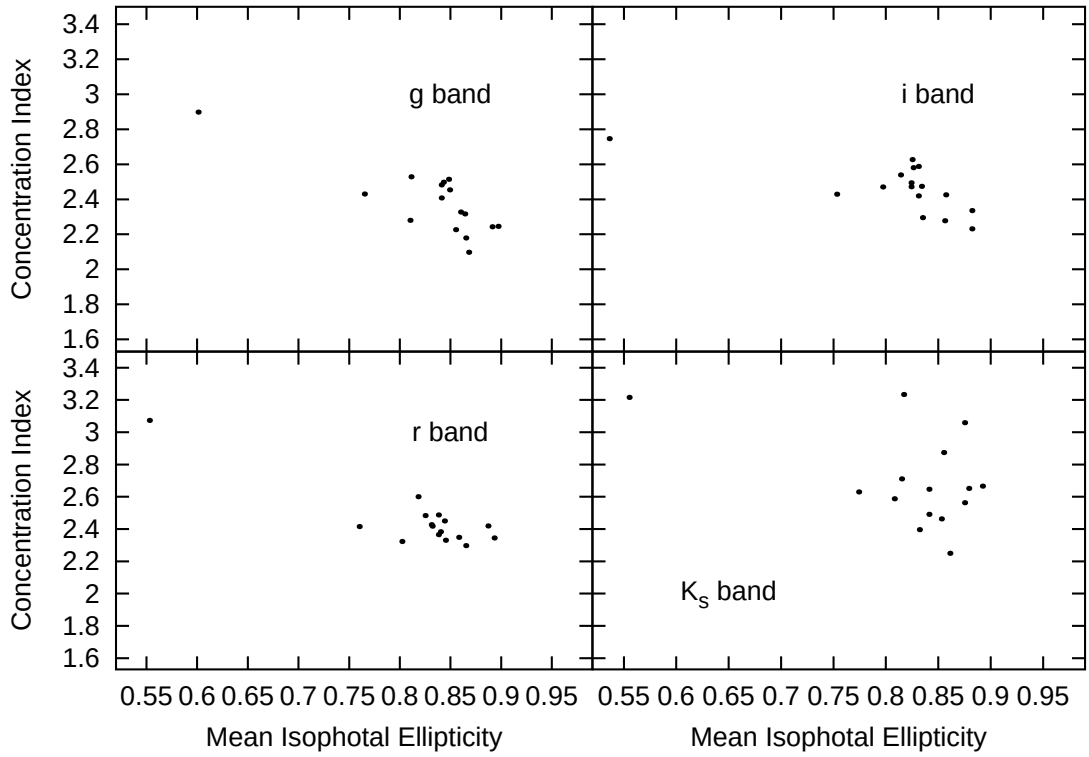

Figure 5.15: The separation diagrams in the optical and the NIR bands.

and significantly more porous (Matthews & Wood 2001) in galaxies with a rotation speed lower than 120 km s^{-1} (Dalcanton et al. 2004). The objects with the lowest concentration are generally those with low surface brightnesses and low internal velocity dispersions (Graham et al. 2001; Conselice et al 2002) which is expected to be observed in passively evolving simple disk galaxies.

5.4.4 Discussion

Generally, the CI gives information about the stellar build up of a galaxy and therefore about its formation history. In the hierarchical evolution scenario the stellar mass is focused into a (flattened) spheroidal component by the loss of angular momentum of the system. This causes the infall of matter into this component and the subsequent concentration in this hot dynamical center. Such loss of angular momentum can be the result of various forms of interaction such as mergers and the ejection

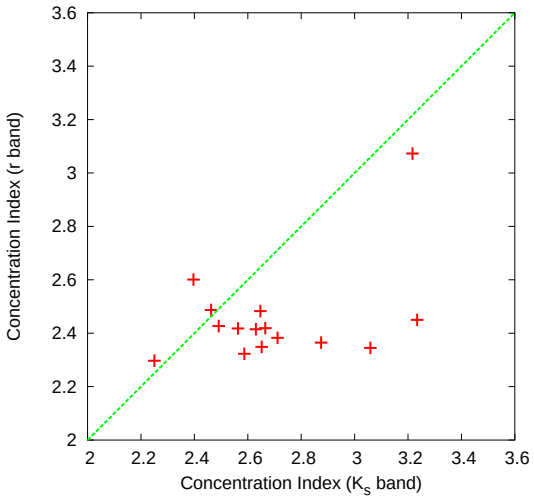

Figure 5.16: The differences between the concentration index in the optical r and NIR K_s filter. The green line shows the relationship $CI_r = CI_{K_s}$

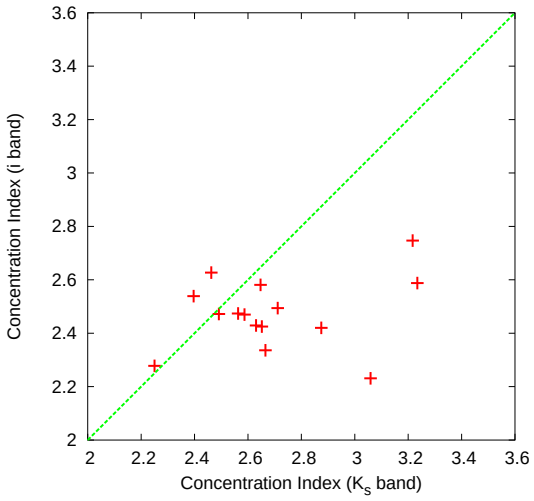

Figure 5.17: The differences between the concentration index in the optical i and NIR K_s filter. The green line shows the relationship $CI_i = CI_{K_s}$

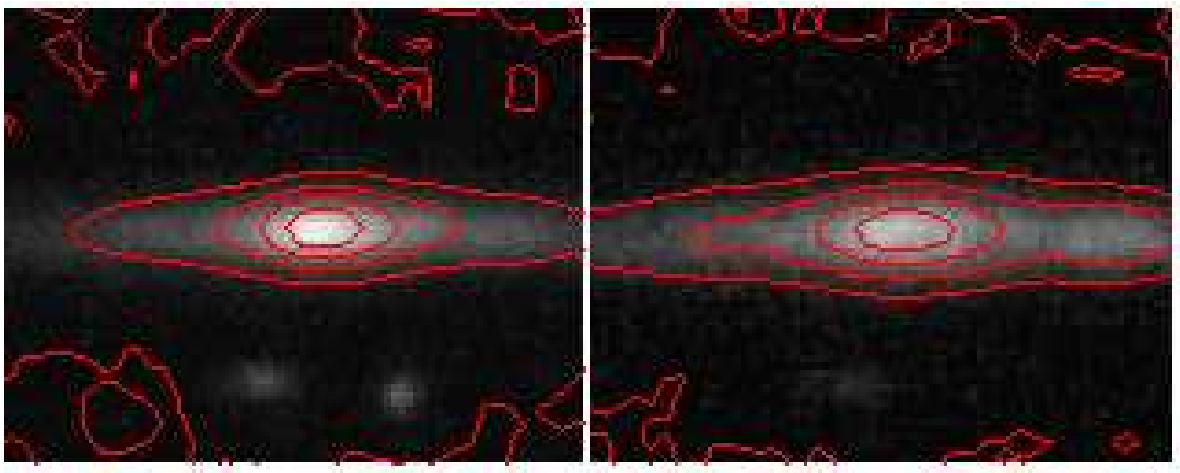

Figure 5.18: The contours of the central region of 1C in the K_s (left) and r (right) band. CI_{K_s} - CI_r = 0.328. The scale is $30'' \times 18''$.

of tidal tails of material.

The contrary view is given by the monolithic collapse scenario where the stars are concentrated in a spheroidal component because of the fast collapse of gas and stars formed from that gas. Material can be then accreted and form an extended disk around this spheroid (Steinmetz 2003; Samland 2004). In this case, the angular momentum determines the properties of the formed disk including its light concentration, which will be high for rapidly rotating systems (Dalcanton et al. 2004). Some correlations do support the physical meaning of the CI (and subsequently the spheroidal component) because it is connected to Hubble type and surface brightness (see the Catalog and Okamura et al.

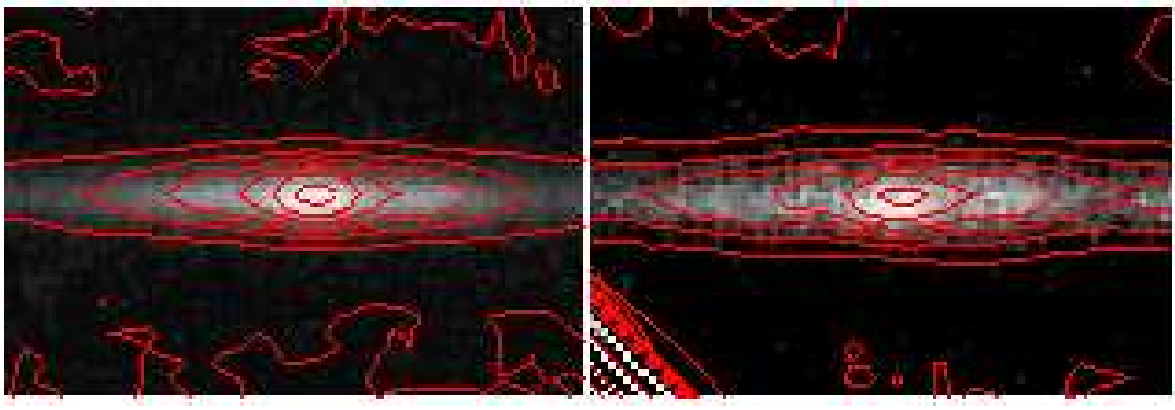

Figure 5.19: The contours of the central region of 1D in the K_s (left) and r (right) band. CI_{K_s} - CI_r = 0.714. The scale is $30'' \times 18''$.

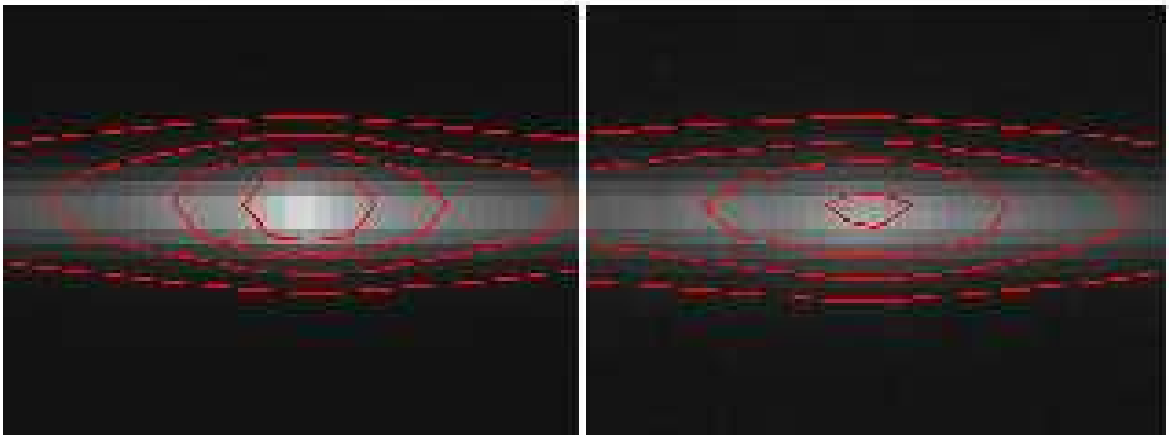

Figure 5.20: The contours of the central region of 1A in the K_s (left) and r (right) band. CI_{K_s} - CI_r = 0.303. The scale is $14'' \times 10''$.

1984) and luminosity, velocity dispersion, black hole mass and galaxy size (Graham et al. 2001). It is not difficult to imagine that the CI correlates with the bulge to total light flux ratio (B/T) of galaxies (Conselice 2003).

Beside this global meaning of the CI its effectiveness for edge-on disk galaxies is somewhat special. This is because the CI strongly depends on the attenuation of the dust and thus on the wavelength used for the observation (see Fig. 5.16 and Fig. 5.17 and Table 5.7). Therefore the use of a multi-wavelength CI is a quantifier of the existence of dust. When using dust-free observations the CI could be an indicator of the existence of a bulge/nucleus. In the case where large bulges overshine the disk

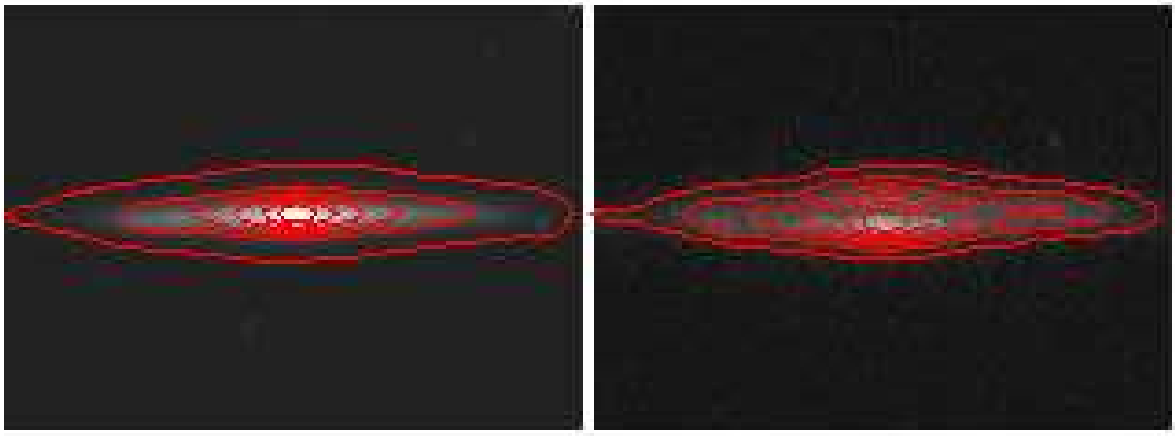

Figure 5.21: The contours of the of 3D in the K_s (left) and r (right) band. CI_{K_s} - $\mathsf{CI}_r = 0.146$. The scale is $61'' \times 44''$.

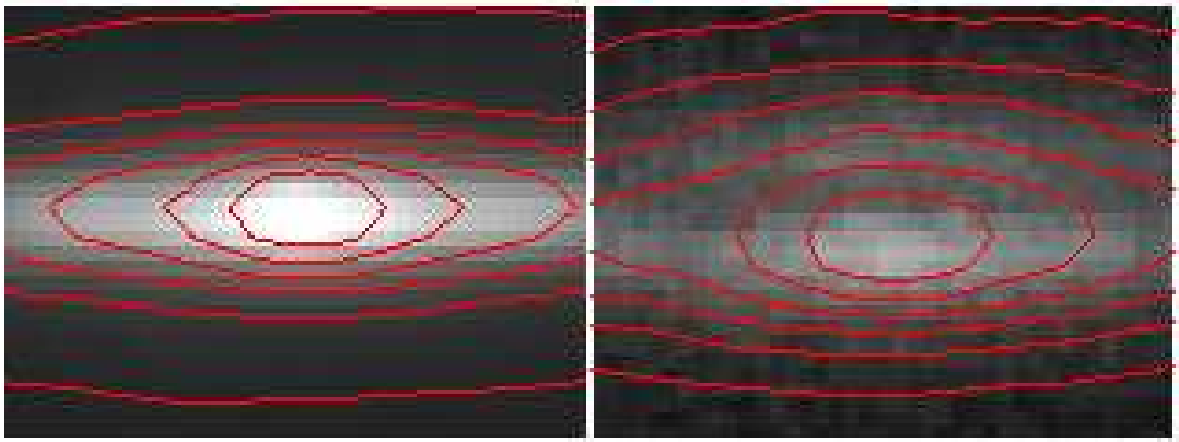

Figure 5.22: The contours of the central region of 3D in the K_s (left) and r (right) band. CI_{K_s} - CI_r = 0.146. The scale is $14'' \times 10''$.

also the optical CI can be used as morphological discriminators.

Another case is shown in Fig. 5.21 for the galaxy 3D. The isophotes are plotted using six isophotal levels. The shapes of these contours are similar for the optical and NIR image on the right and left side, respectively. This is surprising, because the galaxy contains a dominant dust lane in the optical image. It is not an effect of resolution as shown in Fig. 5.22. In this Figure the central $14'' \times 10''$ of that galaxy are shown and the similar shape of the central isophotes is obvious. Therefore the difference if the CIs in r and K_s is small. This is because the dust lane in disk galaxies is concentrated to the

thin disk and has a small scale height compared to the disk stars (Dalcanton et al 2004), so that the stellar light can exceed the dark zone of dust.

In summary, the largest effect of the CI difference between the wavelength bands is shown for simple disk galaxies with a flocculent, knot-like distribution of dust. They have a smooth light distribution in the optical and a more concentrated light in the NIR. As was shown by Dalcanton et al. (2004), a knotty dust distribution is often observed in slowly rotating and low mass bulgeless galaxies. In the more rapidly rotating and massive galaxies the dust is gathered in an thin layer representing a typical organized dust lane. In addition, these more mass rich galaxies more often show bulges compared to the slowly rotating galaxies. The central light can overshine the dust lane in these objects and subsequently the CI is similar in the different filters.

5.4.5 CAS Morphology

The CI used in the previous chapter is part of a classification system which is known under the term CAS. This system was developed for quantitative morphological analysis of large datasamples where it is impossible to use only classification by eye inspection. The letter "C" means the CI as described in the section above. An "A" stands for the parameter which describes the asymmetry of an object. This A is determined by rotating an individual image about its center and then subtracting the rotated image from the original image. To compute the clumpiness or smoothness "S" the galaxy image will be smoothed and the smoothed image will be then subtracted from the original.

The CAS parameters can be derived with AMOR. The input file for AMOR has to be configured. These fine tunings for AMOR are presented in the Appendix C.

5.4.6 Results

The results of the CAS parameters from AMOR are given in Table 5.8. The first Col. of this table contains the galaxy name, the second contains the program identity. The Col. (3) and Col. (4) are the asymmetry indices for the absolute pixel value method and the square pixel method as described by the formulae C.1 and C.2, respectively. The same holds for the clumpiness index in Cols. (5) and (6) which are based on the formulae C.3 and C.4. The Col. (7) shows the concentration index derived using the formula given at B.2. In the last Col. (8) the total surface brightness is derived using Eq. 5.6.

Table 5.8: Results of the CAS

SDSS Name	A180AB[5]	A180SQ	CLUAB[6]	CLUSQ	CI[7]	μ	
g							
SDSS J005624.60-010834.7	1A	0.082	0.006	0.233	0.04	1.95	21.43
SDSS J011904.42-000818.7	1B	–	–	–	–	–	–
SDSS J014102.09-092022.6	1C	–	–	–	–	–	–
SDSS J031144.77+010241.4	1D	–	–	–	–	–	–
SDSS J093008.57-003809.4	1E	0.234	0.036	0.371	0.081	1.83	22.98
SDSS J013551.83-095646.5	2B	0.271	0.062	0.329	0.072	2.12	22.55
SDSS J095849.83+005012.1	2Eal	0.221	0.031	0.385	0.083	1.97	23.18
SDSS J092353.77+014912.1	2E	0.307	0.042	0.535	0.166	2.11	23.62
SDSS J012302.78-091745.7	3B	0.143	0.025	0.272	0.050	2.19	22.46
SDSS J012731.32-102347.1	3C	0.323	0.062	0.594	0.204	1.76	24.09
SDSS J031513.32-071614.6	3D	–	–	–	–	–	–
SDSS J094801.01+020111.2	3E	–	–	–	–	–	–
SDSS J033923.33-053631.2	3Eal	0.287	0.047	0.326	0.056	1.96	22.81
SDSS J031136.44-003341.6	2C	0.347	0.064	0.472	0.213	2.30	23.04
SDSS J031538.62-070443.8	2D	0.214	0.052	0.270	0.079	2.37	22.23
SDSS J005315.44-084416.4	3A	0.182	0.015	0.487	0.127	2.24	23.35
r							
SDSS J005624.60-010834.7	1A	–	–	–	–	–	–

Table 5.8: continued.

SDSS Name	Prog. ID	A180AB	A180SQ	CLUAB	CLUSQ	CI	μ
SDSS J011904.42-000818.7	1B	–	–	–	–	–	–
SDSS J014102.09-092022.6	1C	0.214	0.043	0.341	0.074	2.07	22.25
SDSS J031144.77+010241.4	1D	–	–	–	–	–	–
SDSS J093008.57-003809.4	1E	0.294	0.050	0.308	0.090	1.95	22.22
SDSS J013551.83-095646.5	2B	0.230	0.051	0.348	0.081	2.19	22.15
SDSS J095849.83+005012.1	2Eal	0.073	0.003	0.361	0.074	1.98	22.62
SDSS J092353.77+014912.1	2E	0.189	0.016	0.389	0.078	2.01	22.60
SDSS J012302.78-091745.7	3B	0.137	0.018	0.224	0.043	2.11	21.60
SDSS J012731.32-102347.1	3C	–	–	–	–	–	–
SDSS J031513.32-071614.6	3D	0.471	0.154	0.395	0.101	2.04	22.52
SDSS J094801.01+020111.2	3E	0.141	0.011	0.276	0.065	2.10	22.05
SDSS J033923.33-053631.2	3Eal	0.094	0.006	0.382	0.072	2.16	22.10
SDSS J031136.44-003341.6	2C	0.288	0.042	0.439	0.180	2.36	22.31
SDSS J031538.62-070443.8	2D	0.146	0.023	0.266	0.075	2.36	21.69
SDSS J005315.44-084416.4	3A	0.187	0.031	0.358	0.069	2.23	22.28
i							
SDSS J005624.60-010834.7	1A	0.051	0.002	0.239	0.048	2.12	20.27
SDSS J011904.42-000818.7	1B	–	–	–	–	2.01	20.76
SDSS J014102.09-092022.6	1C	–	–	–	–	–	–
SDSS J031144.77+010241.4	1D	–	–	–	–	–	–
SDSS J093008.57-003809.4	1E	–	–	–	–	–	–
SDSS J013551.83-095646.5	2B	0.213	0.024	0.396	0.094	2.24	21.85
SDSS J095849.83+005012.1	2Eal	0.155	0.016	0.437	0.107	2.11	22.35
SDSS J092353.77+014912.1	2E	0.173	0.012	0.484	0.121	2.36	22.28
SDSS J012302.78-091745.7	3B	0.143	0.013	0.248	0.049	2.19	21.15
SDSS J012731.32-102347.1	3C	–	–	–	–	–	–
SDSS J031513.32-071614.6	3D	–	–	–	–	–	–
SDSS J094801.01+020111.2	3E	0.109	0.006	0.394	0.110	2.05	21.89
SDSS J033923.33-053631.2	3Eal	0.099	0.004	0.383	0.073	2.10	22.27
SDSS J031136.44-003341.6	2C	–	–	–	–	–	–
SDSS J031538.62-070443.8	2D	–	–	–	–	–	–
SDSS J005315.44-084416.4	3A	0.160	0.013	0.347	0.066	2.21	21.68
K_s							
SDSS J005624.60-010834.7	1A	0.073	0.003	0.218	0.076	2.23	17.37
SDSS J011904.42-000818.7	1B	–	–	–	–	–	–
SDSS J014102.09-092022.6	1C	0.142	0.016	0.280	0.074	2.15	19.33
SDSS J031144.77+010241.4	1D	–	–	–	–	–	–
SDSS J093008.57-003809.4	1E	0.103	0.006	0.152	0.052	2.34	17.62
SDSS J013551.83-095646.5	2B	0.112	0.007	0.299	0.070	2.26	19.27
SDSS J095849.83+005012.1	2Ea	–	–	–	–	–	–
SDSS J092353.77+014912.1	2E	0.078	0.004	0.182	0.028	2.21	18.28
SDSS J012302.78-091745.7	3B	0.129	0.007	0.176	0.036	2.28	17.92
SDSS J012731.32-102347.1	3C	–	–	–	–	–	–
SDSS J031513.32-071614.6	3D	0.067	0.002	0.217	0.073	2.16	18.03
SDSS J094801.01+020111.2	3E	0.062	0.002	0.222	0.065	2.07	18.44
SDSS J033923.33-053631.2	3Ealtern	0.079	0.003	0.234	0.046	2.17	18.83
SDSS J031136.44-003341.6	2C	0.138	0.010	0.408	0.148	2.53	19.66
SDSS J031538.62-070443.8	2D	–	–	–	–	–	–
SDSS J005315.44-084416.4	3A	0.065	0.002	0.160	0.050	2.16	17.92

[5]The typical error for the A180AB is 0.005
[6]For the CLUAB the typical error is 0.01
[7]The typical error for the CI is 0.01

A versus S The Fig. 5.23 shows the distribution of the asymmetry index of Col. (3) in Table 5.8 relative to the distribution of the clumpiness index (see Col. (5) in Table 5.8) from the target galaxies analyzed with AMOR. In general, the range of values for the S is slightly increasing to higher values from the K_s to the g band.

The values of A are widely distributed in optical bands but concentrated at a very low level at longer wavelengths. A small trend is visible in all filters: higher values of A exhibit larger clumpiness, i.e., more asymmetric galaxies tend to be more clumpy. This trend is more obvious in the optical than in the NIR because of the small value range in K_s. In the NIR, the targets appear more symmetric. The reason for this wavelength differences from g, r, i to K_s band is due to the contribution of the dust attenuation to the optical images. This is already shown in Fig. 5.18 and 5.19. There, the clumpy distribution of the dust is dominant in the optical images. This knotty distribution causes an asymmetric appearance of the isophotes in the optical compared to the dust-free NIR images. In addition, this effect is the stronger the more dust knots are visible which is especially the case in dust-sensitive bands (g band).

Using the square method to derive the A and S parameter this trend is less strong as shown in Fig. 5.24. The square method was developed for the classification of faint and small objects, it is therefore not the best discriminator for our target galaxies. A description of the square method and its definition can be found in the Appendix C.

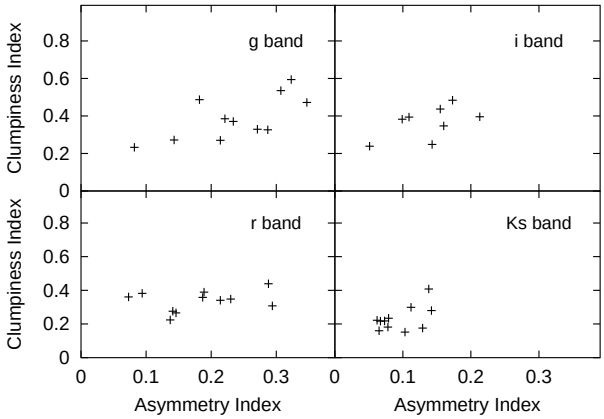

Figure 5.23: The correlation between asymmetry and clumpiness of the target galaxies in the optical and the NIR bands. The optical values show a relation between A and S. A and S are derived using the absolute value method.

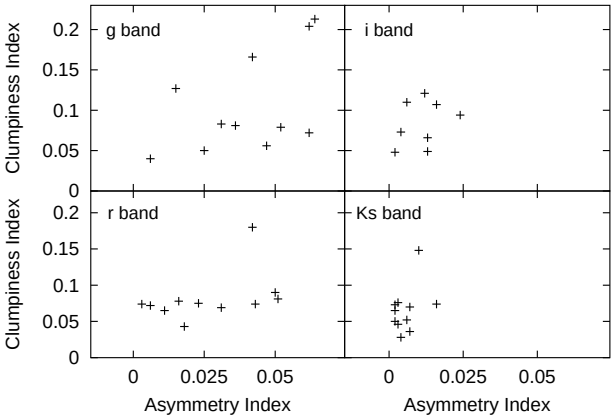

Figure 5.24: Same as Fig. 5.23 but A and S are derived using the square method

CI versus A The correlation between CI and A is shown in the Figs. 5.25 and 5.26. The concentration index here is derived within elliptical apertures. Therefore these values are somewhat different compared to the CI values in Table 5.7. However, the behavior is the same as shown in Figs. 5.16 and 5.17 because on average the CI values are larger in the NIR compared to the optical. In the g and r band no trend is seen.

A small trend is maybe shown in the i and K_s band where more concentrated galaxies are more asymmetric. It is difficult to interpret this trend because it could be affected by a technical detection

effect. On the other hand this trend could be also explained by real asymmetries in galaxies with central light concentrations because of signs of interaction like warps and tidal tails.

However, the asymmetries in K_s are very small which speaks against the interaction signs. The technical detection effect is important if the center of a galaxy could be measured only if a central light is detectable. If no center can be measured (in the case of small CI) then the asymmetry cannot be determined correctly. It is shown again that the optical images appear to be more asymmetric due to the strong influence of dust in these wavelengths. The results are the same (see Fig. 5.26) for the CI and A if A is derived using the square method as given in Formula C.2.

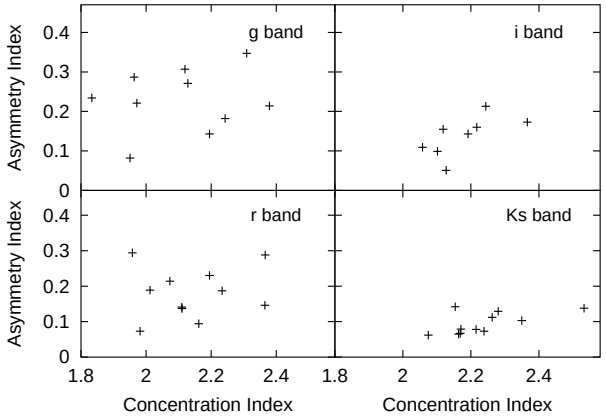

Figure 5.25: Concentration index versus asymmetry of the galaxies in the optical and the NIR bands. The correlation between these two morphological discriminators is very small. The values of the CI and the A are smaller in the K_s band than in the optical bands. CI and A are derived using the absolute value of these objects.

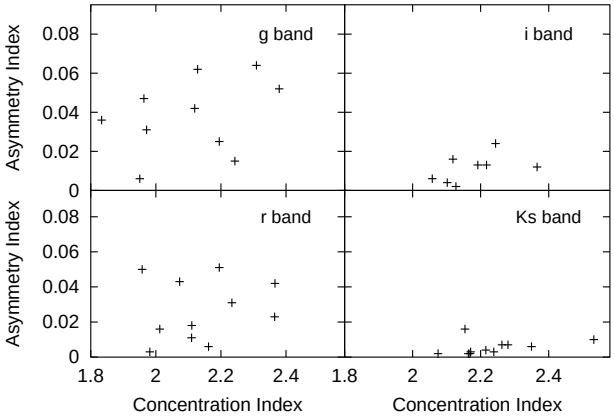

Figure 5.26: Same as Fig. 5.25 but using the square method for deriving the parameters.

CI versus S The Fig. 5.27 does not show any correlation between the central light concentration and the clumpiness of an object. The same result is given when using the square method for deriving S (see Fig. 5.28).

The CAS parameters are probably correlated with the total surface brightness μ of the target galaxies. For that reason we plotted the CAS values against μ which is derived by using the following definition:

$$\mu = mag + 5\log(r_{eq}) \tag{5.6}$$

where *mag* is the Petrosian magnitude derived by AMOR and presented in Table 5.9. The equivalent radius is

$$r_{eq} = \sqrt{a[''] \cdot b['']} \tag{5.7}$$

with the semi minor axis b and semi major axis a of the galaxy in arcsec.

No correlation is shown for **CI versus** μ in Fig. 5.29.

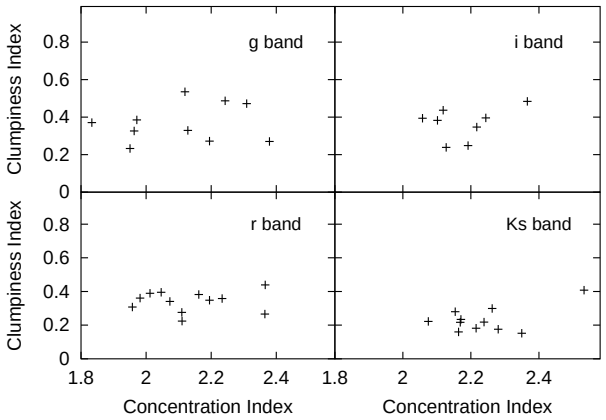

Figure 5.27: No correlation is shown in this figure between the clumpiness and the central light concentration, i.e., bulgesize of the targets. S is derived using the absolute value method.

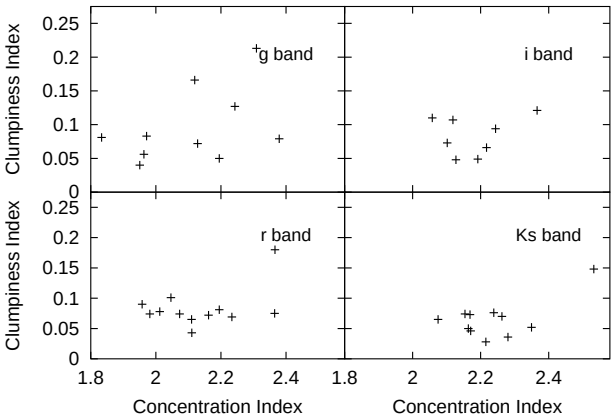

Figure 5.28: Same as Fig. 5.27 but using the square method for deriving S.

In Fig. 5.30 the A is plotted against surface brightnesses of the galaxies. The trend shown in the **A versus** μ diagram is very small. However, galaxies with lower μ seem to be more asymmetric. This is maybe again an effect of AMOR where the program cannot derive an accurate value for A if the center of a galaxy can not be determined because of a low central brightness. Or the trend is due to the influence of dust: galaxies at low μ tend to have a more chaotic and knotty dust structure compared to the symmetric appearance of dust lanes at higher μ values. This effect is again more dominant at optical dust sensitive bands.

S versus μ A clear correlation is shown between the clumpiness values and the μ in Fig. 5.31 (and Fig. 5.32 using the square method for S): galaxies with higher μ are less clumpy than galaxies with low μ. That means that the dust distribution seems to be more chaotic in low μ galaxies.

5.4.7 Discussion

The meaning of the CI is described in the last section. Here the other parameters of the CAS system are discussed. A is sensitive to any feature that produces asymmetric light distribution such as star formation, signs of interaction (tidal tails, warps, lopsided disks, etc.) and flocculent attenuation by dust. For non edge-on galaxies A is found to be especially sensitive to features most probably caused by interaction and mergers (Conselice et al. 2000a,b). The symmetry of an object will be significantly distorted while the object undergoes a major merger event (Conselice 2003). In addition, the sensitivity of A depends on the phase of the merger and Conselice (2003) showed that the largest asymmetries occur during the central phase of a major merger.

The most obvious trend of the A edge-on galaxies is that A ranges between 0.05 and 0.35 in the g band whereas in the K_s the values are much more at a lower level (0.05 - 0.15). Therefore, the value of A depends mostly on the used band for this investigation: A galaxy seems to be symmetric in a dust-free image but if the dust is added to this image the galaxy appears to be more asymmetric. This trend is also similar for the clumpiness parameter S. In the optical bands (g, r, i) A is correlated with the distribution of dust: larger A values are visible in the systems with clumped structures. A can

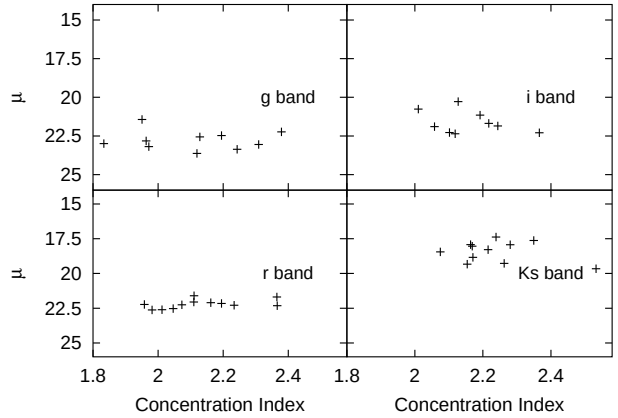

Figure 5.29: Correlation between the concentration index and the total surface brightness in the optical and the NIR bands. No correlation between these two parameters is found.

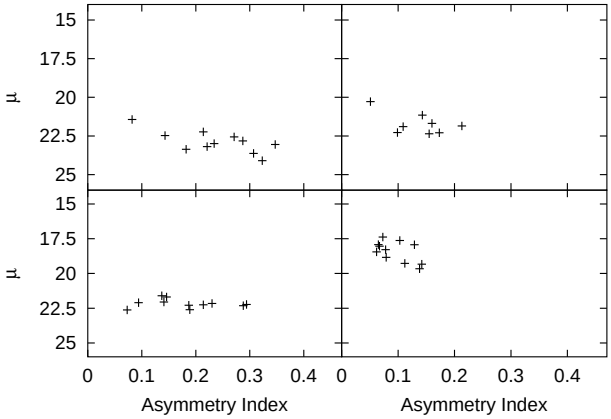

Figure 5.30: Correlation between the asymmetry index and the total surface brightness in the optical and the NIR bands. No correlation between these two parameters is found.

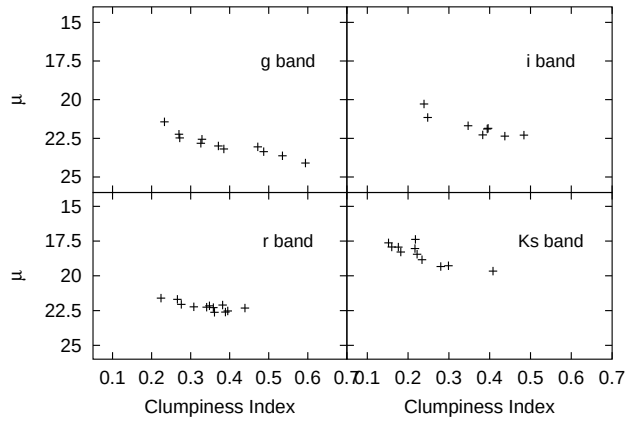

Figure 5.31: Correlation between the clumpiness index (absolute values method) and the total surface brightness in the optical and the NIR bands. Galaxies with lower surface brightnesses have a more clumpy distribution.

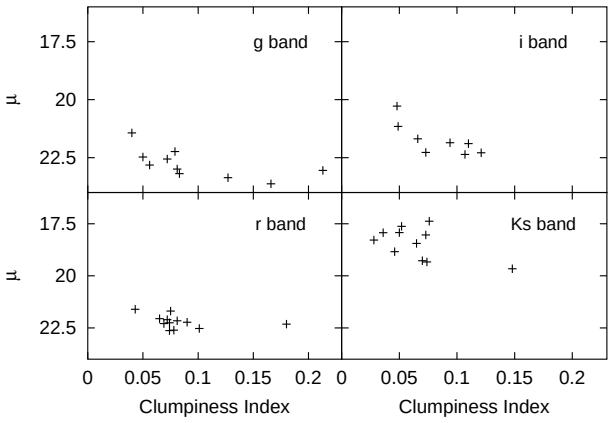

Figure 5.32: Correlation between the clumpiness index (square values method) and the total surface brightness in the optical and the NIR bands. Galaxies with lower surface brightnesses have a more clumpy distribution.

possibly disturbed by a technical detection effect of the program AMOR as discussed before. But the trend in Fig. 5.25 can be also interpreted due to physical effects of interaction, e.g., warps, lopsided disks or tidals in galaxies with central light distribution. However, the values of A are generally below

the merger limit value of 0.35 as defined by Conselice (2003).

The smoothness or clumpiness factor S is sensitive to star formation which produces knots and other clumpy features in galaxy images. Therefore S is used as a morphological discriminator because it is known that star formation is a function of the Hubble type. Early-type galaxies have low star formation but with later types the fraction of forming stars increases.

For edge-on disk galaxies the S is a discriminator of the distribution of dust. It can only be used for measuring the star formation if the images have a high resolution because star formation regions are much smaller than dust knots in edge-on seen galaxies. Galaxies with low μ exhibit a more chaotic distribution of dust. This result is in agreement with the observation of the bulgeless edge-on low surface brightness galaxy UGC 7321, a typical superthin simple disk galaxy. This galaxy is relatively near (21 Mpc) and the dust structure is therefore studied in detail by Matthews & Wood (2001). They found that the dust in this galaxy has a clumpy and patchy distribution.

Dalcanton et al. (2004) found that the appearance of the dust in edge-on galaxies is correlated with the rotation velocity of the disk stars, i.e., galaxy mass. Organized dust lanes appear in high surface brightness objects with a relatively rapid rotation velocity. In galaxies with rotation velocities below $V_c = 120$ km s^{-1} the dust has not yet settled into a thin dust lane. The dust distribution of these simple disk galaxies with typically a low surface brightness is clumpy and diffuse out to large scale heights.

The clumpy distribution of dust in LSB galaxies may also be connected with the amount of the dark halo. It is shown by Karachentsev (1991) that the ratio of total mass to luminosity of a simple disk galaxy is seen to increase with a decrease in surface brightness indicating that the relative fraction of dark matter increases from normal spirals to LSB simple disk galaxies.

5.5 Detailed Structure Analysis

5.5.1 Sample Selection

In this section we analyze the vertical structure of the observed galaxies in great detail For that reason it is important to use only extended galaxies with good quality of the observations. That means that all galaxies were visually inspected in order to select only those objects that are extended and not too small or faint.

The final sample consists out of ten galaxies. The names, K_s band magnitudes and K_s band Petrosian major axes are presented in the Table 5.9. The magnitudes and axes were again derived with AMOR using elliptical apertures around the galaxies. In addition, this Table contains the magnitudes and semi-major axes of the same galaxies taken from the 2MASS-selected Flat Galaxy Catalog (2MFGC) by Mitronova et al. (2004) for comparison. The values compared with ours are very similar. This 2MFGC contains 18020 disk-like galaxies selected from the Extended Source Catalog of the Two Micron All-Sky Survey (XSC 2MASS Cutry & Skrutski 1998) based on their 2MASS axial ratio $a/b \geq 3$. The 2MASS was carried out in the NIR J, H, and K_s bands with two 1.3 m telescopes in Chile and Arizona, respectively (Skrutskie et al. 1997).

5.5.2 Isophote Fitting

We are using the MIDAS `FIT/ELL3` task to fit elliptical isophotes to the selected galaxies in the K_s band as described in Sect. 5.4.1. The aim is to create surface brightness profiles from the azimuthally averaged elliptical isophote levels. The process is the same as given in Sect. 5.4.1. The steps of the fitted isophote levels was selected in order to have ≈ 2 measured data points at each pixel for the vertical profiles, i.e., steps of 0.1 for the larger galaxies and 0.075 for the smaller objects. The output tables of `FIT/ELL3` will be used for the creation of the azimuthally averaged surface brightness profiles.

In order to have an estimation of the quality of the plots we derived the magnitude of the background noise on the one sigma level, i.e., the magnitude of the sigma/standard deviation of the background (S/N=1). This value is computed on all images with masked objects using the IRAF

Table 5.9: The Magnitudes and Petrosian Radii of the Targets in Comparison with 2MFGC

SDSS Name	Prog. ID	2MFGC Name	Petro mag$_{K_s}$	2MFGC mag$_{K_s}$	Petrorad [″]	2MFGC rad[″]
SDSS J005315.44-084416.4	3A	2MFGC 641	13.291 ± 0.002486572	13.24	23.49619	16.9
SDSS J005624.60-010834.7	1A	2MFGC 682	12.307 ± 0.001215454	12.31	26.93059	21.1
SDSS J012302.78-091745.7	3B	–	13.245 ± 0.002915194	0	22.95533	0
SDSS J013551.83-095646.5	2B	2MFGC 1214	13.453 ± 0.005364452	13.43	39.05338	20.5
SDSS J014102.09-092022.6	1C	2MFGC 1271	13.327 ± 0.004411795	13.42	43.075	18.7
SDSS J031144.77+010241.4	1D	2MFGC 2610	13.586 ± 0.007286271	13.81	59.69664	30.24
SDSS J031513.32-071614.6	3D	2MFGC 2660	11.776 ± 9.349901E-4	11.86	47.56262	35.4
SDSS J033923.33-053631.2	3E-altern	2MFGC 3032	13.477 ± 0.00430552	13.4	27.01843	18.3
SDSS J094801.01+020111.2	3E	2MFGC 7595	12.76 ± 0.003079429	11.89	33.86678	23.5
SDSS J095849.83+005012.1	2E-altern	–	13.45 ± 0.007312807	0	55.11945	0

`imstat` task. Then, the magnitude of the 1σ level is given by

$$mag(1\sigma) = -2.5\log(\frac{Flux(1\sigma)}{0.288^2}) \tag{5.8}$$

Additionally, also the 0.5 σ and the 2 σ levels are derived with, e.g., $mag(0.5\sigma) = mag(1\sigma) = (-2.5\log(0.5))$. The total magnitude error as given in in Table 5.9 is

$$err_{tot} = \frac{1}{S/N_{tot}} \tag{5.9}$$

with

$$S/N_{tot} = \frac{flux_{tot}}{\sqrt{\#_{pixel}} \cdot \sigma} \tag{5.10}$$

where the $flux_{tot}$ and the $\#_{pixel}$ are outputs from AMOR and are the total flux within the elliptical aperture and the number of pixels within this aperture, respectively. The σ is the standard deviation of the background of the masked images as explained above.

5.5.3 Creation of Color Maps

In order to analyze the trends of the vertical structure of these targets in the NIR K_s and optical r band and produce color maps, the images have to be scaled to a common pixel scale and corrected for a common seeing in both passbands. Before that, all images in K_s and r were rotated to be horizontal. This is performed using IRAF's `rotate` command with a spline interpolation for the flux in the rotated pixels. The position angles of the objects where obtained from the outtables of the before performed ellipse fittings. The pixel scale of the K_s images (with 0.288 arcsec/pixel) was corrected to that of the r band images from the SDSS (0.396 arcsec/pixel) using the IRAF `magnify` command with spline interpolation and flux conservation of the magnified pixels.

Although the pixel scale is now set to a common value, the images in both bands are observed under different seeing conditions. In order to correct for this effect, the broadening of radial stellar profiles had to be determined. The value which quantifies the broadening due to the atmospheric seeing is called "full width half maximum" (FWHM) of the profile. This was measured on several stars (≈10 stars) around the objects on the r and K_s band images with IRAF's `imexam`. This task computes a Moffat profile of the measured stars and prints the value of the FWHM. We took the median value of the measured FWHMs and derived the standard deviation σ of the median FWHM:

$$\sigma = \frac{Median(FWHM)}{2\sqrt{2 \cdot \ln(2)}} = \frac{Median(FWHM)}{2.3548} \tag{5.11}$$

In all cases (except for object 1D) the seeing is much better for the K_s than the r images. Therefore the seeing of the NIR images has to be downgraded.

In order to derive this convolution value for the NIR images (or for the SDSS image for object 1D) we used the following expression

$$\sigma_{corr} = \sqrt{\sigma(SDSS)^2 - \sigma(K_s)^2} \tag{5.12}$$

This means that the σ value of the current band has to be subtracted from the larger σ value from the other band in order to convolve the current band with the smaller σ for a common seeing. This correction was performed with the IRAF `gauss` task using a smoothing value σ_{corr} and a truncation of three pixels. The new seeing values of the corrected images were checked then with `imexam`.

After that, the frames in both filters have the same orientation, pixel size and seeing values. The galaxy image plus a common region around the target was extracted from these corrected images and the position offsets between the optical and NIR image were measured with `xregister`. The offsets were then used to shift the object in both filters to a common position. The color maps of the positioned images was the created with the extracted and shifted images:

$$CM_i = \frac{K_{s_{image}}}{r_{image}} \tag{5.13}$$

where CM_i is the inverse color map frame. We decided to use the inverse color map because it emphasizes the dominant zones in the NIR with bright pixels. The optical (r band) regions in the frame are indicated as dark pixels. In addition, we used the corrected frames (which are used for the color maps) for again fitting elliptical isophotes in the same way as described in Sect. 5.5.2.

5.5.4 Galaxy Model Fitting

The fitting of the vertical and radial surface brightness profiles of galaxies with the aid of adequate models has a long tradition for the analysis of structural parameters. The first approaches to model the brightness distributions of face-on or moderately inclined disk galaxies were outlined by de Vaucelours (1948) and Freeman (1970). The distribution of light in a spiral galaxy assumes i) a spheroidal component–the bulge–which can be fitted using an "$r^{1/4}$" law: $\log I(r) \propto -r^{1/4}$, where I is the surface brightness and r the distance from the center; ii) an infinitesimally thin disk following the exponential behavior $I(r) = I_0 \exp(\frac{-r}{h})$ where I_0 is the central surface brightness and h the scale parameter. The scale parameter is the scale length where I_0 has decreased to a value of $I_0 \cdot (1/e)$. The galaxy components can be fitted very successful with this function but it can not be explained within any physical framework.

A pioneering study was published 1981 by van der Kruit & Searle where they presented a model for the three-dimensional distribution of light in galactic disks. Their model assumes a locally isothermal, self gravitating disk which is derived from observations of the Galactic disk in the solar neighborhood—the "old stellar disk." The space-luminosity L can be described by

$$L(r,z) = L_0 \cdot e^{\frac{-r}{h}} \cdot \nu(z) \tag{5.14}$$

$$\nu(z) = \mathrm{sech}^2(\frac{z}{z_0}) \tag{5.15}$$

L_0 is the central luminosity surface density, z is the distance from the galactic midplane and z_0 the vertical scale parameter. The function $\nu(z)$ has a useful approximation for large and small heights, respectively:

$$\frac{z}{z_0} \gg 1: \qquad \nu(z) = 4\exp(\frac{-2z}{z_0}) \tag{5.16}$$

$$\frac{z}{z_0} \ll 1: \qquad \nu(z) = \exp(\frac{-z^2}{z_0^2}) \tag{5.17}$$

This model includes dust and assumes that the vertical scale parameter z_0 is independent from the radial radius r. z_0 is derived from the vertical stellar velocity dispersion and is connected with the

scale height $z_0 = 2h_z$. Today, the preferred models of surface photometry vary slightly at different studies. For this study we follow the models used by Matthews et al. (1999b) for the radial and an exponential model (Matthews 2000) for the vertical light distribution, respectively.

Matthews et al. (1999b) studied the edge-on superthin galaxy UGC 7321 and followed the model by van der Kruit & Searle (1981a). The disk with an exponential radial brightness distribution viewed edge-on can be expressed along the galaxy midplane (z=0) as

$$L(r) = L_0 \cdot (\frac{r}{h_r}) K_1(\frac{r}{h_r}) \tag{5.18}$$

where K_1 is the modified Bessel function of first order and h_r is the scale length (e.g., van der Kruit & Searle 1981). At small radii ($r/h_r \ll 1$), this expression can be approximated as

$$L(r) \approx L_0[1 + (\frac{r^2}{2h_r^2} \ln(\frac{r}{2h_r})] \tag{5.19}$$

This model implies a slight flattening of the light profile at small radii compared with a simple, unprojected exponential function (i.e., $L(r) = L_0 \exp(\frac{-r}{h})$). At large radii ($r/h_r \gg 1$), one can write

$$L(r) \approx L_0(\frac{\pi r}{2h_r})^{\frac{1}{2}} \cdot \exp(\frac{-r}{h_r}). \tag{5.20}$$

From Eq. 5.20 we see that the radial distribution will tend to the simple exponential for $r \to \infty$ but the term $\sqrt{r}$ prevents this from occurring rapidly. Because of the $\sqrt{r}$ factor, this produces a slightly less steep profile than a pure exponential model with the same scale length. As a result, the scale length of a simple exponential profile to an edge-on disk will be overestimated by a factor of less than 10% at $r > 2h$ (van der Kruit & Searle 1981a).

For the vertical distribution of the well resolved galaxy UGC 7321, Matthews (2000) used different model approaches to fit this galaxy. Firstly, she used the van der Kruit & Searle (1981a) model of a disk as self-gravitating locally isothermally sheets:

$$L(z) = L_0 \cdot \nu(z) = L_0 \cdot \mathrm{sech}^2(\frac{z}{z_0}). \tag{5.21}$$

Disks may deviate from isothermal near the galactic midplane (van der Kruit & Searle 1981a) and therefore Matthews (2000) included a model in her analysis which differs from a $\mathrm{sech}^2(z)$ model only at small heights z:

$$L(z) = L_0 \cdot \mathrm{sech}(\frac{z}{h_z}). \tag{5.22}$$

The scale height $h_z = z_0/2$ and this model successfully fits the light distributions of some nearby galaxies (e.g., Rice et al. 1996). With these two models Matthews (2000) can fit the found multi-component vertical structure in UGC 7321. However, for the general distribution of less well resolved galaxies and for studying the large-scale components of edge-ons with azimuthally averaged profiles we prefer to use a simple exponential profile

$$L(z) = L_0 \exp(\frac{z}{h_z}). \tag{5.23}$$

This model should be exact enough in order to account for general disk structure deviations (e.g., bulge, thick disks) and is already successfully used to model the vertical disk structure in the MW and other galaxies (e.g., Barteldrees & Dettmar 1994; de Grijs & Peletier 1997; Fry et al. 1999; Matthews & van Driel 2000). However, small scale variations due to, e.g., HII-regions, perturbations and other signs or interaction, may be better fitted with the sech models. The models 5.21, 5.22, 5.23 are found to be special cases of a more general family of fitting functions (de Grijs et al. 1997).

In order to translate the luminosity density into the observed surface brightness we assume that the galaxies are inclined perfectly edge on. van der Kruit & Searle (1981a) as well as de Grijs et al. (1997) demonstrated that a slightly non-90° inclination has minimal impact on the derived structure

parameters, only that the scale height is slightly overestimated and the central surface brightness is underestimated (larger numerical value for μ_0) (Bizyaev & Kajsin 2004). We also assume that the scale heights are independent of projected radius for late-type galaxies (van der Kruit & Searle 1981a; de Grijs & Peletier 1997; Bizyaev & Mitronova 2002).[7] Because our sample contains mostly simple disk galaxies with negligible bulge components no attempt was performed to decompose a bulge component from the surface brightness distributions. For that reason, the innermost pixels were excluded (see later).

Method of Fitting

The azimuthally averaged surface brightness profiles in the K_s band of our target galaxies were fitted with a nonlinear least-squares Marquart-Levenberg algorithm using gnuplot. gnuplot is a command-driven interactive function and data plotting program (Williams et al. 1998). We used gnuplot to find the best parameters (central surface brightness and scale parameters) which describe the light distributions of the targets.

gnuplot provides the possibility to include the error bars and to use these values for weighting the fit function ($\frac{1}{s^2}$). The innermost pixels of the profiles were excluded from the fitting in order to avoid light contamination from central star clusters (Seth et al. 2006), bulges and nuclei which can affect the light distribution of the target galaxies. In order to evaluate the existence of a bulge or a similar component we assume that these components would create a central light excess. Therefore we plotted the central part of the radius r of the targets versus surface brightness μ in Fig. 5.33. Here it is seen, that the central light excess is small and affects only the innermost 2-4 pixels of the galaxies on average. Hence the target galaxies are assumed to be mostly bulgeless.

In order to quantify the number of pixels where the central component dominates over the disk we assume that the light from the bulge/nucleus can be indicated as a central light excess with a round shape. The change of the shape of the isophote levels can be illustrated in Fig. 5.34 where the minor axis z is plotted versus the axial ratio $\frac{r}{z}$. This figure is then used to determine the bulge contamination by counting the pixels which have round shape before they change the slope to flatter shapes.

[7] de Grijs & Peletier (1997) and Narayan & Jog (2002) showed that the stellar scale height is radially increasing in disk galaxies of types earlier than Sc.

5.5.5 Results

Vertical Surface Brightness Profiles

The vertical profiles of the azimuthally averaged elliptical isophotes are presented at the left side of Figs. 5.35 - 5.44. The dotted, vertical lines represent the 2σ (black), 1σ (blue) and 0.5σ (yellow) levels above the background. The error bars are printed from the noise values as provided by the profile fitting task `FIT/ELL3` and are converted into magnitudes. These error bars are included in the profile fitting process in order to perform weighted fits. The galaxy profiles were fit from the center out to a surface brightness limit of 2 σ above the background.

The distance from the galactic midplane (or height z) is given in pixels and the surface brightness in mag arcsec^{-2} in the K_s band. The vertical model of Eq. 5.23 is translated into surface brightness via $\mu(z) = -2.5\log(\frac{L_0}{0.288^2}\cdot\exp(\frac{z}{h_z}))$. And due to the logarithmic expression of magnitudes the vertical model can plotted using the linear function $\mu(z) = \mu_0 + k\cdot z$ where μ_0 is the central surface brightness (the cut through the ordinate) and k is the slope of the function. The slope from the linear function can be translated into scale height by setting the surface brightness $\mu = \mu_0$ and the height $z = h_z$ (i.e., the height where the central surface brightness has decreased by a factor of $\frac{1}{e}$):

$$k = \frac{\Delta\mu}{\Delta z} = \frac{\mu_0}{h_z} = \frac{\log(2.5)\cdot e}{h_z} = \frac{1.081713}{h_z} \tag{5.24}$$

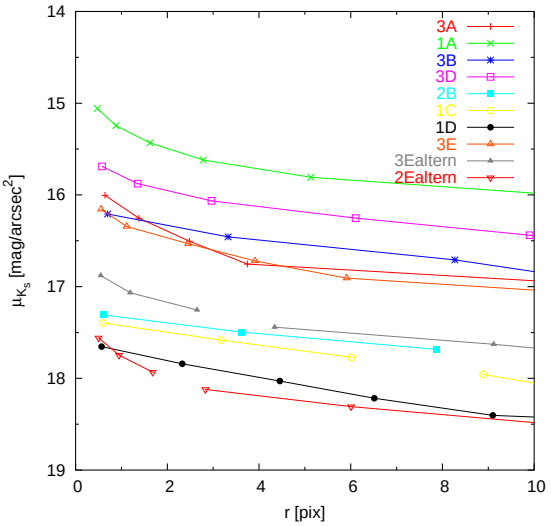

Figure 5.33: This figure shows the radial surface brightness profiles of the central ten pixels of the galaxy's radius. The profiles of the different colors indicate the different target galaxies as shown in the legend. The central light excess is very small indicating that the galaxies are nearly bulgeless.

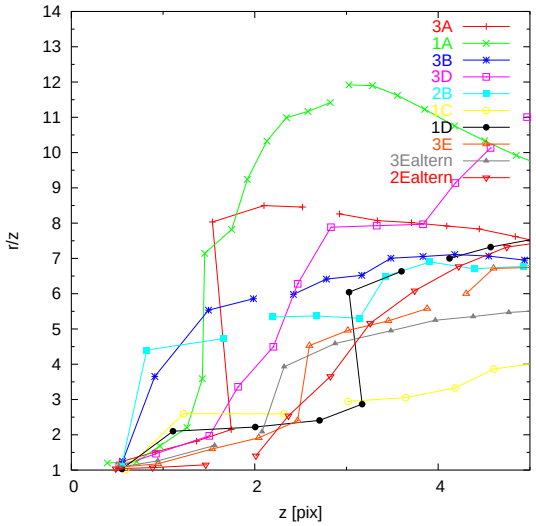

Figure 5.34: This figure shows the axial ratio (ordinate) in correlation with the central five pixels of the vertical averaged height (abscissa). The different color coded lines corresponds to the different target galaxies as indicated in the legend. This figure shows that the innermost pixels have small axial ratios and then their value is suddenly rising to high values. This indicates round isophotes at the nuclear region but the disk is already dominant at small vertical distances.

The vertical profile of three (3E, 3Ealtern, 1D) out of the ten targets can be fitted with a single exponential disk model, see Eq. 5.23 down to the 2σ level. This model is illustrated with a green line and indicated as "Disk" in the legend. The profile of at least three targets (1A, 3B, 3D) shows light excess at large heights above the midplane similar to what is expected from a thick disk (TD) (Burstein 1979; van der Kruit & Searle 1981a,b). The light can not be fitted with a single disk indicating an

additional disk component. This TD surrounds the inner disk, which is the "old thin disk." Because of the differences in the stellar density distribution, both disks have different slopes of their profiles. Otherwise, both disks show the general exponential character of galactic disks and can therefore be fitted with the Eq. 5.23.

The objects 1C, 2Ealtern and 3A show also a double disk structure and their profiles can be fitted with two disks. But these objects show their light excess at very low luminosity isophotes near the 2σ limit. This excess exceeds this limit and remains until the 0.5σ limit above the background. In these cases we conclude that we detect faint TD. However, it must be admitted that the profiles of 1C, 2Ealtern, 3A and particularly 2B have large error bars and consequently can be fitted with a single exponential disk model. The fitting parameters (μ_0, h_z) are different for both disks because the TD has a smaller central stellar density which is expressed via a lower surface brightness. The TD is also more extended (i.e., larger scale height) than the smaller and more compact thin disk. The existence of the two vertical disk components is clearly shown by a break in the vertical profile. If the TD is observed then both disk components are fitted and indicated as "Disk" (green line) and "Thick Disk" (blue line) in the figure's legend.

The vertical fitting parameters are collected in Table 5.10. It contains the name of the galaxy in Col. (1) and the program ID in Col. (2). The scale height of the thin disk in pixel values and in kpc are shown in Cols. (3) and (4), respectively. The same is given in Cols. (5) and (6) for the TD if detected. In order to derive the scale parameters in kpc we used the geometrical expression derived from the theorem of tangent $h_z[kpc] = \frac{h_z[pix] \cdot d \cdot 0.288 \cdot 1000}{206264.8}$, using 0.288 pixel per arcsec and the factor 1000 to convert the result into Mpc. The factor 206264.8 is one radians in arcsec. The distance $d[Mpc] = \frac{cz}{H_0}$ is derived from the redshifts of Table 5.1 using a speed of light $c = 299792.458 \mathrm{km\ s^{-1}}$ and a Hubble constant $H_0 = 70 (\mathrm{km\ s^{-1}})\ \mathrm{Mpc^{-1}}$. The central surface brightness μ_0 for the thin disk and TD is given in Cols. (7) and (8) respectively. The position of the break of the slope (i.e., where the thick disk starts to dominate the vertical luminosity distribution above the thin disk) is noticed in Col. (9) in kpc. This position is placed by eye using the two surrounding full pixel of z as lower and upper value of where the break occurs. The errors of the fitted parameters are the asymptotic standard errors as derived with gnuplot. In addition, the error of the physical scale heights in kpc contains also the redshift error from Table 5.1 but it does not include any correction of peculiar velocities of the galaxy.

The values for the scale height in Table 5.10 of the old thin disk are comparable with typical spiral galaxy values which range $470\mathrm{pc} \leq h_z \leq 620\mathrm{pc}$ (de Grijs & van der Kruit 1996), and some of our targets have lower values. The scale heights for the thin disk found by Yoachim & Dalcanton (2006) for their flat galaxy sample with two component plots have also comparable values. Their values range from 100pc to 550pc with an average of 305pc. Our mean is 426pc±147pc for all galaxies and 403pc±156pc for the objects fitted with two exponential disks. The reason that our values are below of those of (de Grijs & van der Kruit 1996) are that they used the best model out of a pool of disk models instead of a simple exponential model as we did.

The offset between the sample by Yoachim & Dalcanton (2006) and ours is due to the use of different filters. We used the NIR K_s filter and they used the optical R band. This means that we trace in the NIR the light from redder and probably older stars and the light is not affected from the dust extinction. As shown in the introduction, the older stars exhibit larger scale heights. In addition, differences between these studies are also the effect of resolution of the galaxies because Yoachim & Dalcanton (2006)'s objects are generally brighter and more extended than ours. Our values of the scale height of the thin disks are also comparable to that of the old thin disk of the MW which is about 300pc for G, K, M stars (Buser 2000). Resolution effects are may an additional reason that our scale heights are larger compared to the galaxy fits for the closer flat galaxies from the sample of Yoachim & Dalcanton (2006).

The mean of the scale heights of the TD is 543pc±206pc for all galaxies with a thin disk and TD component. The mean for the objects with the strongest TD evidence (1A, 3B, 3D) is 698pc±136pc. This value is also comparable with the value of the TD scale height in the MW ($600\mathrm{pc} < h_z TD < 1300\mathrm{pc}$ (Buser 2000)). Our result has also a similar value as found by Yoachim & Dalcanton (2006) which is 700pc on average. Their scale heights range between 325pc and 2000pc whereas our sample shows

values between 260pc and 850pc of the different targets.

We measured the position of the break of the slope in the vertical surface brightness profiles where the TD starts to dominate the thin disk light (Col. 9 in Table 5.10). This break generally occurs between 500pc and 2000pc distance from the galactic midplanes. The mean value of the break for galaxies with clear TD (1A, 3B, 3D) is 1601pc±335pc. This is similar to the heights of the break shown in other studies (e.g., van der Kruit & Searle 1981a,b) where the break is located at ≈2kpc. Also Burstein (1979) reported flattening of the vertical profiles with typical distance scale of a few kpc.

Correlation between Thin Disk and Thick Disk Parameters

The ratio of the scale heights of the TD and the thin disk is 1.6±1.3 for the clear TD galaxies 1A, 3B and 3D and it is 1.4±1.8 for all objects with a TD detection in their profiles. These values lie at the lower end of the value spectrum found by Yoachim & Dalcanton (2006). Their values are $1.5< \frac{h_z TD}{h_z} <4.5$ with a median ratio of 2.35. The difference to our value is due to the differences of the scale heights of the thin disks between these studies as discussed above.

In the Fig. 5.45 the scale height of the thin disk versus the central surface brightness of the thin disk is plotted. The same is shown in Fig. 5.46 for the TD. In these figures, the central surface brightnesses and the scale heights do not exhibit a clear correlation. If plotting the scale height of the thin disk and the TD in pixel values (Fig. 5.47) or in kpc (Fig. 5.48) a clear correlation between these two disk components is shown. Also the central surface brightnesses of both disks are correlated as shown in Fig. 5.49. The green line in the Figs. 5.47, 5.48, 5.49 indicates the linear correlation function of the same values.

Figure 5.51 and Fig. 5.52 shows the ratios between the scale height and central surface brightness of the thin disk versus that of the TD for the scale height in pixels (Fig. 5.51) and kpc (Fig. 5.52). And the inverse ratio of Fig. 5.52 are presented in Fig. 5.50. The last three figures show obvious correlations between the thin disk and the TD parameters although the scale height and central surface brightness are not correlated within the disk component (see Figs. 5.45 and 5.46). The correlations between the TD and thin disk implies that both structures have either a common origin or a common evolution, it weakens the theories where the TD stars are additionally placed into the galaxy. However, this direct accretion model may not be ruled out because our sample is small and by no means complete.

Radial Surface Brightness Profiles

On the right side of Figs. 5.35 - 5.44 the radial profiles of the azimuthally averaged elliptical isophote levels are given. The abscissa is the radius r, i.e., the major axis of the galaxy. The surface brightness μ is plotted along the ordinate. The horizontal lines represent the same sigma levels above the background as described for the vertical profiles.

The overplotted functions are the radial models as given in Eq. 5.19 and 5.20. The models are translated into surface brightnesses: $\mu(r) = -2.5\log(\frac{L_0}{0.288^2}) \cdot (1 + ((\frac{r^2}{2h_r^2}) \cdot \ln(\frac{r}{2h_r})))$ and $\mu(r) = -2.5\log(\frac{L_0}{0.288^2}) - 2.5\log(\sqrt{\frac{\pi r}{2h_r}}) - 2.5\log(\exp(\frac{-r}{h_r}))$. The model that fits the central part of the galaxy is indicated with a green line and the outer galaxy model with a blue line. The fitting parameters are initial values.

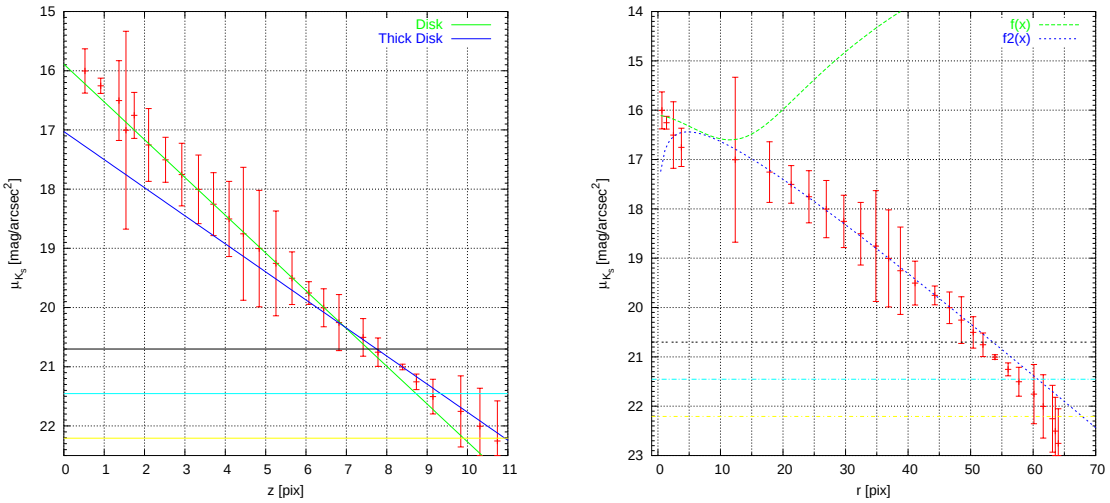

Figure 5.35: Left: Vertical K_s surface brightness distribution of the azimuthally averaged elliptical isophote levels of the galaxy 3A. The height z perpendicular to the galaxy midplane is given in pixel values. The green line illustrates the exponential old thin disk model. The blue line shows the exponential thick disk model. Right: Radial K_s surface brightness distribution of the azimuthally averaged elliptical isophote levels of 3A. The green and the blue curve presents the inner and outer part of the galaxy model by Matthews et al. (1999b). The vertical lines in both surface brightness diagrams show the 2 (black), 1 (turquoise) and 0.5 (yellow) σ levels above the background.

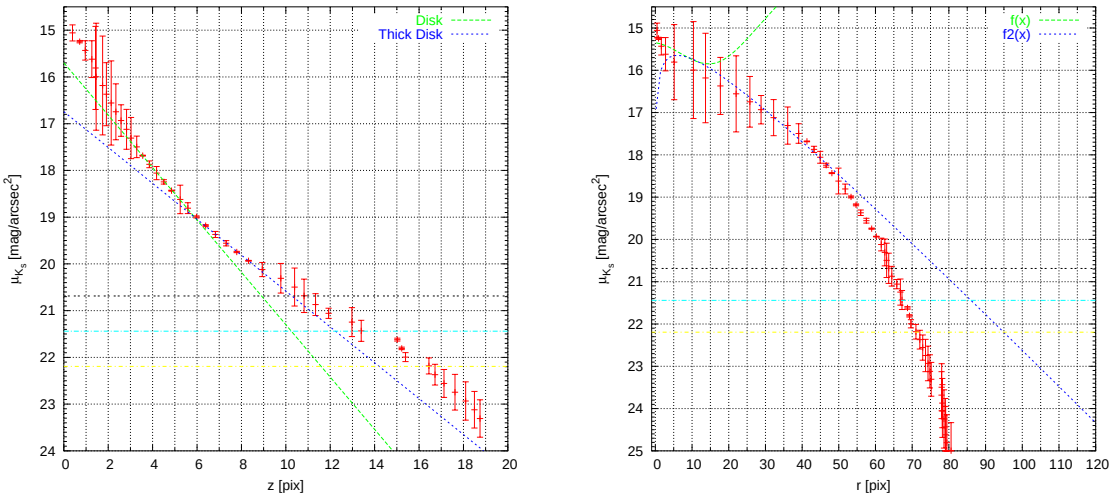

Figure 5.36: Left: Vertical K_s surface brightness distribution of the azimuthally averaged elliptical isophote levels of the galaxy 1A. The height z perpendicular to the galaxy midplane is given in pixel values. The green line illustrates the exponential old thin disk model. The blue line shows the exponential thick disk model.
Right: Radial K_s surface brightness distribution of the azimuthally averaged elliptical isophote levels of 1A. The green and the blue curve presents the inner and outer part of the galaxy model by Matthews et al. (1999b). The vertical lines in both surface brightness diagrams show the 2 (black), 1 (turquoise) and 0.5 (yellow) σ level above the background.

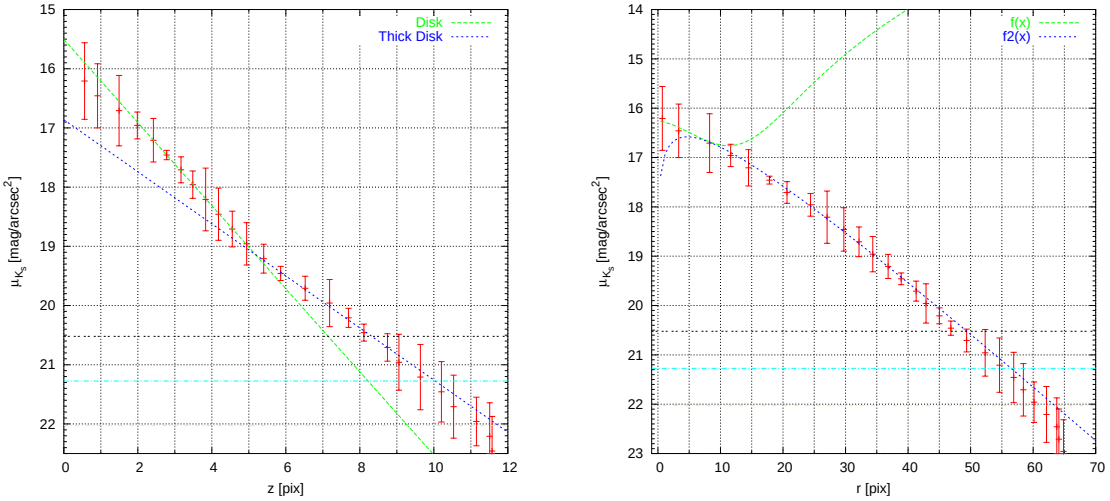

Figure 5.37: Left: Vertical K_s surface brightness distribution of the azimuthally averaged elliptical isophote levels of the galaxy 3B. The height z perpendicular to the galaxy midplane is given in pixel values. The green line illustrates the exponential old thin disk model. The blue line shows the exponential thick disk model.
Right: Radial K_s surface brightness distribution of the azimuthally averaged elliptical isophote levels of 3B. The green and the blue curve presents the inner and outer part of the galaxy model by Matthews et al. (1999b). The vertical lines in both surface brightness diagrams show the 2 (black), 1 (turquoise) and 0.5 (yellow) σ level above the background.

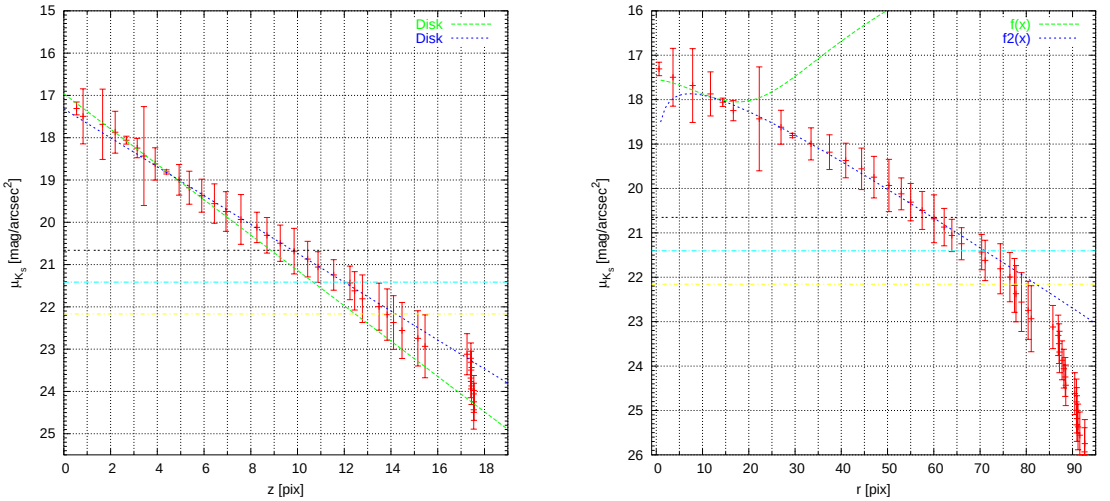

Figure 5.38: Left: Vertical K_s surface brightness distribution of the azimuthally averaged elliptical isophote levels of the galaxy 2B. The height z perpendicular to the galaxy midplane is given in pixel values. The green line illustrates the exponential old thin disk model. The blue line shows the exponential thick disk model.
Right: Radial K_s surface brightness distribution of the azimuthally averaged elliptical isophote levels of 2B. The green and the blue curve presents the inner and outer part of the galaxy model by Matthews et al. (1999b). The vertical lines in both surface brightness diagrams show the 2 (black), 1 (turquoise) and 0.5 (yellow) σ level above the background.

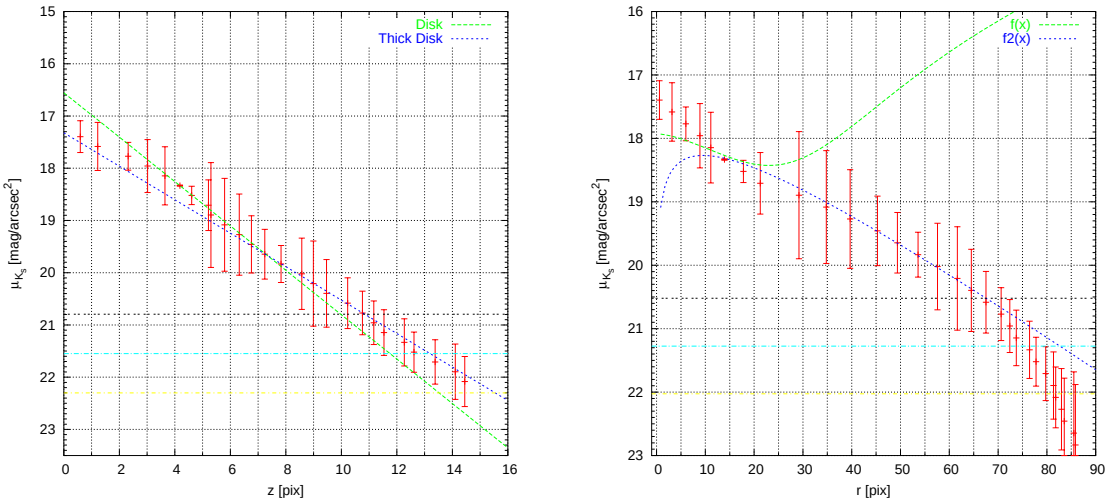

Figure 5.39: Left: Vertical K_s surface brightness distribution of the azimuthally averaged elliptical isophote levels of the galaxy 1C. The height z perpendicular to the galaxy midplane is given in pixel values. The green line illustrates the exponential old thin disk model. The blue line shows the exponential thick disk model.
Right: Radial K_s surface brightness distribution of the azimuthally averaged elliptical isophote levels of 1C. The green and the blue curve presents the inner and outer part of the galaxy model by Matthews et al. (1999b). The vertical lines in both surface brightness diagrams show the 2 (black), 1 (turquoise) and 0.5 (yellow) σ level above the background.

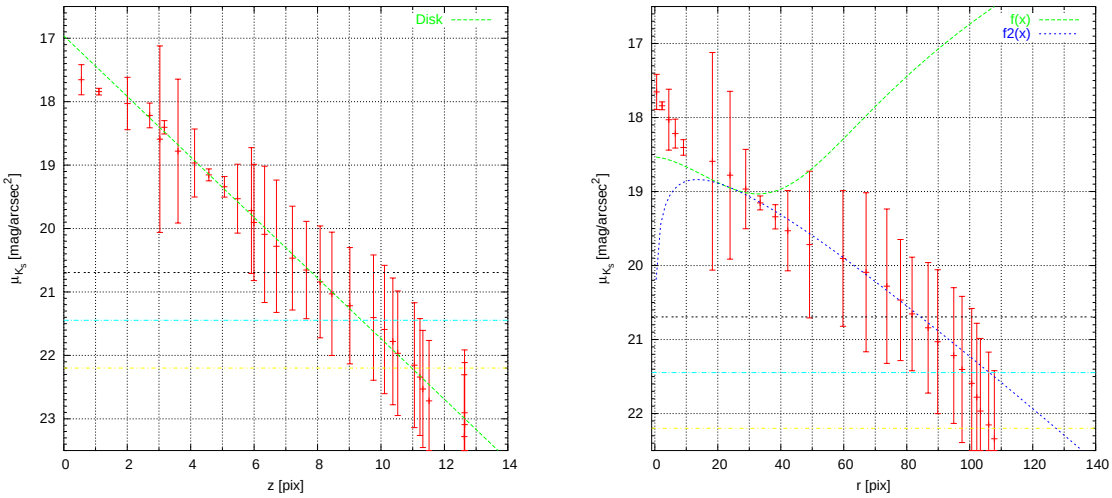

Figure 5.40: Left: Vertical K_s surface brightness distribution of the azimuthally averaged elliptical isophote levels of the galaxy 1D. The height z perpendicular to the galaxy midplane is given in pixel values. The green line illustrates the exponential old thin disk model.
Right: Radial K_s surface brightness distribution of the azimuthally averaged elliptical isophote levels of 1D. The green and the blue curve presents the inner and outer part of the galaxy model by Matthews et al. (1999b). The vertical lines in both surface brightness diagrams show the 2 (black), 1 (turquoise) and 0.5 (yellow) σ level above the background.

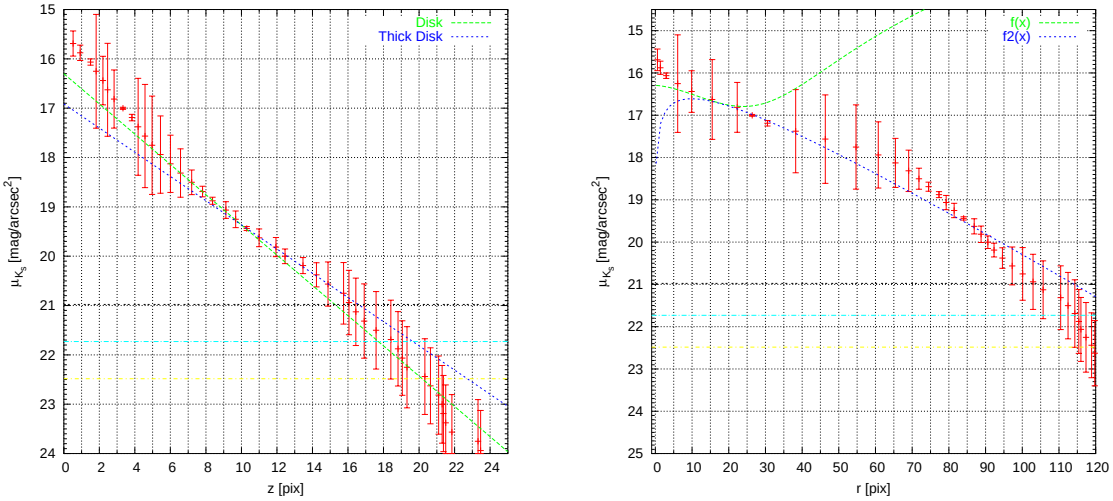

Figure 5.41: Left: Vertical K_s surface brightness distribution of the azimuthally averaged elliptical isophote levels of the galaxy 3D. The height z perpendicular to the galaxy midplane is given in pixel values. The green line illustrates the exponential old thin disk model. The blue line shows the exponential thick disk model.
Right: Radial K_s surface brightness distribution of the azimuthally averaged elliptical isophote levels of 3D. The green and the blue curve presents the inner and outer part of the galaxy model by Matthews et al. (1999b). The vertical lines in both surface brightness diagrams show the 2 (black), 1 (turquoise) and 0.5 (yellow) σ level above the background.

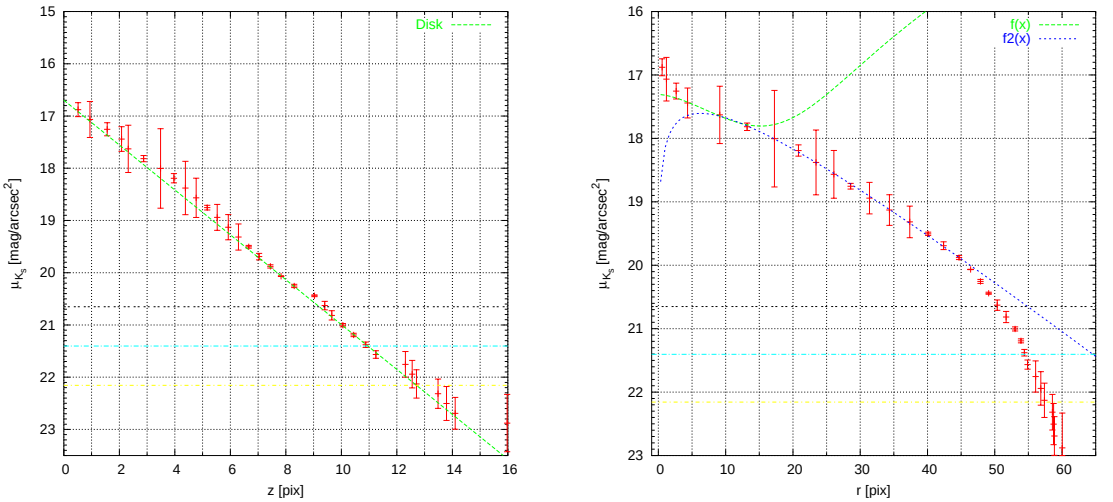

Figure 5.42: Left: Vertical K_s surface brightness distribution of the azimuthally averaged elliptical isophote levels of the galaxy 3Ealtern. The height z perpendicular to the galaxy midplane is given in pixel values. The green line illustrates the exponential old thin disk model.
Right: Radial K_s surface brightness distribution of the azimuthally averaged elliptical isophote levels of 3Ealtern. The green and the blue curve presents the inner and outer part of the galaxy model by Matthews et al. (1999b). The vertical lines in both surface brightness diagrams show the 2 (black), 1 (turquoise) and 0.5 (yellow) σ level above the background.

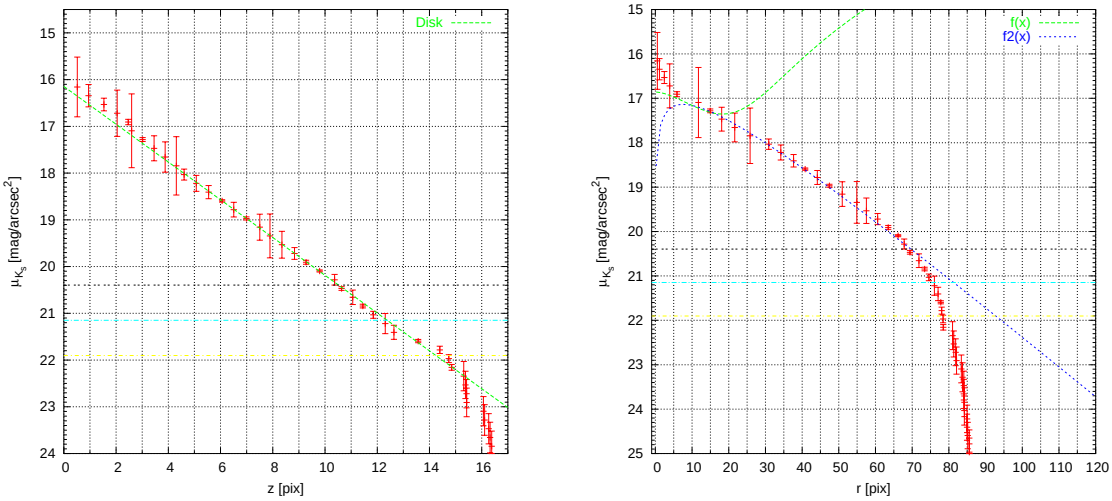

Figure 5.43: Left: Vertical K_s surface brightness distribution of the azimuthally averaged elliptical isophote levels of the galaxy 3E. The height z perpendicular to the galaxy midplane is given in pixel values. The green line illustrates the exponential old thin disk model.
Right: Radial K_s surface brightness distribution of the azimuthally averaged elliptical isophote levels of 3E. The green and the blue curve presents the inner and outer part of the galaxy model by Matthews et al. (1999b). The vertical lines in both surface brightness diagrams show the 2 (black), 1 (turquoise) and 0.5 (yellow) σ level above the background.

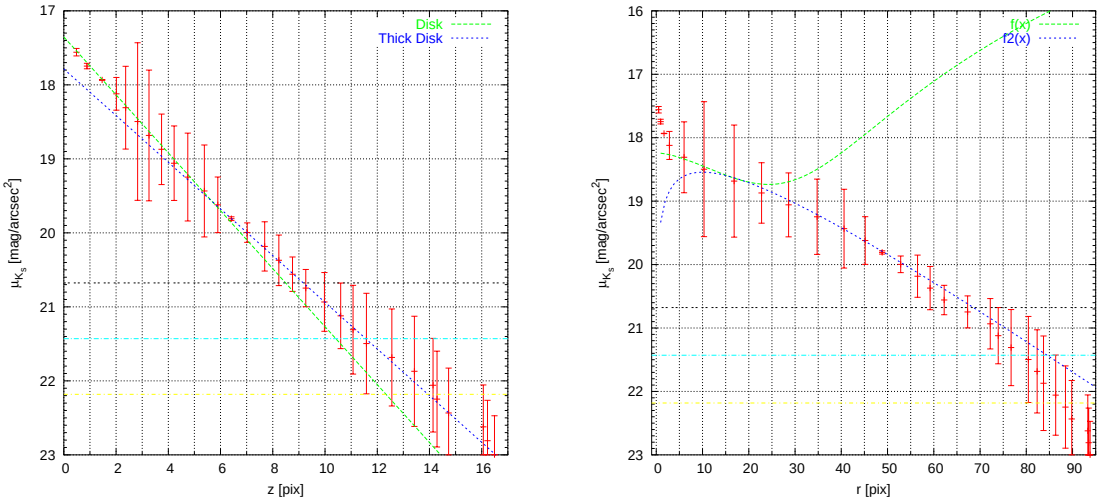

Figure 5.44: Left: Vertical K_s surface brightness distribution of the azimuthally averaged elliptical isophote levels of the galaxy 2Ealtern. The height z perpendicular to the galaxy midplane is given in pixel values. The green line illustrates the exponential old thin disk model. The blue line shows the exponential thick disk model.
Right: Radial K_s surface brightness distribution of the azimuthally averaged elliptical isophote levels of 2Ealtern. The green and the blue curve presents the inner and outer part of the galaxy model by Matthews et al. (1999b). The vertical lines in both surface brightness diagrams show the 2 (black), 1 (turquoise) and 0.5 (yellow) σ level above the background.

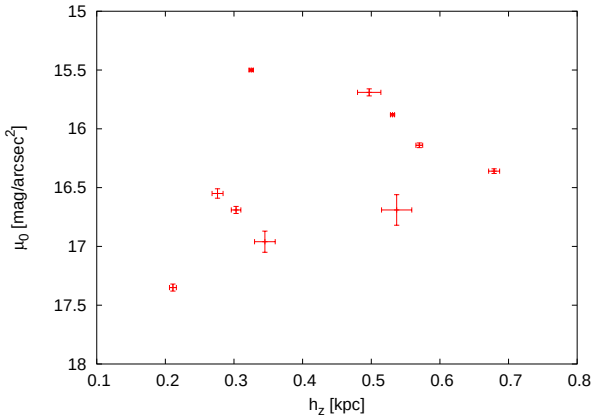

Figure 5.45: scale height versus central surface brightness of the thin disk. No correlation is shown.

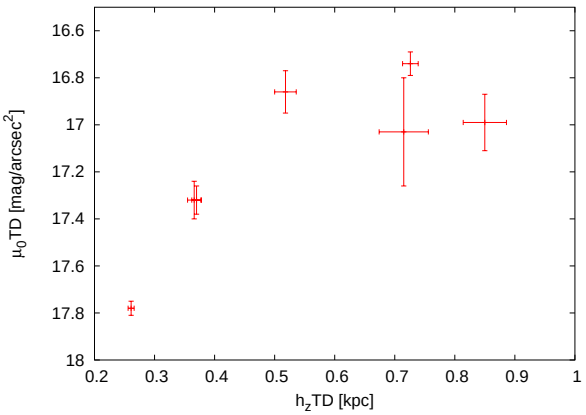

Figure 5.46: scale height versus central surface brightness of the thick disk. No correlation is shown.

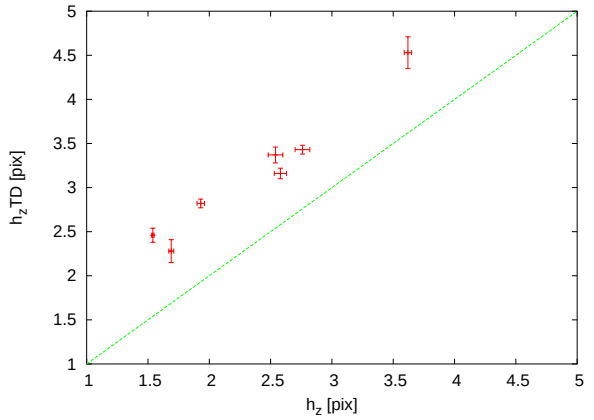

Figure 5.47: scale height of the thin disk versus scale height of the thick disk in pixel values. Galaxies with large scale heights of the thin disk have also large scale heights of the thick disk. The green line shows the correlation $h_z = h_{zTD}$.

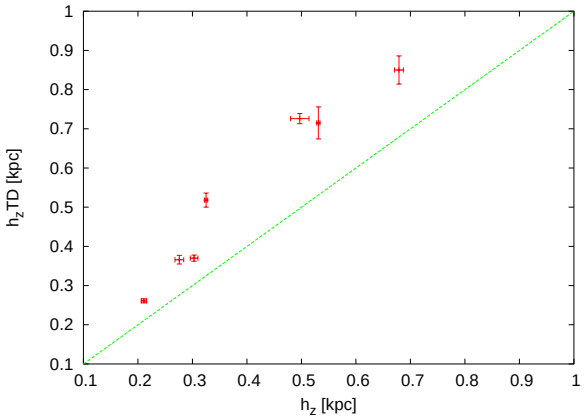

Figure 5.48: scale height of the thin disk versus scale height of the thick disk in kiloparsecs. Galaxies with large scale heights of the thin disk have also large scale heights of the thick disk. The green line shows the correlation $h_z = h_{zTD}$.

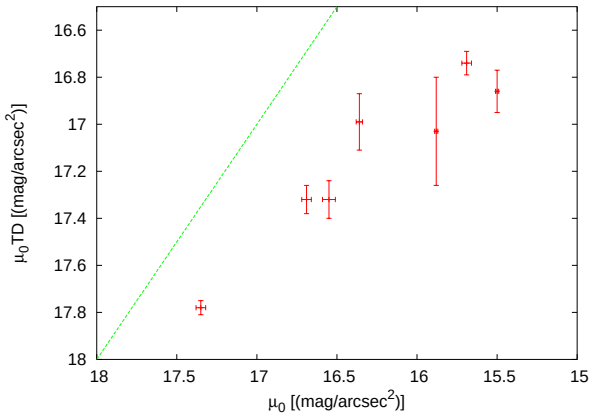

Figure 5.49: entral surface brightness of the thin disk versus the central surface brightness of the thick disk. The data seem to be linearly correlated. The green line shows the correlation $\mu_0 = \mu_{0TD}$.

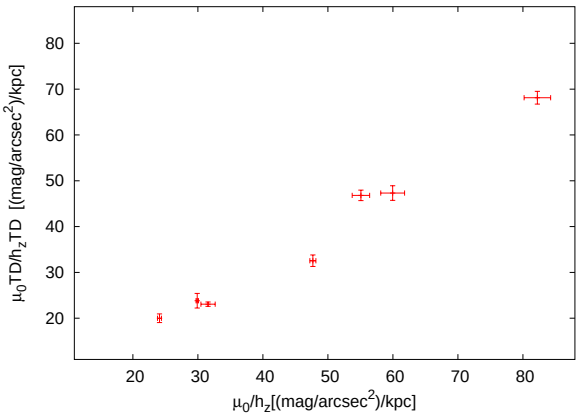

Figure 5.50: The ratio of central surface brightness to the scale height of the thin disk versus the ratio of the central surface brightness to the scale height of the thick disk. This figure shows a linear correlation of the thin and thick disk components. The scale heights are given in kiloparsecs.

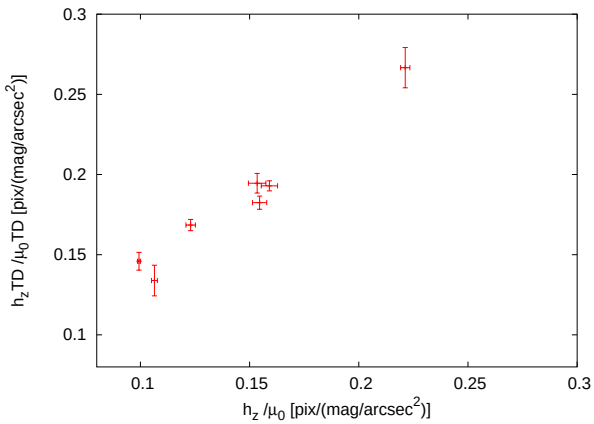

Figure 5.51: The ratio of the scale height to the central surface brightness of the thin disk versus the ratio of the scale height to the central surface brightness of the thick disk. This figure shows a linear correlation of the thin and thick disk components. The scale heights are given in pixel values.

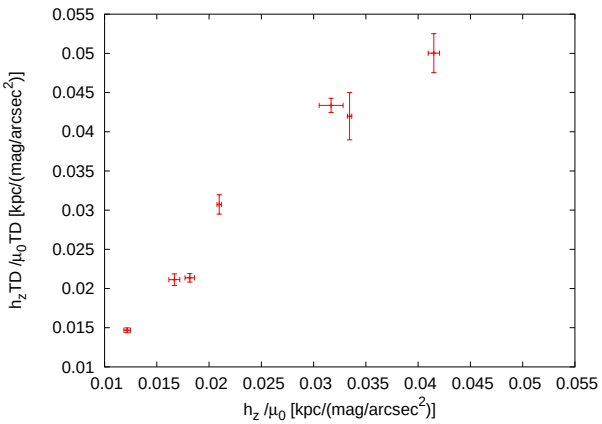

Figure 5.52: The ratio of the scale height to the central surface brightness of the thin disk versus the ratio of the scale height to the central surface brightness of the thick disk. This figure shows a linear correlation of the thin and thick disk components. The scale heights are given in kiloparsecs.

Table 5.10: The derived Structural Parameters of the Galaxies. The mean value of the thin disk scale height is $\langle h_z \rangle = 426 \pm 147$pc. For the thick disk it is $\langle h_z TD \rangle = 543 \pm 205$pc. The mean of the ratios of the scale heights is $\langle \frac{h_z TD}{h_z} \rangle = 1.4 \pm 1.8$.

Name	Prog. ID	h_z [pix]	h_z [kpc]	$h_{z_{TD}}$ [pix]	$h_{z_{TD}}$ [kpc]	μ_0	$\mu_{0_{TD}}$	bz [kpc]
SDSS J005315.44-084416.4	3A	1.69±0.02	0.531±0.003	2.28±0.13	0.715±0.041	15.88±0.01	17.03±0.23	1.882-2.195
SDSS J005624.60-010834.7	1A	1.93±0.03	0.497±0.017	2.82±0.05	0.726±0.013	15.69±0.03	16.74±0.05	1.547-1.805
SDSS J012302.78-091745.7	3B	1.54±0.01	0.325±0.003	2.46±0.08	0.518±0.018	15.50±0.01	16.86±0.09	1.054-1.265
SDSS J013551.83-095646.5	2B	2.58±0.05	0.303±0.007	3.16±0.06	0.370±0.008	16.69±0.03	17.32±0.06	0.584
SDSS J014102.09-092022.6	1C	2.54±0.06	0.276±0.008	3.37±0.09	0.366±0.011	16.55±0.04	17.32±0.08	0.759-0.867
SDSS J031144.77+010241.4	1D	2.26±0.09	0.345±0.015	–	–	16.96±0.09	–	–
SDSS J031513.32-071614.6	3D	3.62±0.03	0.679±0.008	4.53±0.18	0.850±0.036	16.36±0.02	16.99±0.12	1.876-2.064
SDSS J033923.33-053631.2	3E-altern	2.52±0.10	0.537±0.022	–	–	16.69±0.13	–	–
SDSS J094801.01+020111.2	3E	2.67±0.01	0.570±0.005	–	–	16.14±0.02	–	–
SDSS J095849.83+005012.1	2E-altern	2.76±0.06	0.211±0.005	3.43±0.05	0.261±0.005	17.35±0.03	17.78±0.03	0.457-0.533

The Shape of the Thick Disks

Fig. 5.34 already shows that the isophotes change their roundness at different isophote levels with increasing distance from the midplane. Several objects show smaller axial ratios at distant altitudes from the galactic midplane after a maximal flatness value. This behavior suggests that the outer isophotes have rounder shapes. Dalcanton & Bernstein (2002) interpret this trend as an indication of a thick disk surrounding the thin disk. In order to study this trend we present Figs. 5.53 - 5.62. These multiple diagrams contain the vertical surface brightness profile (top left) with the 2σ limit (horizontal black line) and the fitted models as described before. The bottom diagram represents the vertical profile of the axial ratio of the azimuthally averaged isophote levels and the top right diagram shows the axial ratio as a function of surface brightness.

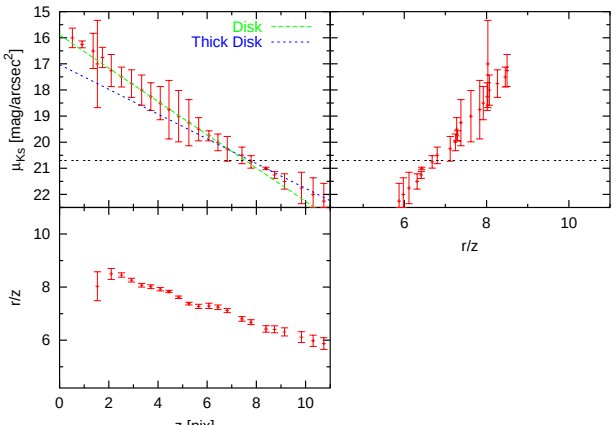

Figure 5.53: Top left: Vertical K_s surface brightness distribution of the azimuthally averaged elliptical isophote levels of 3A. The green and blue line illustrates the exponential old thin disk and thick disk model, respectively.
Top right: Axial ratio of the azimuthally averaged elliptical isophote levels in relation to the surface brightness of the levels. The vertical black line shows the 2 σ level above the background.
Bottom left: The change of the axial ratios (ordinate) with increasing distance z from the galaxy midplane (abscissa) is shown in this diagram.

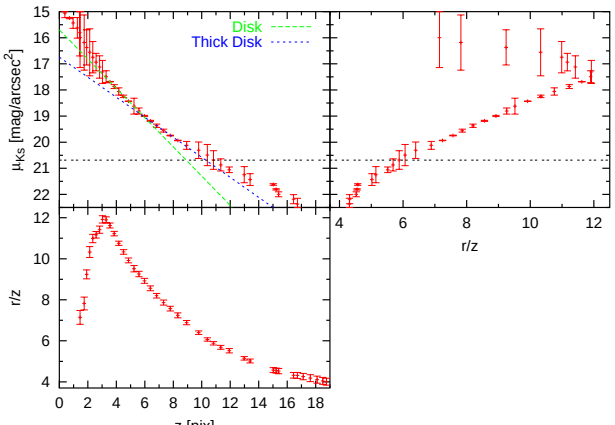

Figure 5.54: Top left: Vertical K_s surface brightness distribution of the azimuthally averaged elliptical isophote levels of 1A. The green and blue line illustrates the exponential old thin disk and thick disk model, respectively.
Top right: Axial ratio of the azimuthally averaged elliptical isophote levels in relation to the surface brightness of the levels. The vertical black line shows the 2 σ level above the background.
Bottom left: The change of the axial ratios (ordinate) with increasing distance z from the galaxy midplane (abscissa) is shown in this diagram.

Most of the galaxies have round isophotes at the galactic center. Then they rapidly turn to very flat ellipses and are tracing the main "old thin disk." The isophotes reach a peak value of maximal flatness. This maximum flatness is $\frac{r}{z} \gtrsim 11$ in the objects 1A, 1D, 3D. It is $\frac{r}{z} \approx 8$ in the objects 2Eltern and 3A. The rest (1C, 2B, 3B, 3E) has axial ratio maximum values of $\frac{r}{z} \approx 6$. However, the value of the maximum $\frac{r}{z}$ is unrelated to the detection of a TD and its strength. These maximum values corresponds to a wide range of surface brightnesses. It is conspicuous that the galaxies with clear identifications of a TD (1A, 3B, 3D) exhibit a bright surface brightness at the corresponding $\frac{r}{z}$ values ($\mu_{K_s} \approx 18$ mag arcsec^{-2} at $\frac{r}{z}$ maxi).

The surface brightness at the $\frac{r}{z}$ maximum values are much lower for the objects with a detected

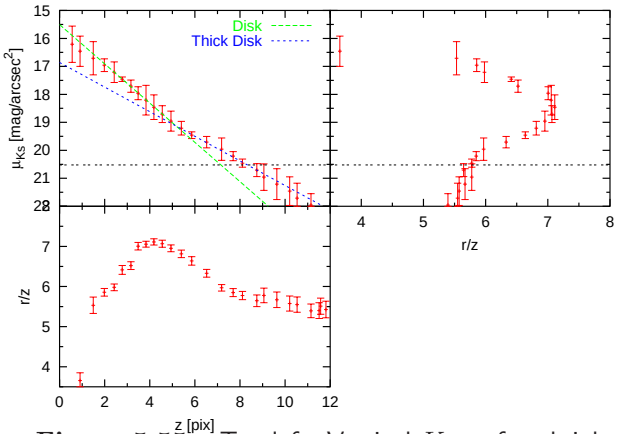

Figure 5.55: Top left: Vertical K_s surface brightness distribution of the azimuthally averaged elliptical isophote levels of 3B. The green and blue line illustrates the exponential old thin disk and thick disk model, respectively.
Top right: Axial ratio of the azimuthally averaged elliptical isophote levels in relation to the surface brightness of the levels. The vertical black line shows the 2 σ level above the background.
Bottom left: The change of the axial ratios (ordinate) with increasing distance z from the galaxy midplane (abscissa) is shown in this diagram.

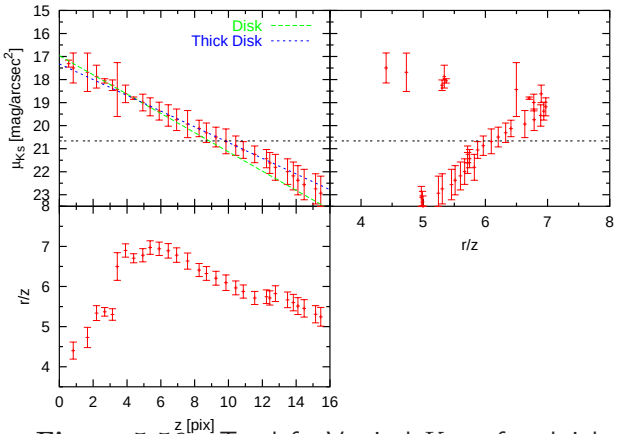

Figure 5.56: Top left: Vertical K_s surface brightness distribution of the azimuthally averaged elliptical isophote levels of 2B. The green and blue line illustrates the exponential old thin disk and thick disk model, respectively.
Top right: Axial ratio of the azimuthally averaged elliptical isophote levels in relation to the surface brightness of the levels. The vertical black line shows the 2 σ level above the background.
Bottom left: The change of the axial ratios (ordinate) with increasing distance z from the galaxy midplane (abscissa) is shown in this diagram.

single disk (μ_{K_s}(1D) = 20.25 mag arcsec^{-2}, μ_{K_s}(3E) = 19.4 mag arcsec^{-2}, μ_{K_s}(3Ealtern) = 19.7 mag arcsec^{-2}). The objects with faint TD have values between 20< μ_{K_s} <19.5, only 3A is an exception with μ_{K_s} = 17.25 mag arcsec^{-2}. So, galaxies with clear TD have thin disks with higher stellar densities than the galaxies with a single disk. After this maximal point the axial ratio decreases again at higher altitudes and lower surface brightness indicating an increase of rounder isophotes at large heights and low surface brightness. The increase of the roundness depends on the behavior of the vertical surface brightness profiles. For the objects where the profiles can be best fitted with a single disk (1D, 3E, 3Ealtern) the axial ratios of the individual isophotes remain at a relatively constant value beyond the maximal point. That means that the outer isophotes do not change their shape with a maximum difference between the peak value $\frac{r}{z}_{maxi}$ and the noise limit $\frac{r}{z}_{2\sigma}$ of about 1: $\Delta\frac{r}{z} = \frac{r}{z}_{maxi} - \frac{r}{z}_{2\sigma} \leq 1$. After the 2σ limit the shape does also not change much its flatness. The contrary is observed at the objects where the vertical profile can be fitted with a thin disk and a TD component. In these cases the gradient of the axial ratios in the outer parts becomes to be larger than 1: $\Delta\frac{r}{z} = \frac{r}{z}_{maxi} - \frac{r}{z}_{2\sigma} \geq 1$. The rounder shape of the isophotes is indicative of a second disk in these galaxies. This is expected from a faint thick disk component which surrounds the old thin disk.

The most interesting correlation between the disk components is that the stellar surface brightness (stellar density) is correlated with the shape of the galaxies for galaxies with a clear TD component (1A, 3B, 3D and also 3A). In all of these objects the position where the TD dominates the thin disk corresponds to a relative fixed surface brightness of $\mu_{K_s} \approx 19$ mag arcsec^{-2}. In addition, the isophote

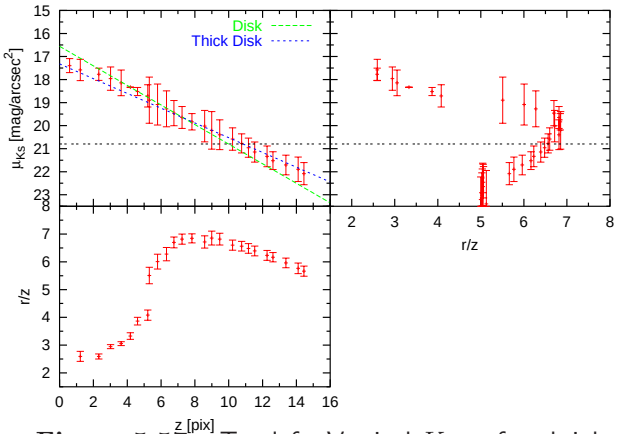

Figure 5.57: Top left: Vertical K_s surface brightness distribution of the azimuthally averaged elliptical isophote levels of 1C. The green and blue line illustrates the exponential old thin disk and thick disk model, respectively.
Top right: Axial ratio of the azimuthally averaged elliptical isophote levels in relation to the surface brightness of the levels. The vertical black line shows the 2 σ level above the background.
Bottom left: The change of the axial ratios (ordinate) with increasing distance z from the galaxy midplane (abscissa) is shown in this diagram.

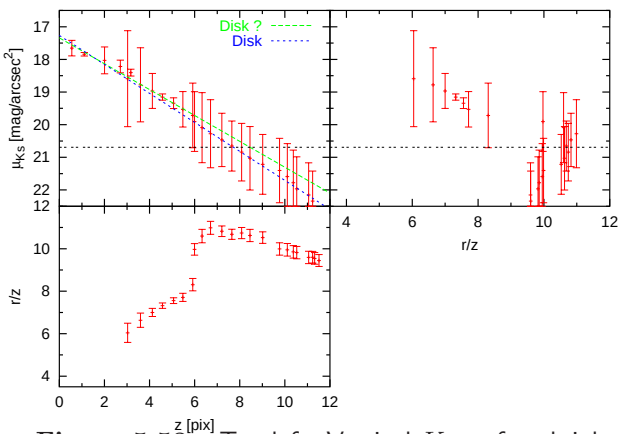

Figure 5.58: Top left: Vertical K_s surface brightness distribution of the azimuthally averaged elliptical isophote levels of 1D. The green and blue line illustrates the possible exponential thin disk models, respectively.
Top right: Axial ratio of the azimuthally averaged elliptical isophote levels in relation to the surface brightness of the levels. The vertical black line shows the 2 σ level above the background.
Bottom left: The change of the axial ratios (ordinate) with increasing distance z from the galaxy midplane (abscissa) is shown in this diagram.

at this surface brightness level has an axial ratio of $\frac{r}{z} \approx 8$ in these targets. In addition, the break of the slope in the vertical surface brightness profiles corresponds to the break of the slope in the axial ratio profiles. This is shown in the Figs. 5.54, 5.53, 5.55, 5.59. The vertical distance in kpc of the break above/below the galactic planes is shown in Col. 9 in Table 5.10.

The TD seems to be directly correlated with a change in the shape of the disks and surface brightness. An effect coming from the surrounding spheroidal halo detected by Zibetti & Ferguson (2004), Zibetti et al. (2004) and Caldwell & Bergvall (2006) can be excluded because the halo light is expected to be at much lower surface brightness levels and the halo cannot be fitted with an exponential disk model. The objects with a single disk component reach the maximum axial ratio, i.e., their flattest shape at large distances from their midplane. This indicates rounder isophotes of the central plane. After this maximum the axial ratios decrease at larger heights without showing a break also after the 2σ level and have a flat slope.

Color Maps

Dalcanton & Bernstein (2002) used optical-NIR band color maps in order to verify the existence of a TD in their sample of flat galaxies. They interpreted the color maps such that the old thin disks of their targets are embedded in a low surface brightness envelope with red colors. In the last section we showed that some of our late-type spirals are indeed composed out of two disk components where the TD surrounds the old thin disk at large distances and low surface brightnesses. In addition, the

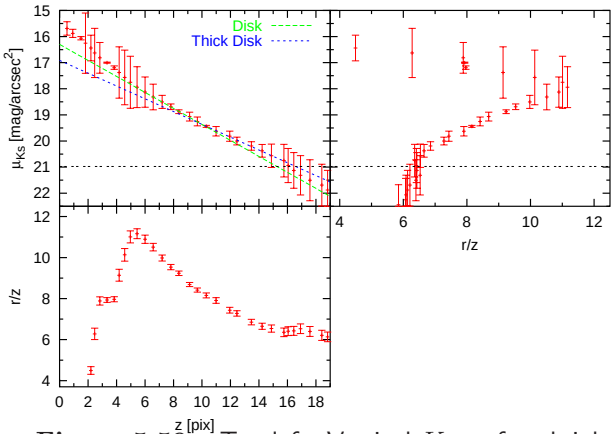

Figure 5.59: Top left: Vertical K_s surface brightness distribution of the azimuthally averaged elliptical isophote levels of 3D. The green and blue line illustrates the exponential old thin disk and thick disk model, respectively.
Top right: Axial ratio of the azimuthally averaged elliptical isophote levels in relation to the surface brightness of the levels. The vertical black line shows the 2 σ level above the background.
Bottom left: The change of the axial ratios (ordinate) with increasing distance z from the galaxy midplane (abscissa) is shown in this diagram.

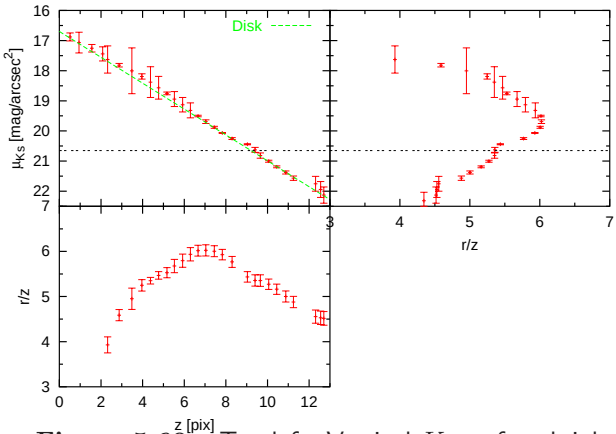

Figure 5.60: Top left: Vertical K_s surface brightness distribution of the azimuthally averaged elliptical isophote levels of 3Ealtern. The green line illustrates the exponential old thin disk model.
Top right: Axial ratio of the azimuthally averaged elliptical isophote levels in relation to the surface brightness of the levels. The vertical black line shows the 2 σ level above the background.
Bottom left: The change of the axial ratios (ordinate) with increasing distance z from the galaxy midplane (abscissa) is shown in this diagram.

surface brightness profiles of these objects can only be fitted using two exponential disk components.

The left part of Figs. 5.63 - 5.72 shows the inverse color map of the target objects. The clumpy and bright zones are the regions where the K_s band dominates the map. This can be seen in the dust attenuated regions of the galactic midplane where the optical disk is hidden behind the dust clouds. At intermediate radii and altitudes the gray regions indicate similar intensities of the optical and NIR band. The outer parts of some galaxies show an overdensity of bright pixels which is probably coming from a red thick disk envelope. The right side of the Figs. 5.63 - 5.72 show the vertical surface brightness profiles in the NIR K_s band and the optical r band. The objects 1A, 2Ealtern, and 3B show–at least–a small excess to redder colors at large heights from their midplanes. These objects are also fitted with a thin disk and a TD as described before. The red color envelope is probably the light of a TD component in these galaxies and comparable with the red TD found by Dalcanton & Bernstein (2002). The galaxies 1C, 2B, 3A and 3D do not show this envelope in the color maps although they were fitted with two disk components.

The galaxies 1D and 3E with a fitted single disk also do not show the red envelope. The other single component disk galaxy 3Ealtern shows a clear red envelope at low surface brightness. This possibly means that 3Ealtern has a red TD but does not have a corresponding fitted TD component in its surface brightness profile. As shown in the vertical profile of 3Ealtern, this target can be eventually fitted with a thin disk and a TD and its red envelope could be actually a TD. The other way around is similarly effective for the galaxies 1C, 2B, 3A and 3D. Here we did not find a red envelope but a

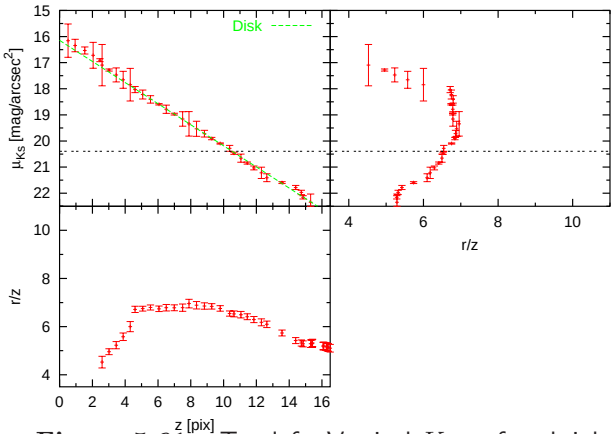

Figure 5.61: Top left: Vertical K_s surface brightness distribution of the azimuthally averaged elliptical isophote levels of 3E. The green illustrates the exponential old thin disk disk model.
Top right: Axial ratio of the azimuthally averaged elliptical isophote levels in relation to the surface brightness of the levels. The vertical black line shows the 2 σ level above the background.
Bottom left: The change of the axial ratios (ordinate) with increasing distance z from the galaxy midplane (abscissa) is shown in this diagram.

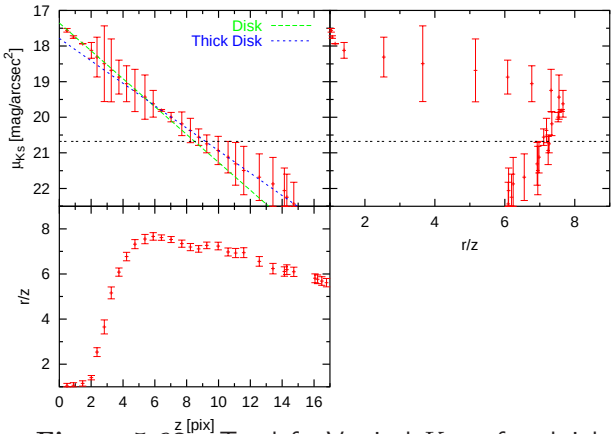

Figure 5.62: Top left: Vertical K_s surface brightness distribution of the azimuthally averaged elliptical isophote levels of 2Ealtern. The green and blue line illustrates the exponential old thin disk and thick disk model, respectively.
Top right: Axial ratio of the azimuthally averaged elliptical isophote levels in relation to the surface brightness of the levels. The vertical black line shows the 2 σ level above the background.
Bottom left: The change of the axial ratios (ordinate) with increasing distance z from the galaxy midplane (abscissa) is shown in this diagram.

TD component in their vertical surface brightness profiles. It is possible that this TD is not of red color and therefore not detected. This result shows, that the detection of a red envelope surrounding an edge-on disk galaxy is not necessarily connected with the existence of a TD component in their vertical surface brightness distributions.

5.5.6 Discussion and Summary

We presented one-dimensional vertical surface brightness profiles of ten late-type bulgeless disk galaxies. The galaxies were observed in the near-infrared K_s band in order to trace the stellar mass distribution and to reduce dust attenuation in these targets. The vertical surface brightness distributions are created with the aid of azimuthally averaged elliptical isophote levels. Exponential disk models were used to fit the vertical profiles.

Three out of the ten targets exhibit a single exponential disk—it cannot be excluded that a deviation from the edge-on view prevented the detection of a TD in these objects. The rest of the objects show a light excess at large heights from the galactic midplane and can not be fitted with a single exponential disk model alone. This light excess causes a flattening of the vertical profiles and can be best fitted with a second exponential disk model. This second disk comprises a thick disk (TD) as shown in the observations. The TD is clearly observed in three target galaxies and in other four targets the TD is faint and therefore fitted with larger uncertainties. Comparing with earlier studies (Dalcanton & Bernstein 2002; Yoachim & Dalcanton 2006), we confirm the existence of a TD

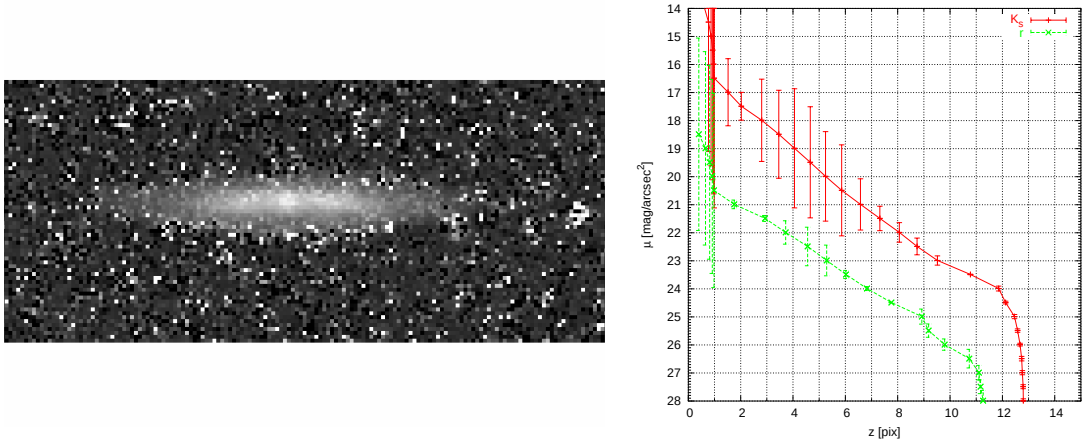

Figure 5.63: Left: $K_s - r$ color map of 3A. We use the inverse illustration: Bright pixels indicate regions of dominating K_s NIR light. In dark regions, the optical r band light dominates. The scale is $76.''1 \times 26.''5$. Right: Vertical surface brightness distribution of the azimuthally averaged elliptical isophote levels in K_s (red) and r (green) band of 3A, respectively.

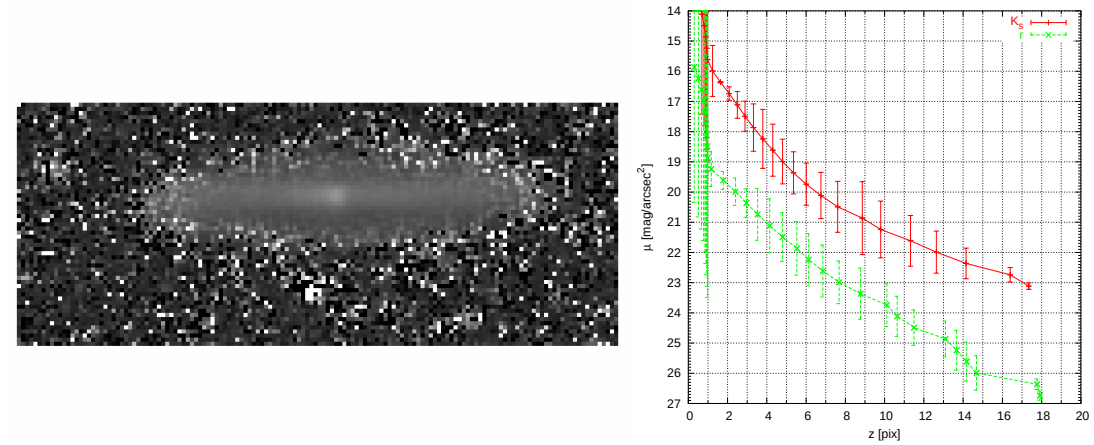

Figure 5.64: Left: $K_s - r$ color map of 1A. We use the inverse illustration: Bright pixels indicate regions of dominating K_s NIR light. In dark regions, the optical r band light dominates. The scale is $57.''9 \times 23.''4$. Right: Vertical surface brightness distribution of the azimuthally averaged elliptical isophote levels in K_s (red) and r (green) band of 1A, respectively.

in late disk galaxies. We do not detect pure thin disks in the sample and argue that these galaxies must undergo an evolution that creates the two disk components. With the aid of the two component models we derived the values of the scale height and the central surface brightness of the thin disk and the TD. These computed values are similar to those found in the study by Yoachim & Dalcanton (2006) and are also comparable to that of our Galaxy (MW) (Buser et al. 1999; Buser 2000).

In addition, we found that the galaxies with detected TD have rounder isophotes at large vertical distances than galaxies with a single disk. Moreover, the isophotes of these galaxies become suddenly rounder at a similar vertical height in all targets where the TD starts to dominate the vertical light. This supports the existence of a distinct TD surrounding the thin disk. This TD envelope dominates over the thin disk above a surface brightness level of ≈19 mag arcsec^{-2} and a corresponding axial ratio of 8 of the isophote level. This discrete transition between the thin disk and the TD indicates a separate origin of the disk components. This assumption is also supported by our results that the

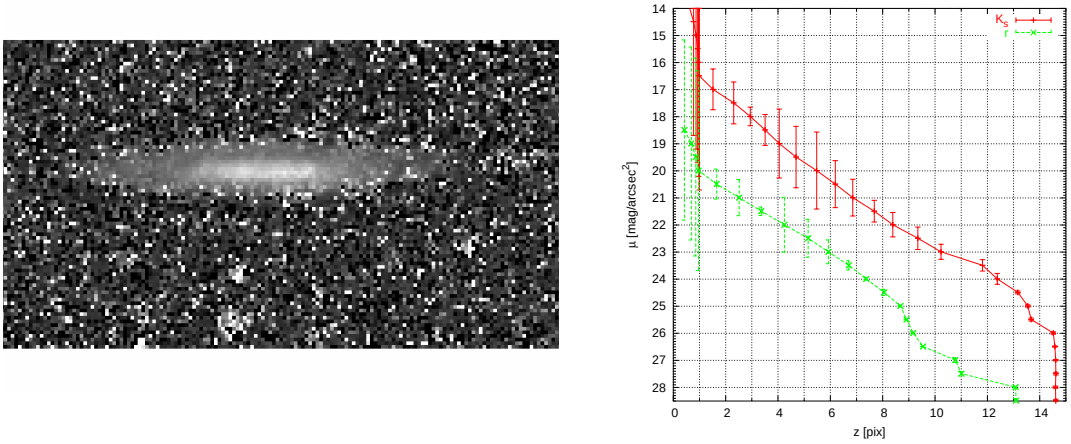

Figure 5.65: Left: $K_s - r$ color map of 3B. We use the inverse illustration: Bright pixels indicate regions of dominating K_s NIR light. In dark regions, the optical r band light dominates. The scale is $97.''5 \times 34.''1$. Right: Vertical surface brightness distribution of the azimuthally averaged elliptical isophote levels in K_s (red) and r (green) band of 3B, respectively.

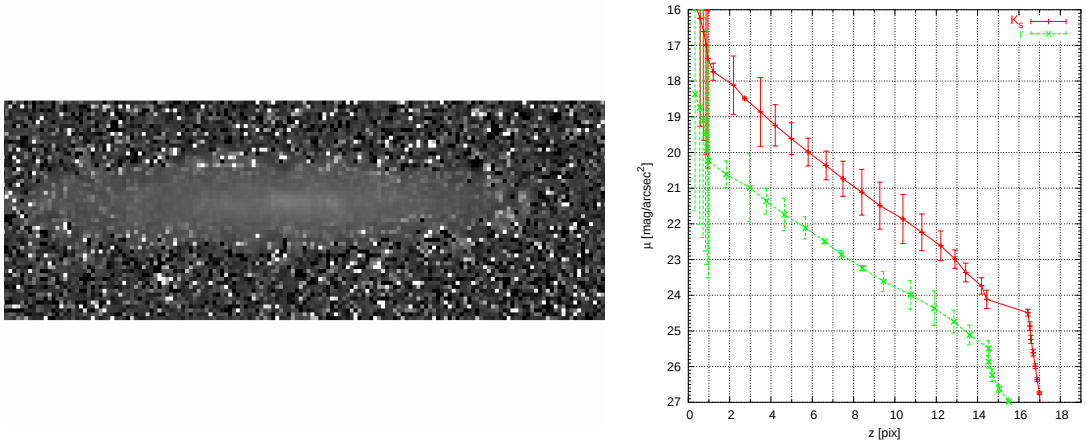

Figure 5.66: Left: $K_s - r$ color map of 2B. We use the inverse illustration: Bright pixels indicate regions of dominating K_s NIR light. In dark regions, the optical r band light dominates. The scale is $75.''7 \times 22.''2$. Right: Vertical surface brightness distribution of the azimuthally averaged elliptical isophote levels in K_s (red) and r (green) band of 2B, respectively.

objects with a bright TD have also thin disks with high surface brightnesses at their flattest extensions. The galaxies without a TD have low surface brightnesses of the thin disk.

Although the surface brightness and the shape of the galaxies change abruptly between the disk components, we found that the scale height and central surface brightness of the thin disks and the TD are linearly correlated with each other: the larger the scale height of the thin disk the larger the scale height of the TD in a galaxy. And the same correlation is also found for the central surface brightness as well as the ratio of central surface brightness to the scale height of the thin disk versus the TD. The detection of a TD in the vertical surface brightness distribution that surrounds the thin disk is not necessarily connected with a vertical color gradient towards redder colors and probably older stars as controversially found by Dalcanton & Bernstein (2002).

In summary, we found that about $\frac{2}{3}$ of our sample galaxies have a TD. This disk component has similar scale heights in all the objects and occurs at the same vertical height away from the galactic

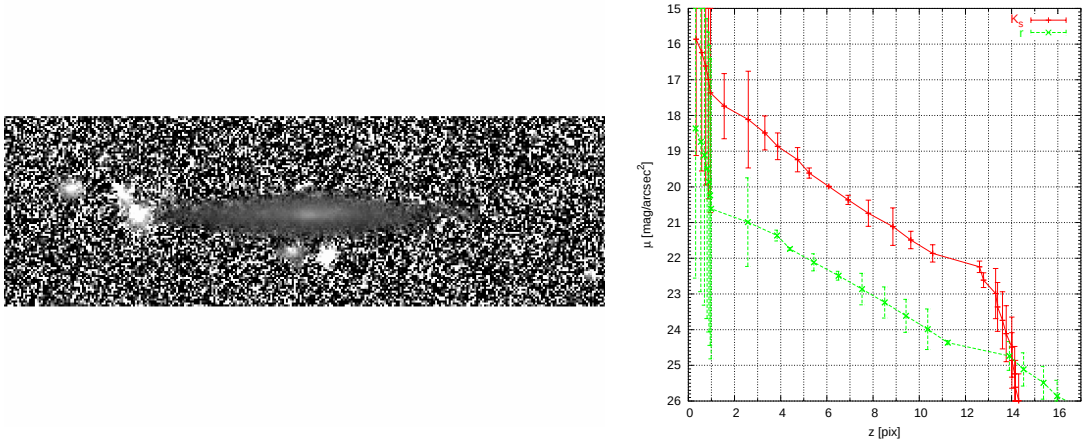

Figure 5.67: Left: $K_s - r$ color map of 1C. We use the inverse illustration: Bright pixels indicate regions of dominating K_s NIR light. In dark regions, the optical r band light dominates. The scale is $124'' \times 38.''5$.
Right: Vertical surface brightness distribution of the azimuthally averaged elliptical isophote levels in K_s (red) and r (green) band of 1C, respectively.

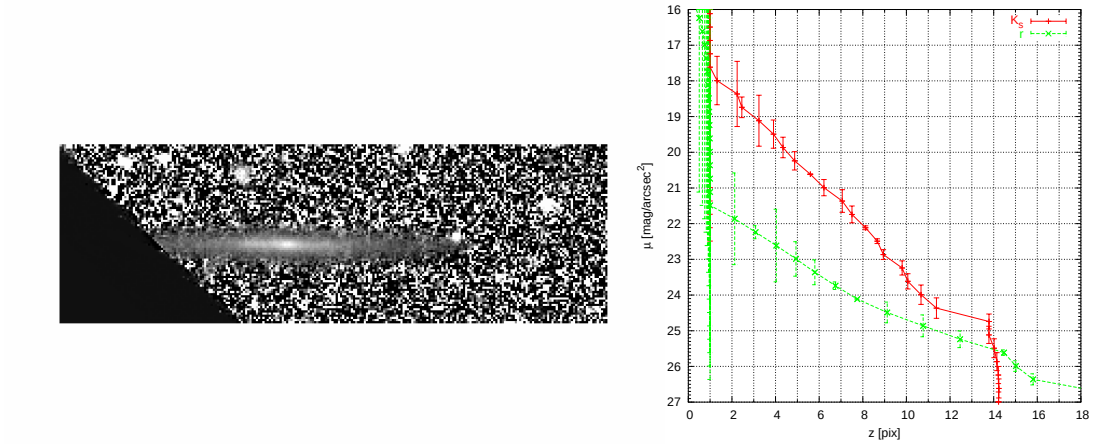

Figure 5.68: Left: $K_s - r$ color map of 1D. We use the inverse illustration: Bright pixels indicate regions of dominating K_s NIR light. In dark regions, the optical r band light dominates. The scale is $100.''6 \times 32.''5$.
Right: Vertical surface brightness distribution of the azimuthally averaged elliptical isophote levels in K_s (red) and r (green) band of 1D, respectively.

midplanes. Additionally, the values of the surface brightness and the axial ratio at the transition zone between thin disk and TD are similar in all targets. This transition between the thin disk and the TD causes a discrete and abrupt change of the isophotal properties. Otherwise, scale heights and central surface brightness of the thin and TD are linearly correlated suggesting a connection of the two disk components. We did not find a correlation between vertical color gradients and the existence of a TD.

Multi Component Merger Origin of the Thick Disk

On the one hand we detect the TD in the majority of the targets and therefore we argue against that the disks are solely formed through slow infall. On the other hand, the TD are not ubiquitous and

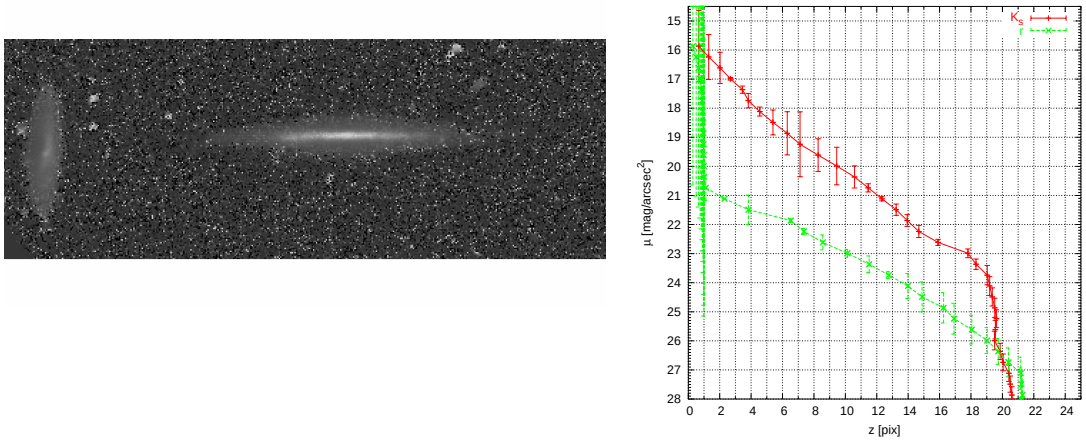

Figure 5.69: Left: $K_s - r$ color map of 3D. The galaxy lies vertical in this image. We use the inverse illustration: Bright pixels indicate regions of dominating K_s NIR light. In dark regions, the optical r band light dominates. The scale is $177.''1 \times 60.''6$.
Right: Vertical surface brightness distribution of the azimuthally averaged elliptical isophote levels in K_s (red) and r (green) band of 3D, respectively.

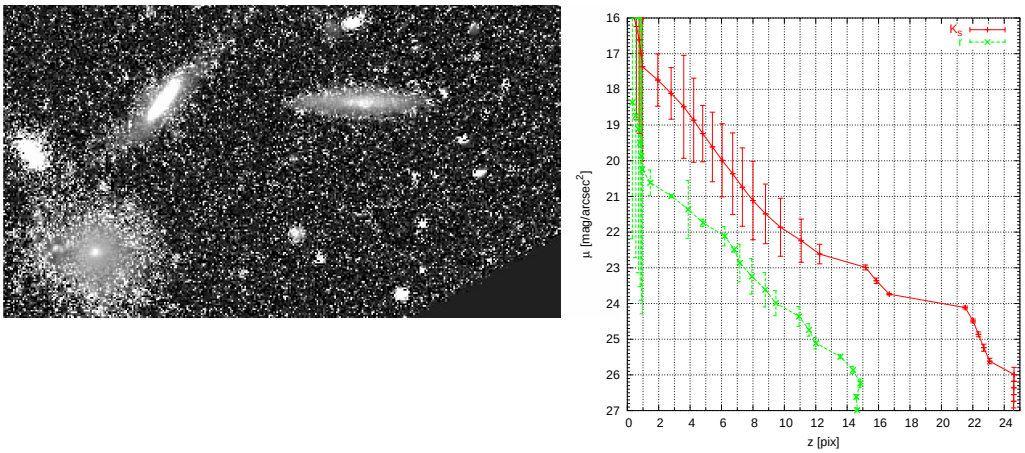

Figure 5.70: Left: $K_s - r$ color map of 3Ealtern. The galaxy lies vertical in this image. We use the inverse illustration: Bright pixels indicate regions of dominating K_s NIR light. In dark regions, the optical r band light dominates. The scale is $137.''1 \times 88.''4$.
Right: Vertical surface brightness distribution of the azimuthally averaged elliptical isophote levels in K_s (red) and r (green) band of 3Ealtern, respectively.

do not represent fundamental components of disk formation. The galaxy formation scenario proposed by Yoachim & Dalcanton (2006) shows that the TD are formed out of merging galactic subunits with later formation of the thin disk from the settled gas. This hypothesis can not explain our detection of pure single exponential disk galaxies. In addition, it proposes that the TD are redder and older than the thin disks. Thus, this scenario can not be responsible for pure single disks and not red-coloured TD. Therefore, it is possibly not the main TD formation scenario because it is expected that nearly every disk galaxy should have a red TD component.

We instead favor the formation of the TD during an ancient epoch of interactions and mergers between the galaxies. At this time, strong close-by encounters with other galaxies leads to a heating of the thin disk via dynamical friction with its companion. The TD formed by this vertical heating

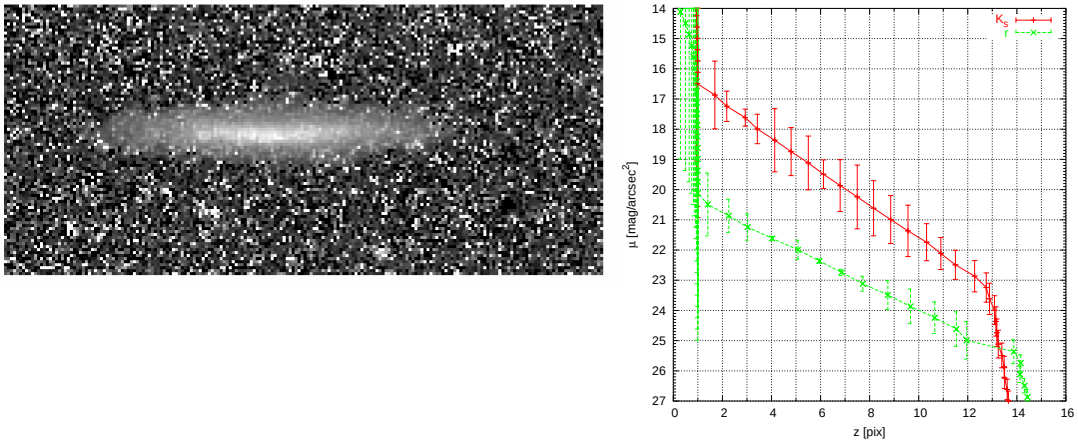

Figure 5.71: Left: $K_s - r$ color map of 3E. We use the inverse illustration: Bright pixels indicate regions of dominating K_s NIR light. In dark regions, the optical r band light dominates. The scale is $79.''3 \times 35.''7$. Right: Vertical surface brightness distribution of the azimuthally averaged elliptical isophote levels in K_s (red) and r (green) band of 3E, respectively.

should be observed as old and probably red and fluffy component. In addition, if the dynamical friction is effective (i.e., the relative velocities of the interacting pair are small), gas and stars were accreted from the captured and infalling companion onto the pre-existing disk. The stars of the companion galaxy can directly form the envelope that we observe as the distinct TD. The external origin would also explain the distinct properties between the thin disk and the TD. This direct accretion process took place in a relatively short epoch of the history and this causes that we observe similar isophotal properties (shape, distance and surface brightness where the TD dominates the thin disk). It seems that these properties are frozen at the time of accretion. Several n-body simulations seem to support a scenario where TD stars are directly accreted from infalling satellites (e.g., Steinmetz 2003). The direct accretion scenario would also imply that one could find differences in metallicities and age between the thin disk and the TD.

The infalling objects deposit also gas in the pre-existing thin disk. Subsequent vigorous star formation in the gas dense thin disk is then responsible for an additional puffing-up of the thin disk. This scenario by Burkert et al. (1992), Samland & Gerhard (2003) and Brook et al. (2006) can explain the linear correlation between the fitting parameters (scale length and central surface brightness) of the thin and the TD. This is because a part of the TD stars are created from the accreted gas in the thin disk. The differences of the amount of the accreted gas and subsequent different star formation efficiencies and star formation timescales can lead to different observed scale heights and central surface brightnesses. Also the observed differences of the vertical color gradients would depend on the different star formation histories due to different accreted gas fractions.

Summarizing this discussion, we prefer a TD formation scenario where the TD is composed out of a dynamical heated thin disk and directly accreted stars and stars formed in the thin disk from the accreted gas of captured galaxies during an universal epoch of merging. With this model we can explain both the discrete and continuous properties of the thin and the TD components as well as the differences in the vertical color gradients.

In addition, the above suggested scenario could also explain that some of the properties of the thin and the TD of the MW are smoothly related such as metallicities and kinematics, while others (e.g., age) seem to be independent from each other as discussed in the Introduction, see Sect. 5.1.1. The satellite accretion took place at a epoch of merging as shown in many simulations (Brook et al. 2004, 2005, 2006). Therefore the disk properties of the directly accreted stars are frozen at that time and are similar in all these objects. The transformation of the accreted gas of the satellites can vary between the individual galaxies depending on the amount of the accreted gas and the star formation

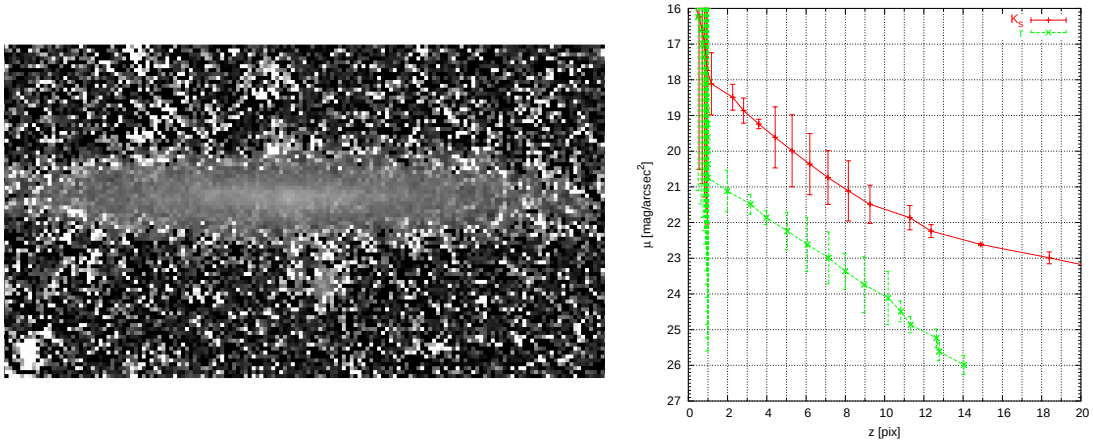

Figure 5.72: Left: $K_s - r$ color map of 2Ealtern. We use the inverse illustration: Bright pixels indicate regions of dominating K_s NIR light. In dark regions, the optical r band light dominates. The scale is $100.''6 \times 31.''1$.
Right: Vertical surface brightness distribution of the azimuthally averaged elliptical isophote levels in K_s (red) and r (green) band of 2Ealtern, respectively.

efficiency in the galaxies.

Some galaxies avoided such accretion events and could not efficiently built up a TD component. These objects without a TD show more puffy disks and lower stellar densities. This is probably due to internal disintegration and vertical dynamical heating which creates a fluffy disk but not two distinct disk components.

Appendix A

morf_invest

This Appendix shows the code `morf_invest` which is implemented in FORTRAN 77. This program computes the luminosity-weighted mean ellipticity of the elliptical isophotes ε of an object and the concentration index CI used for the Catalog, see Sect. 2. This code has also additional other features. The program `Mini_Morf_Invest` is a shorter version of the general program `morp_invest` presented here. `Mini_Morf_Invest` was used to derive ε for the K_s band observations, see Sect. 5.4.1. In the following, the general code `morf_invest` is shown and some explanations and comments are added after a "c":

```
c Name of the program:
        program morf_invest
        implicit none
c Definition of the variables:
        integer n,i,r,v,je,q
        integer p
        real a(100),b(100),pa(100),ellip(100),averellip,ra,ra_b,dec,dec_b
        real FBKra,FBKdec
        real pr50u,pr50g,pr50r,pr50i,pr50z,pr90u,pr90g,pr90r,pr90i,pr90z
        real petrorad_u(3),petrorad_g(3),petrorad_r(3)
        real petrorad_i(3),petrorad_z(3)
        real averellip_u,averellip_g,averellip_r,averellip_i,averellip_z
        real limitrad,limitrad_u,limitrad_g,limitrad_r,limitrad_i
        real limitrad_z,diffellip
        real limitPArad,limitPArad_u,limitPArad_g,limitPArad_r
        real limitPArad_i,limitPArad_z,diffPA
        real limitell,limitell_u,limitell_g,limitell_r,limitell_i,limitell_z
        real limitPAell,limitPAell_u,limitPAell_g,limitPAell_r
        real limitPAell_i,limitPAell_z
        real in(100),oa(100),ob(100),int(100),tint
        real qaverellip,saverellip,averellip_25
        real saverellip_u,saverellip_g,saverellip_r,saverellip_i
        real saverellip_z
        real averellip_25_u,averellip_25_g,averellip_25_r
        real averellip_25_i,averellip_25_z
        real a_25,a_25_u,a_25_g,a_25_r,a_25_i,a_25_z
        character inname*20,outname*32,printname*32,flag*2,text*80,band*1
        character run(2)*4,cc(2)*1,field(2)*4,class*1
c Opening some files:
        open(1,file='in_midasB.dat',status='unknown')
        open(2,file='mu.dat',status='unknown')
```

```
        open(4,file='iqsgr_formatiert.dat',status='unknown')
        open(5,file='FBK_neuB.dat',status='unknown')
c Setting several variables to zero:
        r = 0
        ra_b = 0
c Setting the weighted mean ellipticity to zero:
10      averellip_u = 0
        averellip_g = 0
        averellip_r = 0
        averellip_i = 0
        averellip_z = 0
c Setting the ellipticity of the 25 mag/arcsec2 isophote to zero:
        averellip_25_u = 0
        averellip_25_g = 0
        averellip_25_r = 0
        averellip_25_i = 0
        averellip_25_z = 0
c Setting the mean ellipticity to zero:
        saverellip_u = 0
        saverellip_g = 0
        saverellip_r = 0
        saverellip_i = 0
        saverellip_z = 0
c Setting the radius of the 25 mag/arcsec2 isophote to zero:
        a_25_u = 0
        a_25_g = 0
        a_25_r = 0
        a_25_i = 0
        a_25_z = 0
c Read the input table which contains the names and positions of the
c objects in oder to create the outname which is used in the next
c step to open the individual result files from MIDAS FIT/ELL3
c ellipse fitting process:
15      read(1,'(a20,19x,a2,2f13.7)',iostat = v) inname,flag,ra,dec
        if(v.lt.0) go to 40
        if(r.ne.0.and.ra.ne.ra_b) then
                backspace 1
                r = 0
                ra = ra_b
                dec = dec_b
                goto 40
        end if
        r = r+1
        ra_b = ra
        dec_b = dec
        if(flag.eq.' 0') goto 15
        if(flag(1:1).eq.' ') then
                outname = inname // '_mor000' // flag(2:2) // '.dat'
        else
                outname = inname // '_mor00' // flag // '.dat'
        end if
        printname = inname(1:11) // '?' // outname(13:32)
        band = outname(12:12)
```

```
        n = 1
        averellip = 0
        averellip_25 = 0
        qaverellip = 0
        saverellip = 0
        a_25 = 0
        tint = 0

        do je=1,100
        a(je) = 0.0
        b(je) = 0.0
        in(je) = 0.0
        int(je) = 0.0
        ellip(je) = 0.0
        enddo

c Open a galaxy file from the MIDAS FIT/ELL3 ellipse fitting which contains the isophotal
c fitting results of a galaxy. The used parameters are the intensity,
c the major and the minor axis and the position angle of each isophotal level:
        open(3,file=outname,status='unknown')
20      oa(n) = a(n)
        ob(n) = b(n)
        read(3,'(11x,e11.5,e15.5,2e16.5)',end=80) in(n),a(n),b(n),pa(n)
c Computing the luminosity weighted ellipticity for every isophote level:
        int(n) = in(n)*(((a(n)*b(n))-(oa(n)*ob(n)))*3.141592654)
        ellip(n) = 1-b(n)/a(n)
        n = n+1
        go to 20
80      n = n-1
c Computing the ellipticity of the isophote with 25 mag/arcsec2:
        do q=1,n
            averellip_25 = max(averellip_25,ellip(q))
            a_25 = max(a_25,a(q))
        enddo
        a_25 = a_25*0.396
c Computing the radius in arcsec of the isophote with 25 mag/arcsec2:
C       do p=1,n
C       a_25 = max(a_25,a(p))
C       enddo
C       a_25 = a_25*0.396
        limitrad = 0
        limitPArad = 0
        do i = 1,n,1
        if(i.ne.1) then
c Computing the isophotal ellipticity where its value changes more
c than 0.07 between two isophotes and store the radius at this ellipticity:
                diffellip = abs(ellip(i)-ellip(i-1))
                if(diffellip.lt.0.07*ellip(i-1)) then
                        if(limitrad.eq.0) limitrad = a(i)
                else
                        limitrad = 0
                end if
c Computing the position angle where its value changes more than 3
```

```
c between two isophotes and store the radius at this condition:
        diffPA = abs(pa(i)-pa(i-1))
                if(diffPA.lt.3) then
                        if(limitPArad.eq.0) limitPArad = a(i)
                else
                        limitPArad = 0
                endif
c Computing the isophotal ellipticity where its value changes more
c than 0.07 between two isophotes and store this ellipticity:
        diffellip = abs(ellip(i)-ellip(i-1))
                if(diffellip.lt.0.07*ellip(i-1)) then
                        if(limitell.eq.0) limitell = ellip(i)
                else
                        limitell = 0
                end if
c Computing the position angle where its value changes more than 3
c between two isophotes and store the ellipticity at this radius:
        diffPA = abs(pa(i)-pa(i-1))
                if(diffPA.lt.3) then
                        if(limitPAell.eq.0) limitPAell = ellip(i-1)
                else
                        limitPAell = 0
                endif
        endif
c Computing the mean of the luminosity weighted ellipticities:
        averellip = averellip+ellip(i)*int(i)
        qaverellip = qaverellip+ellip(i)**2.*int(i)
        tint = tint+int(i)
c Computing the mean position angle, axes and position of an object:
c       pam = pam+pa(i)
        pam = pa(i)
        xm = xm+x(i)
        ym = ym+y(i)
        am = a(i)
        bm = b(i)
        end do
        averellip = averellip/tint
c Computing the standard deviation of the luminosity weighted ellipticities:
        saverellip = SQRT((1./tint)*abs(qaverellip-tint*averellip**2.))/
&       SQRT(FLOAT(n))
c       pam = pam/i
        pam = 90+pam
        xm = xm/i
        ym = ym/i
        am = am
        bm = bm
c Ordering the resulting value in the different SDSS filters:
        if(band.eq.'u') then
                averellip_u = averellip
                averellip_25_u = averellip_25
                saverellip_u = saverellip
                a_25_u = a_25
                limitrad_u = limitrad
```

```
                limitPArad_u = limitPArad
                limitell_u = limitell
                limitPAell_u = limitPAell
        else if(band.eq.'g') then
                averellip_g = averellip
                averellip_25_g = averellip_25
                saverellip_g = saverellip
                a_25_g = a_25
                limitrad_g = limitrad
                limitPArad_g = limitPArad
                limitell_g = limitell
                limitPAell_g = limitPAell
        else if(band.eq.'r') then
                averellip_r = averellip
                averellip_25_r = averellip_25
                saverellip_r = saverellip
                a_25_r = a_25
                limitrad_r = limitrad
                limitPArad_r = limitPArad
                limitell_r = limitell
                limitPAell_r = limitPAell
        else if(band.eq.'i') then
                averellip_i = averellip
                averellip_25_i = averellip_25
                saverellip_i = saverellip
                a_25_i = a_25
                limitrad_i = limitrad
                limitPArad_i = limitPArad
                limitell_i = limitell
                limitPAell_i = limitPAell
        else if(band.eq.'z') then
                averellip_z = averellip
                averellip_25_z = averellip_25
                saverellip_z = saverellip
                a_25_z = a_25
                limitrad_z = limitrad
                limitPArad_z = limitPArad
                limitell_z = limitell
                limitPAell_z = limitPAell
        end if
        close(3)
        goto 15
c Reading the input table with the SDSS parameters:
40       read(5,'(a1,f20.16,1x,f22.16,1x,f11.9,1x,f9.7,1x,f9.7,1x,
&        f10.8,1x,f10.8,1x,f10.8,1x,f9.7,1x,f9.7,1x,f10.8,1x,f10.8)',
&        end=100) class,FBKra,FBKdec,pr50u,pr50g,pr50r,pr50i,pr50z,
&        pr90u,pr90g,pr90r,pr90i,pr90z
c Matching and connecting the objects between this SDSS table and that which was
C used for deriving the isophotal values above:
        if(FBKra.gt.(ra-0.0001).and.FBKra.lt.(ra+0.0001)) then
                if(FBKdec.gt.(dec-0.0001).and.FBKdec.lt.(dec+0.0001)) then
c Deriving the concentration index:
                        petrorad_g(1) = pr50g
```

```
                        petrorad_g(2) = pr90g
                        petrorad_g(3) = petrorad_g(2)/petrorad_g(1)
                        petrorad_i(1) = pr50i
                        petrorad_i(2) = pr90i
                        petrorad_i(3) = petrorad_i(2)/petrorad_i(1)
                        petrorad_r(1) = pr50r
                        petrorad_r(2) = pr90r
                        petrorad_r(3) = petrorad_r(2)/petrorad_r(1)
                        petrorad_u(1) = pr50u
                        petrorad_u(2) = pr90u
                        petrorad_u(3) = petrorad_u(2)/petrorad_u(1)
                        petrorad_z(1) = pr50z
                        petrorad_z(2) = pr90z
                        petrorad_z(3) = petrorad_z(2)/petrorad_z(1)
                        rewind 5
                        goto 70
                else
                        goto 40
                end if
        else
                goto 40
        end if
c Some comments:
c70     limitrad_u = limitrad_u*0.4
c       limitrad_g = limitrad_g*0.4
c       limitrad_r = limitrad_r*0.4
c       limitrad_i = limitrad_i*0.4
c       limitrad_z = limitrad_z*0.4
c       limitPArad_u = limitPArad_u*0.4
c       limitPArad_g = limitPArad_g*0.4
c       limitPArad_r = limitPArad_r*0.4
c       limitPArad_i = limitPArad_i*0.4
c       limitPArad_z = limitPArad_z*0.4
70      limitrad_u = limitrad_u*0.4/petrorad_u(1)
        limitrad_g = limitrad_g*0.4/petrorad_g(1)
        limitrad_r = limitrad_r*0.4/petrorad_r(1)
        limitrad_i = limitrad_i*0.4/petrorad_i(1)
        limitrad_z = limitrad_z*0.4/petrorad_z(1)
c Normalizing the radii by dividing them with the half-light radius:
               limitPArad_u = limitPArad_u*0.4/petrorad_u(1)
               limitPArad_g = limitPArad_g*0.4/petrorad_g(1)
               limitPArad_r = limitPArad_r*0.4/petrorad_r(1)
               limitPArad_i = limitPArad_i*0.4/petrorad_i(1)
               limitPArad_z = limitPArad_z*0.4/petrorad_z(1)
c Writing out the outputs:
c       write(2,'(2a1,a32,2f13.7,1x,12f8.3)') class," ",printname,ra,dec,
c&      averellip_g,averellip_25_g,saverellip_g,petrorad_g(3),
c&      averellip_r,averellip_25_r,saverellip_r,petrorad_r(3),
c&      averellip_i,averellip_25_i,saverellip_i,petrorad_i(3),
        write( 2,* ) ra,dec,a_25_g,a_25_r,a_25_i

        if(v.lt.0) then
                go to 90
```

```
        else
                go to 10
        end if

100     write(*,*) outname,'nicht gefunden'
        rewind 5
        go to 10
90      close(1)
        close(2)
        close(4)
        close(5)
        end
```

Appendix B

AMOR for CI

AMOR (Automated Determination of Galaxy Morphology) has been programmed in C++ by Thorsten Lisker. This program has been designed for computing automatically various morphological parameters for galaxies on a FITS image. For that, it requires several input files.

One input file contains the paths to the image file, the input source list with the position and ID of the targets and the paths to the other input files (e.g., the shape of the targets and the links to optional source masks and segmentation images). The input file above contains also some input constants like the level of the background. It is set to 0 in our case because we do not provide a file with the background level for each source.

Another input file stores several constant input parameters which do not change during one run. These are the size of the image in pixels and important parameters for deriving the Petrosian radius. If using the SDSS method the Petrosian radius is the radius of a circular/elliptical aperture at which the "Petrosian ratio" is set to a fixed value of $\eta = 0.2$. This "Petrosian ratio" is the ratio of the surface brightness in an annulus at a certain radius to the mean surface brightness within a circle/ellipse with this radius. Similarly, the Petrosian magnitudes are derived from the Petrosian flux using a circular aperture centered on every object. AMOR needs the values for determining the Petrosian radius and magnitude in this input file as constants. For deriving the surface brightness at a radius we have to choose the discriminating values. When using the SDSS method (WHICHPETRO=2) we defined that the surface brightness at a radius is computed within PETMIN=0.9 times the current radius. This value is somewhat larger than that used originally by the SDSS pipeline (PETMIN=0.8) because lower values are optimized for smaller objects.

The computations and the output of this program are controlled by giving number codes as input for the commands with sometimes more numbers following for the selection of sub-options of the commands. The numbers represent therefore a code for the program to execute and are written into a "Control File." Our intention is to compute the CI in the same way as done in the SDSS. We therefore used the a control file as shown in Table B.1. The different number codes of this Control File are explained in the following paragraphs:

The first number in this control file means that the program starts with a Petrosian radius using circular apertures (2) and the η value is set to (0.2) like in the SDSS. The (0) in the next line means that the half light radius (or effective radius, r_e) is computed using a circular aperture. The (0) then avoids the printing of the "basic parameters" (magnitude, total flux, S/N ratio, number of pixels, r_e, and ellipse-defining parameters) into the output table.

10 0.3 0 0 3 1 Then the code computes iteratively the minimum asymmetry within a (3×3) box and recenter the source until the iteration converges and remains on the same position. (0.3) is the value relative to the current xy position where the search box is considered. The determination of the minimum is done by using an absolute value of asymmetry (0) and using the 180° comparison of the symmetry (0). Then (3) means no printing of the new center but the following computations are derived from the new source center (1). This asymmetry centering has the advantage of an automatic

Table B.1: AMOR Control File for Computing the Concentration Index

Code	Description
stamps/	Path for the newly created stamps
%	Name of the stamps
2 -0.2	Start with circular aperture
0	Half-light radius computed using circles
0	Do not printout basic parameters here
10 0.3 0 0 3 1	Search the minimum asymmetry by dithering around
99 2 -0.2 2	Change the aperture: circle with 2*Petrosian radii
2 0.9 0.5 0	Concentration index using circles

centering of the source if the input position does not contain the optimal values.

99 2 -0.2 2 This line defines that the program should use a circular aperture (2) in order to derive the Petrosian radius using circles with η=(0.2) and a multiplication factor of (2). I.e., the new aperture is 2 $\times$ Petrosian radius.

2 0.9 0.5 0 The CI is derived in this command line. The original definition by Bershady et al. (2000) computes the CI out of the radius ratio of the radii that enclose 80% and 20% of the total flux:

$$C = 5\log(\frac{r_{80}}{r_{20}}) \tag{B.1}$$

In contrast to that, the CI in the Catalog is defined as

$$CI = \frac{r_{90}}{r_{50}} \tag{B.2}$$

For that reason we set the total flux fraction of the radii to (0.9) and (0.5) using circular (0) apertures for this calculation. The resulting values of the CI in the K_s band are given in Col. (10) of the Table 5.7. The typical errors of the CI are $\pm$0.01.

Appendix C

AMOR for CAS

In this appendix we describe how to perform CAS morphology quantification with AMOR. The input parameter file for AMOR was configured for starting with circular apertures as initial guess and AMOR derives the best fitting ellipses. The parameter file for this study is given in the Table C.1 and will be described in detail in the next paragraphs.

The effective radius r_e is computed using the semi-major axis of the internally derived ellipse. Then, after asymmetry centering the Petrosian radius is derived in an elliptical aperture defined by the current ellipticity with a semi-major radius that is two times the current semi-major axis and an η of 0.2.

With the line **95 1 1 1** the basic parameters are recomputed from the current aperture and redefine the ellipse according the new computed position angle and ellipticity. The CI is then computed within this redefined ellipse.

Before the asymmetry is measured the galaxy is smoothed (97) with a Gaussian filter of (1) and a σ of (0.1) relative (1) to the galaxy radius (i.e., 0.1·2 Petrosian radii). The Gaussian curve is truncated at a σ of (3), the aperture is elliptical (1). This smoothing is important to make the asymmetry measurement sensitive only to large-scale distributions.

The asymmetry (7) is measured by rotating the source with 180° and subtract it from the original source, and taking the absolute value and the square of it. These pixel values will be then summed and normalized by the total flux of the original image (which is the image with either absolute value or the square of each pixel). Then both (2) values are printed out without noise correction (3). The asymmetry with absolute pixels is defined as

$$A = \frac{\sum_i |I - I_{180}|}{\sum_i I} \tag{C.1}$$

and the asymmetry derived with the square method is

$$A = \frac{\sum_i (I - I_{180})^2}{\sum_i I}. \tag{C.2}$$

The command (96) recovers the source that has been saved before the first use of the smoothing at (97).

In the last step the clumpiness of the targets is computed. The source is smoothed in the same way as described for the smoothing command line (97) and then creating a poststamp image of the smoothed source with suffix 2 and using the method with absolute and squared pixel values of the original image (2) but without noise correction (3). The clumpiness with absolute pixels is defined as

$$S = \frac{\sum_i |I - B|}{\sum_i I} \tag{C.3}$$

Table C.1: AMOR Control File for the Computation of CAS Morphological Parameters

Code	Description
stamps/	Path for the newly created stamps
%	Name of the stamps
1	Start with elliptical aperture
1	Half-light radius computed using ellipses
0	Do not printout basic parameters here
99 1 -0.2 2	Change the aperture: ellipse with 2*Petrosian radii
10 0.3 0 0 3 1	Search the minimum asymmetry by dithering around
99 1 -0.2 2	Change the aperture after asymmetry centering: ellipse with 2*Petrosian radii
95 1 1 1	Recompute basic parameters & redefine ellipse accordingly
2 0.9 0.5 1	Concentration index using ellipses
97 1 0.1 1 3 1	Smooth source with a Gaussian
7 2 3	Asymmetry with 180° rotation and compare with original
96	Recover saved source from before smoothing
9 1 0.1 1 3 1 1 2 3	Clumpiness smoothing the source and compare with original

and for the square method

$$S = \frac{\sum_i (I - B)^2}{\sum_i I} \tag{C.4}$$

with B as the image after smoothing like described in the command (97) above. Although we derived the asymmetry and the clumpiness with both methods, i.e., using the absolute values of the pixels and the squared values of the pixels, we use only the method of the absolute values for our interpretation. The results derived with the square method are only shown for comparison. The reason for that is that the method with the absolute values is better to detect large scale variations and therefore more practical for our objects. The square method is more interesting for small and faint objects with variations in the size of pixels. Therefore this method is more sensitive for distant galaxies in deep field images. The results are shown in Table 5.8. The typical error for the A180AB is 0.005. For the CLUAB the typical error is 0.01. The typical error for the CI is 0.01.

Appendix D

Observed Galaxies in the Near Infrared

The following figures present the full target sample from the K_s band observation with the NTT. The right side of the figures shows the target galaxy and the left side shows the residual image of the target after the fitted elliptical isophotes were subtracted.

Figure D.1: 1A. The scale is 3.55×2.06 arcmin.

Figure D.2: 1B. The scale is 3.55×2.06 arcmin.

Figure D.3: 1C. The scale is 3.55×2.06 arcmin.

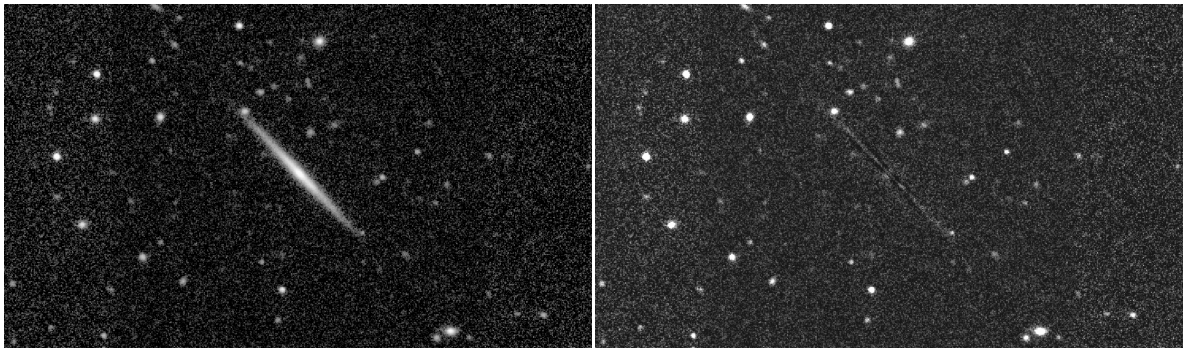

Figure D.4: 1D. The scale is 3.55×2.06 arcmin.

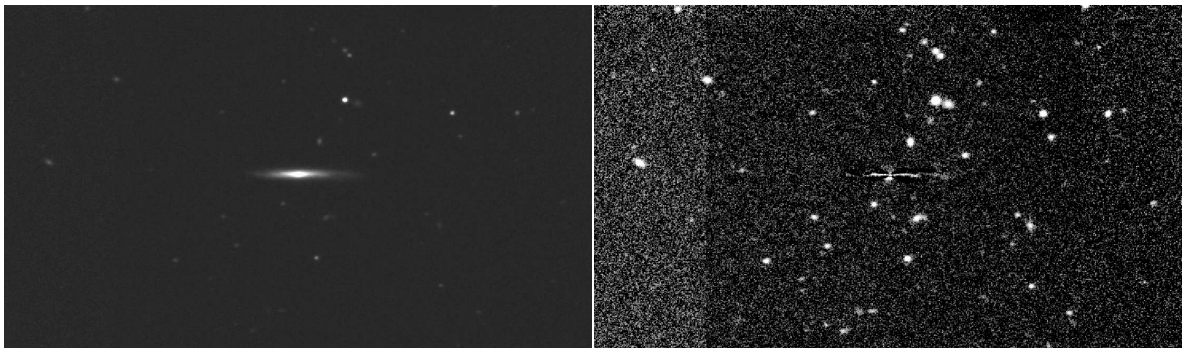

Figure D.5: 1E. The scale is 3.55×2.06 arcmin.

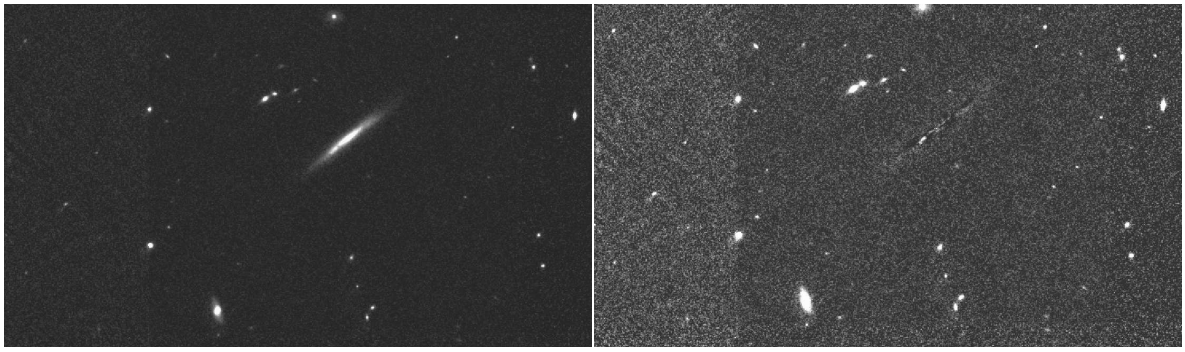

Figure D.6: 2B. The scale is 3.55×2.06 arcmin.

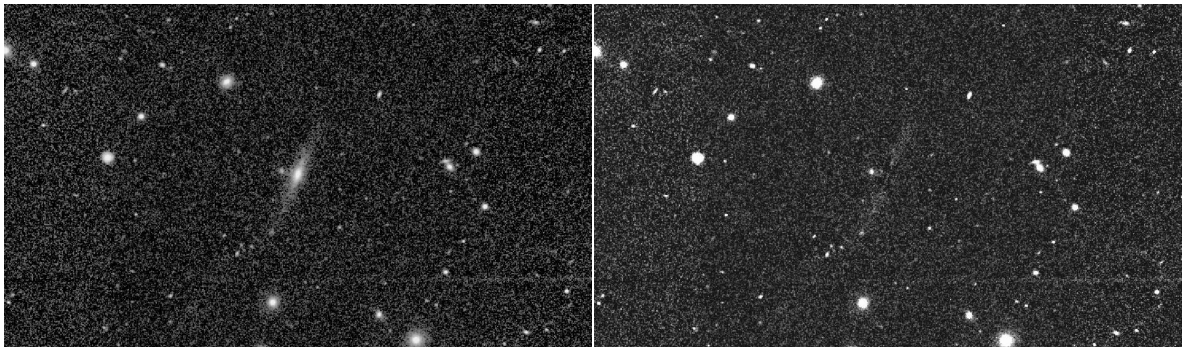

Figure D.7: 2C. The scale is 3.55×2.06 arcmin.

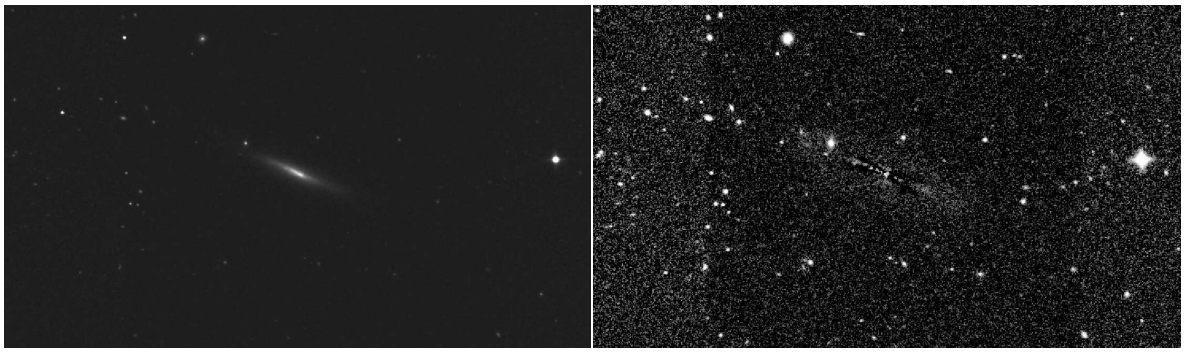

Figure D.8: 2D. The scale is 3.55×2.06 arcmin.

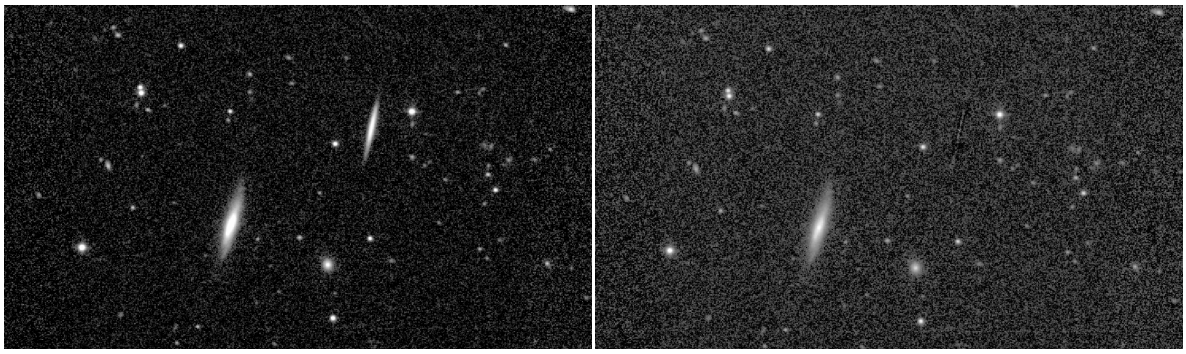

Figure D.9: 2E. The scale is 3.55×2.06 arcmin.

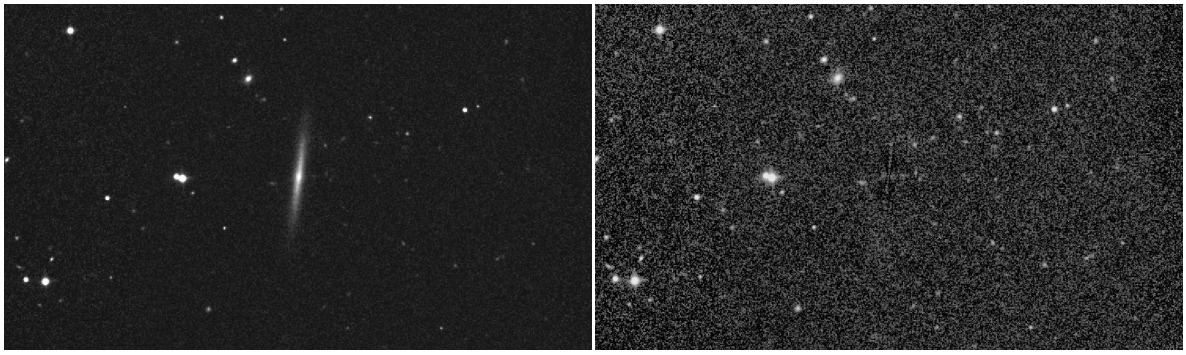

Figure D.10: 2Ealtern. The scale is 3.55×2.06 arcmin.

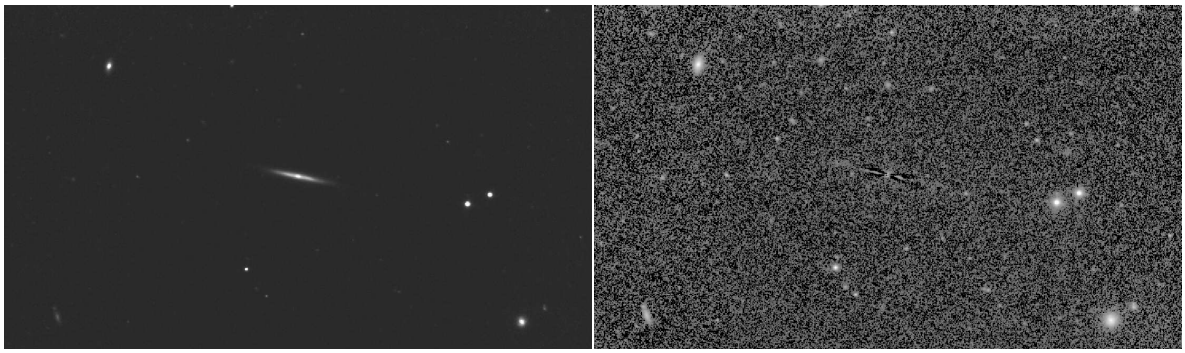

Figure D.11: 3A. The scale is 3.55×2.06 arcmin.

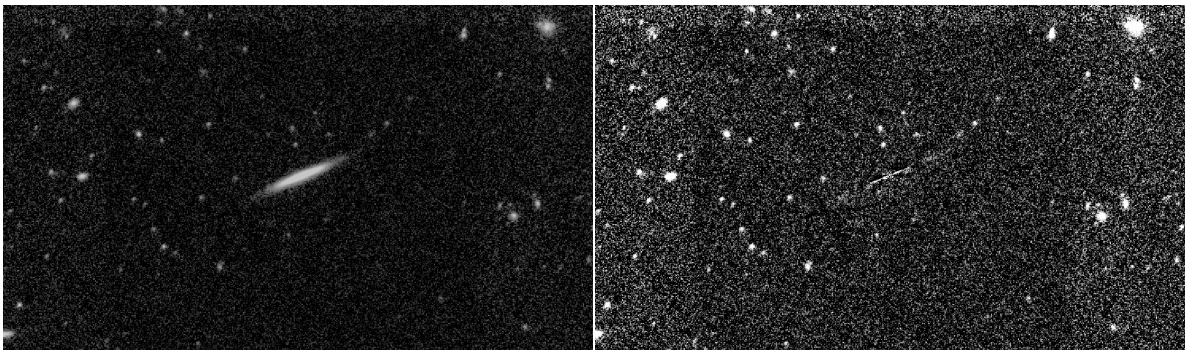

Figure D.12: 3B. The scale is 3.55×2.06 arcmin.

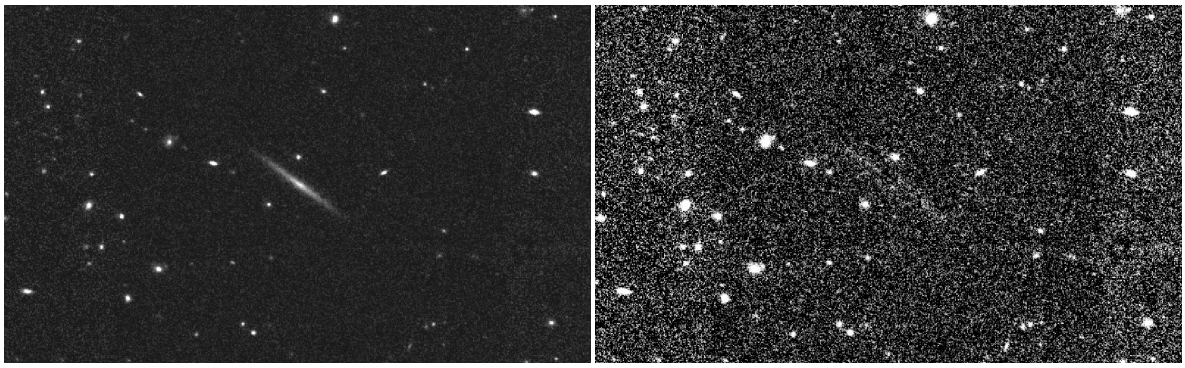

Figure D.13: 3C. The scale is 3.55×2.06 arcmin.

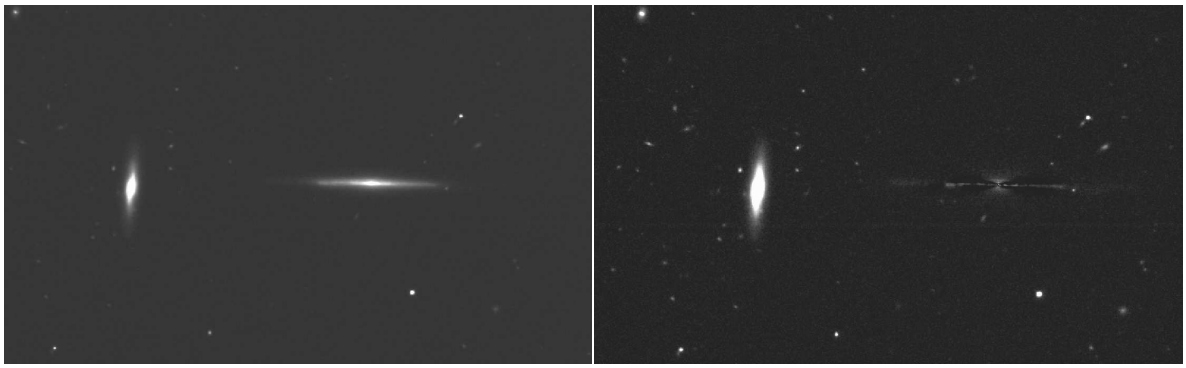

Figure D.14: 3D. The scale is 3.55×2.06 arcmin.

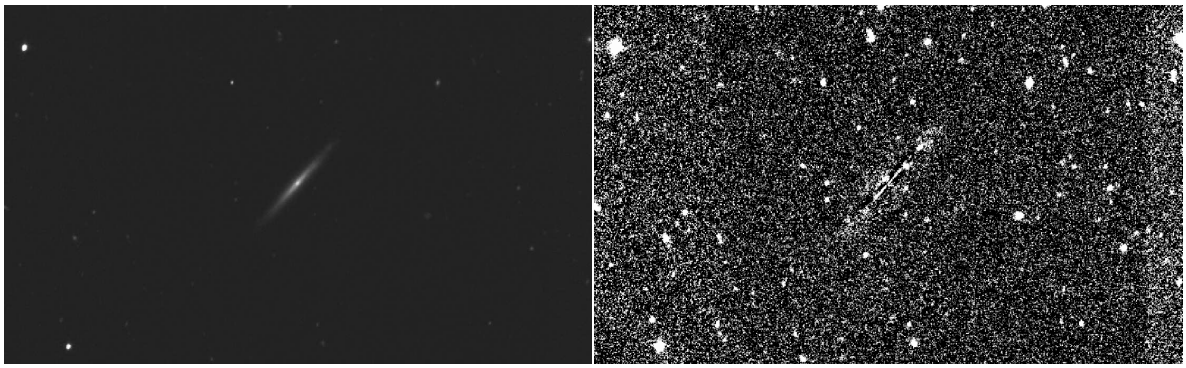

Figure D.15: 3E. The scale is 3.55×2.06 arcmin.

Figure D.16: 3Ealtern. The scale is 3.55×2.06 arcmin.

Bibliography

Abadi, M. G., Navarro, J. F., Steinmetz, M., & Eke, V. R. 2003a, ApJ, 591, 499

Abadi, M. G., Navarro, J. F., Steinmetz, M., & Eke, V. R. 2003b, ApJ, 597, 21

Abazajian, K., et al. 2003, AJ, 126, 2081

Abazajian, K., et al. 2004, AJ, 128, 502

Abazajian, K., et al. 2005, AJ, 129, 1755

Abell, G. O., Corwin, H. G., Jr., & Olowin, R. P. 1989, ApJS, 70, 1

Abraham, R. G., van den Bergh, S., & Nair, P. 2003, ApJ, 588, 218

Adelman-McCarthy, J. K., et al. 2005, ApJS, submitted (astro-ph/0507711)

Aguilar, L., Hut, P., & Ostriker, J. P. 1988, ApJ, 335, 720

Allam, S. S., Tucker, D. L., Lee, B. C., & Smith, J. A. 2005, AJ, 129, 2062

Athanassoula, E. 2005a, MNRAS, 358, 1477

Athanassoula, E. 2005b, preprint (astro-ph/0510808)

Avila-Reese, V., Colín, P., Gottlöber, S., Firmani, C., & Maulbetsch, C. 2005, ApJ, 634, 51

Barteldrees, A., & Dettmar, R.-J. 1994, A&AS, 103, 475

Baugh, C. M., Cole, S., & Frenk, C. S. 1996, MNRAS, 283, 1361

Becker, W. 1965, ZA, 62, 54

Becker, W. 1972, Quarterly Journal of the Royal Astronomical Society, 13, 226

Becker, W. 1980, A&A, 87, 80

Beers, T., & Sommer-Larsen, J. 1995, ApJS, 96, 175

Bell, E. F., & de Jong, R. S. 2001, ApJ, 550, 212

Bender, R., & Moellenhof, C. 1987, A&A, 177, 71

Benson, A. J., Lacey, C. G., Frenk, C. S., Baugh, C. M., & Cole, S. 2004, MNRAS, 351, 1215

Bergvall, N., & Rönnback, J. 1995, MNRAS, 273, 603

Bernardi, M., Sheth, R. K., Annis, J., et al. 2003, AJ, 125, 1817

Bernardi, M., Sheth, R. K., Nichol, R. C., Schneider, D. P., & Brinkmann, J. 2005, AJ, 129, 61

Bernstein, G. M., & Jarvis, M. 2002, AJ, 123, 583

Bershady, M. A., Jangren, A., & Conselice, C. J., 2000, AJ, 119, 2645

Bertin, E., & Arnouts, S. 1996, A&AS, 117, 393

Bizyaev, D., & Kajsin, S. 2004, AJ, 613, 886

Bizyaev, D., & Mitronova, S., 2002, A&A. 389, 795

Blanton, M. R., et al. 2001, AJ, 121, 2358

Bothun, G. D., Schombert, J. M., Impey, C. D., Sprayberry, D., & McGaugh, S. S. 1993 AJ, 106, 530

Böker, T., Lisenfeld, U., & Schinnerer, E. 2003, A&A, 406, 87

Bruzual, G., & Charlot, S. 2003, MNRAS, 344, 1000

Brook, C. B., Kawata, D., Gibson, B. K., & Freeman, K. C. 2004 ApJ, 612, 894

Brook, C. B., Gibson, B. K., Martel, H., & Kawata, D. 2005, ApJ, 630, 298

Brook, C. B., Kawata, D., Martel, H., Gibson, B. K., & Bailin, J. 2006, ApJ, 639, 126

Bureau, M., & Athanassoula, E. 2005, ApJ, 626, 159

Burkert, A., Truran, J. W., & Hensler, G. 1992, ApJ, 391, 651

Burstein, D. 1979, ApJ, 234, 829

Buser, R. 2000, Science, 287, 69

Buser, R., Rong, X. J., & Karaali, S. 1999, A&A, 348, 98

Caldwell, B., & Bergvall, N. 2006, Poster contribution to the IAU General Assambly 2006

Carney, B. W. 2001 in Star Clusters, Saas-Fee Advanced Course 28, L. Labhardt and B. Binggeli editors (Berlin: Sringer-Verlag), 1

Carter, B. S., & Meadows, V. S. 1995, MNRAS, 276, 734

Chen, B., Stoughton, C., Smith, J. A. et al. 2001, ApJ, 553, 184

Chiba, M., & Beers, T. C. 2000, AJ, 119, 2843

Cole, S. M., Baugh, C., Frenk, C., Lacey, C., & Benson, A. 2000, Phil. Trans. R. Soc. Lond. A, 358, 2093

Cortés, J. R., Kenney, J. D. P., & Hardy, E. 2006, AJ, 131, 747

Conselice, C. J., 2003 ApJS, 147,1

Conselice, C. J., Bershady, M. A., & Gallagher, J. S., 2000a, A&A, 354, L21

Conselice, C. J., Bershady, M. A., & Jangren, A., 2000b, ApJ, 529, 886

Conselice, C. J., Gallagher, J. S., III, & Wyse, R. F. G. 2002, AJ, 123, 2246

Couch, W. J., & Sharples, R. M. 1987, MNRAS, 229, 423

Cutry, R. M., & Skrutskie, M. F., 1998, BAAS, 30, 1374

Dalcanton, J. J., & Bernstein, R. A. 2000, AJ, 120, 203

Dalcanton, J. J., & Bernstein, R. A. 2002, AJ, 124, 1328

Dalcanton, J. J., Spergel, D. N., & Summers, F. J. 1997, ApJ, 482, 659

Dalcanton, J. J., Yoachim, P., & Bernstein, R. A. 2004, ApJ, 608, 189

D'Onghia, E., & Burkert, A. 2004, ApJl, 612, 13

de Grijs, R., & Peletier, R. F. 1997, A&A,320L, 21

de Grijs, R., Peletier, R. F., van der Kruit, P. C. 1997, A&A, 327, 966

de Grijs, R., & van der Kruit, P. C. 1996, A&AS, 117, 19

de Vaucouleurs, G. 1959, Handbuch der Physik, Vol. 53, Astrophysik IV: Stellar Systems (Berlin, Goettingen, Heidelberg: Springer-Verlag)

de Vaucelours, G. 1948, Ann. Astrophys, 11, 247

Diaferio, A., Kauffmann, G., Balogh, M. L., et al. 2001, MNRAS, 323, 999

Dressler, A. 1980, ApJ, 236, 351

Eggen, O. J. 1977 ApJ, 215, 812

Eggen, O. J., Lynden-Bell, D., & Sandage, A. R. 1962, ApJ, 136, 748

Elmegreen, B. G. 2002, ApJ, 577, 206

Fall, S. M., & Efstathiou, G. 1980, MNRAS, 193, 189

Fenkart, R. 1989, A&AS, 81, 187

Freeman, K. C. 1970, ApJ, 160, 811

Freeman, K. C. 1978, in Structure and Properties of nearby Galaxies, IAU Symp. 77, E. M. Berkhuijsen & R. Wielebinsky editors, (Dortrecht: Reidel), 3

Freeman, K. C. 1980, in Photometry, Kinematics, and Dynamivs in Galaxies, D. S. Evans editor, (Austin: Univ. of Texas Press), 85

Freeman, K. C. 1987, ARAA, 25, 603

Freeman, K. C. 1996, in New Light on Galaxy Evolution, IAU Symp. 171, R. Bender & R. L. Davies editors, (Dortrecht: Kluwer), 3

Fry, A. M., Morrison, H. L., Harding, P., Boroson, T. A. 1999, AJ, 118, 1209

Fujimoto, M. 1968, ApJ, 152, 523

Fujita, Y. 2004, PAS Jap., 56, 29

Gallagher, J. S., & Hudson, H. S. 1976, ApJ, 209, 389

Gardner, J. P. 2001, ApJ, 557, 616

Genzel, R., Eckart, A., Ott, T., & Eisenhauer, F. 1997, MNRAS, 291, 219

Ghigna, S., Moore, B., Governato, F., et al. 1998, MNRAS, 300, 146

Gilmore, G. 1995, in Stellar Populations, IAU Symp. 164, P. C. van der Kruit & G. Gilmore editors (Dortrecht: Kluwer), 99

Gilmore, G., & Reid, N. 1983, MNRAS, 202, 1025

Goad, J. W., & Roberts, M. S. 1979, BAAS, 11, 668

Goad, J. W., & Roberts, M. S. 1981, ApJ, 250, 79

Gómez, P. L., Nichol, R. C., Miller, C. J., et al. 2003, ApJ, 584, 210

Gordon, K. D., Misselt, K. A., Witt, A. N., & Clayton, G. C. 2001, ApJ, 551, 269

Goto, T., Yamauchi, C., Fujita, Y., et al. 2003, MNRAS, 346, 601

Governato, F., Mayer, L., Wadsley, J., et al. 2004, ApJ, 607, 688

Graham, A. W., Trujillo, I., & Caon, N. 2001, AJ, 122, 1707

Grogin, N. A., & Geller, M. J. 1999, AJ, 118, 2561

Grogin, N. A., & Geller, M. J. 2000, AJ, 119, 32

Gunn, J. E., & Gott, J. R., III 1972, ApJ, 176, 1

Guthrie, B. N. G. 1992, A&AS, 93, 255

Hartwick, F. D. A. 2000, AJAJ, 119, 2248

Heidmann, J., Heidmann, N., & de Vaucouleurs, G. 1972, Men. R. A. S., 75, 85

Henry, R. B. C. & Worthey, G. 1999, PASP, 111, 919

Hernandez, X., & Cervantes-Sodi, B. 2006, MNRAS, 368, 351

Hoyle, F., Rojas, R. R., Vogeley, M. S., & Brinkmann, J. 2005, ApJ, 620, 618

Immeli, A., Samland, M., Gerhard, O., & Westera, P. 2004, A&A, 413, 547

Jones, M. H., & Lambourne, R. J. A. An introduction to galaxies and cosmology, Cambridge, UK: Cambridge University Press, 2004

Karachentsev, I. 1989, AJ, 97, 1566

Karachentsev, I. D. 1991, Soviet Astronomy Letters, 17, 4

Karachentsev, I. D. 1999, Astronomy Letters, 25, 318

Karachentsev, I. D. 2005, AJ, 129, 178

Karachentsev, I. D., & Karachentseva, V. E. 1974, Astronomicheskii Zhurnal, 51, 724

Karachentsev, I. D., & Xu, Z. 1991, Soviet Astronomy Letters, 17, 135

Karachentsev, I. D., & Marakov D. A. 1996 AJ, 111, 94

Karachentsev, I. D., Karachentseva, V. E., & Parnovskij, S. L. 1993, Astronomische Nachrichten, 314, 97

Karachentsev, I. D., Karachentseva, V. E., Kudrya, Y. N., & Parnovsky, S. L. 1997, Astronomy Letters, 23, 573

Karachentsev, I. D., Karachentseva, V. E., Kudrya, Yu. N., Sharina, M. E., & Parnovsky, S. L. 1999, Bull. Special Astrophys. Obs., 47, 5

Karachentsev, I. D., Mitronova, S. N., Karachentseva, V. E., Kudrya, Yu. N., & Jarrett, T. H. 2002, A&A, 396, 431

Karachentsev, I. D., Karachentseva, V. E., Huchtmeier, W. K., & Makarov, D. I. 2004 AJ, 127, 2031

Karachentseva, V. E. 1973, Soobshch. Spets. Astrofiz. Obs., 8, 3

Kauffmann, G. 1996, MNRAS, 281, 487

Kauffmann, G., White, S. D. M., Heckman, T. M., et al. 2004, MNRAS, 353, 713

Kauffmann, G., & White, S. D. M. 1993, MNRAS, 261, 921

Kautsch, S. J., & Grebel, E. K. 2003a, Astronomical Notes Supplementary Issue 3, 324, 149

Kautsch, S. J., & Grebel, E. K. 2003b, ETH-BIB (Zürich), http://e-collection.ethbib.ethz.ch/show?type=poster&nr=8

Kautsch, S. J., & Grebel, E. K. 2004, Astron. Nachr. Suppl., 325 (S1), 50

Kautsch, S. J., Grebel, E. K., & Gallagher, J. S. 2005, Astron. Nachr., 326, 496

Kautsch, S. J., Grebel, E. K., Barazza, F. D., & Gallagher, J. S. 2006a, A&A, 445, 765

Kautsch, S. J., Grebel, E. K., Barazza, F. D., & Gallagher, J. S. 2006b, A&A, 451, 1171

Kautsch, S. J., & Grebel, E. K. 2003, Astron. Nachr. Suppl., 324 (S3), 149

Kelly, B. C., & McKay, T. A. 2004, AJ, 127, 625

Kennicutt, R. J., Jr. 1989, ApJ, 344, 685

Kerber, L. O., Javial, S. C., & Santiago, B. X. 2001, A&A, 365, 424

Kniazev, A. Y., Grebel, E. K., Pustilnik, S. A., Pramskij, A. G., Kniazeva, T. F., Prada, F., & Harbeck, D. 2004a, AJ, 127, 704

Kniazev, A. Y., Pustilnik, S. A., Grebel, E. K., Lee, H., & Pramskij, A. G. 2004b, ApJs, 153, 429

Koch, A., & Grebel, E. K. 2006, AJ, 131, 1405

Kormendy, J. & Kennicutt, R. C., Jr. 2004, ARAA, 42, 603

Kormendy, J. & Fisher, D. B. 2005, in The Ninth Texas-Mexico Conference on Astrophysics, RevMexA&A, (Serie de Conferencias), 23, 101

Kroupa, P. 2002, MNRAS, 330, 707

Kroupa, P., Theis, C., & Boily, C. M. 2005, A&A, 431, 517

Kuchinsky, L. E., Terndrup, D. M., Gordon, K. D., & Witt, A. D. 1998, AJ, 115, 1438

Kuehn, F., & Ryden, B. S. 2005, ApJ, 634, 1032

Kylafis, N. D., & Xilouris, E. M. 2005, AIP Conf. Proc., vol. 761, in The Spectral Energy Distributions of Gas-Rich Galaxies: Confronting Models with Data, ed. C. C. Popescu, & R. J. Tuffs (Melville: AIP), 3

Lacey, C., & Cole, S. 1993, MNRAS, 262, 627

Larsen, J. A., & Humphreys R. M. 2003, AJ, 125, 1958

Lee, J. 2006, ApJ, 644L, 5

Lewis, I., Balogh, M., De Propris, R., et al. 2002, MNRAS, 334, 673L

Li, Y., Mac Low, M., & Klessen, R. S. 2006, ApJ, 639, 879

Lisenfeld, U., & Ferrara, A.1998, Apj, 496, 145

Lotz, J. M., Primack, J., & Madau, P. 2004, AJ, 128, 163

Lütticke, R., Dettmar, R.-J., & Pohlen, M. 2000, A&A, 362, 435

Majewski, S. 1994, ApJ, 431, L17

Mastropietro, C., Moore, B., Mayer, L., et al. 2005, MNRAS, 364, 607

Matthews, L. D. 2000, AJ, 120, 1764

Matthews, L. D. & Gallagher, J. S. 1997, AJ, 114, 1899

Matthews, L. D., & van Driel, W. 2000, A&AS, 143, 421

Matthews, L. D., & Gao, Y. 2001, ApJ, 549L, 191

Matthews, L. D., & Wood, K. 2001, ApJ, 548, 150

Matthews, L. D., & de Grijs, R. 2004, AJ, 128, 137

Matthews, L., & Uson, J. M. 2004, in Baryons in Dark Matter Halos, R.-J. Dettmar, U. Klein, P. Salucci, editors (Trieste: SISSA), 70

Matthews, L. D., van Driel, W., & Gallagher, J. S. 1999a, preprint (astro-ph/9911022)

Matthews, L. D., Gallagher, J. S., & van Driel, W. 1999b, AJ, 118, 2751

Matthews, L. D., van Driel, W., & Monnier-Ragaigne, D. 2001, A&A, 365, 1

Matthews, L. D., Gao, Y., Uson, J. M., & Combes, F. 2005, AJ, 29, 1849

Melnick, J., & Sargent, W. L. W. 1977, ApJ, 215, 401

Minkowski, R., & Abell, G. O. 1963, Stars and Stellar Systems, Vol. 3, Basic Astronomical Data (Chicago: Univ. Chicago Press)

Misiriotis, A., & Bianchi, S. 2002, A&A, 384, 866

Mitronova, S. N., Karachentsev, I. D., Karachentseva, V. E., Jarrett, T. H., & Kudrya, Yu. N. 2004, Bull. Special Astrophys. Obs., 57, 5

Moore, B., Lake, G., & Katz, N. 1998, ApJ, 495, 139

Moore, B., Lake, G., Quinn, T., & Stadel, J. 1999, MNRAS, 304, 465

Nagashima, M., Yahagi, H., Enoki, M., Yoshii, Y., & Gouda, N. 2005, ApJ, 634, 26

Nakamura, O., Fukugita, M., Yasuda, N., et al. 2003, AJ, 125, 1682

Nakamura, O., Fukugita, M., Yasuda, N., Loveday, J., Brinkmann, J., Schneider, D. P., Shimasaku, K., & SubbaRao, M. 2003, AJ, 125, 1682

Narayan, C. A., & Jog, C. J. 2002, A&A, 390, L35

Nilson, P., 1973, Uppsala General Catalogue of Galaxies, 1973, Acta Universitatis Upsalienis, Nova Regiae Societatis Upsaliensis, Series v: a Vol.

Noguchi, M. 2000, MNRAS, 312, 194

Noguchi, M. 2001, ApJ, 555, 289

Parodi, B. R., Barazza, F. D., & Binggeli, B. 2002, A&A, 388, 29

Paturel, G., Fouque, P., Bottinelli, L., & Gouguenheim, L. 1989, A&AS, 80, 299

Persson, S. E., Murphy, D. C., Krzeminski, W., Roth, M., & Rieke, M. J., 1998, AJ, 116, 2475

Petrosian, V. 1976, ApJ, 209, L1

Pohlen, M., Dettmar, R.-J., Lütticke, R., & Schwarzkopf, U. 2000, A&As, 144, 405

Pohlen, M., & Trujillo, I. 2006, astro-ph/0603682

Popescu, C. C., Misiriotis, A., Kylafis, N. D., Tuffs, R. J., & Fischera, J. 2000, A&A, 362, 138

Ogorodnikov, K. F. 1957, Soviet Astronomy, 1, 748

Ogorodnikov, K. F. 1958, Soviet Astronomy, 2, 375

Ojha, D. K., Bienaymé, O., Robin, A. C., & Mohan, V. 1994, A&A, 290, 771

Okamoto, T., Eke, V. R., Frenk, C. S., & Jenkins, A. 2005, MNRAS, 363, 1299

Okamura, S., Kodaira, K., & Watanabe, M. 1984, ApJ, 280, 7

Oemler, A., Jr. 1974, ApJ, 194, 1

Okamoto, T., & Nagashima, M. 2001, ApJ, 547, 109

Okamoto, T., & Nagashima, M. 2003, ApJ, 587, 500

Ostriker, J. P., & Peebles, P. J. E. 1973, ApJ, 186, 467

Prada, F., Vitvitska, M., Klypin, A. et al. 2003, ApJ, 598, 260

Pearce, F. R., Jenkins, A., Frenk, C. S. et al. 2001, MNRAS, 326, 649

Pfleiderer, J., & Siedentopf, H. 1961, Zeitschrift für Astrophysik, 51, 201

Pfleiderer, J. 1963, Zeitschrift für Astrophysik, 58, 12

Postman, M., & Geller, M. J. 1984, ApJ, 281, 95

Quinn, P., Hernquist, L., & Fullagar, D. 1993, ApJ, 403, 74

Qirk, W. J. 1972, ApJ, 176L, 9

Ramella, M., Geller, M. J., Pisani, A., & da Costa, L. N. 2002, AJ, 123, 2976

Reid, I. N., et al. 1991, PASP, 103, 661

Reid, N, & Majewski, S. R. 1993, Apj, 409, 635

Reshetnikov, V. P. 1995, Astronomical and Astrophysical Transactions, 8, 31

Reshetnikov, V., & Combes, F. 1997 A&A, 324, 80

Rice, W., Merrill, K. M., Gatley, I., Gillett, F. C., 1996 AJ, 112, 114

Rix, H.-W., & Rieke, M. J. 1993, ApJ, 418, 123

Robertson, B., Hernquist, L., Bullock, J. S., Cox, T. J., Di Matteo, T., Springel, V. & Yoshida, N. 2005, preprint (astro-ph/0503369)

Roediger, E., & Hensler, G. 2005, A&A, 433, 875

Rojas, R. R., Vogeley, M. S., Hoyle, F., & Brinkmann, J. 2004, ApJ, 617, 50

Rojas, R. R., Vogeley, M. S., Hoyle, F., & Brinkmann, J. 2005, ApJ, 624, 571

Rosenbaum, S. D., & Bomans, D. J. 2004, A&A, 422L, 5

Samland, M. 2004, PASA, 21, 175

Samland, M., & Gerhard, O. E. 2003, A&A, 399, 961

Sandage, A., & Tammann, G. A. 1981, A Revised Shapley-Ames Catalog of Bright Galaxies (Washington: Carnegie Institute)

Sandage, A. R., & Fouts, G. 1987, AJ, 93, 74

Sandage, A., & Binggeli, B. 1984, AJ, 89, 919

Sawa, T., & Fujimoto, M. 2005, PAS Jap, 57, 429

Schlegel, D. J., Finkbeiner, D. P., & Davis, M. 1998, ApJ, 500, 525

Schombert, J. M., Bothun, G. D., Schneider, S. E., & McGaugh, S. S. 1992, AJ, 103, 1107

Schwarzkopf, U., & Dettmar, R.-J. 2000, A&AS, 144, 85

Schwarzkopf, U., & Dettmar, R.-J. 2000, A&A, 361, 451

Searle L., & Zinn, R. 1978, ApJ, 225, 357

Seth, A. C., Dalcanton, J. J., Hodge, P. W., & Debattista, V. P. preprint (astro-ph/0606066)

Shen, S., Mo, H. J., White, S. D. M., Blanton, M. R., Kauffmann, G., Voges, W., Brinkmann, J., & Csabai, I. 2003, MNRAS, 343, 978

Shimasaku, K., et al. 2001, AJ, 122, 1238

Skrutskie, M. F., Schneider, S. E., Stiening, R., et al. 1997, in: The impact of Large Scale Near-IR Sky Surveys, F. Garzon et al. editors, (Dortrecht: Kluwer) 25

Sommer-Larsen, J., Goetz, M., & Portinari, L. 2003, ApJ, 596, 47

Sotnikova, N. Ya., & Rodionov, S. A. 2006 preprint (astro-ph/0609163), to appear in Astronomy Letters

Springel, V., & Hernquist, L. 2005, ApJ, 622, L9

Steinmetz, M. 2003, APSS, 284, 325

Steinmetz, M., & Navarro, J. F. 2002, Nature, 7, 155

Stevens, J. A., Amure, M., & Gear, W. K. 2005, MNRAS, 357, 361

Stocke, S. T., Keeney, B. A., Lewis, A. D., Epps, H. W., & Schild, R. E. 2004, AJ, 127, 1336

Stoughton, C., et al. 2002, AJ, 123, 485

Strateva, I., et al. 2001, AJ, 122, 1861

Strauss, M. A., et al. 2002, AJ, 124, 1810

Sulentic, J. W., Verdes-Montenegro, L., Bergond, G., et al. 2006, A&A, 449, 937

Taylor, J. E., & Babul, A. 2003, APSS, 284, 405

Teerikorpi, P. 1997, Ann Rev A&A, 35, 101

Thomas, T. & Katgert, P. 2006, A&A, 446, 31

Toomre, A. 1977, in Evolution of Galaxies and Stellar Populations, B. M. Tinsley & R. B. Larsen, editors (New Haven: Yale University Observatory), 402

Tran, K.-V. H., Simard, L., Zabludoff, A. I., & Mulchaey, J. S. 2001, ApJ, 549, 172

Tremaine, S. D., Ostriker, J. P., & Spitzer, L. 1975, ApJ, 196, 407

Tsikoudi, V. 1979, ApJ, 234, 842

Tuffs, R. J., Popescu, C. C., Völk, H. J., Kylafis, N. D., & Dopita, M. A. 2004, A&A, 419, 821

van der Kruit, P. C., & Searle, L. 1981a, A&A, 95, 105

van der Kruit, P. C., & Searle, L. 1981b, A&A, 95, 116

Varela, J., Moles, M., Mrquez, I., et al. 2004, A&A, 420, 873

Vincent, R. A., & Ryden, B. S. 2005, ApJ, 623, 137

Vorontsov-Vel'yaminov, B. 1967, in Modern Astrophysics, ed. M. Hack (Paris: Gauthier-Villars, Gordon, & Breach), 347

Vorontsov-Vel'yaminov, B. 1974, Soviet Astronomy, 17, 452

Westera, P., Samland, M., Buser, R., & Gerhard, O. E. 2002, A&A, 389, 761

Whitmore, B. C. 1995, in Groups of Galaxies. ASP Conference Series, Volume 70, O.-G. Richter, K. Borne, editors, (San Francisco: Astronomical Society of the Pacific), 41

Wielen, R. 1977, A&A, 60 263

Wild, V., Peacock, J. A., Lahav, O., et al. 2005, MNRAS, 356, 247

Williams, Y., Kelley, C., Denholm, D. et al. 1998, gnuplot An interactine Plotting Program, Version 3.7

Wood, M. A., Oswalt, T. D., & Smith, J. A. 1995, Bull. Am. Astron. Soc., 27, 1310

Wyse, R. F. G., & Gilmore, G. 1995, AJ, 110, 2771

Wyse, R. F. G., Gilmore, G., & Franx, M. 1997, Ann Rev A&A, 35, 673

Xilouris, E. M., Kylafis, N. D., Papamastorakis, J., Palealogou, E. V., & Haerendel, G. 1997, A&A, 325, 135

Xilouris, E. M., Alton, P. B., Davies, J. I., Kylafis, N. D., Papamastorakis, J., & Trewhella, M. 1998, A&A, 331, 894

Yasuda, N., et al. 2001, AJ, 122, 1104

Yoachim, P., & Dalcanton, J. J. 2005, ApJ, 624, 701

Yoachim, P., & Dalcanton, J. J. 2006, AJ, 131, 226

York, D. G., et al. 2000, AJ, 120, 1579

Zasov, A. V., Bizyaev, D. V., Makarov, D. I., & Tyurina, N. V. 2002, Astronomy Letters, 28, 527

Zibetti, S., & Ferguson, A. M. N. 2004, MNRAS, 352L, 6

Zibetti, S., White, S. D. M., & Brinkmann, J., 2004, MNRAS, 347, 556

Publications

Kautsch, S. J., Grebel, E. K., Barazza, F. D., and Gallagher, J. S. 2006, Astronomy and Astrophysics, "A Catalog of Edge-on Disk Galaxies: From Galaxies with a Bulge to Superthin Galaxies," 445, 765
Kautsch, S. J., Grebel, E. K., Barazza, F. D., and Gallagher, J. S. 2006, Astronomy and Astrophysics, "A Catalog of Edge-on Disk Galaxies: From Galaxies with a Bulge to Superthin Galaxies," 451, 1171
Kautsch, S. J., Grebel, E. K., Barazza, F. D., and Gallagher, J. S. 2006, VizieR On-line Data Catalog: J/A+A/445/765, "A Catalog of Edge-on Disk Galaxies"
Kautsch, S. J., Grebel, E. K., and Gallagher, J. S. 2005, Astronomical Notes, "The Influence of Environment on the Morphological Evolution of Disk Galaxies," 326, 496
Kautsch, S. J., Grebel, E. K., Barazza, F. D., and Gallagher, J. S. 2005, Astronomical Notes, "An Edge-on Disk Galaxy Catalog," 326, 595
Kautsch, S. J., Grebel, E. K., and Barazza, F. D. 2004, "A Survey for Flat Edge-On Galaxies," in Poster Papers of the STScI May Symposium, ed. M. Livio & S. Casertano, (Baltimore: Space Telescope Science Institute), 50
Kautsch, S. J., Grebel, E. K., and Barazza, F. D. 2004, Astronomical Notes Supplementary Issue 1, "Structure and Morphology of Flat Disk Galaxies," 325, 113
Kautsch, S. J., and Grebel, E. K. 2004, Astronomical Notes Supplementary Issue 1, "The Influence of Interaction on Flat Disk Galaxies," 325, 50
Kautsch, S. J., and Grebel, E. K. 2003, Astronomical Notes Supplementary Issue 3, "Properties of Flat Disk Galaxies," 324, 149
Kautsch, S. J., and Grebel, E. K. 2003, ETH-BIB (Zürich), "A Search for Pure Disk Galaxies," http://e-collection.ethbib.ethz.ch/show?type=poster&nr=8
Kautsch, S. J., and Zeilinger, W. W. 2003, Astronomical Notes Supplementary Issue 3, "Stellar Populations in the Centers of Active Early-Type Galaxies," 324, 153
Kautsch, S. J., and Zeilinger, W. W. 2003, Astronomical Notes Supplementary Issue 2, "UV Spectral Properties and Line Indices of Active Early-Type Galaxies," 324, 38
Kautsch, S. J., and Zeilinger, W. W. 2003, Astrophysics and Space Science, "UV and Optical Spectral Properties in Early-Type Galaxies," 284, 929
Kautsch, S. J., and Zeilinger, W. W. 2002, Hvar Observatory Bulletin, "Characteristics of Active Galactic Nuclei in the Ultraviolet," 26, 69
Kautsch, S. J., Zeilinger, W. W., Padoan, F., Rampazzo, R., and Pierfederici, F. 2001, Astronomische Gesellschaft Abstract Series, "The Spectral Energy Distribution of Early-Type Galaxies," 18, P 139
Jesacher, M. O., **Kautsch**, S. J., Kimeswenger, S., Muhlbacher, M. S., Saurer, W., Schmeja, S., and Scholz, C. K. 2000, IAU Circular, "CI Aquilae," 7426, 3

Erklärung

Ich erkläre, dass ich die Dissertation "The Nature of Flat Galaxies" nur mit der darin angegebenen Hilfe verfasst und bei keiner anderen Universität und keiner anderen Fakultät der Universität Basel eingereicht habe.

Stefan Johann Kautsch Binningen, den 7. Oktober 2006